Walter Lacarbonara
Balakumar Balachandran
Jun Ma · J. A. Tenreiro Machado
Gabor Stepan   *Editors*

Nonlinear Dynamics and Control

Proceedings of the First International
Nonlinear Dynamics Conference
(NODYCON 2019), Volume II

Springer

Nonlinear Dynamics and Control

Walter Lacarbonara • Balakumar Balachandran
Jun Ma • J. A. Tenreiro Machado • Gabor Stepan
Editors

Nonlinear Dynamics and Control

Proceedings of the First International Nonlinear Dynamics Conference (NODYCON 2019), Volume II

Springer

Editors
Walter Lacarbonara (iD)
Department of Structural and Geotechnical
Engineering
Sapienza University of Rome
Rome, Italy

Jun Ma
Department of Physics
Lanzhou University of Technology
Lanzhou, Gansu, China

Gabor Stepan
Department of Applied Mechanics
Budapest University of Technology
and Economics
Budapest, Hungary

Balakumar Balachandran
Department of Mechanical Engineering
University of Maryland
College Park, MD, USA

J. A. Tenreiro Machado
Department of Electrical Engineering
Polytechnic of Porto - School
of Engineering (ISEP)
Porto, Portugal

Preface

This volume is part of three volumes collecting the *Proceedings of the First International Nonlinear Dynamics Conference (NODYCON 2019)* held in Rome, February 17–20, 2019. NODYCON was launched to foster the tradition of the conference series originally established by Prof. Ali H. Nayfeh in 1986 at Virginia Polytechnic Institute and State University (Virginia Tech), Blacksburg, VA, USA, as the Nonlinear Vibrations, Stability, and Dynamics of Structures Conference. With the passing in 2017 of Prof. Nayfeh, who was also the founder of the Springer journal *Nonlinear Dynamics* in 1990, NODYCON 2019 was organized as a collective tribute of the community to Prof. Nayfeh for being one of the most influential leaders of nonlinear dynamics. NODYCON 2019 was also established to look to and dream about the future. The call for papers attracted contributions dealing with established nonlinear dynamics research topics as well as with the latest trends and developments. At the same time, to reflect the rich spectrum of topics covered by the journal *Nonlinear Dynamics*, the call included diverse and multidisciplinary topics, to mention a few, multi-scale dynamics, experimental dynamics, dynamics of structures/industrial machines/equipment/facilities, dynamics of adaptive, multifunctional, metamaterial structures, dynamics of composite/nanocomposite structures, reduced-order modeling, nonsmooth dynamics, fractional-order system dynamics, nonlinear interactions and parametric vibrations, computational techniques, nonlinear system identification, dynamics of NEMS/MEMS/nanomaterials, multibody dynamics, fluid/structure interaction, influence of nonlinearities on vibration control systems, human–machine interaction, nonlinear wave propagation in discrete and continuous media, chaotic map-based cryptography, ecosystem dynamics, social media dynamics, complexity in engineering, and network dynamics.

For NODYCON 2019, the organizers received 450 two-page abstracts and based on 467 reviews from the Program Committee, the Steering and Advisory Committees, and external reviewers, 391 papers and 17 posters were accepted, published in the Book of Abstracts (NODYS Publications, Rome, ISBN 978-88-944229-0-0), and presented by nearly 400 participants from 68 countries. The diverse topics covered by the papers were organized along four major themes to organize the technical sessions:

(a) Concepts and methods in nonlinear dynamics
(b) Nonlinear dynamics of mechanical and structural systems
(c) Nonlinear dynamics and control
(d) Recent trends in nonlinear dynamics

The authors of a selection of approximately 60 papers were invited to publish in the Special Issue of *Nonlinear Dynamics* entitled "NODYCON 2019 First International Nonlinear Dynamics Conference." Over 200 full papers were submitted to the *Proceedings of the First International Nonlinear Dynamics Conference* (NODYCON 2019) and only 121 of them were accepted. These papers have been collected into three volumes, which are listed below together with a sub-topical organization.

Volume 1: Nonlinear Dynamics of Structures, Systems, and Devices

(a) Methods for nonlinear dynamics
(b) Bifurcations and nonsmooth systems
(c) Nonlinear phenomena in mechanical systems and structures
(d) Experimental dynamics, system identification and monitoring
(e) Fluid–structure interaction, multibody system dynamics
(f) Turning processes, rotating systems, and systems with time delays

Volume 2: Nonlinear Dynamics and Control

(g) Vibration absorbers and isolators
(h) Control of nonlinear systems
(i) Sensors and actuators
(j) Network synchronization

Volume 3: New Trends in Nonlinear Dynamics

(k) Smart materials, metamaterials, composite and nanocomposite materials, and structures
(l) MEMS/NEMS and energy harvesters
(m) Nonlinear phenomena in bio- and ecosystem dynamics
(n) Chaos in electronic systems
(o) Fractional-order systems

I wish to acknowledge the work of the Co-Editors of the NODYCON 2019 Proceedings: Prof. Balakumar Balachandran (University of Maryland, College Park, MD, USA), Prof. Jun Ma (Lanzhou University of Technology, China), Prof. J. A. Tenreiro Machado (Instituto Superior de Engenharia do Porto, Portugal), Prof. Gabor Stepan (Budapest University of Technology and Economics, Hungary).

The success of NODYCON 2019 relied primarily on the efforts, talent, energy, and enthusiasm of researchers in the field of nonlinear dynamics who wrote and submitted these papers. Special praise is also deserved for the reviewers who invested significant time in reading, examining, and assessing multiple papers, thus ensuring a high standard of quality for this conference proceedings.

Rome, Italy   Walter Lacarbonara
August 2019

Preface for Volume 2: Nonlinear Dynamics and Control

Volume 2 of the NODYCON 2019 Proceedings is composed of 33 papers, in which different kinds of control are applied for nonlinear dynamical systems. The first section of this volume groups together ten papers; in these studies, the aim of the applied control is to absorb and/or isolate the vibrations of a physical system. The second section presents the results of 17 research papers, where the quality of the applied control strategies is assessed, or sophisticated nonlinear control strategies are implemented to achieve the desired behavior of a given dynamical system. The third section involves two papers in which the effects of nonlinearities within sensors and/or actuators are discussed. Finally, the four papers of the fourth section investigate synchronization phenomena in networks of nonlinear dynamical systems and coupled oscillators.

The primary view point of the grouping of the papers was the goal of the research and not the applied methodology. Independently from the actual placement of a paper in a given section, the authors make use of a wide range of experimental, analytical, and numerical techniques for study of nonlinear dynamics.

In the work of S. Mohanty and S. K. Dwivedy, an active nonlinear vibration absorber is analyzed for a harmonically excited beam system. Z. Lu, D.-H. Gu, Y.-W. Zhang, H. Ding, W. Lacarbonara, and L.-Q. Chen compare linear and nonlinear damping effects in case of a ring vibration isolator. T. Lebrun, M. Wijnand, T. Hélie, D. Roze, and B. d'Andréa-Novel numerically examine electroacoustic absorbers based on the passive finite-time control of the loudspeakers. The seismic response of multiple base-isolated structures is predicted by F. Potenza, V. Gattulli, and S. Nagarajaiah for monitoring purposes. H. S. Kizilay and E. Cigeroglu analyze liquid-filled column dampers by means of nonlinear modeling in the frequency domain. M. E. Dogan and E. Cigeroglu achieve vibration reduction by means of two tuned mass dampers with dry friction. The nonlinear behavior of pendulum-tuned mass dampers is examined by K. Xu, X. Hua, and Z. Chen for vibration control. Resonance behavior is studied by Y. Mikhlin and Anton Onizhuk in a non-ideal system containing a snap-through truss absorber. A. Salvatore, B. Carboni, L.-Q. Chen, and W. Lacarbonara experimentally study the dynamic response of

a nonlinear wire rope isolator. In the work of A. Boccamazzo, B. Carboni, G. Quaranta, and W. Lacarbonara, optimization strategies of hysteretic tuned mass dampers are discussed for seismic control.

A. Younespour and S. Cheng examine sliding mode control of nonlinear systems under nonstationary random vibrations via the equivalent linearization method. G. Stefani, M. De Angelis, and U. Andreaus discuss the experimental dynamic response of a harmonically excited SDOF oscillator constrained by two symmetrically arranged deformable and dissipative bumpers. Active sling load stabilization is considered by A. Morock, A. Arena, M. Lanzerotti, J. Capps, B. Huff, and W. Lacarbonara. In the work of D. Jing, J.-Q. Sun, C.-B. Ren, and X.-H. Zhang, the multi-objective optimization is studied for control of an active vehicle suspension system. P. Domański and M. Ławryńczuk assess the quality of nonlinear model predictive control by means of fractal and entropy measures. M. Gidlewski, L. Jemioł, and D. Żardecki analyze the impact of the controller algorithm on the motor vehicle steering during a lane-change manoeuver. The application of fractional-order impedance control is considered by G. Chen, S. Guo, B. Hou, J. Wang, and X. Wang. In the study of I. Krzysztofik and Z. Koruba, the quadcopter dynamics are analyzed during programmed movement and under external disturbance. The same authors study the nonlinear model of quadrotor dynamics during observation and laser target illumination. D. Li, C. Xu, M. Gola, and D. Botto consider the problem of reduced-order modeling of friction in case of the line contact in a turbine blade damper system. M. Galicki examines the finite-time control of omnidirectional mobile robots. L. Nesi, D. Antonelli, G. Pepe, and A. Carcaterra apply the feedback local optimality principle for rocket vertical landing. Time-delayed feedback control is applied by A. M. Tusset, J. M. Balthazar, R. T. Rocha, M. A. Ribeiro, W. B. Lenz, and F. C. Janzen for a non-ideal system with chaotic behavior. The distributed event-triggered output feedback control is used for semilinear time fractional diffusion systems by F. Ge and Y.-Q. Chen. Control performance assessment of the disturbance with fractional-order dynamics is carried out by K. Liu, Y.-Q. Chen, and P. Domański. The work of W. Tang, Y. Qi, and H. Gao addresses model correction-based multivariable predictive functional control for uncertain nonlinear systems.

J. Yuan, S. Fei, and Y.-Q. Chen investigate compensation strategies for actuator rate limit effect on first-order time-delay systems. The work of C.-E. Park, N. K. Kwon, and P.-G. Park examines the reliability of output feedback control for Markovian jump descriptor systems with sensor failure and actuator saturation.

L.-X. Yang and X.-J. Liu discuss the synchronization of coupled oscillatory networks with different node arrangements. The work of G. Panovko and A. Shokhin considers the synchronization of unbalance vibration exciters near resonance. J. P. Ramirez and J. Alvarez examine the mixed synchronization in unidirectionally coupled chaotic oscillators. Finally, in this volume, the effect of synchronized hopping induced by the interplay of coupling and noise is studied by M. Aravind, K. Murali, and S. Sinha.

We hope that readers will benefit from the collection of works here reported on the interplay between control and nonlinear dynamics and that these efforts will inspire new ideas in the future.

Rome, Italy	Walter Lacarbonara
College Park, MD, USA	Balakumar Balachandran
Lanzhou, China	Jun Ma
Porto, Portugal	J. A. Tenreiro Machado
Budapest, Hungary	Gabor Stepan
August 2019	

Contents

Contributors

Joaquin Alvarez CICESE, Applied Physics Division, Electronics and Tele-communications Department, Ensenada, BC, Mexico

Ugo Andreaus Department of Structural and Geotechnical Engineering,"Sapienza" University of Rome, Rome, Italy

Dario Antonelli Department of Mechanical and Aerospace Engineering, Sapienza University of Rome, Rome, Italy

Andrea Arena Department of Structural and Geotechnical Engineering, Sapienza University of Rome, Rome, Italy

Jose M. Balthazar Federal University of Technology—Paraná, Ponta Grossa, PR, Brazil

Balakumar Balachandran Department of Mechanical Engineering, University of Maryland, College Park, MD, USA

Antonio Boccamazzo Department of Structural and Geotechnical Engineering, Sapienza University of Rome, Rome, Italy

Daniele Botto Department of Mechanical and Aerospace Engineering, Politecnico di Torino, Torino, Italy

Jacob Capps USMA, Department of Physics and Nuclear Engineering, West Point, NY, USA

Biagio Carboni Department of Structural and Geotechnical Engineering, Sapienza University of Rome, Rome, Italy

Antonio Carcaterra Department of Mechanical and Aerospace Engineering, Sapienza University of Rome, Rome, Italy

Guangrong Chen Robotics Research Center, Beijing Jiaotong University, Beijing, China

Li-Qun Chen Shanghai Institute of Applied Mathematics and Mechanics, Shanghai University, Shanghai, China

YangQuan Chen Department of Mechanical Engineering (MESA-Lab), University of California, Merced, CA, USA

Zhengqing Chen Key Laboratory for Wind and Bridge Engineering of Hunan Province, College of Civil Engineering, Hunan University, Changsha, China

Shaohong Cheng Department of Civil and Environmental Engineering, University of Windsor, Windsor, ON, Canada

Ender Cigeroglu Department of Mechanical Engineering, Middle East Technical University, Ankara, Turkey

Brigitte d'Andréa-Novel CNRS, STMS Lab (UMR 9912, IRCAM-CNRS-SU), Paris, France

Maurizio De Angelis Department of Structural and Geotechnical Engineering,"Sapienza" University of Rome, Rome, Italy

Hu Ding Shanghai Institute of Applied Mathematics and Mechanics, Shanghai University, Shanghai, China

Muhammed Emin Dogan Department of Mechanical Engineering, Middle East Technical University, Ankara, Turkey

Paweł D. Domański Institute of Control and Computation Engineering, Warsaw University of Technology, Warsaw, Poland

S. K. Dwivedy Department of Mechanical Engineering, Indian Institute of Technology Guwahati, Guwahati, Assam, India

Shumin Fei Key Laboratory of Measurement and Control of CSE, Ministry of Education, School of Automation, Southeast University, Nanjing, China

Mirosław Galicki University of Zielona Góra, Zielona Góra, Poland

Haiyan Gao High-Voltage Key Laboratory of Fujian Province, Xiamen University of Technology, Xiamen, China

Vincenzo Gattulli Department of Structural and Geotechnical Engineering, Sapienza University of Rome, Rome, Italy

Fudong Ge School of Computer Science, China University of Geosciences, Wuhan, China

Mirosław Gidlewski Automotive Industry Institute (PIMOT), Warsaw, Poland University of Technology and Humanities (UTH), Radom, Poland

Muzio Gola Department of Mechanical and Aerospace Engineering, Politecnico di Torino, Torino, Italy

Dong-Hao Gu Shanghai Institute of Applied Mathematics and Mechanics, Shanghai University, Shanghai, China

Mengke Guo College of Electrical and Information Engineering, Lanzhou University of Technology, Lanzhou, China

Sheng Guo Robotics Research Center, Beijing Jiaotong University, Beijing, China

Thomas Hélie CNRS, STMS Lab (UMR 9912, IRCAM-CNRS-SU), Paris, France

Bowen Hou Beijing Engineering and Technology Research Center of Rail Transit Line Safety and Disaster Prevention, Beijing, China

Xugang Hua Key Laboratory for Wind and Bridge Engineering of Hunan Province, College of Civil Engineering, Hunan University, Changsha, China

Blake Huff USMA, Department of Physics and Nuclear Engineering, West Point, NY, USA

Frederic C. Janzen Federal University of Technology—Paraná, Ponta Grossa, PR, Brazil

Leszek Jemioł University of Technology and Humanities (UTH), Radom, Poland

Dong Jing School of Transportation and Vehicle Engineering, Shandong University of Technology, Zibo, Shandong, China

H. Sefa Kizilay Middle East Technical University, Ankara, Turkey

Zbigniew Koruba Kielce University of Technology, Kielce, Poland

Izabela Krzysztofik Kielce University of Technology, Kielce, Poland

Nam Kyu Kwon Division of Electrical Engineering, Yeungnam Unicersity, Gyeongsan, Korea

Walter Lacarbonara Department of Structural and Geotechnical Engineering, Sapienza University of Rome, Rome, Italy

Mary Lanzerotti USMA, Department of Physics and Nuclear Engineering, West Point, NY, USA

Maciej Ławryńczuk Institute of Control and Computation Engineering, Warsaw University of Technology, Warsaw, Poland

Tristan Lebrun Sorbonne University, STMS Lab (UMR 9912, IRCAM-CNRS-SU), Paris, France

Wagner B. Lenz Federal University of Technology—Paraná, Ponta Grossa, PR, Brazil

Dongwu Li School of Astronautics, Northwestern Polytechnical University, Xi'an, China

Kai Liu School of Engineering, University of California, Merced, CA, USA

Xiao-jun Liu Tianshui Normal University, Tianshui, China

Ze-Qi Lu Shanghai Institute of Applied Mathematics and Mechanics, Shanghai University, Shanghai, China

Jun Ma Department of Physics, Lanzhou University of Technology, Lanzhou, Gansu, China

V. Manaoj Aravind Indian Institute of Science Education and Research Mohali, Punjab, India

Yuri Mikhlin Department of Applied Mathematics, National Technical University "KPI", Kharkov, Ukraine

S. Mohanty Department of Mechanical Engineering, Indian Institute of Technology Guwahati, Guwahati, Assam, India

Austin Morock Department of Civil and Mechanical Engineering, United States Military Academy (USMA), West Point, NY, USA

K. Murali Department of Physics, Anna University, Chennai, India

Satish Nagarajaiah Department of Civil and Environmental Engineering, Rice University, Houston, TX, USA

Leandro Nesi Department of Mechanical and Aerospace Engineering, Sapienza University of Rome, Rome, Italy

Anton Onizhuk A. Podgorny Institute for Mechanical Engineering Problems, National Academy of Sciences, Kharkov, Ukraine

Grigory Panovko Mechanical Engineering Research Institute of the Russian Academy of Sciences, Moscow, Russia

Chan-eun Park Division of Electrical Engineering, Pohang University of Science and Technology, Pohang, Korea

PooGyeon Park Division of Electrical Engineering, Pohang University of Science and Technology, Pohang, Korea

Gianluca Pepe Department of Mechanical and Aerospace Engineering, Sapienza University of Rome, Rome, Italy

Francesco Potenza Department of Civil Architectural and Environmental Engineering, University of L'Aquila, L'Aquila, Italy

Yongda Qi College of Electrical and Information Engineering, Lanzhou University of Technology, Lanzhou, China

Giuseppe Quaranta Department of Structural and Geotechnical Engineering, Sapienza University of Rome, Rome, Italy

Jonatan Pena Ramirez CONACYT-CICESE, Applied Physics Division, Electronics and Telecommunications Department, Ensenada, BC, Mexico

Chuan-Bo Ren School of Transportation and Vehicle Engineering, Shandong University of Technology, Zibo, Shandong, China

Mauricio A. Ribeiro Federal University of Technology—Paraná, Ponta Grossa, PR, Brazil

Rodrigo T. Rocha Federal University of Technology—Paraná, Ponta Grossa, PR, Brazil

David Roze CNRS, STMS Lab (UMR 9912, IRCAM-CNRS-SU), Paris, France

Andrea Salvatore Department of Structural and Geotechnical Engineering, Sapienza University of Rome, Rome, Italy

Alexander Shokhin Mechanical Engineering Research Institute of the Russian Academy of Sciences, Moscow, Russia

Sudeshna Sinha Indian Institute of Science Education and Research Mohali, Punjab, India

Giulia Stefani Department of Structural and Geotechnical Engineering, "Sapienza" University of Rome, Rome, Italy

Gabor Stepan Department of Applied Mechanics, Budapest University of Technology and Economics, Budapest, Hungary

Jian-Qiao Sun School of Engineering, University of California Merced, Merced, CA, USA

Weiqiang Tang College of Electrical and Information Engineering, Lanzhou University of Technology, Lanzhou, China

J. A. Tenreiro Machado Department of Electrical Engineering, Polytechnic of Porto - School of Engineering (ISEP), Porto, Portugal

Angelo M. Tusset Federal University of Technology—Paraná, Ponta Grossa, PR, Brazil

Junzheng Wang State Key Laboratory of Intelligent Control and Decision of Complex Systems, School of Automation, Beijing Institute of Technology, Beijing, China

Xiangyang Wang Robotics Research Center, Beijing Jiaotong University, Beijing, China

Marc Wijnand Sorbonne University, STMS Lab (UMR 9912, IRCAM-CNRS-SU), Paris, France

Chao Xu School of Astronautics, Northwestern Polytechnical University, Xi'an, China

Kai Xu Key Laboratory for Wind and Bridge Engineering of Hunan Province, College of Civil Engineering, Hunan University, Changsha, China

Li-xin Yang School of Arts and Sciences, Shaanxi University of Science and Technology, Xi'an, China

Amir Younespour Department of Civil and Environmental Engineering, University of Windsor, Windsor, ON, Canada

Jie Yuan School of Automation, Southeast University, Nanjing, China
Key Laboratory of Measurement and Control of CSE, Ministry of Education, School of Automation, Southeast University, Nanjing, China
Mechatronics, Embedded Systems and Automation Lab, University of California, Merced, CA, USA

Dariusz Żardecki Automotive Industry Institute (PIMOT), Warsaw, Poland
Military University of Technology (WAT), Warsaw, Poland

Xiu-hua Zhang Department of Electrical Engineering, Shandong Vocational College of Industry, Zibo, Shandong, China

Ye-Wei Zhang Shanghai Institute of Applied Mathematics and Mechanics, Shanghai University, Shanghai, China

Part I
Vibration Absorbers and Isolators

Active Nonlinear Vibration Absorber for a Harmonically Excited Beam System

S. Mohanty and S. K. Dwivedy

Abstract An active nonlinear vibration absorber (ANVA) using displacement, velocity, and acceleration feedback from the absorber mass is proposed to reduce the vibration of an Euler–Bernoulli beam subjected to a harmonical point force. The ANVA comprises mass, linear spring, cubic nonlinear spring and actuator. The steady-state equation of the system is obtained by solving the governing differential equation by harmonic balance method. From the steady state equations, the stability and vibration reduction of the beam are investigated by frequency responses, time responses and phase portraits using Newton's method and fourth-order Runge–Kutta method. The analysis is carried out by studying the effects of different feedback control gains and cubic nonlinear stiffness of the absorber to suppress the vibration of the beam for the first three modal frequencies under different boundary conditions, namely fixed-fixed, simply supported and cantilevered type. The performance of the absorber is found to be better with cubic nonlinear stiffness in the absorber which reduces the vibration of the beam more effectively than the linear passive or active vibration absorber.

Keywords Vibration absorber · Harmonic balance method · Feedback

1 Introduction

The tuned mass damper (TMD) is an auxiliary mechanical device consisting of spring, mass and damper with optimal configuration which is attached to the vibrating primary structure to suppress its vibration by absorbing its vibrational energy [1]. The energy transformed from the host vibrating structure to the TMDs makes it to vibrate at higher amplitude which leads to nonlinear response in the auxiliary mass [2, 3]. The passive TMDs are not useful for wider range of

S. Mohanty (✉) · S. K. Dwivedy
Department of Mechanical Engineering, Indian Institute of Technology Guwahati, Guwahati, Assam, India
e-mail: siba.mech@gmail.com

frequency of operation with lower mass ratio. To avoid these problems, linear and nonlinear TMDs are designed with various optimization techniques, along with the use of active control devices to suppress the vibration for a broader range of operating frequencies [4, 5]. Hua et al. [6] designed a beam-based dynamic vibration absorber (DVA) to suppress vibration of a cantilevered beam. They showed that the proposed DVA outperforms traditional DVAs under same mass ratio. Chatterjee [7] considered linear analysis and proportional displacement and velocity feedback to suppress the vibration of a fixed-fixed beam excited by a point load. The present work is an extension of [7] where nonlinear secondary system is considered by taking different boundary conditions of the beam with different feedback conditions.

In the proposed model, the auxiliary system consists of a nonlinear spring, mass and an actuator, which is attached to the beam to suppress its vibration. The beam that is modelled as an Euler–Bernoulli beam is excited by an external harmonic point force. Three different feedbacks, namely proportional displacement or velocity or acceleration or combination of these, are used by the actuator to suppress the first three modes of vibrations of the beam for various boundary conditions. In the following section, the mathematical modelling of the system is described.

2   System Description and Mathematical Formulations

The schematic diagram of a fixed-fixed beam subjected to a harmonic excitation $F \cos \omega t$ at distance b from left end is shown in Fig. 1. The parameters ρ, A, L, E and I denote density, elastic modulus, moment of inertia, cross-sectional area and length of the beam, respectively. The mass, spring and cubic nonlinear stiffness of the auxiliary system are denoted by m, k_1 and k_{13}, respectively. The auxiliary system is attached at a distance a from the left end of the beam. The active control force F_c by the actuator is considered to be proportional to displacement or velocity or acceleration feedback or combination of these taken from the absorber mass. The transverse displacement of the beam about the neutral axis at any point x and time t is denoted by $W(x, t)$. The governing differential equation of motion of the system is obtained by considering equilibrium of the forces and moments, which are given below.
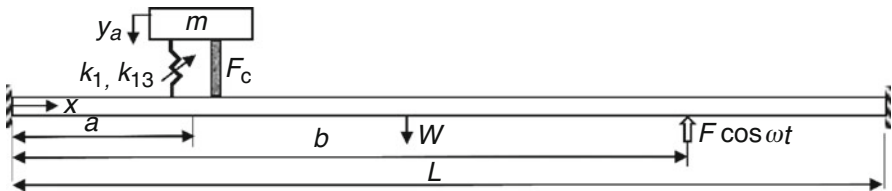
Fig. 1 Vibration control of a fixed-fixed beam subjected to harmonically excited point load by using an active nonlinear vibration absorber

$$\rho A \frac{\partial^2 W(x,t)}{\partial t^2} + EI \frac{\partial^4 W(x,t)}{\partial x^4} + W(x(a),t)(k_1(W(x(a),t) - y_a))$$
$$+ W(x(a),t)(k_{13}(W(x(a),t) - y_a)^3) = F \cos \omega t - F_c \tag{1}$$

$$m\ddot{y}_a + k_1(y_a - W(a,t)) + k_{13}(y_a - W(a,t))^3 = F_c \tag{2}$$

$$F_c = -\left(K_p y_a - K_v \dot{y}_a + K_I \ddot{y}_a\right) \tag{3}$$

where K_p, K_v and K_I are the control gains of the absorber mass, for displacement, velocity and acceleration feedback, respectively. The term y_a is the displacement of the absorber mass. Taking $W(x,t) = \sum_{i=1}^{3} \phi_i(x) q_i(t)$ in Eqs. (1) and (2), where $\phi_i(x)$ is the mode shape function and $q_i(t)$ is the time modulation of the ith mode of the beam vibration, the temporal equations of the system is obtained by using Galerkin's method. Here normalization criteria is taken as $\int_0^L \left(\phi_i{}^2(x)\right) dx = 1$. Following non-dimensional parameters are used for further analysis. Modal displacement of the beam for ith mode: $w_i = q_i/\delta_{st}$, displacement of the absorber: $y = y_a/\delta_{st}$, mass ratio: $\mu = m/(\rho AL)$, $\omega_a = \sqrt{k_1/m}/\omega_0$, $\omega_0 =$ reference frequency, normalized natural frequency of ith mode the beam $= \omega_{ni}$, cubic nonlinear stiffness coefficient: $\alpha = k_{13}/k_1$, excitation force: $f = F/\left(\rho AL\omega_0^2 \delta_{st}\right)$, control gains: $k_p = K_p/\left(\rho AL\omega_0^2\right)$, $k_v = K_v/\left(\rho AL\omega_0^2\right)$, $k_I = K_I/\left(\rho AL\omega_0^2\right)$, $\Omega = \omega/\omega_0$ and non-dimensional time $\tau = \omega_0 t$. The obtained non-dimensional equations of motion are given below.

$$\ddot{w}_i(\tau) + \omega_{ni}^2 w_i(\tau) + \mu \omega_a^2 \phi_i(a) \left\{ \sum_{i=1}^{3} \phi_1(a) w_i(\tau) - y(\tau) \right\}$$
$$+ \phi_i(a)\left\{k_p y(\tau) - k_v \dot{y}(\tau)\right\} + \alpha \mu \omega_a^2 \phi_i(a) \left\{ \sum_{i=1}^{3} \phi_1(a) w_i(\tau) - y(\tau) \right\}^3 \tag{4}$$
$$+ \phi_i(a) k_I \ddot{y}(\tau) = \phi_i(b) f \cos(\Omega\tau)$$

$$\mu \ddot{y}(t) + \mu \omega_a^2 \left\{ y(\tau) - \sum_{i=1}^{3} \phi_i(a) w_i(\tau) \right\} + \alpha \mu \omega_a^2 \left\{ y(\tau) - \sum_{i=1}^{3} \phi_i(a) w_i(\tau) \right\}^3$$
$$- k_p y(t) + k_v \dot{y}(\tau) - k_I \ddot{y}(\tau) = 0 \tag{5}$$

It may be noted that Eqs. (4) and (5) are similar to Chatterjee [5], but here the cubic nonlinear stiffness in the absorber and different feedback forces are considered for various boundary conditions of the beam. Eqs. (4) and (5) are solved for the first three modal displacement of the beam, i.e. for $i = 1, 2$ and 3 using harmonic balance method which is discussed in the following section.

2.1 Approximate Solution by Harmonic Balance Method

In this section, the harmonic balance method with slowly varying parameters are employed to Eqs. (4) and (5) to analyse the steady-state response of the system. The assumed solution are stated as follows:

$$w_n (\tau) = A_n (\tau) \cos (\Omega \tau + \varphi_n (\tau)) \text{ for } n = 1, 2, 3 \qquad (6)$$

$$y (\tau) = B (\tau) \cos (\Omega \tau + \varphi_4 (\tau)) \qquad (7)$$

where $A_1(\tau), A_2(\tau), A_3(\tau), B(\tau), \phi_1(\tau), \phi_2(\tau), \phi_3(\tau)$ and $\phi_4(\tau)$ are slowly varying functions of time τ such that one can neglect the higher order or multiplication of derivatives. Substituting Eqs. (6) and (7) into Eqs. (4) and (5) and equating the coefficient of $\sin \Omega \tau$ and $\cos \Omega \tau$ terms separately to zero yield the following set algebraic equations in the matrix form.

$$\begin{bmatrix} a_{11} \ldots a_{18} \\ \vdots \ddots \vdots \\ a_{81} \cdots a_{88} \end{bmatrix} \left\{ \dot{A}_1 \ \dot{\varphi}_1 \ \dot{A}_2 \ \dot{\varphi}_2 \ \dot{A}_3 \ \dot{\varphi}_3 \ \dot{B} \ \dot{\varphi}_4 \right\}^\text{T} = \left\{ b_1 \cdots b_8 \right\}^\text{T} \qquad (8)$$

From Eq. (8), the following amplitude and phase equations are obtained.

$$\dot{A}_n = f_n (A_1, \ A_2, \ A_3, \ B, \ \varphi_1, \ \varphi_2, \ \varphi_3, \ \varphi_4) \text{ for } n = 1, 2, 3 \qquad (9)$$

$$\dot{\varphi}_n = f_n (A_1, A_2, A_3, B, \ \varphi_1, \ \varphi_2, \ \varphi_3, \ \varphi_4) \text{ for } n = 4, 5, 6 \qquad (10)$$

$$\dot{B} = f_7 (A_1, A_2, A_3, B, \ \varphi_1, \ \varphi_2, \ \varphi_3, \ \varphi_4) \qquad (11)$$

$$\dot{\varphi}_4 = f_8 (A_1, A_2, A_3, B, \ \varphi_1, \ \varphi_2, \ \varphi_3, \ \varphi_4) \qquad (12)$$

The steady-state solutions of the equations are obtained by setting the first derivatives of the slowly varying amplitudes and phases equals to zero, i.e., $\dot{A}_1 = \dot{A}_2 = \dot{A}_3 = \dot{B} = \dot{\varphi}_1 = \dot{\varphi}_2 = \dot{\varphi}_3 = \dot{\varphi}_4 = 0$ in Eqs. (9–12), and the stability of the system is studied by obtaining the eigenvalues of the Jacobian matrix from Eq. (8). In the following section, the performance of the active nonlinear vibration absorber is discussed for various system parameters and control gains to suppress the vibration of the beam for the first three modal frequencies.

3 Results and Discussions

In this section, the performance of the active nonlinear vibration absorber on the beam is studied by the time responses, phase portraits and frequency responses of the system for the first three modal frequencies and also compared with the passive linear vibration absorber. The optimum absorber parameters and the control gains for displacement (k_p) and velocity feedback (k_v) are considered from Chatterjee [7]. The system parameters are considered as follows: mass ratio $\mu = 0.2$, amplitude of external excitation $f = 1$, absorber frequency $\omega_a = 2$ and the first three modal frequencies of the beam are $\omega_{n1} = 1$, 4 and 9. The parametric study is carried out by varying cubic nonlinear stiffness coefficient α and control gains k_p, k_v and k_I for various boundary conditions of the beam. The time responses and phase portraits of the system are obtained by solving Eqs. (4) and (5) using fourth order Runge–Kutta method, and the frequency responses of the system are obtained by solving the steady Eqs. (9–12) using Newton's method. The stability of a particular solution is ensured by the negative real part of the eigenvalues of the Jacobian matrix from the Eq. (8).

3.1 Time Responses Curves of the System

The time responses and phase portraits of the fixed-fixed beam and the absorber are shown in Fig. 2 for studying the effects of α and control gains in the vibration suppression of the beam. In Fig. 2a–d comparison of time responses at the first modal frequency ($\omega_{n1} = \Omega = 1$) of the beam for linear (red) and nonlinear (black) passive absorber are shown. From Fig. 2a one can observe that with cubic nonlinear stiffness, the response amplitude of the beam and the absorber decreases by 24% and 50%, respectively, than the linear absorber. The corresponding phase portraits of the system are shown in Fig. 2b, d where the beam and absorber show quasi periodic responses. In Fig. 3 responses of the fixed-fixed beam is studied for $\alpha = 0.1$ and 0.2 with different control gains. In Fig. 3a–d the black line shows the system response with only control gain k_v, and red lines shows with zero control gain for the first modal frequency ($\omega_{n1} = \Omega = 1$) of operation. It is observed from Fig. 3a, c that with $k_v = 0.3578$ the response of the beam and the absorber decreases by 52% and 28%, respectively, than the passive nonlinear absorber. In Fig. 3b, d phase portraits of the beam and the absorber show quasiperiodic responses. In Fig. 3e–f time responses are shown to control second modal frequency ($\omega_{n1} = \Omega = 4$) of the beam with $k_v = -1$, while all other system parameters are considered the same as in Fig. 3a–d. Here it is observed that the system amplitude reduces by the application of control gain in the feedback. In Fig. 3g, h comparison of time responses of the fixed-fixed beam system are shown, with acceleration feedback (continuous black line) and both displacement and velocity feedback (dotted black line) for $\alpha = 0.2$. From these figures, one can observe that with both k_p and k_v the system amplitude is more while
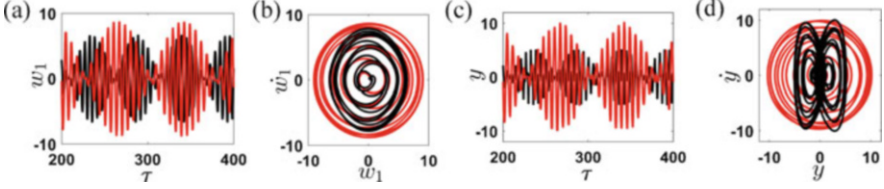
Fig. 2 Comparison of time responses (**a**, **c**) and phase portraits (**b**, **d**) of the passive fixed-fixed beam system at ($\omega_{n1} = \Omega = 1$) for linear ($\alpha = 0$) (red) and nonlinear absorber ($\alpha = 0.1$) (black)
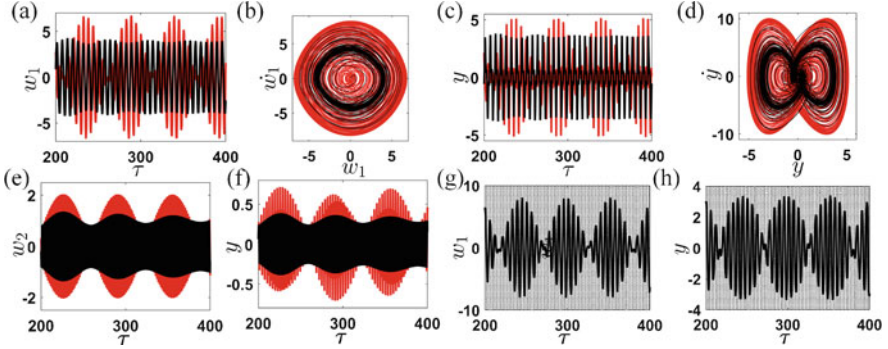
Fig. 3 Time responses and phase portraits of the system with fixed-fixed boundary conditions for different feedbacks and nonlinear stiffness in the absorber, where passive (red) and active (black). (**a–d**) $k_v = 0.3578$ and $\alpha = 0.1$ at $\omega_{n1} = \Omega = 1$, (**e**, **f**) $k_v = 1$ and $\alpha = 0.1$ at $\omega_{n1} = \Omega = 4$. (**g**, **h**) $k_p = 0.6$, $k_v = 0.3578$ (dotted lines) and $k_I = 0.9$ (solid lines) for $\alpha = 0.2$ at $\omega_{n1} = \Omega = 1$
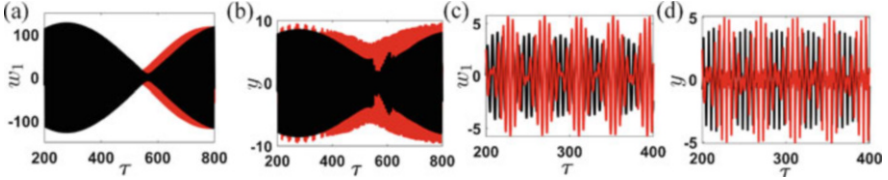
Fig. 4 Time responses of the (**a**, **b**) cantilevered beam and (**c**, **d**) simply supported beam at ($\omega_{n1} = \Omega = 1$ for $\alpha = 0.1$), where passive (red) and active ($k_v = 0.3578$) (black)

with only k_I the system amplitude is lower. From Fig. 3 it is observed that for the nonlinear absorber, control gain with velocity feedback reduces the amplitude of the system, but when the nonlinearity in the absorber increases than acceleration feedback is more suitable to suppress vibrations of the fixed-fixed beam. In Fig. 4 the response of the system is studied for the simply supported beam (Fig. 4a, b) and the cantilevered beam (Fig. 4c, d) with same α and control gains as in Fig. 3a–d.

From Fig. 4a, b the same beating time responses are observed, but with higher amplitude, though with the control gain (black), the amplitude is lower. For the cantilever beam shown in Fig. 4c, d the vibration suppression is better than the simply supported beam with the same applied control gain.

3.2 Frequency Response Curves

In this section, parametric study is undertaken to analyses the frequency response of the system with different values of α, boundary conditions of the beam (fixed-fixed, simply supported, cantilevered) and control gains for displacement (k_p) and velocity feedback (k_v). In Fig. 5a, b, a comparison of frequency responses between the linear (black) and nonlinear active vibration absorber (blue) with k_p and k_v is shown to suppress the first modal frequency ($\omega_{n1} = \Omega = 1$) of vibration in the fixed-fixed beam. From these figures, it is observed that for $\alpha = 0.01$ the amplitude of the beam and the absorber decreases for the first three modal frequencies than the linear absorber. In Fig. 5c, d only velocity feedback is used to suppress the second modal vibration ($\omega_{n1} = \Omega = 4$) of the beam. It is observed from these figures that with only k_v the second mode of vibration of the beam is suppressed and also the same analogy can be interpreted for the absorber. It may be noted that Fig. 5a, c are similar to the results obtained by Chatterjee [7] where only linear analysis has been carried out. In Fig. 5e, f the same k_v and negative k_p are considered to suppress the vibration of the beam at the third mode ($\omega_{n1} = \Omega = 9$). It is observed from these figures that with the control gains both the third mode and the second mode of vibration of the beam decrease. In Fig. 5g for $\alpha = 0.05$ it is observed that the vibration of the beam further reduces in the first two modal frequencies than Fig. 5a. But for $\alpha = 0.1$ the beam vibration increases which is shown in Fig. 5h. In Fig. 5i, j the vibration suppression
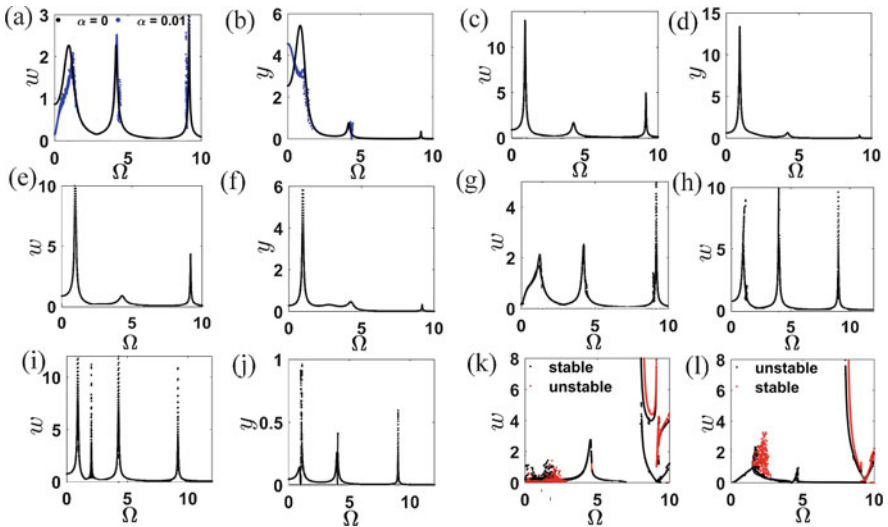
Fig. 5 Frequency responses of the fixed-fixed beam at the first three modal frequencies with $k_v = 0.3578$ and different k_p and α. (**a, b**) $k_p = 0.6$, at $\omega_{n1} = \Omega = 1$, (**c, d**) $k_p = 0$, $\alpha = 0$ at $\omega_{n1} = \Omega = 4$, (**e, f**) $k_p = -1$, $\alpha = 0.05$ at $\omega_{n1} = \Omega = 9$, (**g**) $k_p = 0.6$, $\alpha = 0.05$ at $\omega_{n1} = \Omega = 1$, (**h**) $k_p = -0.6$, $\alpha = 0.1$ at $\omega_{n1} = \Omega = 1$, (**i, j**) $k_p = -1$, $\alpha = 0.01$ at $\omega_{n1} = \Omega = 1$ and (**k, l**) $k_p = -1$, $\alpha = 1$ at $\omega_{n1} = \Omega = 1$
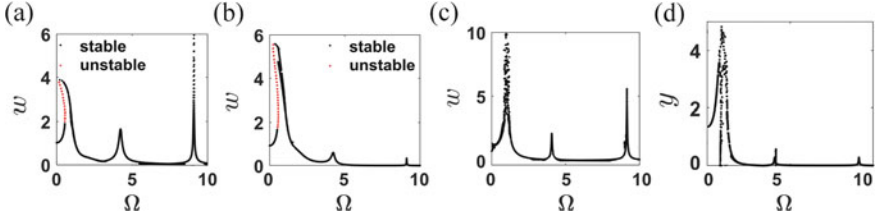
Fig. 6 Frequency responses of (**a**, **b**) the simply supported beam and (**c**, **d**) the cantilever beam for $k_p = 0.6$, $k_v = 0.3578$ and $\alpha = 0.01$ at $\omega_{n1} = \Omega = 1$

of the third mode is analysed for $\alpha = 0.01$ with k_v and negative k_p. It is observed that the vibration suppression of the beam in the third mode is not achieved with the applied control gains. In Fig. 5k, l, $\alpha = 1$ is considered to suppress the first mode of vibration ($\omega_{n1} = \Omega = 1$) of the beam. From Fig. 5k, l, high response amplitude and unstable regions are observed in the system. From Fig. 5 it is observed that for α in the range of 0 to 0.1 with the applied control gains, the response amplitude of the system reduces for the first three modal frequencies, but higher values of α, i.e. for $\alpha = 1$, make the system unstable with high response amplitude. In Fig. 6a, d the simply supported beam and cantilever beam are considered with k_p, k_v and α, while all other parameters are same as in Fig. 3a–d. In simply supported beam (Fig. 6a, b), the unstable region is observed for $0.85 < \Omega < 0.95$ with jump-up and jump-down phenomena. For cantilever beam (Fig. 6c, d), the response amplitude is higher than in the fixed-fixed beam with the same control gains.

4 Conclusions

In the present chapter, it is observed that the proposed passive nonlinear vibration absorber reduces the vibration up to 24% than that of the corresponding linear vibration absorber. In the active linear and nonlinear vibration absorber, by suitably taking the optimized displacement and velocity gains, one may reduce the vibration of beams with fixed-fixed, simply supported and cantilevered beam for different modal frequencies. For higher nonlinear stiffness in the absorber, it is shown that the acceleration feedback is more useful than that of the displacement or velocity feedback. The results obtained by using the harmonic balance method is found to be in good agreement with those obtained by using Runge–Kutta method. Hence one may use the developed equations using harmonic balance method to study the passive and active vibration absorber to effectively suppress the vibration of the system with less computational time and memory space.

References

1. Den Hartog, J.P.: Mechanical Vibrations. Dover Publications, New York (1985)
2. Oueini, S.S., Chin, C.M., Nayfeh, A.H.: Dynamics of a cubic nonlinear vibration absorber. Nonlinear Dyn. **20**(3), 283–295 (1999)
3. Jo, H., Yabuno, H.: Amplitude reduction of primary resonance of nonlinear oscillator by a dynamic vibration absorber using nonlinear coupling. Nonlinear Dyn. **55**(1–2), 67–78 (2009)
4. Oueini, S.S., Nayfeh, A.H., Pratt, J.R.: A review of development and implementation of an active nonlinear vibration absorber. Arch. Appl. Mech. **69**(8), 585–620 (1999)
5. Parseh, M., Dardel, M., Ghasemi, M.H.: Performance comparison of nonlinear energy sink and linear tuned mass damper in steady-state dynamics of a linear beam. Nonlinear Dyn. **81**(4), 1981–2002 (2015)
6. Hua, Y., Wong, W., Cheng, L.: Optimal design of a beam-based dynamic vibration absorber using fixed-points theory. J. Sound Vib. **421**, 111–131 (2018)
7. Chatterjee, S.: Optimal active absorber with internal state feedback for controlling resonant and transient vibration. J. Sound Vib. **329**(26), 5397–5414 (2010)

Comparison of Linear and Nonlinear Damping Effects on a Ring Vibration Isolator

Ze-Qi Lu, Dong-Hao Gu, Ye-Wei Zhang, Hu Ding, Walter Lacarbonara (ID),
and Li-Qun Chen

Abstract Nonlinear isolators in the shape of a circular ring have been shown to have an advantage over linear isolators in that they allow low-frequency vibration isolation. These isolators have generally been assumed to possess linear viscous damping, which degrades the performance of the isolator at high frequencies. An alternative design is to make use of nonlinear damping, where the nonlinear behavior is achieved by placing linear dampers, so that they are orthogonal to the motion of the isolator. In this work, the performance of circular ring isolators with this type of damping is compared with the corresponding isolators exhibiting linear viscous damping only. It is found that the isolators with linear viscous damping perform better around the resonance frequencies, but the isolators with nonlinear damping perform better at high frequencies.

Keywords Nonlinear vibration · Vibration isolation · Ring · Damping nonlinearity

1 Introduction

One way to improve low-frequency vibration without incurring static deflections is to use a nonlinear isolator which has high-static-low-dynamic stiffness [1]. There are many ways to achieve this goal (see [2–5] and the references therein). Wang et al. [6] studied dynamic characteristics of a nonlinear stiffness vibration isolator. de Haro Silva et al. [7] studied the influence of a nonlinear cubic stiffness on the transmissibility. A nonlinear cubic stiffness could improve the isolation performance at frequencies around and above the resonance. Mojahed et al. [8]

Z.-Q. Lu · D.-H. Gu · Y.-W. Zhang · H. Ding · L.-Q. Chen (✉)
Shanghai Institute of Applied Mathematics and Mechanics, Shanghai University, Shanghai, China
e-mail: luzeqi@shu.edu.cn; lqchen@shu.edu.cn

W. Lacarbonara
Department of Structural and Geotechnical Engineering, Sapienza University of Rome, Rome, Italy

addressed a nonlinear isolator with geometrically nonlinear stiffness. Huang et al. [9] designed a nonlinear isolator using Euler buckled beams as negative stiffness element. Both analytical and experimental results demonstrated that the nonlinear spring characteristic of the ring beam is beneficial to vibration isolation. In all these cases, the damping was due to a linear viscous damper in parallel with the vertical spring.

However, damping nonlinearity has some advantages compared to linear viscous damping in overcoming the trade-off between mitigating the response at resonance and maintaining good performance at high frequencies. Anomalous behavior of damping nonlinearity inspired researchers to exploit the damping nonlinearity for vibration isolation [10]. Wang et al. [11] compared the effects of linear and nonlinear dampers in a nonlinear hinged-hinged beam. Ho et al. [12] have studied a 1-dof nonlinear vibration isolation system with both stiffness and cubic damping nonlinearity. They used relatively simple analytical models to characterize the system in terms of power flow, using output frequency response functions (OFRFs). Recently, the effects of lateral dampers, which offer some advantages compared to vertical damping, have been considered in combination with a vertical linear spring [13]. It was shown that this arrangement has the advantage of improving the performance at the resonance frequency without degrading the isolation performance at high frequencies for both force and displacement excited systems.

The aim of this chapter is to investigate the differences between having linear and nonlinear damping in a ring isolator. The two damping configurations are (a) a linear viscous damper aligned with the direction of excitation and (b) lateral linear viscous dampers placed orthogonally to the excitation direction (the nonlinear damping is due to the geometry). The direct separation of motion is used to analyze the displacement transmissibility of the ring beam combined with linear or nonlinear damper.

2   Formulation

Figure 1 presents a model of a vibration isolator with stiffness and damping nonlinearity for a suspended mass m. The stiffness nonlinearity is achieved by the circular ring. The geometry of the ring is described by radius R, thickness H, and width W. Two cases are compared: (a) the system with linear viscous damping c_v due to the vertical damper and (b) the system with horizontal linear dampers c_h providing geometrically nonlinear effects.

The static force–displacement relationships of the pre-deformed ring due to the weight of the isolation mass are given by

$$f_{\mathrm{s}(i)}(x) = mg - A_i/(x + x_0)^2 \quad (i = 1, 2, 3) \tag{1}$$
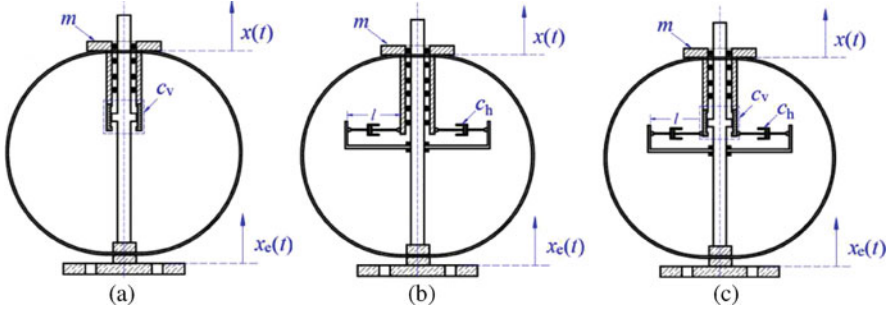
Fig. 1 Schematic of circle ring isolators: (**a**) only linear damping, (**b**) only nonlinear damping, (**c**) both linear and nonlinear damping

where x_0 is the static deflection of the ring at equilibrium under its own weight, x is the displacement measured from the equilibrium. In Eq. (1) A_i represents the index associated with different branches of the load-displacement for the ring whereby

Stage 1 (for low compressed levels, the eccentricity is large to maintain the bending moment): $m \leq 0.6296LD/R^2g$,

$$A_1 = 8LD[(2p/\pi + 2/p - p)\, F\,(p, \pi/4) - (2/p)\, E\,(p, \pi/4)]^2 \qquad (2)$$

Stage 2 (for moderate values, the deformed elastica curve relies on an undulating elastica): $0.6296LD/R^2g \leq m \leq 2.7864LD/R^2g$,

$$A_2 = 8LD[(2/\pi + 1)\, F\,(p, \phi_B) - 2E\,(p, \phi_B)]^2 \qquad (3)$$

Stage 3 (for large levels, a negative curvature is created): $m \geq 2.7864LD/R^2g$,

$$A_3 = 8LD[(4/\pi + 2)\, F(p) - (2/\pi + 1)\, F\,(p, \phi_B) - 4E(p) + 2E\,(p, \phi_B)]^2 \qquad (4)$$

in which $\phi_B = \sin^{-1}\left(1/p\sqrt{2}\right)$, $D = H^3 E_{22}/12$ is flexural stiffness, E_{22} is Young's modulus, L is equivalent length, $E(p,\phi)$ and $F(p,\phi)$ are the incomplete elliptic integral of the second kind and first kind, respectively, $p = 2\sqrt{WD/(mgh^2)}$, h is deflected ring radius. Under base motion $x_e = X_e \cos(\omega t)$, the equation of motion for the suspended mass m accounting for both damping scenarios (a) and (b) is given by

$$m\ddot{x}_r + c_v \dot{x}_r + 2c_h \frac{x_r^2}{x_r^2 + l^2}\dot{x}_r + f_{s(i)}(x_r) = m\omega^2 X_e \cos(\omega t) \qquad (5)$$

where $x_r = x - x_e$ is the relative displacement between the mass and base. X_e and ω denote the amplitude and frequency of the base motion, respectively. The linear and

nonlinear damping terms in Eq. (5) are $c_v \dot{x}_r$ and $c_h \left(x_r^2 / \left(x_r^2 + l^2 \right) \right) \dot{x}_r$, respectively. These terms are taken into account separately or comprehensively, in other words, the effects of linear and nonlinear damping on circle beam vibration isolation can be compared clearly.

3 Displacement Transmissibility

3.1 Direct Separation of Motion Method

Direct separation of motion method is applied to analyze the frequency response. The solution to Eq. (5) is assumed as

$$x_r = \alpha (T_1) + \psi (T_1, T_0) \tag{6}$$

where new timescales T_1 and T_0 are denoted as $T_0 = \omega t$, $T_1 = \varepsilon T_0$, ε is a book-keeping small parameter, α is the slow parameter, ψ is the fast parameter. The average of ψ in a periodic subject to T_0 is zero, i.e., $\langle \psi(T_1, T_0) \rangle = 0$. Equations of slow and fast motions can be given, respectively

$$m\varepsilon^2 \frac{d^2\alpha}{dT_1^2} + \varepsilon c_v \frac{d\alpha}{dT_1} + \varepsilon c_h \frac{\alpha^2 + \psi^2 + 2\alpha\psi}{\alpha^2 + \psi^2 + 2\alpha\psi + l^2} \frac{d\alpha}{dT_1} = 0 \tag{7}$$

$$m\frac{\partial^2\psi}{\partial T_0^2} + 2m\varepsilon \frac{\partial^2\psi}{\partial T_1 \partial T_0} + m\varepsilon^2 \frac{\partial^2\psi}{\partial T_1^2} + c_v \left(\frac{\partial\psi}{\partial T_0} + \varepsilon \frac{\partial\psi}{\partial T_1} \right) + c_h \frac{\alpha^2 + \psi^2 + 2\alpha\psi}{\alpha^2 + \psi^2 + 2\alpha\psi + l^2}$$
$$\times \left(\frac{\partial\psi}{\partial T_0} + \varepsilon \frac{\partial\psi}{\partial T_1} \right) - \frac{A_i}{\alpha^2 + \psi^2 + 2\alpha\psi + 2x_0(\alpha+\psi) + x_0^2} = m\omega^2 X_e \cos(\omega t) - mg \tag{8}$$

Considering that $\psi(T_1, T_0)$ is a time T_0 periodic function, the solution of Eq. (8) is expanded in series form as

$$\psi = B_1 (T_1) \cos (T_0 + \theta_1 (T_1)) + B_2 (T_2) \cos (2T_0 + \theta_2 (T_1)) + \cdots \tag{9}$$

The term containing B_2 and θ_2 neglected. Thus, substituting Eq. (9) into Eq. (8) results in

$$m\varepsilon^2 \frac{d^2 B_1}{dT_1^2} + \varepsilon c_v \frac{dB_1}{dT_1} - mB_1 \left(1 + \varepsilon \frac{d\theta_1}{dT_1} \right)^2 + 2c_h \varepsilon \frac{2\alpha B_1}{l^2} \frac{dB_1}{dT_1}$$
$$+ k_1 B_1 - 2k_2 \alpha B_1 + (3/4) k_3 B_1^3 + 3k_3 \alpha^2 B_1 = m\omega^2 X_e \cos\theta_1 \tag{10}$$

$$m\varepsilon^2 B_1 \frac{d^2\theta_1}{dT_1^2} + \left(c_{\mathrm{v}} B_1 + 2m\varepsilon \frac{dB_1}{dT_1}\right)\left(1 + \varepsilon \frac{d\theta_1}{dT_1}\right) + 2c_{\mathrm{h}} \frac{2\alpha B_1}{l^2}\left(B_1 + \varepsilon B_1 \frac{d\theta_1}{dT_1}\right)$$

$$= -m\omega^2 X_{\mathrm{e}} \sin\theta_1$$

(11)

where $k_1 = 2A_i/x_0^3$, $k_2 = 3A_i/x_0^4$, and $k_3 = 4A_i/x_0^5$.

The steady response for the slow motion could be defined by

$$k_1\alpha - k_2\left(\alpha^2 + B_1^2/2\right) + k_3\left(\alpha^3 + 3\alpha B_1^2/2\right) = 0 \tag{12}$$

$$-m\omega^2 B_1 + k_1 B_1 - 2k_2\alpha B_1 + (3/4)\,k_3 B_1^3 + 3k_3\alpha^2 B_1 = m\omega^2 X_{\mathrm{e}} \cos(\theta_1) \tag{13}$$

$$c_{\mathrm{v}}\omega B_1 + 2c_{\mathrm{h}}2\alpha B_1^2 \omega/l^2 = -m\omega^2 X_{\mathrm{e}} \sin(\theta_1) \tag{14}$$

With the application of $\sin^2\theta + \cos^2\theta = 1$, the amplitude–frequency relationship can be derived by

$$\left(-2k_2\alpha B_1 + (3/4)\,k_3 B_1^3 + 3k_3\alpha^2 B_1 + \left(k_1 - m\omega^2\right) B_1\right)^2$$

$$+ \left(c_{\mathrm{v}}\omega B_1 + 2c_{\mathrm{h}}2\alpha B_1^2 \omega/l^2\right)^2 = m^2\omega^4 X_{\mathrm{e}}^2 \tag{15}$$

Equation (15) is a quadratic equation in ω^2 and can be solved analytically, if $k_{\mathrm{e}} = k_1 - 2k_2\alpha + (3/4)\,k_3 B_1^2 + 3k_3\alpha^2$, $c = c_{\mathrm{v}} + 2c_{\mathrm{h}}2\alpha B_1/l^2$, which yields

$$\omega_{1,2} \approx \left\{\frac{c^2 - 2mk_{\mathrm{e}}}{2m^2\left(X_{\mathrm{e}}^2/B_1^2 - 1\right)} \pm \frac{\left[\left(c^2 - 2mk_{\mathrm{e}}\right)^2 + 4m^2\left(X_{\mathrm{e}}^2/B_1^2 - 1\right)\left(c^2 - 2mk_{\mathrm{e}}\right)^2\right]^{1/2}}{2m^2\left(X_{\mathrm{e}}^2/B_1^2 - 1\right)}\right\}^{1/2}$$

(16)

The phase–frequency relationship of the system can be given by

$$\theta_1 = \arctan\left(\frac{-cB_1}{-m\omega^2 B_1 + k_1 B_1 - 2k_2\alpha B_1 + (3/4)\,k_3 B_1^3 + 3k_3\alpha^2 B_1}\right) \tag{17}$$

The absolute displacement transmissibility of the ring beam isolator can be given by

$$\mid T_{\mathrm{D}} \mid = |X| / |X_{\mathrm{e}}| = \sqrt{(B_1 \cos\theta_1 + X_{\mathrm{e}})^2 + (B_1 \sin\theta_1)^2}/X_{\mathrm{e}} \tag{18}$$

Table 1 Physical and geometrical properties of the ring beam

| Item	Notation	Value
Mass	m (kg)	0.2
Vertical damping coefficient	c_v (Ns/m)	0.5
Horizontal damping coefficient	c_h (Ns/m)	50
Thickness of ring beam	H (m)	0.001
Radius of ring beam	R (m)	0.3
Width of the ring beam	W (m)	0.05
Young's modulus	E_{22} (Pa)	2.06×10^{11}
Length of the horizontal damper	l (m)	0.03
Base excitation	X_e (m)	0.00035

3.2 Discussion and Results

To investigate whether it is better to place vertical or horizontal dampers in the ring isolator, the amplitude of the base motion is fixed. Both physical and geometrical properties of the ring beam are shown in Table 1. In the following study, the corresponding parameter values of the circular ring beam are assigned as listed in Table 1 if there is no special mention.

For three stages ($m = 0.2$, 1.0, 3.1 kg), it can be seen in Fig. 2a–c that the vertical damper is effective in reducing the response around the resonance frequency, but it degrades the vibration performance at high frequencies. In Fig. 2a–c, it can be seen that the horizontal dampers are not as effective around the resonance frequency, but do not degrade the isolator performance at high frequencies, in the isolation region. Higher damping could, however, improve the performance at resonance. Thus, the investigated horizontal dampers offer a clear advantage compared to the vertical damper for weak excitation. The reason for this is that the nonlinear damping is correlated positively with the displacement response, and the displacement response is relatively high at resonance frequency but low at high frequency.

4   Linear and Nonlinear Damping Work Together

To optimize the ring isolator, both vertical and horizontal dampers are used. As shown in Fig. 3, it has the advantages of linear and nonlinear damping combined. Compared with the undamped system, the ring isolator equipped with both vertical damping and horizontal damping could suppress the resonance vibration more effectively, and simultaneously, the system works well at high frequencies. The peak reduction increases as the ring thickness increases. A reduction in the transmissibility is about 23.1 at $H = 0.0012$ m. The peak reduction decreases as the ring radius increases. A reduction in the transmissibility is about 24.1 at $R = 0.25$ m.
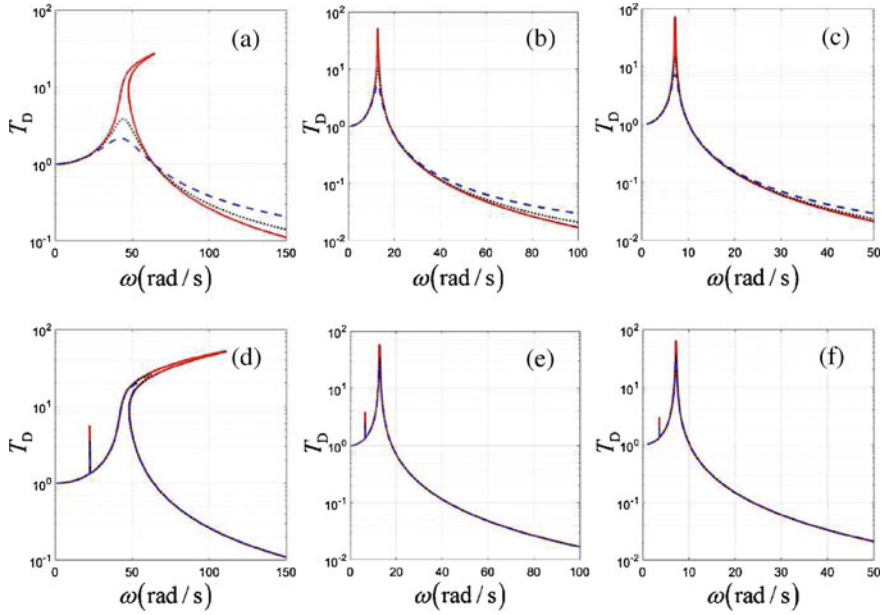
Fig. 2 Comparison of linear and nonlinear damping effects on the dispalcement transmissibility, for $H = 0.001$ m, $R = 0.3$ m, $W = 0.05$ m, $m = 0.2$ kg (**a**, **d**) 1.0 kg (**b**, **e**) 3.1 kg (**c**, **f**); (**a–c**) No horizontal damping while vertical damping is changed (red solid line for $c_v = 0.5$ Ns/m, black dotted line for $c_v = 2.5$ Ns/m, blue dotted line for $c_v = 5$ Ns/m); (**d**, **e**, **f**) No vertical damping while horizontal damping is changed (red solid line for $c_h = 1$ Ns/m, black dashed line for $c_h = 5$ Ns/m, blue dotted line for $c_h = 10$ Ns/m)
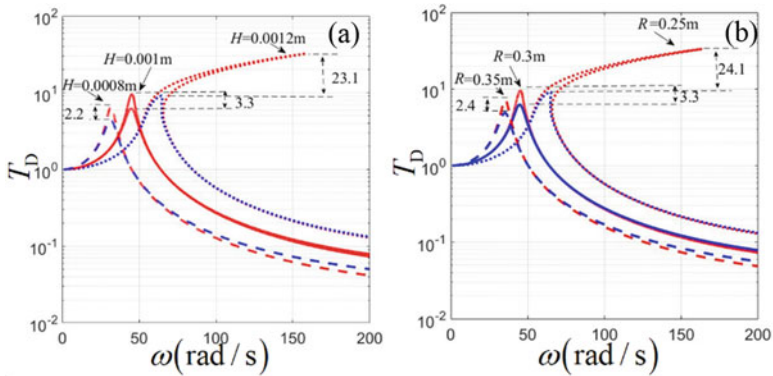
Fig. 3 Comparison of the displacement transmissibility between undamped system and damped system for various values of thickness H and radius R. Red line: undamped system, blue line: $c_v = 1$ Ns/m, $c_h = 2$ Ns/m. (**a**) changing ring thickness H; (**b**) changing ring radius R
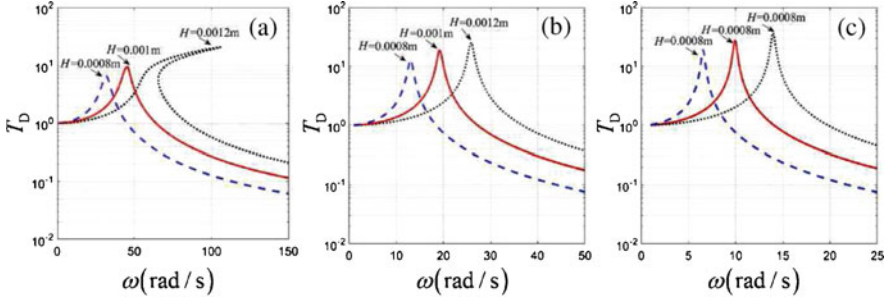
Fig. 4 The displacement transmissibility of the isolation with both linear and nonlinear damping for various values of thickness H. $c_v = 1$ Ns/m, $c_h = 2$ Ns/m. (**a**) stage 1, $m = 0.2$ kg (**b**) stage 2, $m = 1.0$ kg (**c**) stage 3, $m = 3.1$ kg
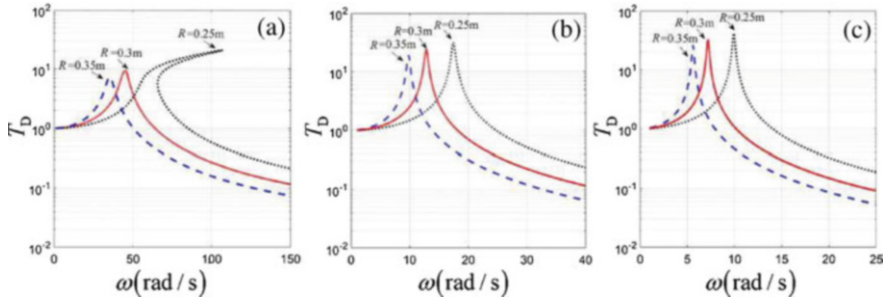
Fig. 5 The displacement transmissibility with both linear and nonlinear damping for various values of the radius R. $c_v = 1$ Ns/m, $c_h = 2$ Ns/m. (**a**) Stage 1, $m = 0.2$ kg; (**b**) stage 2, $m = 1.0$ kg; (**c**) stage 3, $m = 3.1$ kg

To evaluate the isolation performance of both linear and nonlinear damping designed, the different geometrical parameters of the circle ring beam are addressed. The thickness H of ring is changed and the radius is fixed at $R = 0.3$ m. The analytical results for the displacement transmissibility of the ring isolator are illustrated in Fig. 4. All the curves of the displacement transmissibility bend to the right for different thickness H (0.0008, 0.001, 0.0012 m). The primary peak values decrease due to the thickness reduction. The vibration isolation range increases as the thickness decreases at the different pre-loaded mass, and simultaneously, the high frequency transmissibilities decrease. Figure 5 demonstrates the effect of ring radius. The radius of the ring is changed R (0.35, 0.3, 0.25 m), when the thickness is fixed at $H = 0.001$ m. As the radius increases, the resonant frequency and peak value of the transmissibility decrease. In Fig. 6, numerical results for the displacement transmissibility of the circle ring vibration isolator are achieved by the Runge–Kutta scheme and marked with "o" for increasing frequency and "+" for decreasing frequency. The approximate analytical results obtained via the proposed method agree well with the numerical results.
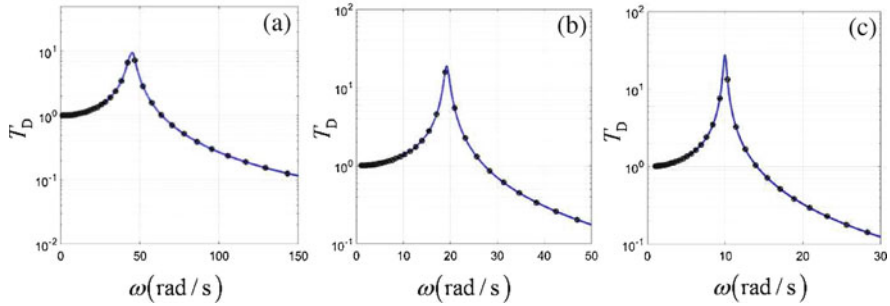
Fig. 6 The analytical and numerical displacement transmissibility of the isolator when the linear and nonlinear damping working together, $c_v = 1$ Ns/m, $c_h = 2$ Ns/m. Solid line: the analytical solution, "+": forward sweep numerical solution, "o": backward sweep numerical solution. (**a**) Stage 1, $m = 0.2$ kg; (**b**) stage 2, $m = 1.0$ kg; (**c**) stage 3, $m = 3.1$ kg

5   Conclusions

The nonlinear damping effects in a circular ring isolator were investigated. The ring delivers a nonlinear stiffness which depends largely on the initial deflection. The dampers were either aligned with the direction of motion or orthogonal to it. It was found that the circular ring isolator is advantageous over other linear isolators, allowing isolation at low frequencies. Concerning the damping elements, it was found that linear viscous damping provided in the direction of the excitation force has good performance at the resonance frequencies but is detrimental to the isolation performance at high frequencies. This was in contrast to the dampers orthogonal to the excitation direction which performs better at high frequencies, but not as well at resonance. Linear and nonlinear damping working together will achieve good performance.

References

1. Lacarbonara, W.: Nonlinear Structural Mechanics. Springer, New York (2013)
2. Carrella, A., Brennan, M., Waters, T., Lopes, V.: Force and displacement transmissibility of a nonlinear isolator with high-static-low-dynamic-stiffness. Int. J. Mech. Sci. **55**, 22–29 (2012)
3. Lu, Z., Yang, T., Brennan, M., Li, X., Liu, Z.: On the performance of a two-stage vibration isolation system which has geometrically nonlinear stiffness. ASME J. Vib. Acoust. **136**(6), 064501 (2014)

4. Zhang, W., Zhao, J.: Analysis on nonlinear stiffness and vibration isolation performance of scissor-like structure with full types. Nonlinear Dyn. **86**, 17–36 (2016)
5. Lu, Z., Yang, T., Brennan, M., Liu, Z., Chen, L.: Experimental investigation of a two-stage nonlinear vibration isolation system with high-static-low-dynamic stiffness. ASME J. Appl. Mech. **84**, 021001 (2017)
6. Wang, X., Liu, H., Chen, Y., Gao, P.: Beneficial stiffness design of a high-static-low-dynamic stiffness vibration isolator based on static and dynamic analysis. Int. J. Mech. Sci. **142–143**, 235–244 (2018)
7. de Haro Silva, L., Paupitz Goncalves, P., Wagg, D.: On the dynamic of the Zener model with nonlinear stiffness for harmonic vibration isolation. Mech. Syst. Signal Process. **112**, 343–358 (2018)
8. Mojahed, A., Moore, K., Bergman, L.: Strong geometric softening-hardening nonlinearities in an oscillator composed of linear stiffness and damping elements. Int. J. Nonlin. Mech. **107**, 94–111 (2018)
9. Huang, X., Liu, X., Su, J., Zhang, Z.: Vibration isolation characteristics of a nonlinear isolator using Euler buckled beam as negative stiffness corrector: a theoretical and experimental study. J. Sound Vib. **333**, 1132–1148 (2014)
10. Xiao, Z., Jing, X., Cheng, L.: The transmissibility of vibration isolators with cubic nonlinear damping under both force and base excitations. J. Sound Vib. **332**(5), 1335–1354 (2013)
11. Wang, Y., Feng, C., Chen, S.: Damping effects of linear and nonlinear tuned mass dampers on nonlinear hinged-hinged beam. J. Sound Vib. **430**, 150–173 (2018)
12. Ho, C., Lang, Z., Billings, S.: Design of vibration isolators by exploiting the beneficial effects of stiffness and damping nonlinearities. J. Sound Vib. **333**(12), 2489–2504 (2014)
13. Carranza, J., Brennan, M., Tang, B.: Sources and propagation of nonlinearity in a vibration isolator with geometrically nonlinear damping. ASME J. Vib. Acoust. **138**, 024501 (2016)

Electroacoustic Absorbers Based on Passive Finite-Time Control of Loudspeakers: A Numerical Investigation

Tristan Lebrun, Marc Wijnand, Thomas Hélie, David Roze, and Brigitte d'Andréa-Novel

Abstract This paper proposes a numerical investigation of a controlled loudspeaker designed to absorb acoustic plane waves at a duct termination. More precisely, a nonlinear control for a current-driven loudspeaker is presented, that relies on (1) measurements of velocity and acoustic pressure at the membrane, (2) a linear electroacoustic loudspeaker model and (3) a nonlinear finite-time control method. Numerical tests are carried out by a passive-guaranteed simulation of the loudspeaker dynamics in the port-Hamiltonian systems formalism. The sound absorption efficiency is evaluated up to 300 Hz by computing the reflected pressure at the membrane. The results are compared with a similar control architecture: the finite-time control for sound absorption proves effective, especially in the low frequency range.

Keywords Finite-time control · Port-Hamiltonian systems · Electroacoustic transducer

1 Introduction

One limitation of passive sound absorbers is the bad efficiency at low frequencies due to the required size of the material. Electrically controlled loudspeakers used as active absorbers have shown to be a way to extend the frequency bandwidth of absorption. A possible approach consists in controlling the loudspeaker dynamics in order to match the membrane impedance to the acoustic characteristic impedance of

---

T. Lebrun (✉) · M. Wijnand (✉)
Sorbonne University, STMS Lab (UMR 9912, IRCAM-CNRS-SU), Paris, France
e-mail: tristan.lebrun@ircam.fr; marc.wijnand@ircam.fr

T. Hélie · D. Roze · B. d'Andréa-Novel
CNRS, STMS Lab (UMR 9912, IRCAM-CNRS-SU), Paris, France

the medium, thus forcing the system to behave like an acoustic transmission line [1]. In particular, Rivet et al. [2] propose an active absorber that uses a feedback based on pressure or velocity for a current-driven boxed loudspeaker, showing broadband absorption results. The present paper restates the model and the impedance matching approach proposed in [2] and describes a new feedback law that combines (1) passive-guaranteed control based on the port-Hamiltonian systems formalism [3, 4] and (2) a (nonlinear) finite-time control law [5, 6], an alternative to asymptotic or exponential control methods. The efficiency of the proposed controller in terms of sound absorption is evaluated numerically.

2   Open-Loop Electroacoustic System

This section presents the considered models for the acoustic propagation (Sect. 2.1) and the current-driven loudspeaker (Sect. 2.2).

2.1   *Plane Wave Propagation in a Tube*

Consider a semi-infinite duct with a loudspeaker located at $z = 0$, with a membrane modelled as a flat piston (see Fig. 1). Acoustic plane wave propagation is assumed, therefore the pressure field can be decomposed into progressive waves $p^+(t - z/c)$ and $p^-(t + z/c)$, where c is the speed of sound. At $z = 0$, the particle velocity field equals the piston velocity, leading to the following relation between the pressure field $p_{ac}(t)$ at $z = 0$ and the piston velocity $\dot{\xi}(t)$,

$$p_{ac}(t) = 2p^+(t) - \rho c\, \dot{\xi}(t), \qquad (1)$$

where ρ is the air density.

2.2   *Current-Driven Electrodynamic Loudspeaker Model*

Physical Model A lumped model of boxed loudspeaker is adopted, considered as a mechanical oscillator with displacement $\xi(t)$ and momentum $\mathfrak{p}(t) = M_m \dot{\xi}(t)$,

Fig. 1 Plane wave propagation in a semi-infinite duct. A loudspeaker, modelled as a flat piston, is located at $z = 0$
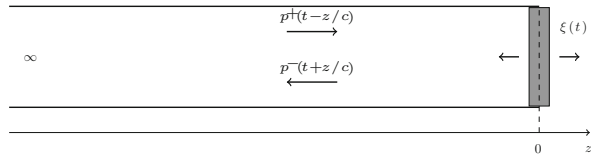
where M_m is the moving mass. The oscillator is excited by the Lorentz force $Bl\,i(t)$ and the force due to the acoustic pressure $S_d\,p_{ac}(t)$. This yields the following mechanical equation that states the force balance of the system,

$$K_m\,\xi(t) + R_m\,\dot{\xi}(t) + \dot{\mathfrak{p}}(t) + Bl\,i(t) = S_d\,p_{ac}(t), \tag{2}$$

where K_m (N/m) is the stiffness coefficient associated with the suspension and the sealed enclosure, R_m (Ns/m) is the mechanical damping coefficient, Bl (N/A) is the electromechanical coupling factor and i is the input electric current. The current drive enables rejection of undesired electric behaviour due to induction effect of the coil, usually described by a resistance R_e (Ω) and an inductance L_e (H).

Port-Hamiltonian Formulation The loudspeaker model described in (2) is restated in the port-Hamiltonian formalism [3], that relies on the expression of the system energy,

$$\mathcal{H}(\xi, \mathfrak{p}) = \frac{K_m\xi^2}{2} + \frac{\mathfrak{p}^2}{2M_m}, \tag{3}$$

namely the sum of the potential and kinetic energy stored by the system. Denoting the state and input of the system by, respectively,

$$\mathbf{x}(t) = \begin{bmatrix} \xi(t) : \text{displacement} \\ \mathfrak{p}(t) : \text{momentum} \end{bmatrix}, \qquad \mathbf{u}(t) = \begin{bmatrix} i(t) : \text{electric current} \\ p_{ac}(t) : \text{acoustic pressure} \end{bmatrix},$$

a state-space representation of the loudspeaker dynamics can be derived:

$$\{\mathcal{S}\}: \quad \begin{aligned} \dot{\mathbf{x}} &= \left(\underbrace{\begin{bmatrix} 0 & 1 \\ -1 & 0 \end{bmatrix}}_{J} - \underbrace{\begin{bmatrix} 0 & 0 \\ 0 & R_m \end{bmatrix}}_{R} \right) \nabla\mathcal{H}(\mathbf{x}) + \underbrace{\begin{bmatrix} G_i & G_p \end{bmatrix}}_{G} \mathbf{u}, \\ \mathbf{y} &= \underbrace{\begin{bmatrix} G_i^\mathsf{T} \\ G_p^\mathsf{T} \end{bmatrix}}_{G^\mathsf{T}} \nabla\mathcal{H}(\mathbf{x}), \end{aligned} \tag{4}$$

where J is skew-symmetric, R is positive semi-definite, $G_i = \begin{bmatrix} 0 & -Bl \end{bmatrix}^\mathsf{T}$ and $G_p = \begin{bmatrix} 0 & S_d \end{bmatrix}^\mathsf{T}$. The outputs are defined as the dual quantities of the inputs $\mathbf{u}(t)$:

$$\mathbf{y}(t) = \begin{bmatrix} e(t) : \text{back-EMF voltage} \\ v_{ac}(t) : \text{acoustic outflow} \end{bmatrix}.$$

The port-Hamiltonian formulation (4) ensures the passivity property of the physical system through its power balance

$$\frac{\mathrm{d}\mathcal{H}\left(\mathbf{x}(t)\right)}{\mathrm{d}t} = \underbrace{\nabla\mathcal{H}(\mathbf{x})^{\mathsf{T}}\dot{\mathbf{x}}}_{\mathcal{P}_{\text{stored}}} = -\underbrace{\nabla\mathcal{H}(\mathbf{x})^{\mathsf{T}}\boldsymbol{R}\nabla\mathcal{H}(\mathbf{x})}_{\mathcal{P}_{\text{diss}}} + \underbrace{\mathbf{y}^{\mathsf{T}}\mathbf{u}}_{\mathcal{P}_{\text{ext}}}, \tag{5}$$

where $\mathcal{P}_{\text{stored}}$, $\mathcal{P}_{\text{diss}}$ and $\mathcal{P}_{\text{ext}}$ are, respectively, the stored, dissipated and external power.

3 Closed-Loop System

This section describes the derivation of a controller that provides an input current $i^{\star}(t)$ given (1) a target membrane motion $\xi^{\star}(t)$, $\dot{\xi}^{\star}(t)$ and (2) the measurement of the acoustic pressure $p_{\text{ac}}(t)$ and the velocity $\dot{\xi}(t)$ at the loudspeaker membrane. The target membrane velocity can be deduced from the measured pressure

$$\dot{\xi}^{\star}(t) = \frac{p_{\text{ac}}(t)}{\rho c} \tag{6}$$

so that the acoustic impedance at the membrane equals the characteristic specific acoustic impedance ρc. First, a nonlinear control law that reaches the target $\dot{\xi}^{\star}(t)$ in finite-time is presented in Sect. 3.1. Then the law is recast as a port-Hamiltonian system in order to guarantee the passivity of the controller, and thus of the closed-loop system, in Sect. 3.2.

3.1 Finite-Time Control Law

A system controlled in finite time will reach an equilibrium point in a finite time (see [7] for a formal definition). Thus, finite-time stability is a stronger property than asymptotic or exponential stability. It is useful for time-constrained and robust control. We first state the following result.

Theorem 1 (Finite-Time Control of a Double Integrator [5]) *Consider the double integrator $\dot{z}_1 = z_2$, $\dot{z}_2 = v$. The origin is a finite-time stable equilibrium point of this system when it is controlled by the input $v = -k_1 \lfloor z_1 \rceil^{\frac{\alpha}{2-\alpha}} - k_2 \lfloor z_2 \rceil^{\alpha}$, with $k_1, k_2 > 0$, $\alpha \in \,]0, 1[$ and $\lfloor x \rceil^{\alpha} \triangleq \text{sgn}(x)|x|^{\alpha}$.*

By identification (cf. [6]), one can find a transformation between the system (4) and the double integrator controlled in finite time. We thus obtain the resulting nonlinear law on the input current that reads

$$i^{\star}(t) = \frac{S_d\, p_{\text{ac}}(t) - K_m\xi(t) - R_m\dot{\xi}(t) + M_m\left(k_1\lfloor\xi(t) - \xi^{\star}(t)\rceil^{\frac{\alpha}{2-\alpha}} + k_2\lfloor\dot{\xi}(t) - \dot{\xi}^{\star}(t)\rceil^{\alpha}\right)}{Bl}. \tag{7}$$

3.2 Passive Finite-Time Control Law

Principle The aim of this part is the derivation of a controller that guarantees (1) convergence towards specific system dynamics $\xi^\star(t)$ and (2) stability in case of badly tuned control parameters. In order to meet these requirements, we impose to the controller the following port-Hamiltonian structure,

$$\{\mathcal{C}\}: \quad \begin{aligned} \dot{\mathbf{x}}_c &= (\boldsymbol{J}_c - \boldsymbol{R}_c)\, \nabla \mathcal{H}_c(\mathbf{x}_c) + \boldsymbol{G}_c \mathbf{u}_c \\ \mathbf{y}_c &= \boldsymbol{G}_c^\mathsf{T} \nabla \mathcal{H}_c(\mathbf{x}_c), \end{aligned} \tag{8}$$

with $\boldsymbol{J}_c$ skew-symmetric and $\boldsymbol{R}_c$ positive semi-definite. The power-preserving interconnection [4] of $\{\mathcal{C}\}$ with $\{\mathcal{S}\}$ is achieved by (see Fig. 2)

$$\begin{bmatrix} i(t) \\ \mathbf{u}_c(t) \end{bmatrix} = \begin{bmatrix} 0 & -1 \\ 1 & 0 \end{bmatrix} \begin{bmatrix} e(t) \\ \mathbf{y}_c(t) \end{bmatrix}, \tag{9}$$

allowing the closed-loop system to be written as a port-Hamiltonian system

$$\{\mathcal{S}+\mathcal{C}\}: \quad \begin{aligned} \begin{bmatrix} \dot{\mathbf{x}} \\ \dot{\mathbf{x}}_c \end{bmatrix} &= \left(\begin{bmatrix} \boldsymbol{J} & -\boldsymbol{G}_i \boldsymbol{G}_c^\mathsf{T} \\ \boldsymbol{G}_c \boldsymbol{G}_i^\mathsf{T} & \boldsymbol{J}_c \end{bmatrix} - \begin{bmatrix} \boldsymbol{R} & \mathbf{0}_{2\times2} \\ \mathbf{0}_{2\times2} & \boldsymbol{R}_c \end{bmatrix} \right) \begin{bmatrix} \nabla \mathcal{H}(\mathbf{x}) \\ \nabla \mathcal{H}_c(\mathbf{x}_c) \end{bmatrix} + \begin{bmatrix} \boldsymbol{G}_p \\ \mathbf{0}_{2\times1} \end{bmatrix} p_{ac} \\ v_{ac} &= \begin{bmatrix} \boldsymbol{G}_p^\mathsf{T} & \mathbf{0}_{1\times2} \end{bmatrix} \begin{bmatrix} \nabla \mathcal{H}(\mathbf{x}) \\ \nabla \mathcal{H}_c(\mathbf{x}_c) \end{bmatrix}. \end{aligned} \tag{10}$$

In the sequel, we choose the same states for the system and the controller: $\mathbf{x} = \mathbf{x}_c$. Modifying the total energy $\mathcal{H}_{s+c}(\mathbf{x})$ and the interconnection matrices in (10) corresponds to an IDA-PBC control [8].

The controller $\{\mathcal{C}\}$ is derived by following the steps below:

1. Choose an energy $\mathcal{H}_{s+c}(\mathbf{x}) \geq 0$ for the closed-loop system that has a minimum at a desired target state $\mathbf{x}^\star$, so that it converges to $\mathbf{x}^\star$.
2. Deduce the energy of the controller by $\mathcal{H}_c(\mathbf{x}) = \mathcal{H}_{s+c}(\mathbf{x}) - \mathcal{H}(\mathbf{x}) \geq 0$.
3. The control law is provided by the second line of (8) : $\mathbf{y}_c = \boldsymbol{G}_c^\mathsf{T} \nabla \mathcal{H}_c(\mathbf{x})$.

Fig. 2 Block diagram of the proposed control architecture
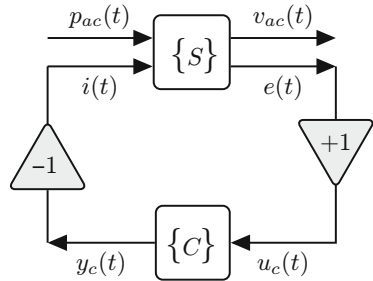
Application to the Proposed Finite-Time Control Law The closed-loop energy is chosen as

$$
\mathcal{H}_{s+c}(\xi, \mathfrak{p}) = M_m k_1 \frac{2-\alpha}{2} \left|\xi - \xi^\star\right|^{\frac{2}{2-\alpha}} + \frac{M_m k_2}{R_m} \frac{1}{\alpha+1} \left|\frac{\mathfrak{p} - \mathfrak{p}^\star}{M_m}\right|^{\alpha+1}
$$
$$
+ \frac{\beta}{2}(\xi - \xi^\star)^2 + \frac{\gamma}{2M_m}(\mathfrak{p} - \mathfrak{p}^\star)^2.
$$
(11)

It has a minimum at $\xi = \xi^\star$ and $\mathfrak{p} = \mathfrak{p}^\star$ so that this energy expression is a good candidate to control the closed-loop system $\{\mathcal{S} + \mathcal{C}\}$ towards the desired targets $\xi^\star$, $\mathfrak{p}^\star$. The energy of the controller is deduced by subtracting (3) from (11), leading to

$$
\mathcal{H}_c(\xi, \mathfrak{p}) = M_m k_1 \frac{2-\alpha}{2} \left|\xi - \xi^\star\right|^{\frac{2}{2-\alpha}} + \frac{M_m k_2}{R_m} \frac{1}{\alpha+1} \left|\frac{\mathfrak{p} - \mathfrak{p}^\star}{M_m}\right|^{\alpha+1}
$$
$$
+ \frac{\beta}{2}(\xi - \xi^\star)^2 + \frac{\gamma}{2M_m}(\mathfrak{p} - \mathfrak{p}^\star)^2 - \frac{1}{2M_m}\mathfrak{p}^2 - \frac{K_m}{2}\xi^2,
$$
(12)

where $\beta > K_m$ and $\gamma > 1$ ensure that $\mathcal{H}_c(\xi, \mathfrak{p})$ has a global minimum. Finally, by imposing the following port-Hamiltonian formulation:

$$
\{\mathcal{C}\}: \quad
\begin{aligned}
\dot{\mathbf{x}} &= \left(\underbrace{\begin{bmatrix} 0 & 0 \\ 0 & 0 \end{bmatrix}}_{\mathbf{J}_c} - \underbrace{\begin{bmatrix} 0 & 0 \\ 0 & 0 \end{bmatrix}}_{\mathbf{R}_c}\right) \nabla \mathcal{H}_c(\mathbf{x}) + \underbrace{\begin{bmatrix} \frac{1}{Bl} \\ \frac{R_m}{Bl} \end{bmatrix}}_{\mathbf{G}_c} \mathbf{u}_c \\
\mathbf{y}_c &= \underbrace{\begin{bmatrix} \frac{1}{Bl} & \frac{R_m}{Bl} \end{bmatrix}}_{\mathbf{G}_c^\intercal} \nabla \mathcal{H}_c(\mathbf{x}_c),
\end{aligned}
$$
(13)

the controller output yields

$$
\mathbf{y}_c = \frac{1}{Bl}\left[M_m k_1 \left\lfloor \xi - \xi^\star \right\rceil^{\frac{\alpha}{2-\alpha}} + M_m \, k_2 \left\lfloor \frac{\mathfrak{p} - \mathfrak{p}^\star}{M_m} \right\rceil^\alpha - K_m \, \xi - R_m \frac{\mathfrak{p}}{M_m} \right.
$$
$$
\left. + \gamma R_m \left(\frac{\mathfrak{p} - \mathfrak{p}^\star}{M_m}\right) + \beta(\xi - \xi^\star) \right].
$$
(14)

The proposed finite-time control law (14) is a passive version of (7) presented in Sect. 3.1, whatever its parameter values satisfying $\beta > K_m$ and $\gamma > 1$.

4   Numerical Results

Two control laws are assessed for an up-chirp pressure excitation $p_{\mathrm{ac}}(t)$ from 20 to 300 Hz at levels 94 and 106 dB.

Law 1: passive finite-time control law (14).   The law is evaluated through simu-
lations of the closed-loop system $\{\mathcal{S}+\mathcal{C}\}$ based on a dedicated numerical scheme
[9, 10] that preserves the power balance in discrete time.

Law 2: proposed in [2].   The law relies on a modification of the inherent elec-
tromechanical properties of the loudspeaker, taking the form of a transfer
function between the measured acoustic pressure and the electric current,

$$I^{\star}(s) = \frac{S_d\,\rho c - sM_m(1-\mu) - R_m - \frac{K_m}{s}(1-\mu)}{Bl\left(\mu s\frac{M_m}{S_d} + \rho c + \mu\frac{K_m}{sS_d}\right)}P(s), \qquad (15)$$

where $P(s)$ and $I^{\star}(s)$ are, respectively, the Laplace transforms of $p_{ac}(t)$ and $i^{\star}(t)$
and $\mu \in [0, 1]$ is a control parameter that adjusts the absorption bandwidth.

Simulations take the total acoustic pressure $p_{ac}(t)$ as input and provide electric
currents generated by the control laws and the induced membrane velocities as
outputs. Then the reflected pressure at the membrane is calculated as

$$p^{-}(t) = \frac{p_{ac}(t) - \rho c\,\dot{\xi}(t)}{2}. \qquad (16)$$

The control parameters are set to $k_1 = 750{,}000$, $k_2 = 50$, $\alpha = 0.8$, $\beta = 1.1K_m$,
$\gamma = 1.1$, $\mu = 0.15$ and the loudspeaker model parameters are those used in [2]. The
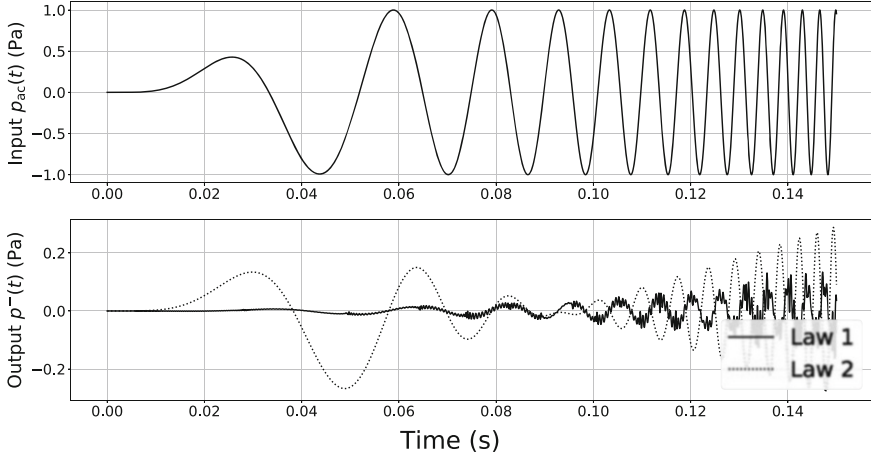sampling rate is set to $f_s = 44{,}100$ Hz.

Time domain simulations of the reflected pressure $p^{-}(t)$ at the loudspeaker
membrane for an input $p_{ac}(t)$ at 94 dB are depicted in Fig. 3. The weak value of the
reflected pressure $p^{-}(t)$ compared to the total pressure $p_{ac}(t)$ reveals an efficient
sound absorption for both control laws.

The absorption capabilities are also evaluated in the frequency domain by
calculating the absorption coefficient as a function of the frequency f defined as

$$\alpha(f) = 1 - \left|\frac{Z(f) - \rho c}{Z(f) + \rho c}\right|^2, \qquad (17)$$

where $Z(f) = P(f)/V(f)$ and $P(f)$ and $V(f)$ are, respectively, the Fourier
transform of the pressure signal $p_{ac}(t)$ and the velocity signal $\dot{\xi}(t)$.

The coefficient $\alpha(f)$ is depicted in Fig. 4. It can be noted that **Law 2** achieves
the best sound absorption (α very close to 1) around the resonance frequency of the
loudspeaker (84 Hz). The proposed **Law 1** is especially efficient at lower frequencies
below and has a slightly broader frequency bandwidth. Note that the closed loop
consisting of a linear model (4) and a nonlinear controller (14) is nonlinear. Thus its
performance varies with the amplitude of the control input, as illustrated in Fig. 4
for $p_{ac}(t)$ at levels 94 and 106 dB.

Fig. 3 Time domain simulations of the reflected pressure $p^-(t)$ at the loudspeaker membrane for an input $p_{ac}(t)$ at 94 dB, for both control laws
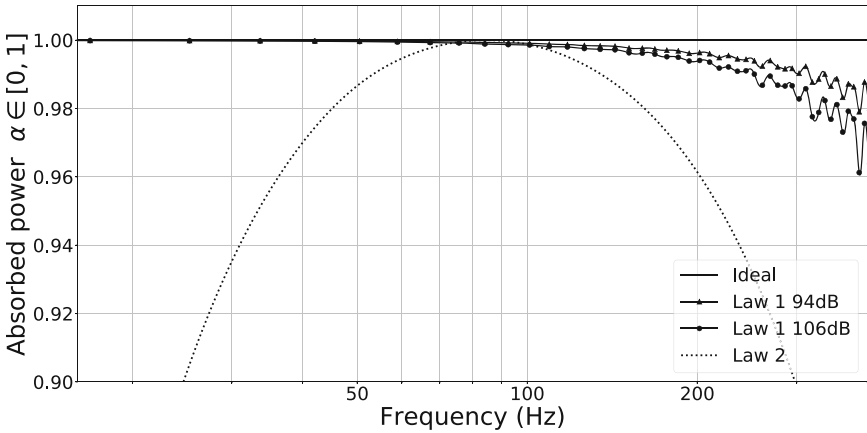
Fig. 4 Absorption coefficient versus frequency for both controls laws at 94 and 106 dB. The (nonlinear) **Law 1** is calculated for two input pressure levels, whereas the (linear) **Law 2** does not depend on the input amplitude

5 Conclusions

This work deals with sound absorption in a duct by a current-driven loudspeaker control. A passive nonlinear control that provides an electric current from the measurements of the acoustic pressure and the membrane velocity has been presented, based on a finite-time control method. Its passivity property ensures robustness against modelling errors. Numerical evaluation of the proposed nonlinear control law shows an efficient sound absorption, especially below the resonance

frequency of the loudspeaker. Further study will focus on a passive control that handles a one-sample delay between the controller input and output, towards its application on a test bench.

References

1. Bobber, R.J.: An active transducer as a characteristic impedance of an acoustic transmission line. J. Acoust. Soc. Am. **48**, 317–324 (1970)
2. Rivet, E., Karkar, S., Lissek, H.: Broadband low-frequency electroacoustic absorbers through hybrid sensor-/shunt-based impedance control. IEEE Trans. Control Syst. Technol. **25**, 63–72 (2017)
3. Maschke, B.M., van der Schaft, A.J.: Port-controlled Hamiltonian systems: modelling origins and systemtheoretic properties. IFAC Proc. Vol. **25**(13), 359–365 (1992)
4. Ortega, R., van der Schaft, A., Maschke, B., Escobar, G.: Energy-shaping of port-controlled Hamiltonian systems by interconnection. In: Proceedings of the 38th IEEE Conference on Decision and Control, vol. 2, pp. 1646–1651 (1999)
5. Bernuau, E., Perruquetti, W., Efimov, D., Moulay, E.: Robust finite-time output feedback stabilisation of the double integrator. Int. J. Control. **88**(3), 451–460 (2015)
6. Wijnand, M., d'Andréa-Novel, B., Hélie, T., Roze, D.: Contrôle des vibrations d'un oscillateur passif : stabilisation en temps fini et par remodelage d'énergie. In: 14ème Congrès Français d'Acoustique, pp. 1370–1375. Le Havre, France (2018)
7. Bhat, S.P., Bernstein, D.S.: Finite-time stability of continuous autonomous systems. SIAM J. Control. Optim. **38**(3), 751–766 (2000)
8. Ortega, R., van der Schaft, A., Maschke, B., Escobar, G.: Interconnection and damping assignment passivity-based control of port-controlled Hamiltonian systems. Automatica **38**(4), 585–596 (2002)
9. Hélie, T., Falaize, A., Lopes, N.: Systèmes Hamiltoniens à Ports avec approche par composants pour la simulation à passivité garantie de problèmes conservatifs et dissipatifs. In: Colloque National en Calcul des Structures, vol. 12 (2015).
10. Falaize, A., Hélie, T.: Passive guaranteed simulations of analog audio circuits: A Port-Hamiltonian approach. Appl. Sci. **6**(10), 273 (2016)

Seismic Response Prediction of Multiple Base-Isolated Structures for Monitoring

Francesco Potenza, Vincenzo Gattulli, and Satish Nagarajaiah

Abstract The seismic response of multiple base-isolated structures is here evaluated through both iterative linearization and numerical solution of the nonlinear structure subjected to stochastic dynamic excitation with the purpose of predicting the behavior of a monitored system. An analytical procedure is used to determine the second-order response statistics of a simple model composed by linear superstructures posed on a common nonlinear base isolation system. The seismic excitation is modeled as a zero-mean filtered white noise and combined with the system equation of motion in an augmented state space representation. Different levels of seismic magnitudes are investigated, and preliminary results are presented here. The study furnishes insights for the design of a permanent seismic monitoring system of the four parts composing the building superstructure of the Department of Human Science at University of L'Aquila laying on a common base isolation system.

F. Potenza (✉)
Department of Civil Architectural and Environmental Engineering, University of L'Aquila, L'Aquila, Italy
e-mail: francesco.potenza@univaq.it

V. Gattulli
Department of Structural and Geotechnical Engineering, Sapienza University of Rome, Rome, Italy
e-mail: vincenzo.gattulli@uniroma1.it

S. Nagarajaiah
Department of Civil and Environmental Engineering, Rice University, Houston, TX, USA
e-mail: satish.nagarajaiah@rice.edu

1   Introduction

Base isolation has become a popular solution to reduce seismically induced acceleration and relative displacement in buildings. Base-isolated structures reach a great number of implementations worldwide [1], and in several cases, the superstructure may consist of several parts separated by seismic or thermal joints. The prediction of seismic response of these structural systems has been simulated by a devoted numerical code in which the nonlinearities are concentrated at the base [2]. However, the approach of the problem by Monte Carlo simulations is extremely onerous. Especially when the aim is related to the reproduction of the seismic behavior of existing structures that have experienced large displacements, bringing the material in the plastic range [3]. Therefore, preliminary design criteria have been proposed for dissipative devices in adjacent structure based on the stochastic evaluation of the structural responses. Moreover, such methods have taken into account the seismic excitation modeled as a filtered white noise considering soil effects [4]. Further, performance-based optimization of nonlinear structures subject to stochastic dynamic excitation has been formulated in terms of the variance of stationary structural responses, which are obtained via equivalent linearization [5]. This approach could provide insights into the optimization of the structural design equipped by dissipative passive systems or base isolated systems. In this respect, the issue to be faced is related to a stochastic structural optimization problem. The problem has been already formulated in a more general context [6], but in recent works, it has been enriched to solve it taking into account the multi-objective nature of the engineering design problems [7]. In this chapter, the prediction of the seismic response of simplified multiple-base isolated structural model could be useful for a preliminary designing of a seismic monitoring system. A further development of the work will be to propose a relationship between the acceleration amplitude induced by environmental noise and the sensor sensitivities.

2   Problem Formulation

Let us consider a simple model composed by n simple oscillators modeling several separated parts of a superstructure posed on a nonlinear base isolation system (Fig. 1a). The model is suitable to evaluate the stochastic dynamic response to seismic excitation of a multiple base-isolated structure (e.g., Fig. 1b).

The equations of motion of a minimum case of two oscillators can be directly derived by D'Alambert principle as follows:

$$
\begin{aligned}
&M_1 \left(\ddot{U}_{\mathrm{b}} + \ddot{D}_1 \right) + C_1 \dot{D}_1 + K_1 D_1 = 0 \\
&M_2 \left(\ddot{U}_{\mathrm{b}} + \ddot{D}_2 \right) + C_2 \dot{D}_2 + K_2 D_2 = 0 \\
&M_{\mathrm{b}} \left(\ddot{U}_{\mathrm{g}} + \ddot{D}_{\mathrm{b}} \right) + M_1 \ddot{D}_1 + M_2 \ddot{D}_2 + C_{\mathrm{b}} \dot{D}_{\mathrm{b}} + K_{\mathrm{b}} D_{\mathrm{b}} = 0
\end{aligned}
\tag{1}
$$
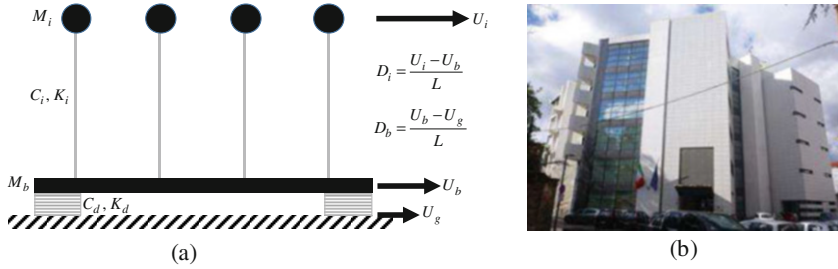
Fig. 1 (a) Simple model composed of linear superstructures posed on a common nonlinear base isolation system. (b) Department of Human Science buildings at L'Aquila

Denoting L as a convenient reference length, the following set of dimensionless variables and mechanical parameters can be introduced:

$$u_i = \frac{U_i}{L}, \quad u_b = \frac{U_b}{L}, \quad u_g = \frac{U_g}{L}, \quad d_i = \frac{U_i - U_b}{L}, \quad d_b = \frac{U_b - U_g}{L}, \quad \rho_i = \frac{M_i}{M_b},$$
$$\omega_i^2 = \frac{K_i}{M_i}, \quad \omega_b^2 = \frac{K_b}{M_b}, \quad \beta_i = \frac{\omega_i}{\omega_b}, \quad \xi_i = \frac{C_i}{2\,\omega_i M_i}, \quad \xi_b = \frac{C_b}{2\,\omega_b M_b}, \quad \tau = \omega_b t$$
$$(2)$$

where u_i, u_b, and u_g are the absolute displacements for i-th pendulum representing a part of the superstructure, base, and ground, respectively, while d_i and d_b are the relative displacements between the superstructures and base and the base and ground, respectively. The relevant parameters to describe the system dynamics are ρ_i and β_i. The first one is defined as the ratio between the mass of the i-th pendulum of the superstructure and the mass of the isolated base while the second one is the ratio between the fundamental frequency of the i-th pendulum of the superstructure and the frequency of the base isolated. The linear dimensionless equations of motion are follows:

$$\ddot{d}_1 + \ddot{d}_b + 2\,\xi_1\,\beta_1\,\dot{d}_1 + \beta_1^2 d_1 = -\ddot{u}_g$$
$$\ddot{d}_2 + \ddot{d}_b + 2\,\xi_2\,\beta_2\,\dot{d}_2 + \beta_2^2 d_2 = -\ddot{u}_g \qquad (3)$$
$$\ddot{d}_b + \rho_1\,\ddot{d}_1 + \rho_2\,\ddot{d}_2 + 2\,\xi_b\,\dot{d}_b + d_b = -\ddot{u}_g$$

where the dots indicate differentiation with respect to the nondimensional time τ. The dimensionless compact form is the following:

$$\mathbf{M}\,\ddot{\mathbf{d}} + \mathbf{C}\,\dot{\mathbf{d}} + \mathbf{K}\,\mathbf{d} = -\mathbf{r}\,\ddot{u}_g \qquad (4)$$

in which $\mathbf{M}$, $\mathbf{K}$, and $\mathbf{C}$ are the mass, stiffness, and damping matrices, respectively. The vector $\mathbf{r}$ allocates the external forces while the vector $\mathbf{d}$ contains the relative displacements. All variable and parameters are as follows:

$$\mathbf{M} = \begin{bmatrix} 1 & 0 & 1 \\ 0 & 1 & 1 \\ \rho_1 & \rho_2 & 1 \end{bmatrix}, \quad C = \begin{bmatrix} 2\xi_1\,\beta_1 & 0 & 0 \\ 0 & 2\xi_2\,\beta_2 & 0 \\ 0 & 0 & 2\xi_b \end{bmatrix}, \quad \mathbf{K} = \begin{bmatrix} \beta_1^2 & 0 & 0 \\ 0 & \beta_2^2 & 0 \\ 0 & 0 & 1 \end{bmatrix},$$
$$\mathbf{r} = \begin{bmatrix} 1 \\ 1 \\ 1 \end{bmatrix}, \quad \mathbf{d} = \begin{bmatrix} d_1 \\ d_2 \\ d_b \end{bmatrix} \tag{5}$$

Considering a hysteretic behavior, the nonlinear equations of motion are given by

$$\mathbf{M}\,\ddot{\mathbf{d}} + \mathbf{C}\,\dot{\mathbf{d}} + \mathbf{f}_N = -\mathbf{r}\,\ddot{u}_g \tag{6}$$

The hysteretic component of the restoring force, $\mathbf{f}_N$, is represented here by an adjunct variable, z, whose evolution is described through a Bouc–Wen model

$$\mathbf{f}_N = \mathbf{K}_L \mathbf{d} + (1 - \alpha)\,\mathbf{h}\,z \tag{7}$$

where $\mathbf{K}_L$ is the linear stiffness matrix, $\mathbf{h}$ is the allocation vector of the hysteretic component, and α is the post- to pre-yielding stiffness ratio. The matrix $\mathbf{K}_L$ and the vector $\mathbf{h}$ have the following expressions:

$$\mathbf{K}_L = \begin{bmatrix} \beta_1^2 & 0 & 0 \\ 0 & \beta_2^2 & 0 \\ 0 & 0 & \alpha \end{bmatrix}, \quad \mathbf{h} = \begin{bmatrix} 0 \\ 0 \\ 1 \end{bmatrix} \tag{8}$$

The new nonlinear system is:

$$\mathbf{M}\,\ddot{\mathbf{d}} + \mathbf{C}\,\dot{\mathbf{d}} + \mathbf{K}_L\,\mathbf{d} + (1 - \alpha)\,\mathbf{h}\,z = -\mathbf{r}\,\ddot{u}_g$$
$$\dot{z} = -\gamma\,\left|\dot{d}_b\right|\,z\,|z|^{n-1} - \beta\,\dot{d}_b\,|z|^n + A\,\dot{d}_b \tag{9}$$

where in the Bouc–Wen model, the parameters γ and β control the shape of the hysteresis loop, A the restoring force amplitude, and n the smooth transition from elastic to plastic response (for large value of n the model tends to an elasto-plastic behavior).

2.1 Stochastic Structural Response

The linear stochastic response of the system described in Eq. (4) can be calculated through the covariance matrix $\mathbf{\Gamma}$. Moreover, defining the state vector as $\mathbf{x}_s = \begin{bmatrix} \mathbf{d}^T & \dot{\mathbf{d}}^T \end{bmatrix}^T$, Eq. (4) can be organized in the space-state formulation:

$$\dot{\mathbf{x}}_s = \mathbf{A}_s\,\mathbf{x} + \mathbf{B}_s\,w \tag{10}$$

where w is a zero-mean stationary Gaussian process while the space-state matrices $\mathbf{A}$ and $\mathbf{B}$ assume the following expression:

$$\mathbf{A}_s = \begin{bmatrix} \mathbf{0}_{3\times3} & \mathbf{I}_{3\times3} \\ -\mathbf{M}^{-1}\mathbf{K} & -\mathbf{M}^{-1}\mathbf{C} \end{bmatrix}, \quad \mathbf{B}_s = \begin{bmatrix} \mathbf{0}_{1\times3}^T & -\mathbf{r}^T \end{bmatrix}^T \tag{11}$$

The stationary stochastic structural responses can be obtained evaluating the covariance matrix $\boldsymbol{\Gamma}$ through the solution of the following Eq. (3):

$$0 = \mathbf{A}_s\,\boldsymbol{\Gamma} + \boldsymbol{\Gamma}\,\mathbf{A}_s + 2\pi\,\mathbf{B}_s\,\mathbf{S}\mathbf{B}_s \tag{12}$$

which is the well-known Lyapunov equation in the unknown $\boldsymbol{\Gamma}$ while $\mathbf{S}$ is the power spectral density of the white noise. It is worth to highlight that the main diagonal of the covariance matrix consists of the expected values (variance and standard deviations) of the displacements and velocity while the mixed expected values are given by the terms out of diagonal.

The nonlinear stochastic response can be approximately determined by an equivalent linear system [4, 7] that allows to easily manage the solution to the previously introduced Lyapunov equation. Consequently, the new form of the equations of motion is follows:

$$\begin{aligned} \mathbf{M}\,\ddot{\mathbf{d}} + \mathbf{C}\,\dot{\mathbf{d}} + \mathbf{K}_L\,\mathbf{d} + (1-\alpha)\,\mathbf{h}\,z &= -\mathbf{r}\,\ddot{u}_g \\ \dot{z} + C_{21}\,\dot{d}_b + K_{22}\,z &= 0 \end{aligned} \tag{13}$$

where the two coefficients C_{21} and K_{22} can be evaluated in terms of the second moments of $\dot{d}_b$ and z [8]:

$$\begin{aligned} C_{21} &= \sqrt{\frac{2}{\pi}}\,\left[\gamma\,\frac{E\left[\dot{d}_b z\right]}{\sigma_{\dot{d}_b}} + \beta\,\sigma_z\right] - A \\ K_{22} &= \sqrt{\frac{2}{\pi}}\,\left[\gamma\,\sigma_{\dot{d}_b} + \beta\,\frac{E\left[\dot{d}_b z\right]}{\sigma_z}\right] \end{aligned} \tag{14}$$

Starting from the equivalent linear system, it is possible to define a new state-space vector as $\tilde{\mathbf{x}} = \begin{bmatrix} \mathbf{d}^T & \dot{\mathbf{d}}^T & z \end{bmatrix}^T$ that brings the system to a new state-space formulation:

$$\dot{\tilde{\mathbf{x}}} = \mathbf{A}_e\,\tilde{\mathbf{x}} + \mathbf{B}_e\,w \tag{15}$$

where the new state-space matrices, $\mathbf{A}_e$ and $\mathbf{B}_e$ (where the subscript stands for equivalent linearization), assume the following form:

$$\mathbf{A}_e = \begin{bmatrix} \mathbf{0}_{3\times3} & \mathbf{I}_{3\times3} & \mathbf{0}_{3\times1} \\ -\mathbf{M}^{-1}\mathbf{K}_L & -\mathbf{M}^{-1}\mathbf{C} - (1-\alpha)\,\mathbf{h}_{3\times1} \\ \mathbf{0}_{1\times3} & C_{21}\mathbf{h}^T & K_{22} \end{bmatrix}_{7\times7}, \quad \mathbf{B}_e = \begin{bmatrix} \mathbf{0}_{3\times1} \\ -\mathbf{r}_{3\times1} \\ 0 \end{bmatrix}_{7\times1} \tag{16}$$

Considering the fact that the coefficients C_{21} and K_{21} depend on the standard deviations, to solve the Lyapunov equation, an iterative solution is required. The iteration can start using the solution of the linear system with a stiffness equal to the pre-yielding stiffness of the nonlinear system.

The stochastic excitation can be represented as a filtered white noise (e.g., Kanai-Tajimi) that in the state space form assumes the following expression:

$$\dot{\mathbf{x}}_f = \mathbf{A}_f \mathbf{x}_f + \mathbf{B}_f w$$
$$\ddot{u} = \mathbf{C}_f \mathbf{x}_f \tag{17}$$

where $\mathbf{x}_f$ is the state vector for the filter while $\mathbf{A}_f$, $\mathbf{B}_f$, and $\mathbf{C}_f$ are chosen to represent the characteristics of the excitation. In particular, combining the equations of the structural model and the ones of the loading model, a new expression of an augmented system is obtained:

$$\dot{\mathbf{x}}_a = \mathbf{A}_a \mathbf{x}_a + \mathbf{B}_a w$$
$$\mathbf{y}_s = \mathbf{C}_a \mathbf{x}_a \tag{18}$$

where

$$\mathbf{x}_a = \left(\mathbf{x}_s^T \ \mathbf{x}_f^T \right)^T, \quad \mathbf{A}_a = \begin{bmatrix} \mathbf{A}_s & \mathbf{B}_s \mathbf{C}_f \\ \mathbf{0} & \mathbf{A}_f \end{bmatrix}, \quad \mathbf{B}_a = \begin{bmatrix} \mathbf{0} \\ \mathbf{B}_f \end{bmatrix}, \quad \mathbf{C}_a = \begin{bmatrix} \mathbf{C}_s & \mathbf{D}_s \mathbf{C}_f \end{bmatrix} \tag{19}$$

In this case, the covariances of the structural responses can be determined through the solution of the following equation:

$$\dot{\boldsymbol{\Gamma}}_{\mathbf{x}_a} = \mathbf{A}_a \, \boldsymbol{\Gamma}_{\mathbf{x}_a} + \boldsymbol{\Gamma}_{\mathbf{x}_a} \mathbf{A}_a + 2\pi \mathbf{B}_a \mathbf{S} \mathbf{B}_a \tag{20}$$

In the case of direct integration, the effect of the nonstationary stochastic process could be considered multiplying the output of the filter by an envelope function $e(t)$ [7].

3   Numerical Results

This section illustrates and describes some preliminary numerical results regarding the linear and nonlinear stochastic structural response. In particular, Fig. 2 reports the results for the linear case while Fig. 3 reports the ones with the nonlinear effects analyzed through the equivalent linearization procedure previously introduced. In the Fig. 2 have been fixed the structural parameters for the first oscillator ($\beta_1 = 8.33$, $\rho_1 = 0.1$) while in the Fig. 3 the ones of the second oscillator ($\beta_2 = 6.25$, $\rho_2 = 0.3$).

Looking at the results obtained considering a linear behavior, as expected, by increasing the β_2 parameters, a quick exponential decay of the standard deviation of the second oscillator is observed, especially for low β_2 values (see Fig. 2b).
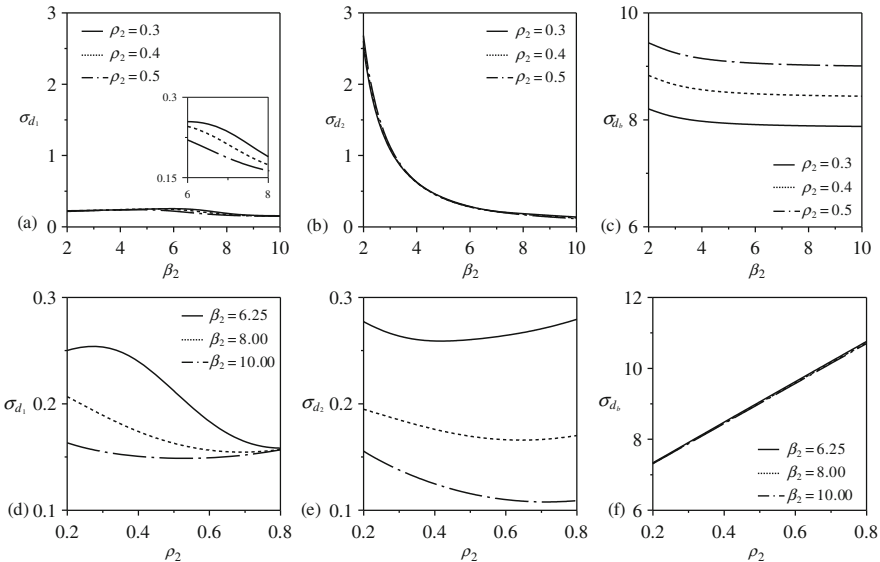
Fig. 2 Linear stochastic structural response for multiple base-isolated structures: For all cases: $\beta_1 = 8.33$ and $\rho_1 = 0.1$. Modal damping: $\xi_1 = \xi_2 = \xi_b = 0.05$. Standard deviations for first oscillator (**a**) and (**d**), second oscillator (**b**) and (**e**), base-isolated (**c**) and (**f**)
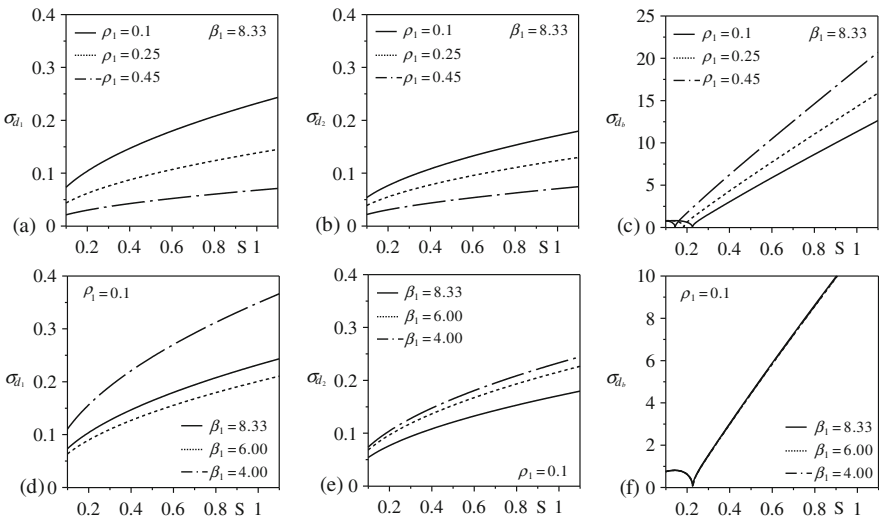
Fig. 3 Nonlinear stochastic structural response for multiple base-isolated structures: For all cases: $\beta_2 = 6.25$ and $\rho_2 = 0.3$. Modal damping: $\xi_1 = \xi_2 = \xi_b = 0.05$. Standard deviations for first oscillator (**a**) and (**d**), second oscillator (**b**) and (**e**), base-isolated (**c**) and (**f**)

The corresponding behavior, shown in the Fig. 2a, remains practically unchanged. The variations caused by increasing ρ_2 are reported in the Fig. 2d, e. Such increasing seems to influence both standard deviations. However, in this case, the responses have been analyzed, preliminary, for high fixed β_2 values, and so the variations have been visualized for a small range of the standard deviations. Some main remarks are the following: (1) in all cases, for fixed ρ-parameters, the standard deviations decrease going towards high β_2 parameters, even if the variations are very small; (2) in Fig. 2d the value of the standard deviation seems to tend to an asymptotic value near to 0.15; (3) it is worth to highlight that in Fig. 2d, e, for all analyzed cases, local minimum (and a maximum only for $\beta_2 = 6.25$) that could suggest the development of the design procedure is found. In the last two Fig. 2c, f, the standard deviation of the base structural response has substantially linear behavior varying the ρ_2 parameter and unchanged varying the β_2 parameters.

The effects of the nonlinear behavior have been evaluated increasing the value of the power spectral density of the white noise, i.e. S. In particular, as described in the previous section, the nonlinearity, introduced to describe the hysteretic component of the restoring force, directly influences the structural response of the base. This appears evident looking at the results reported in Fig. 3c, f. Indeed, for small values of the spectral intensity, the standard deviation of the base assumes a hardening behavior, reaching a minimum point for a certain value of the spectral intensity. Moreover, this particular situation occurs for increasing S-values decreasing the ρ_1 parameter.

This makes a sense because it corresponds to a relative stiffening of the base. Imperceptible variations are observed when the β_1 parameter is changed (see Fig. 3f). After that point, further increasing of the spectral density would seem to produce a linear increasing of the standard deviation. The standard deviations related to the relative displacements of the two oscillator seem to have a more regular behavior. Indeed, the amplitudes grow while increasing the value of the intensity and go down while decreasing both ρ_1 and β_1 parameters. Interesting to note that in Fig. 3d the results seem to show a point of minimum for a particular value of β_1 with S fixed.

4   Conclusion

The work aimed at developing a simple analytical model representative of the dynamic of a multiple base-isolated structures. The evaluation of linear and nonlinear stochastic structural response could be used for both to optimize nonlinear structures equipped by dissipative devise and to select sensor sensitivities for seismic monitoring. Moreover, the application of a linearized iterative procedure permits to evaluate the stochastic stationary response avoiding the execution of very long and onerous numerical simulations. A real case study at L'Aquila will be used to verify the design procedure potentiality.

References

1. Nagarajaiah, S.: 3D BASIS origins, novel developments and its impact in real projects around the world. In: Computational Methods, Seismic Protection, Hybrid Testing and Resilience in Earthquake Engineering. Geotechnical, Geological and Earthquake Engineering, vol. 33. Springer, Cham (2015)
2. Tsopelas, P.C., Nagarajaiah, S., Constantinou, M.C., Reinhorn, A.M.: Nonlinear dynamic of multiple building base isolated structures. Comput. Struct. **50**, 99–110 (1994)
3. Ceci, A.M., Gattulli, V., Potenza, F.: Serviceability and damage scenario in RC irregular structures: post-earthquake observations and modelling predictions. ASCE J. Perform. Constr. Facil. **27**(1), 98–115 (2013)
4. Gattulli, V., Potenza, F., Spencer, B.F.: Design criteria for dissipative devices in coupled oscillators under seismic excitation. Struct. Control. Health Monit. **25**(7), e2167 (2018)
5. Xu, J., Spencer, B.F., Lu, X.: Performance-based optimization of nonlinear structures subject to stochastic dynamic loading. Eng. Struct. **134**, 334–345 (2017)
6. Jensen, H.A., Sepulveda, A.E.: Optimal design of uncertain systems under stochastic excitation. AIAA J. **38**(11), 2133–2141 (2000)
7. Xu, J., Spencer, B.F., Lu, X., Chen, X., Lu, L.: Optimization of structures subject to stochastic dynamic loading. Comput. Aided Civ. Inf. Eng. **32**, 657–673 (2017)
8. Wen, Y.K.: Equivalent linearization for hysteretic systems under random excitation. J. Appl. Mech. **47**, 150–154 (1980)

Frequency Domain Nonlinear Modeling and Analysis of Liquid-Filled Column Dampers

H. Sefa Kizilay and Ender Cigeroglu

Abstract Tuned liquid column dampers (TLCDs) have an extensive usage as effective vibration absorbers to enhance the structure response under the effect of seismic or wind loads. In this study, parameter optimization of nonlinear model of a TLCD in frequency domain under harmonic excitation is proposed in order to improve the performance of TLCDs. The nonlinearity in the model is due to the head-loss caused by the orifice resulting in velocity squared damping. A six-story building with a TLCD is considered as a case study. Describing function method (DFM) is used to model the nonlinear effects in frequency domain which results in a set of nonlinear algebraic equations. The resulting set of nonlinear equations is solved by Newton's method utilizing Homotopy Continuation. The effect of change of TLCD parameters (cross-sectional area, head loss coefficient, total length, horizontal length) on the overall system response is investigated through the developed nonlinear model. TLCD parameters are optimized utilizing genetic algorithm and gradient descent optimization methods. Response of the optimized and non-optimized models is compared in frequency domain. The linear and nonlinear models are also compared, and the necessity of introducing nonlinearity to the frequency domain model is addressed.

Keywords Tuned liquid column damper (TLCD) · Nonlinear vibrations · Describing function method (DFM) · Optimization

H. S. Kizilay
Middle East Technical University, Ankara, Turkey

E. Cigeroglu (✉)
Department of Mechanical Engineering, Middle East Technical University, Ankara, Turkey
e-mail: ender@metu.edu.tr

1 Introduction

Balendra et al. [1] studied the effectiveness of passive TLCDs in reducing the wind-induced vibration of towers. Accordingly, authors used direct time integration method to solve the linearized nonlinear governing differential equations of motion. In their studies, optimum parameters were provided for a series of towers in relation to maximum reduction in acceleration and displacement under harmonic excitations. Those studies subsequently reveal that virtually the same level of reduction in acceleration is achievable for any tower of practical interest when a suitable opening ratio is used for the orifice in the TLCD connected rigidly to the structure.

Gao et al. [2] considered the same problem, where authors employed direct time integration, i.e., Newmark's constant average acceleration method, to solve the nonlinear differential equation of motion of the building coupled with a TLCD. Authors provided optimum TLCD parameters for a variety of flexible structures which reduced the peak structural response to harmonic excitation in a wide frequency range. Authors considered a variation of U- and V-shaped TLCD, which have different cross-sectional areas in vertical and horizontal sections.

In the study of Mohebbi et al. [3], a systemic optimization method is proposed regarding the design of a passive multiple tuned liquid column dampers (MTLCDs) in an effort to enhance seismic behavior of structures. By developing and solving a constrained optimization problem through genetic algorithm (GA), the authors attempt to identify the optimum parameters of TLCDs that minimizes the maximum displacement and the maximum acceleration values. The authors use Wilson's theta numerical procedure to solve the nonlinear differential equation of motion of the structure. A ten-story shear frame exposed to a filtered white noise excitation is used while demonstrating the design procedure. Structure with optimal MTLCDs is tested under the circumstances of real earthquakes.

Ghosh et al. [4] investigated the application of the liquid column damper (LCD) for seismic vibration control of short period structures and viability of the LCD coupled to the structure by a spring. The authors modeled the structure as a linear, viscously damped single-degree-of-freedom system. In linearization of the nonlinear orifice damping of the LCD, the study adopts a stochastic equivalent linearization technique.

A trial and error process of satisfying geometrical constraints and varying controlled response factors for a bi-directional (two-way) liquid damper has been presented by Min et al. [5]. TLCD in which liquid moves through a U-shaped tube and the tuned sloshing damper (TSD) in which liquid sloshes within a container, respectively, for two orthogonal directions, are combined to create the two-way liquid damper. By minimizing the mean square value of the error between the nonlinear and equivalent linearized system, the nonlinear equation of motion is linearized. Tuning the natural frequencies of liquid motion in the damper to those of the building results in the determination of the required dimensions of the damper.

In this chapter, a nonlinear TLCD model is constructed, and the effects of different parameters on the system response are investigated in frequency domain under harmonic excitation. For harmonic excitation, utilizing DFM was developed by Tanrikulu et al. [6], nonlinear differential equations of motion are transformed into a set of nonlinear algebraic equations which are solved by Newton's method with homotopy continuation. It is possible to solve a set of nonlinear algebraic equations by means of time domain methods; yet, DFM is proved to be a more efficient method that provides the solution faster than any other time-domain methods. The nonlinearity generated due to the head loss at the orifice is included in the model as velocity-squared damping element. DFM is used to model the nonlinear element, and a set of nonlinear algebraic equations is obtained through the application. TLCD parameters are optimized in order to minimize the response amplitude of a six-story building by using genetic algorithm and gradient descent optimization methods. Results obtained for optimized and non-optimized models are compared, and the effect of including nonlinearity due to head loss on the system response is shown.

2 Mathematical Modeling

In this part, first, a simple shear building model with a TLCD is considered. It should be noted that location of TLCD has a significant effect on building model. In this chapter, TLCD is placed on the rooftop in order to dissipate energy of the first mode of the structure under the harmonic excitation. However, it is possible to consider multiple TLCDs at different locations.

2.1 Single DOF System with TLCD

Saoka et al. [7] developed equation of motion of SDOF system with a TLCD, and Sakai et al. [8] performed experiments to verify the developed equation of motion. Schematic representation of the SDOF model used in this study is given in Fig. 1.

The nonlinear differential equation of the primary structure and the motion of the fluid in the U-shaped tube are given as

$$
\begin{bmatrix} (M_s + \rho Al) & \rho Ab \\ \rho Ab & \rho Al \end{bmatrix} \begin{Bmatrix} \ddot{X}_s \\ \ddot{x}_f \end{Bmatrix} + \begin{bmatrix} c & 0 \\ 0 & 0 \end{bmatrix} \begin{Bmatrix} \dot{X}_s \\ \dot{x}_f \end{Bmatrix} + \begin{bmatrix} k & 0 \\ 0 & 2\rho Ag \end{bmatrix} \begin{Bmatrix} X_s \\ x_f \end{Bmatrix}
$$
$$
+ \begin{Bmatrix} 0 \\ \frac{\rho}{2} A\xi \, |\dot{x}_f| \, \dot{x}_f \end{Bmatrix} = \begin{bmatrix} F(t) \\ 0 \end{bmatrix}. \tag{1}
$$

M_s, c, and k are mass, damping, and stiffness of the SDOF system, respectively. ρ is the density of liquid , A is cross-sectional area, b is horizontal length, l is total length, and ξ is head loss coefficient.

Fig. 1 SDOF system with TLCD
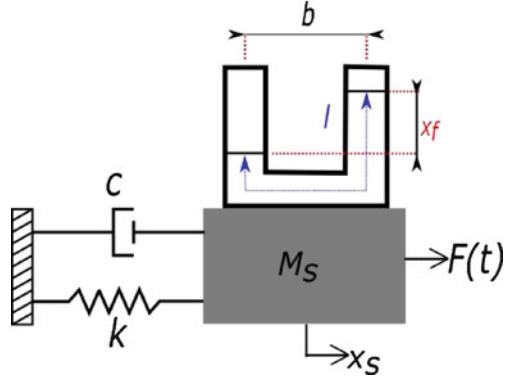
2.2 Multi-Story Shear Building Model with TLCD

A multi-story shear building model with a TLCD is given in Fig. 2 which is used in this study. The equation of motion of the model can be given as follows:

$$[M]\{\ddot{x}\} + [C]\{\dot{x}\} + [K]\{x\} + \{f_{NL}\} = \{f_{exc}\} \tag{2}$$

$$\{f_{exc}\} = -[M]\ddot{x}_g, \tag{3}$$

where $\{x\}$ is the displacement vector, and $[M]$, $[C]$, and $[K]$ denote the mass, damping, and stiffness matrices, respectively. $\{f_{NL}\}$ is the vector of nonlinear forcing due to TLCD, $\{f_{exc}\}$ is the excitation force vector, and $\ddot{x}_g$ is the base acceleration input.

When Eq. (4) is examined, one can understand that total differential equation number is $(n + 1)$ due to the existence of single TLCD, where n is the number of stories in the building. System matrices and forcing vectors can be expressed as

$$\{x\}_{n+1} = \{x_1 \ x_2 \ \ldots \ \ldots \ x_n \ x_f\}^{\mathrm{T}}. \tag{4}$$

2.3 Modeling of Velocity-Squared Damping

Fluid forced rapidly through an orifice causes velocity-squared damping. Nonlinear forcing due to velocity squared damping can be written as

$$n(\dot{x}) = c_n \cdot |\dot{x}| \cdot \dot{x}, \tag{5}$$

where $c_n = \rho A \xi / 2$ is the coefficient of velocity-squared nonlinearity. Nonlinear forcing due to velocity-squared damping as a function of velocity is shown in Fig. 3.

Fig. 2 MDOF n-story building equipped with TLCD
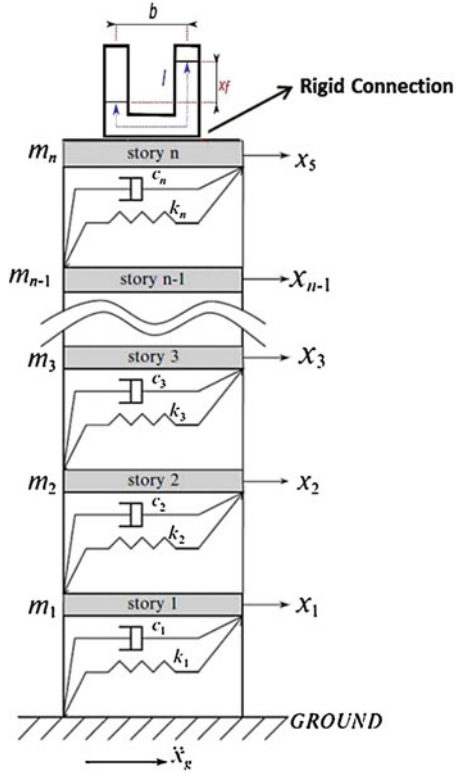
Fig. 3 Nonlinear force vs. velocity for velocity-squared damping
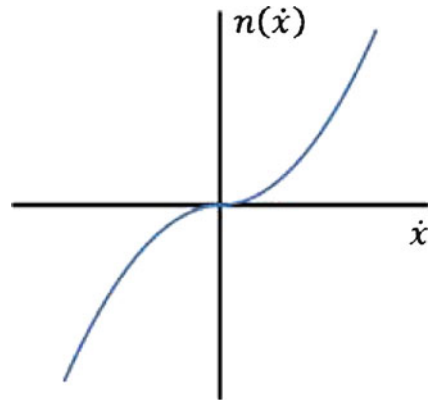
In this study external forcing $\{f_{\text{exc}}\}$ is assumed to be harmonic. For harmonic excitation, response of the systems is also assumed as harmonic which can be written as

$$\{f_{\text{exc}}\} = \text{Im}\left(\{F\}\,\mathrm{e}^{i\omega t}\right), \tag{6}$$

$$\{x\} = \text{Im}\left(\{X\}\,e^{i\omega t}\right), \tag{7}$$

where $\{F\},\{X\}$, and ω are complex amplitude vector of external excitation, complex amplitude vector of displacement response vector, and frequency of excitation.

2.4 Describing Function Method (DFM)

Earthquakes give rise to broadband-type excitation which results in major component of oscillations at the resonance frequencies of buildings. Therefore, frequency domain methods can be used to design and optimize vibration dampers, which are computationally more efficient, compared to time domain methods, since the target is to reduce amplitudes of resonance vibrations.

In linear systems, transfer functions between inputs and outputs are independent of input type and amplitude; however, for nonlinear systems, describing functions, which correspond to the transfer function for linear systems, are different. Using describing functions, system nonlinearity is replaced by a linear gain element chosen in such a way that a similar response of the nonlinearity and its approximation to the same harmonic input is obtained. For single-input describing function (SIDF), the describing function ν can be defined by the ratio of phasor representation of the output components at frequency ω to phasor representation of the input components at the same frequency.

Assume a single harmonic motion as

$$x = \overline{X} \cdot \sin(\omega t) = \overline{X} \cdot \sin(\psi). \tag{8}$$

Using Eqs. (5) and (6), the nonlinear internal force due to velocity-squared damping can be written as follows:

$$n(\dot{x}) = \frac{1}{2}\rho A \xi \cdot \omega^2 \overline{X}^2 \cdot \mid \cos(\omega t) \mid \cdot \cos(\omega t). \tag{9}$$

Describing function, ν, for a nonlinear element can be obtained as follows:

$$\nu = \frac{i}{X \cdot \pi} \cdot \int_0^{2\pi} (n(\dot{x})) \cdot (\cos(\psi) - i \sin(\psi))\, d\psi. \tag{10}$$

For velocity-squared damping, the describing function is obtained as

$$\nu = \frac{4}{3\pi}\rho A \xi \cdot \omega^2 \overline{X} \cdot i \tag{11}$$

The describing function given in Eq. (11) depends on the square of excitation frequency and amplitude of vibration $\overline{X}$. Describing function for velocity-squared damping is pure imaginary. Nonlinear internal forcing for a single TLCD is obtained by multiplying describing function and complex amplitude of motion [6] as

$$F_{\text{NL}} = \frac{4}{3\pi} \rho A \xi \cdot \omega^2 \overline{X} \cdot (i \cdot x_{\text{r}} - x_{\text{i}}), \tag{12}$$

where $\overline{X} = \sqrt{x_{\text{i}}^2 + x_{\text{r}}^2}$ and x_{i} and x_{r} are imaginary and real parts of the relative displacement. For harmonic motion, the following form for Eq. (2) is obtained:

$$\left[[K] - \omega^2 [M] + i\omega [C] \right] * \{X\} + \{F_{\text{NL}}(\{X\})\} = \{f_{\text{exc}}\}. \tag{13}$$

2.5 Solution of Nonlinear Equations

The nonlinear force given by Eq. (12) is displacement and frequency dependent; therefore, a numerical method is necessary to obtain the solution. Eq. (13) is rewritten in terms of a residual vector as

$$\{R(\{X\}, \omega)\} = \left[[K] - \omega^2 [M] + i\omega [C] \right] * \{X\} + \{F_{\text{NL}}(\{X, \omega\})\} - \{f_{\text{exc}}\} = 0. \tag{14}$$

Solution of the nonlinear algebraic equation given by Eq. (14) is obtained by using Newton's method. A single iteration for Newton's method can be expressed as

$$\{X\}_{k+1} = \{X\}_k - \left[\frac{\partial \{R(\{X\}, \omega)\}}{\partial \{X\}} \right]^{-1} \Bigg|_{\{X\}_k, \omega} \{R(\{X\}_k, \omega)\}, \tag{15}$$

where k and $[\partial \{R(\{X\}, \omega)\}/\partial \{X\}]$ are the iteration number and the Jacobian matrix, respectively. Iterations are terminated when the residual norm falls below a predefined error tolerance.

3 Results

Several case studies are performed to investigate the effects of excitation and system parameters on the response of a single-story building. In the first case study, the response of the building is analyzed by changing the amplitude of ground acceleration, $\ddot{x}_{\text{g}}$ from 0.1 to 1 m/s^2. The studied SDOF building system has 5250 kg mass, 840,000 N/m stiffness, and 1160 Ns/m viscous damping coefficient. The
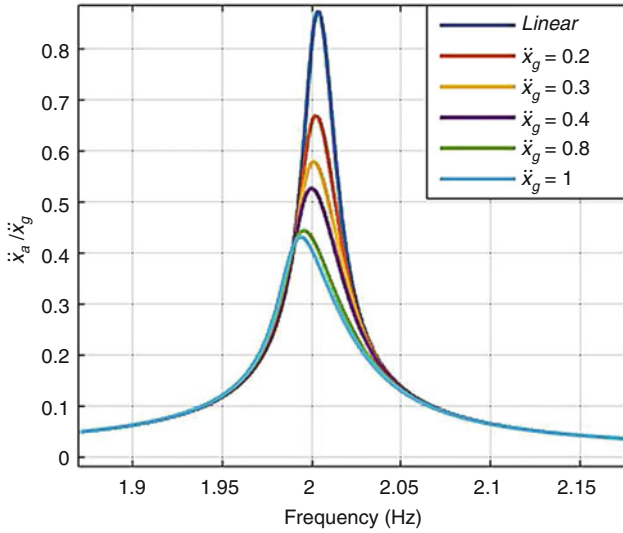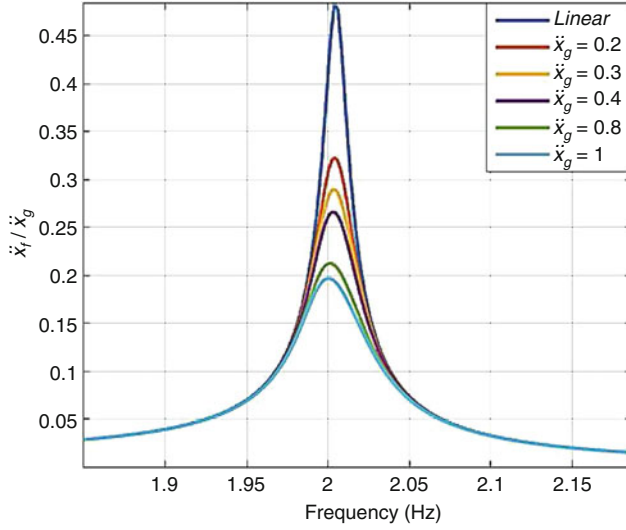
Fig. 4 Displacement of X_s to ground acceleration ratio vs. frequency for different acceleration levels

natural frequency and the damping ratio of the system are 2.01 Hz and 0.01, respectively. Liquid density (ρ), cross-sectional area (A), horizontal length (b), total length (l), and head loss coefficient (ξ) of the U-shaped TLCD are taken as 1000 kg/m^3, 0.5 m^2, 0.5 m, 1 m, and 5, respectively.

Note that, in order to clarify the nonlinear effect of the TLCD on the SDOF system, displacement to ground acceleration ratio for different ground acceleration values is given in Figs. 4 and 5. As the amplitude of harmonic ground acceleration increases, the effect of nonlinear damping of the TLCD on system response increases. Moreover, the resonance frequency of the SDOF system shifts towards lower frequencies. In the second case study, the effects of TLCD parameters on the response of the single-story building are investigated. Four parameters of the TLCD considered analyzed in terms of cross-sectional area (A), horizontal length (b), total length (l), and head loss coefficient (ξ).

System parameters are identical to the ones used in the first case study. However, viscous damping coefficient is reduced to 116 Ns/m, i.e., one tenth of the previous one, in order to observe the effects of parameter changes clearly. While investigating the effects of changes in TLCD parameters, only the parameter under investigation is varied and the other three parameters are kept as constant.

It can be seen from Fig. 6 that as the cross-sectional area of the TLCD increases, the response amplitude decreases, since the nonlinear damping coefficient is linearly proportional to the cross-sectional area. However, it should be noted that an increase in the cross-sectional area increases the amount of fluid used, hence the mass matrix, and decreases the resonance frequency.

Fig. 5 Displacement of X_f to ground acceleration ratio vs. frequency for different acceleration levels
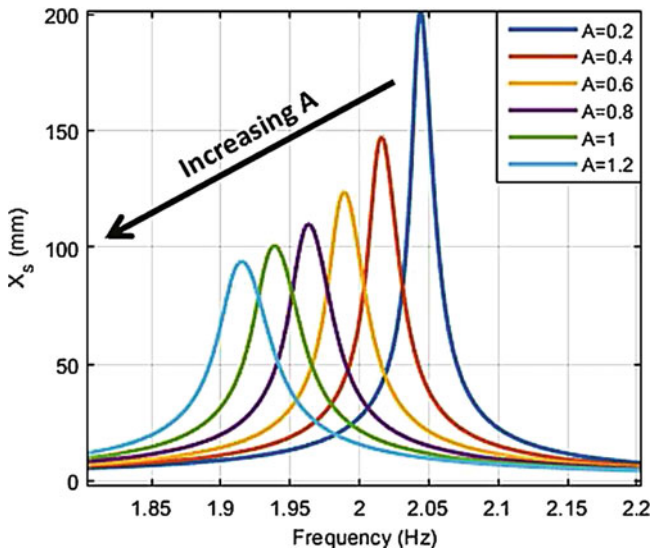
Fig. 6 Effect of cross-sectional area of the TLCD on displacement amplitude

In Figs. 7 and 8, effects of horizontal length and total length of the TLCD are presented. As horizontal length increases, and resonance frequency increases, whereas the response amplitude decreases. However, the opposite behavior is observed for the variation of total length.
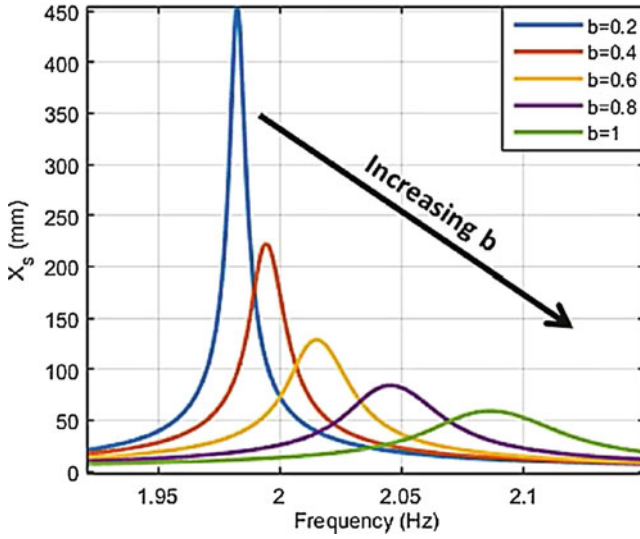
Fig. 7 The effect of horizontal length of the TLCD on displacement amplitude
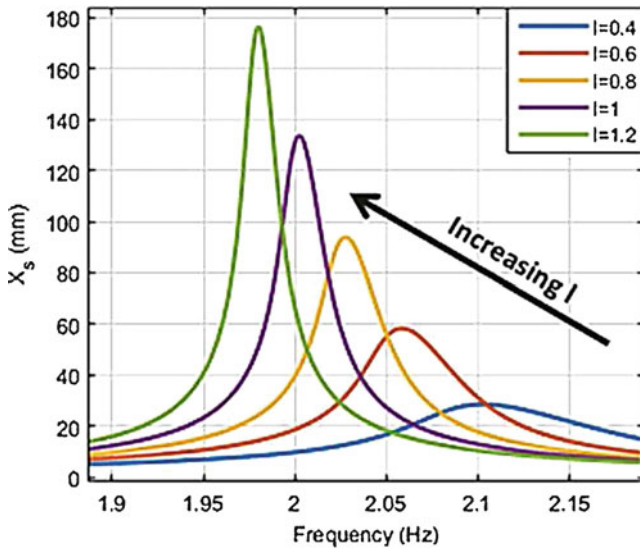
Fig. 8 Effect of total length of the TLCD on displacement amplitude

The effect of head loss coefficient is critical, since its behavior is not monotonic. This fact can be seen in Fig. 9. Decreasing trend in both response amplitude and resonance frequency with increasing head loss coefficient changes after a certain point.
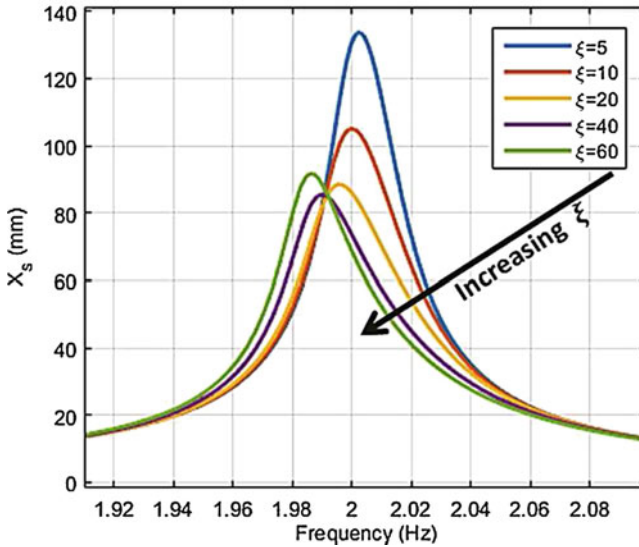
Fig. 9 Effect of head loss coefficients of the TLCD on displacement amplitude

Table 1 Effects of system parameters on response amplitude and resonance frequency

	Increasing area (A)	Increasing horizontal length (b)	Increasing total length (l)	Increasing head loss (ξ)
Vibration amplitude	Decreases	Decreases	Increases	Decreases then increases
Resonance frequency	Decreases	Increases	Decreases	Increases

Overall summary of the effects of system parameters on response amplitude and resonance frequency are tabulated in Table 1. From Table 1, it can be concluded that TLCD parameters that result in minimum response amplitude at a desired resonance frequency can be obtained through optimization. In Sect. 4, optimization of a six-story building model is studied.

4 Optimization Study of a Six-Story Building with a TLCD

In this section, a six-story shear building model (Fig. 2) is considered. Building parameters used in Erisen and Cigeroglu [9] are used for this system, and they are given in Table 2.

TLCD is connected rigidly on top of the building, i.e., on the sixth floor of the building. In the optimization procedure, ground acceleration amplitude is taken constant as 0.067 m/s^2, which is the maximum frequency response value in 1999 Bolu earthquake.

Table 2 Parameters used for six-story building

DOF #	m_n (kg)	k_n (kN/m)	c_n (kNs/m)
1	50,000	74,000	120
2	50,000	66,000	90
3	50,000	56,000	75
4	50,000	44,000	65
5	50,000	31,000	45
6	50,000	16,000	32

Table 3 Upper and lower bounds of TLCD parameters used in optimization

	Cross-sectional area (A) [m^2]	Horizontal length (b) [m]	Total length (l) [m]	Head loss coefficient (ξ)
Lower bound	1	1	2.5	1
Upper bound	4	3	4	10

Table 4 Upper and lower bounds of TLCD parameters used in optimization

Cross-sectional area (A) [m^2]	Horizontal length (b) [m]	Total length (l) [m]	Head loss coefficient (ξ)
3.85	1.97	2.53	8.74

Minimization of the displacement of the top floor is used as the cost function during optimization. Two optimization methods are used successively: genetic algorithm and gradient descent methods resulting in a hybrid algorithm. In order to capture the global optimum, the first genetic algorithm (GA) is applied. Then, the optimum values obtained by GA are used as initial guesses for gradient descent method in order to identify the optimal parameters more accurately. This hybrid optimization approach decreases the computational effort. Upper and lower bounds of TLCD parameters for optimization process are given in Table 3.

There are also geometrical constraints on design variables in order to obtain a reasonable TLCD system. First, the total mass of the TLCD should be between 9000 and 10,000 kg in order not to affect the first resonance frequency of the building considerably. Second, the total length should be greater than the horizontal length.

The optimization resulted in TLCD parameters given in Table 4 and the displacement amplitude vs. frequency of the sixth story are given in Fig. 10.

Moreover, solutions obtained by DFM and time integration method (TIM) are compared in Fig. 10, where Runge–Kutta method is used for time integration, and there is good agreement between both the solutions. It is observed from the figure that the maximum displacement amplitude of the sixth story is reduced from 131.10 to 82.21 mm (37% reduction) at a resonance frequency of 1.24 Hz.

In Table 5, peak displacement amplitude reduction ratios of sixth story of the building with and without optimum TLCD are compared. TLCD constructed with the optimized parameters also provides a considerable reduction for different ground acceleration amplitudes. Displacement of the sixth story for different ground acceleration ratios by using optimal TLCD parameters for 0.067 m/s^2 is given in Fig. 11.
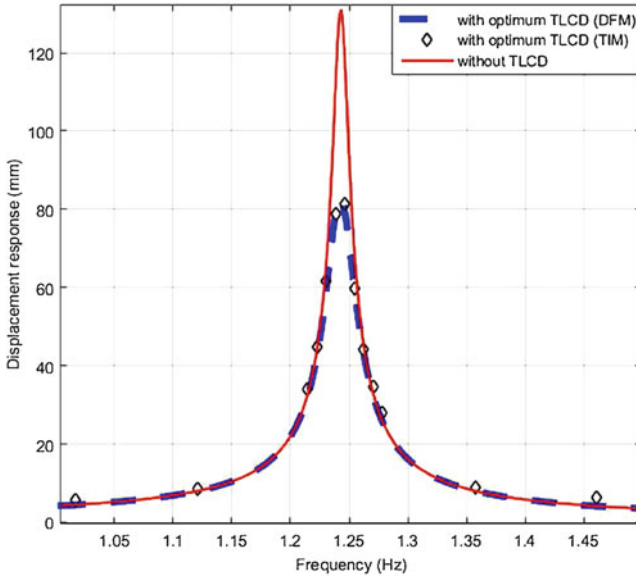
**Fig. 10** Displacement response of the sixth story with and without optimum TLCD

Table 5 The effect of different ground acceleration amplitudes on peak displacement amplitudes with and without TLCD

Natural frequency [Hz]	1.24	1.24	1.23	1.23	1.22
Ground acceleration amplitude [m/s^2]	0.02	0.067	0.12	0.18	0.24
Peak displacement amplitude without TLCD [mm]	40	131	234	352	480
Peak displacement amplitude with optimum TLCD [mm]	32	82	125	166	211
Reduction (%)	20	37	47	53	56

5 Conclusion

In this study, effects of TLCD parameters on a single-story building model are studied in order to understand the effects of TLCD parameters on displacement amplitude. Later, a six-story building with a TLCD rigidly connected to the top floor is considered. Since the parameters of TLCD, i.e., cross-sectional area, horizontal and total length, and head loss coefficient, have been considered as design variables that affect the overall system response, optimum values have been determined by solving an optimization problem. Optimum TLCD parameters are determined by using hybrid optimization utilizing genetic algorithm and gradient descent methods.

It is observed that, for 0.067 m/s^2 ground acceleration considered, 37% reduction in the maximum displacement amplitude of the top floor can be achieved. It should be noted that as the ground acceleration amplitude increases, the damping effect
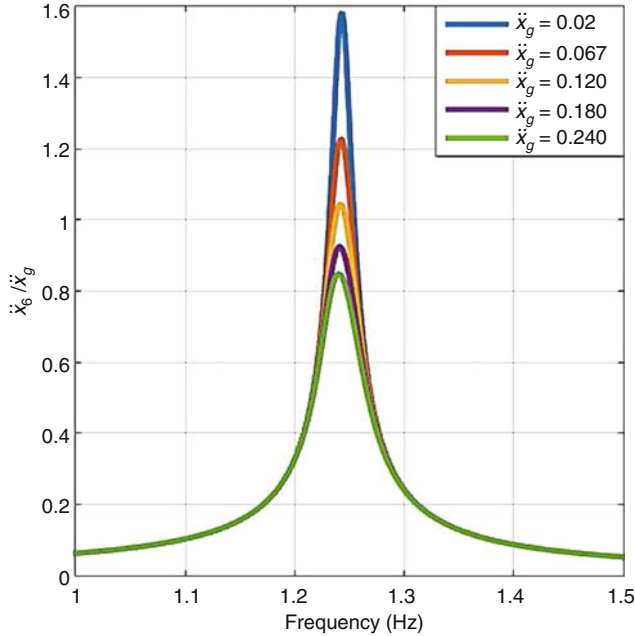
Fig. 11 Displacement of the sixth story for different ground acceleration ratios by using optimal TLCD parameters

of the nonlinear TLCD increases which lowers the displacement amplitudes. It can be concluded that when a TLCD is optimized for lower ground acceleration levels, its performance increases as the ground acceleration amplitude increases, and therefore, it can also be used for higher ground acceleration levels.

References

1. Balendra, T., Wang, C.M., Cheong, H.F.: Effectiveness of tuned liquid column dampers for vibration control of towers. Eng. Struct. **17**(9), 668–675 (1995). https://doi.org/10.1016/0141-0296(95)00036-7
2. Gao, H., Kwok, K.C.S., Samali, B.: Optimization of tuned liquid column dampers. Eng. Struct. **19**(6), 476–486 (1997). https://doi.org/10.1016/S0141-0296(96)00099-5
3. Mohebbi, M., Dabbagh, H.R., Shakeri, K.: Optimal design of multiple tuned liquid column dampers for seismic vibration control of MDOF structures. Period. Polytech. Civ. Eng. **59**(4), 543–558 (2015)
4. Ghosh, A., Basu, B.: Seismic vibration control of short period structures using the liquid column damper. Eng. Struct. **26**(13), 1905–1913 (2004). https://doi.org/10.1016/j.engstruct.2004.07.001
5. Min, K.W., Kim, J., Lee, H.R.: A design procedure of two-way liquid dampers for attenuation of wind-induced responses of tall buildings. J. Wind Eng. Ind. Aerodyn. **129**, 22–30 (2014). https://doi.org/10.1016/j.jweia.2014.03.003

6. Tanrikulu, O., Kuran, B., Ozguven, H.N., Imregun, M.: Forced harmonic response analysis of nonlinear structures using describing functions. AIAA J. **31**, 1313–1320 (1993)
7. Saoka, Y., Sakai, F., Takaeda, S., Tamaki, T.: On the Suppression of Vibrations by Tuned Liquid Column Dampers. In: Annual Meeting of JSCE, JSCE, Tokyo (1988)
8. Sakai, F., Takaeda, S., Tamaki, T.: Tuned liquid column damper—new type device for suppression of building vibration. In: International Conference on High-rise Buildings, pp. 926–931. Nanjing, China (1989).
9. Erisen, Z.E., Cigeroglu, E.: Topics on the dynamics of civil. Structure **1**, 1 (2012). https://doi.org/10.1007/978-1-4614-2413-0.

Vibration Reduction by Using Two Tuned Mass Dampers with Dry Friction Damping

Muhammed Emin Dogan and Ender Cigeroglu

Abstract Vibration reduction of a single-degree-of-freedom system connected to two tuned mass dampers (TMDs) equipped with dry friction dampers is considered in this work. The system is subjected to sinusoidal base excitation. Parameters of TMDs are optimized to minimize the peak values of the response of the primary system. Harmonic balance method (HBM) is used to obtain the steady state solution of the three-degrees-of-freedom nonlinear system in frequency domain. Newton's method with arc length continuation is utilized to solve the resulting nonlinear algebraic equation set. In addition to that, optimum linear system and other nonlinear elements are investigated. Genetic algorithm is used to optimize parameters of TMDs.

Keywords Tuned mass damper · Dry friction · Optimization

1 Introduction

Around resonance frequency, the response of a system can be very large leading to structural damage. The response level can be mitigated by using either vibration isolation systems or TMDs. Use of TMDs is a good solution for vibration reduction of a mechanical system when the inherent damping of the system is low. TMD-like systems were first used by Watts [1] in 1883. In 1909, Frahm [2] patented the classic TMD, which consisted of a mass and a spring. Classic TMDs work by reducing unwanted vibration around a single frequency by tuning the resonance frequency of the TMD to that frequency. With the addition of a classic TMD, the response is almost zero at the previous resonance point under harmonic excitation. However,

M. E. Dogan · E. Cigeroglu (✉)
Department of Mechanical Engineering, Middle East Technical University, Ankara, Turkey
e-mail: ender@metu.edu.tr

addition of a classic TMD introduces two new resonances nearby the tuned frequency. Therefore, classic TMDs are useful for a single stationary frequency; however, excitation is rarely stationary in real applications. Ordmondroyd [3] and Den Hartog [4] introduced damping to the TMD and provided an expression for optimal damping and optimal stiffness, which enables to suppress vibration in a broader band. To improve effective bandwidth, multiple TMDs were considered in [5–7].

Roberson [8] studied the nonlinear TMD to further extend the effective bandwidth. Many other researchers started to study nonlinear vibration absorbers. Ricciardelli and Vickery [9] used TMD with friction dampers. They studied the response of a linear single DOF system, where TMD with dry friction damping is connected by using an equivalent linearized damping for single harmonic motion. They also obtained optimum slip parameters for harmonic excitation.

In this study, a base-excited single-degree-of-freedom (SDOF) mechanical system connected to two TMDs equipped with dry friction dampers is considered as shown in Fig. 1. By the use of multiple TMDs and nonlinear elements, it is aimed to suppress the vibrations of the structures in a broader frequency range. m_b is the mass of the main system. m_1 and m_2 are the masses of the TMDs. k_b, k_1 and k_2 are linear springs. h_b is structural damping elements. k_{t1} and k_{t2} are contact stiffness, and μN_1 and μN_2 are slip load of the friction elements. Friction force is defined as the resistance of the motion when one body is tangentially in contact with another body [10]. Details of the macroslip friction model used in this study are given in papers [11–13] which is preferred due to its mathematical simplicity. Hysteresis curve of the friction damper for single harmonic motion is shown in Fig. 2.
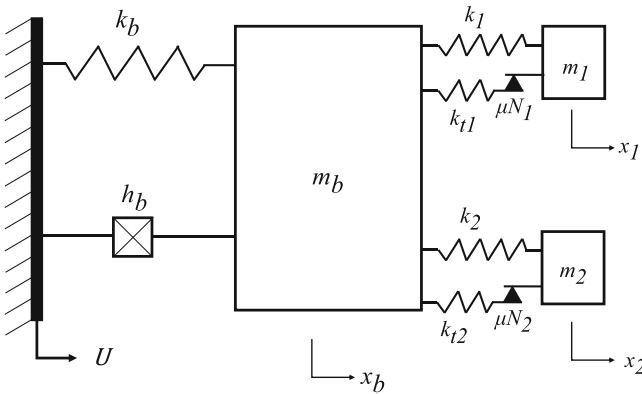
Fig. 1 SDOF systems with two TMDs utilizing dry friction dampers
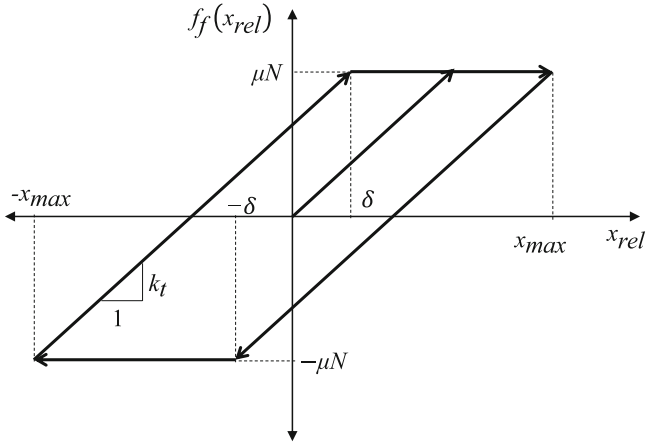
Fig. 2 Hysteresis curve for single harmonic motion

2 Mathematical Modelling

Equations of motion of the three-degrees-of-freedom system are given as follows:

$$
\begin{aligned}
m_{\mathrm{b}}\ddot{x}_{\mathrm{b}} + (k_{\mathrm{b}} + ih_{\mathrm{b}})\, x_{\mathrm{b}} + k_1\,(x_{\mathrm{b}} - x_1) + k_2\,(x_{\mathrm{b}} - x_2) + f_{\mathrm{f},1} + f_{\mathrm{f},2} &= U\,(k_{\mathrm{b}} + ih_{\mathrm{b}}) \\
m_1\ddot{x}_1 + k_1\,(x_1 - x_{\mathrm{b}}) - f_{\mathrm{f},1} &= 0 \\
m_2\ddot{x}_2 + k_2\,(x_2 - x_{\mathrm{b}}) - f_{\mathrm{f},2} &= 0
\end{aligned}
,
$$

$$(1)$$

where x_{b}, x_1 and x_2 are displacements of the main system, the first TMD and the second TMD, respectively. U is base motion and $f_{\mathrm{f},i}$ is the nonlinear internal force. Equation (1) can be written in matrix form as follows:

$$
\mathbf{M}\ddot{\mathbf{x}} + (\mathbf{K} + i\mathbf{H})\,\mathbf{x} + \mathbf{f}_n = \mathbf{f}. \tag{2}
$$

For harmonic base motion, external forcing, $\mathbf{f}$, is harmonic and response of the system can also be assumed harmonic as

$$
x_{\mathrm{rel},\,j}\,(\theta) = x^{\mathrm{s}}_{\mathrm{rel},\,j}\sin\theta + x^{\mathrm{c}}_{\mathrm{rel},\,j}\cos\theta, \tag{3}
$$

where $\theta = \omega t$. Nonlinear friction force shown in Fig. 2 can be expressed as follows:

$$
f_{\mathrm{f},j}\,(\theta) =
\begin{cases}
-\mu N + k_{\mathrm{t}}\left(x_{\mathrm{rel},\,j}\,(\theta) + \delta\right) & \text{if} \quad \psi_1 < \theta < \psi_2 \\
-\mu N & \text{if} \quad \psi_2 < \theta < \psi_1 + \pi \\
\mu N + k_{\mathrm{t}}\left(x_{\mathrm{rel},\,j}\,(\theta) - \delta\right) & \text{if} \quad \psi_1 + \pi < \theta < \psi_2 + \pi \\
\mu N & \text{if} \quad \psi_2 + \pi < \theta < \psi_1 + 2\pi
\end{cases}
, \tag{4}
$$

where

$$x_{\max} = \sqrt{(x^s)^2 + (x^c)^2}, \quad \delta = \frac{2\mu N - kx_{\max}}{k},$$

$$\psi_1 = \tan^{-1}\left(\frac{x^s}{x^c}\right), \quad \psi_2 = \cos^{-1}\left(-\frac{\delta}{x_{\max}}\right) + \psi_1\pi \tag{5}$$

3 Harmonic Balance Method

Harmonic balance method (HBM) is used to solve the resulting system in frequency domain. In HBM, response and nonlinear forces are represented in terms of Fourier series and substituted into the nonlinear differential equations of motion which results in a set of nonlinear algebraic equations.

In this study, only the first harmonic is considered; as a result of this, the following set of nonlinear real algebraic equations is obtained:

$$\begin{bmatrix} -\omega^2\mathbf{M} + \mathbf{K} & -\mathbf{H} \\ \mathbf{H} & -\omega^2\mathbf{M} + \mathbf{K} \end{bmatrix} \begin{Bmatrix} \mathbf{x}^s \\ \mathbf{x}^c \end{Bmatrix} + \begin{Bmatrix} \mathbf{f}_n^s \\ \mathbf{f}_n^c \end{Bmatrix} = \begin{Bmatrix} \mathbf{f}^s \\ \mathbf{f}^c \end{Bmatrix}, \tag{6}$$

where $\mathbf{f}_n^s$ and $\mathbf{f}_n^c$ are the vectors of sine and cosine coefficients of the nonlinear internal forcing which are amplitude dependent.

Each element in nonlinear force vector is calculated by HBM. The response in Eq. (4) is relative displacement between masses where nonlinear element is connected. Nonlinear forces are calculated for each relative displacement.

$$f_{n,j}^s = \frac{1}{\pi} \int_0^{2\pi} f_{f,j}(\theta) \sin\theta\,d\theta, \quad f_{n,j}^c = \frac{1}{\pi} \int_0^{2\pi} f_{f,j}(\theta) \cos\theta\,d\theta \tag{7}$$

Nonlinear force vector is constructed as

$$\{\mathbf{f}_n^s \;\; \mathbf{f}_n^c\}^T = \{f_{n,1}^s + f_{n,2}^s - f_{n,1}^s - f_{n,2}^s \, f_{n,1}^c + f_{n,2}^c - f_{n,1}^c - f_{n,2}^c\}^T. \tag{8}$$

4 Solution of Resulting Nonlinear Algebraic Equations

In order to solve the resulting nonlinear algebraic equations, a residual vector is defined as follows:

$$\mathbf{r}(\mathbf{x}, \omega) = \begin{bmatrix} -\omega^2\mathbf{M} + \mathbf{K} & -\mathbf{H} \\ \mathbf{H} & -\omega^2\mathbf{M} + \mathbf{K} \end{bmatrix} \mathbf{x} + \mathbf{f}_n(\mathbf{x}) - \mathbf{f} = 0. \tag{9}$$

Newton's method with arc-length continuation is used to solve Eq. (9). The following arc-length equation is used.

$$h\,(\mathbf{x}, \omega) = (\mathbf{q}_k - \mathbf{q}_{k-1})^{\mathrm{T}}\,(\mathbf{q}_k - \mathbf{q}_{k-1}) - s^2 = 0, \tag{10}$$

where s is the arc-length parameter, $k - 1$ is the previous solution point and k is the current solution point. With the addition of this new equation, the new vector of unknowns becomes

$$\mathbf{q} = \left\{ \begin{array}{c} \mathbf{x} \\ \omega \end{array} \right\}.$$

A single step of Newton's method becomes

$$\mathbf{q}_k^{i+1} = \mathbf{q}_k^{i} - \left[\begin{array}{cc} \frac{\partial \mathbf{r}}{\partial \mathbf{x}} & \frac{\partial \mathbf{r}}{\partial \omega} \\ \frac{\partial h}{\partial \mathbf{x}} & \frac{\partial h}{\partial \omega} \end{array} \right]_{\mathbf{x_i} \,\&\, \omega_i}^{-1} \left\{ \begin{array}{c} \mathbf{r}\,(\mathbf{x}_i, \omega_i) \\ h\,(\mathbf{x}_i, \omega_i) \end{array} \right\}. \tag{11}$$

Detailed information related to arc-length continuation method can be found in Ref. [14].

5   Results

Parameters of the system under investigation are $m_b = 1\,\mathrm{kg}$, $k_b = 3948\,\mathrm{N/m}$, $h = 39.48\,\mathrm{N/m}$, $m_1 = m_2 = 0.05\,\mathrm{kg}$ and $U_0 = 0.01\,\mathrm{m}$. Remaining parameters are optimized by genetic algorithm (GA) of MATLAB. In addition to the system with frictionally damped TMDs, the same system equipped with linear viscous dampers is also optimized. The cost function is defined as the minimization of the combination of the integral of the displacement amplitude and the maximum displacement of the main system. The values are normalized and their weights are selected. Results obtained are given in Fig. 3. When the weight of the integral of the displacement amplitude is zero, i.e. 100% Max, a third resonance peak occurs which has more vibration amplitude than the linear viscous damping case. This is due to the fact that only the maximum displacement amplitude is used as the cost function, and hence, optimization resulted in three peaks with equal amplitudes. When the weight of the maximum displacement of the main system is zero, i.e. 100% Int, amplitude of the first resonance peak is larger than vibration amplitudes observed in the linear viscous damping case. This is due to the fact that the area under the frequency response function is minimized without considering the amplitudes of the resonance peaks.

66.6% Max and 33.3% Int. are selected for further analysis. In order to observe the performance of having two TMDs, SDOF system equipped with a single TMD associated with dry friction damping, and a linear spring is considered. Moreover,
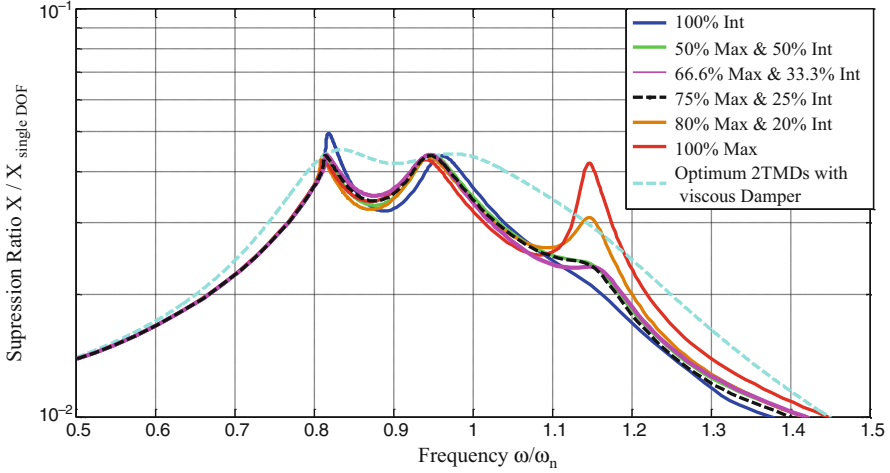
Fig. 3 Normalized displacement amplitude of the main system for different cost functions weights

Table 1 Optimum parameters

Configuration	Parameters
Two DOF TMD with equipped dry friction dampers	$k_1 = 134.7$ N/m, $k_2 = 197.0$ N/m, $k_{t1} = 244.8$ N/m, $k_{t2} = 409.9$ N/m $\mu N_1 = 4.32$ N, $\mu N_2 = 5.36$ N
SDOF TMD with equipped dry friction damper	$k = 192.0$ N/m, $k_t = 473.3$ N/m $\mu N = 17.0$ N
Two DOF TMD with equipped viscous dampers	$k_1 = 220.1$ N/m, $k_2 = 150.2$ N/m $c_1 = 1.27$ Ns/m, $c_2 = 0.71$ Ns/m
SDOF TMD with cubic stiffness and viscous damper	$k_c = 33794.1$ N/m^3, $c = 0.55$ Ns/m

a SDOF system equipped with a single TMD having a cubic stiffness and a viscous damping is investigated. This system is also studied in the literature [15, 16]. Total mass of the TMD is identical in all cases. Remaining parameters are optimized, and the values of the optimized parameters are given in Table 1.

By choosing the appropriate weighting function parameters, the TMDs are optimized. In order to identify the effect of slip load, they are modified and the results are given in Fig. 4. Moreover, suppression ratio changes related to slip forces are presented in Fig. 5.

Results obtained are given in Fig. 6. It is observed that the system with optimum two TMDs equipped with dry friction dampers has slightly less vibration amplitude compared to the viscous damping. System with a single TMD equipped with dry friction damper is generally above the viscous damping case. Also vibration amplitude is slightly higher after normalized frequency of 1.2. In addition, it generally has higher amplitude compared to the two TMDs equipped with dry friction dampers.
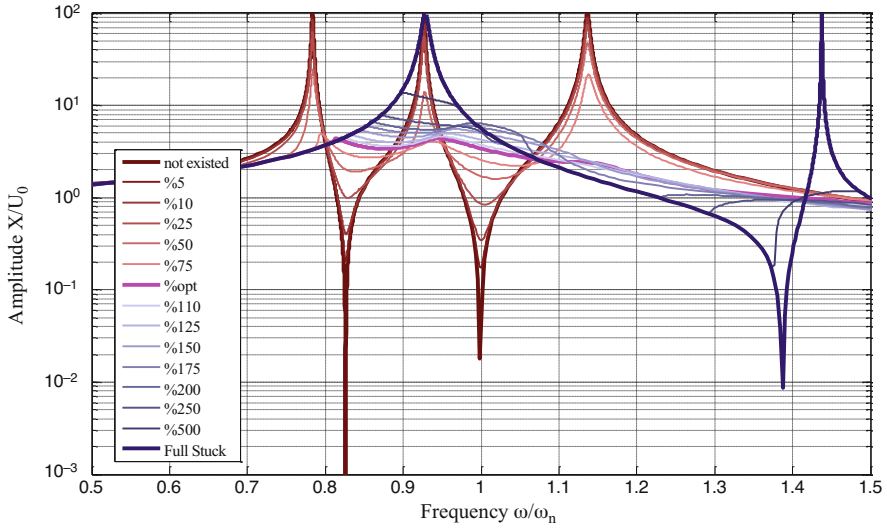
Fig. 4 Effect of slip load change on normalized displacement amplitude
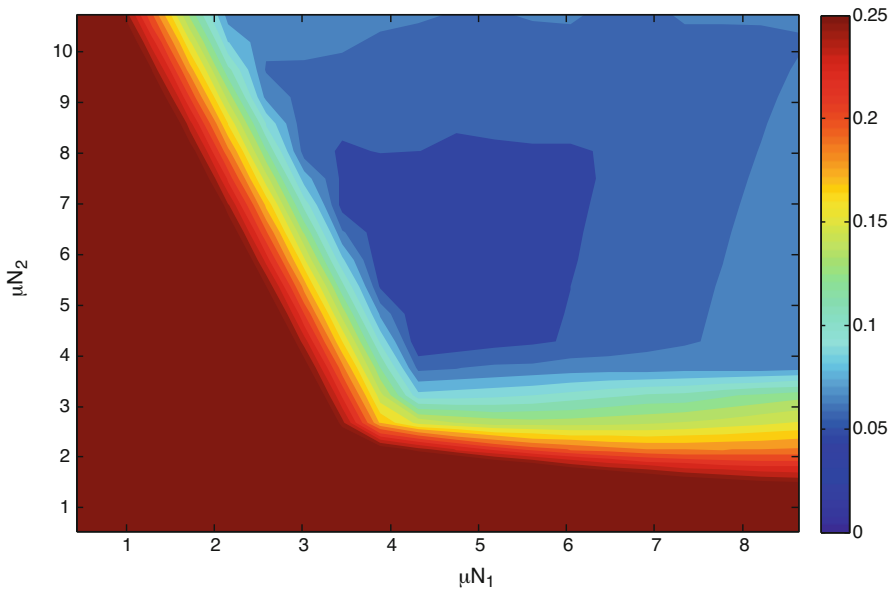
Fig. 5 Effect of slip load on the maximum normalized displacement amplitude

SDOF TMD with cubic stiffness and viscous damping has lower amplitude except between normalized frequency of 1.1–1.35. Optimum values of the parameters are given in Table 1.
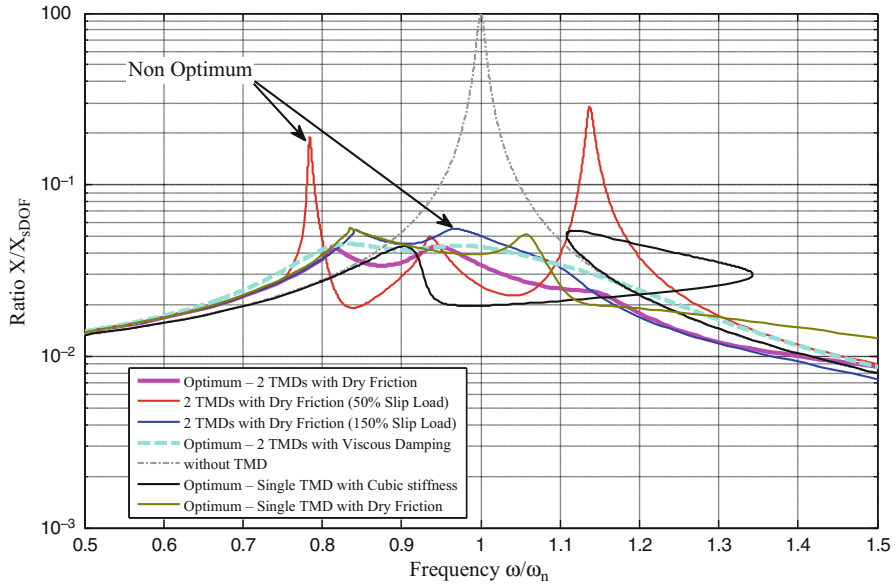
Fig. 6 Comparison of normalized displacement amplitude for different TMD configurations

6   Conclusions

A single-degree-of-freedom mechanical system coupled with nonlinear TMDs equipped with dry friction dampers is considered in this study. HBM is used to convert the nonlinear differential equations of motion to nonlinear algebraic equations which are solved by Newton's method with arc length continuation. Effect of slip load on the performance of two TMDs with friction dampers is studied. Moreover, the obtained results are compared with two TMDs with linear viscous dampers, single TMD with cubic stiffness nonlinearity and viscous damping, and single TMD with dry friction damper. It is observed that utilizing two TMDs with dry friction dampers has a better vibration reduction behaviour in a wide frequency range.

References

1. Watt, P.: On a method of reducing the rolling of ships at sea. Trans. Inst. Nav. Archit. **24**, 165–190 (1883)
2. Frahm, H.: Device for damping vibrations of bodies. US Patent No. 989958 (1911)
3. Ordmondroyd, J., Den Hartog, J.P.: The theory of dynamic vibration absorber. Trans. Am. Soc. Mech. Eng. **50**, 9–22 (1928)
4. Den Hartog, J.P.: Mechanical Vibration, 3rd edn. McGraw-Hill, New York (1947)

5. Patil, S.S., Javehri, S.B., Konapure, C.G.: Effectiveness of multiple tuned mass dampers. Int. J. Eng. Innov. Technol. **1**, 78–83 (2012)
6. Igusa, T., Xu, K.: Vibration control using multiple tuned mass damper. J. Sound Vib. **175**(4), 491–503 (1994)
7. Yamaguchi, H., Harnpornchai, N.: Fundamental characteristics of multiple tuned mass dampers for suppressing harmonically forced oscillations. Earthq. Eng. Struct. Dyn. **22**(1), 51–62 (1993)
8. Roberson, R.E.: Synthesis of a nonlinear dynamic vibration absorber. J. Frankl. Inst. **254**(3), 205–220 (1952)
9. Ricciardelli, F., Vickery, B.J.: Tuned vibration absorbers with dry friction damping. Earthq. Eng. Struct. Dyn. **28**(7), 707–723 (1999)
10. Bhushan, B.: Principles and Applications of Tribology, 2nd edn. Wiley-Interscience, Ohio (2013)
11. Cigeroglu, E., Ozguven, H.: Nonlinear vibration analysis of bladed disks with dry friction dampers. J. Sound Vib. **295**(3–5), 1028–1043 (2006)
12. Erisen, Z.E., Cigeroglu, E.: Frequency Domain Optimization of Dry Friction Dampers on Buildings Under Harmonic Excitation, Topics on the Dynamics of Civil Structures, vol. 1, pp. 113–126. Springer (2012)
13. Boral, C., Cigeroglu, E., Korkmaz, I.: Effect of intentional dry friction damping on the performance of an elastomeric engine mount. In: ASME 2010 10th Biennial Conference on Engineering Systems Design and Analysis, vol. 3, pp. 59–66, ASME (2010)
14. Samandari, H., Cigeroglu, E.: Nonlinear free vibration of double walled carbon nanotubes by using describing function method with multiple trial functions. Phys. E Low-Dimens. Syst. Nanostruct. **46**, 160–173 (2012)
15. Parseh, M., Dartel, M., Ghasemi, M.H.: Investigation of robustness of nonlinear energy sink in steady state dynamics of linear beams with different boundary conditions. Commun. Nonlinear Sci. Numer. Simul. **29**(1–3), 50–71 (2015)
16. Alexander, N.A., Schilder, F.: Exploring the performance of a nonlinear tuned mass damper. J. Sound Vib. **319**(1–2), 445–462 (2009)

Nonlinear Behavior of Pendulum-Tuned Mass Dampers for Vibration Control of H-Section Hangers

Kai Xu, Xugang Hua, and Zhengqing Chen

Abstract The influence of the nonlinearity of pendulum-tuned mass dampers (PTMD) on vibration control of H-section hangers was studied analytically. Firstly, the coupled system of a slender H-section hanger and an attached PTMD was simplified to a two-degree-of-freedom (2-DOF) system. The equations of motion were derived for the system under free vibration and forced excitation. Both linear and nonlinear results were obtained. Results show that the free vibration responses of the system are significantly different for linear and nonlinear solutions when the hanger subjects to the large initial displacements. A small structural damping of the H-section hanger has significant effects on enhancement of the pendulum motion stability. For the case of forced vibration, the displacement responses of the primary structure solved by nonlinear solution are smaller than that solved by the linear solution when the excitation amplitude is less than 0.3. However, the displacement responses of the primary structure considering pendulum nonlinearity are larger than the linear responses when the dimensionless excitation amplitude is gradually increased.

Keywords H-section hanger · Vibration control · Pendulum tuned mass damper · Nonlinear behavior · Energy dissipation

1 Introduction

Long and slender H-sections are extensively adopted as hangers or suspenders in steel arch bridges. However, the H-shaped cross section is a typical bluff body and is often suffered from fatigue issues due to a variety of wind-induced vibrations such

K. Xu (✉) · X. Hua · Z. Chen
Key Laboratory for Wind and Bridge Engineering of Hunan Province, College of Civil Engineering, Hunan University, Changsha, China
e-mail: kaixu@hnu.edu.cn; cexghua@hnu.edu.cn; zqchen@hnu.edu.cn

as vortex-induced, flutter and galloping vibrations [1]. Therefore, many measures were proposed to mitigate wind-induced vibrations of H-section hangers, including: (1) aerodynamic optimizations, (2) the use of wind-resistant cables, and (3) the use of mechanical damping devices [2–4]. Among them, the use of mechanical damping devices is the most effective way to suppress the large amplitude vibrations of H-section hangers due to wind loads.

Recently, tuned mass dampers (TMDs) were proposed for vibration mitigation of H-section hangers [4]. TMDs, also known as dynamic vibration absorbers, are a kind of mechanical damping devices that are attached in low-damping structures to reduce undesirable vibrations due to dynamic loads such as wind, earthquakes, and traffic loads. The TMD system is a single-degree-of-freedom (SDOF) system that consists of a mass, a spring, and a damper. Basically, the large-amplitude vibration of low-damping structures may happen under the various dynamic loads. If the frequency of the TMD is tuned appropriately to the primary structure, a large part of the vibration energy of the primary structure will be transferred to the TMD and then dissipated by the inherent damping of the TMD.

To enhance the control performance and robustness of the conventional TMD system, the pendulum-tuned mass dampers (PTMDs) were utilized to control structural vibrations of low-damping structures [5, 6]. Moreover, several applications of using PTMDs for vibration control of hangers were reported [4]. To the best knowledge of the authors, only few studies were conducted to investigate the nonlinear behavior of PTMDs when the large displacement of PTMDs is considered. Actually, the PTMD is easily affected by nonlinearity at the large displacement and has differently dynamic characteristics from the conventional linear TMD. Normally, the optimal parameters of PTMDs are designed based on the optimization theory of linear TMDs proposed by Den Hartog [7] when the motion of the PTMD is assumed to a small value, generally less than $\pm 5°$. In practical engineering, the natural frequency of the H-section hanger is relatively high. Therefore, the pendulum rod of the PTMD will be normally designed to be of short length and easily produces large angular displacements in these situations. Based on the aforementioned issues, it is necessary to study the nonlinearity effects of the PTMD on its efficiency of the energy dissipation and transformation for vibration control of H-section hangers.

In this study, the coupled system of an H-section hanger attached with a PTMD was considered. The linear and nonlinear equations of motion were derived under free and forced vibration cases. Meanwhile, displacement responses and mechanical energies of the coupled system were analyzed by employing the linear and nonlinear solutions. Finally, the results from the linear and nonlinear solutions were compared.

2 Theoretical Model

2.1 Free Vibration

The hanger vibration is usually excited by vortex-shedding, and the vibration response is dominated by one particular mode based on the observation from field measurements and wind tunnel experiments [1]. Therefore, the coupled PTMD-hanger system can be simplified into a two-degree-of-freedom (2-DOF) model, as illustrated in Fig. 1, where a single controlled mode of the hanger is simplified to a primary structure with concentrated modal mass m_1. In the model, k_1, c_1, and x_1 are the stiffness, damping coefficient, and displacement of the primary structure, respectively. The PTMD with a pendulum mass of m_2 is attached on the primary structure, where c_2, l, and θ are the damping coefficient, pendulum length, and angular displacement of the PTMD, respectively. The gravity is characterized by constant coefficient g.

Governing equations of the coupled system for the free vibration are given by:

$$
\begin{aligned}
&(m_1 + m_2)\ddot{x}_1 + k_1 x + c_1 \dot{x} + m_2 l \left(\ddot{\theta}\cos\theta - \dot{\theta}^2 \sin\theta\right) = 0 \\
&m_2 l^2 \ddot{\theta} + m_2 g l \sin\theta + c_2 l^2 \dot{\theta} + m_2 l \cos\theta \ddot{x}_1 - m_2 l \sin\theta \dot{x}_1 \dot{\theta} = 0
\end{aligned}
\tag{1}
$$

Dimensionless parameters are introduced here:

$$
\mu = \frac{m_2}{m_1};\ \omega_1{}^2 = \frac{k_1}{m_1};\ \omega_2{}^2 = \frac{g}{l};\ \beta = \frac{\omega_2}{\omega_1};\ \zeta_1 = \frac{c_1}{2m_1\omega_1};\ \zeta_2 = \frac{c_2}{2m_2\omega_2};\ \tau = \omega_1 t;\ x = \frac{x_1}{l}
\tag{2}
$$

where τ and x are the dimensionless time and displacement of the primary structure, respectively, μ is the mass ratio of the PTMD, β is the frequency ratio of the PTMD; ω_1, ζ_1 and ω_2, ζ_2 are natural frequencies and damping ratios of the primary structure and the PTMD, respectively.

Fig. 1 Sketch of the coupled PTMD-hanger system
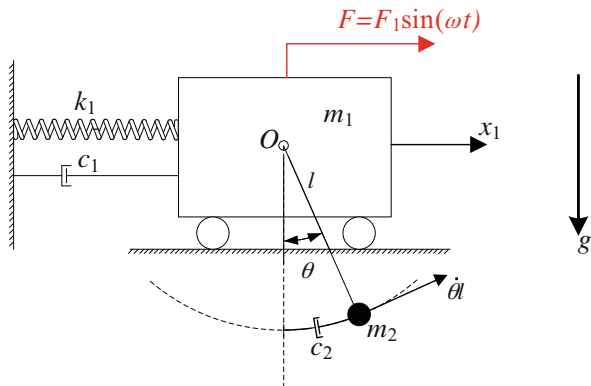
Substituting Eq. (2) into Eq. (1) yields the dimensionless form of the governing equations for the coupled system:

$$[(1 + \mu)\ddot{x} + x + 2\zeta_1\dot{x}] + \mu\left(\ddot{\theta}\cos\theta - \dot{\theta}^2\sin\theta\right) = 0$$
$$\ddot{\theta} + \beta^2\sin\theta + 2\zeta_2\beta\theta' + \cos\theta\ddot{x} - \dot{x}\dot{\theta}\sin\theta = 0 \tag{3}$$

Moreover, the linear governing equations can be obtained after ignoring high-order terms in Eq. (3), and it is expressed as

$$(1 + \mu)\ddot{x}_1 + x_1 + 2\zeta_1\dot{x}_1 + \mu\ddot{\theta} = 0$$
$$\ddot{\theta} + \beta^2\theta + 2\zeta_2\beta\dot{\theta} + \ddot{x}_1 = 0 \tag{4}$$

The decrement rate of mechanical energy (γ) is an important index to evaluate the performance of PTMD; therefore, the amount of mechanical energy of the coupled system in a certain time duration was computed and expressed as

$$\text{Nonlinear}: \gamma_n(\tau) = \frac{(1 + \mu)\dot{x}^2 + x^2 + \mu\left[\dot{\theta}^2 + 2\dot{\theta}\dot{x}\cos\theta + 2\beta^2(1 - \cos\theta)\right]}{(1 + \mu)\dot{x}_0^2 + x_0^2 + \mu\left[\dot{\theta}_0^2 + 2\dot{\theta}_0\dot{x}_0\cos\theta_0 + 2\beta^2(1 - \cos\theta_0)\right]}$$
$$\text{Linear}: \gamma_l(\tau) = \frac{(1 + \mu)\dot{x}^2 + x^2 + \mu\left[\dot{\theta}^2 + 2\dot{\theta}\dot{x} + \beta^2\theta^2\right]}{(1 + \mu)\dot{x}_0^2 + x_0^2 + \mu\left[\dot{\theta}_0^2 + 2\dot{\theta}_0\dot{x}_0 + \beta^2\theta_0^2\right]} \tag{5}$$

where zero indexes correspond to the initial conditions for the coupled system.

2.2 Forced Vibration

When a sinusoidal excitation with an excitation frequency ω and amplitude F_1 is applied on the primary structure, as shown in Fig. 1, the nonlinear governing equations of the coupled system are expressed as

$$(m_1 + m_2)\ddot{x} + k_1 x + c_1\dot{x} + m_2 l\left(\ddot{\theta}\cos\theta - \dot{\theta}^2\sin\theta\right) = F_1\sin(\omega t)$$
$$m_2 l^2\ddot{\theta} + m_2 gl\sin\theta + c_2 l^2\dot{\theta} + m_2 l\cos\theta\ddot{x} - m_2 l\sin\theta\dot{x}\dot{\theta} = 0 \tag{6}$$

Substituting Eq. (2) into Eq. (7) and introducing three new dimensionless parameters,

$$x_f = \frac{k_1 x_1}{F_1} \quad f = \frac{F_1}{m_1 g} \quad \rho = \frac{\omega}{\omega_1} \tag{7}$$

where x_f and f are the dimensionless amplitude of primary structure and the dimensionless amplitude of the sinusoidal excitation, respectively. ρ is the excitation frequency ratio. Then, Eq. (6) can be rewritten as a dimensionless form

$$f\beta^2 \left[(1+\mu)\,\ddot{x}_f + x_f + 2\zeta_1 \dot{x}_f\right] + \mu \left(\ddot{\theta}\cos\theta - \dot{\theta}^2 \sin\theta\right) = f\beta^2 \sin(\rho\tau)$$
$$\ddot{\theta} + \beta^2 \sin\theta + 2\zeta_2 \beta\dot{\theta} + f\beta^2 \dot{x}_f \left(\cos\theta - \dot{\theta}\sin\theta\right) = 0 \tag{8}$$

and the linear governing equations can be obtained after ignoring high-order terms in Eq. (8)

$$f\beta^2 \left[(1+\mu)\,\ddot{x}_f + x_f + 2\zeta_1 \dot{x}_f\right] + \mu\ddot{\theta} = f\beta^2 \sin(\rho\tau)$$
$$\ddot{\theta} + \beta^2 \sin\theta + 2\zeta_2 \beta\dot{\theta} + f\beta^2 \ddot{x}_f = 0 \tag{9}$$

3 Numerical Results

3.1 Free Vibration Analysis

In this section, the responses of primary structure solved by the nonlinear and the linear solutions were compared under various initial displacements x_0. The parameters of the PTMD were obtained by the formulas proposed by Ioi and Ikeda, which is considering the inherent structural damping [8]. The optimum design formulas are as follows:

$$\beta_{\text{opt}} = \frac{1}{1+\mu} - \left(0.241 + 1.74\mu - 2.6\mu^2\right)\zeta_1 - \left(1 - 1.9\mu + \mu^2\right){\zeta_1}^2$$
$$\zeta_{2\text{opt}} = \sqrt{\frac{3\mu}{8(1+\mu)}} + \left(0.13 + 0.12\mu + 0.4\mu^2\right)\zeta_1 + \left(0.16 - 2.6\mu + 5\mu^2\right){\zeta_1}^2 \tag{10}$$

Firstly, the structural damping of the primary structure was ignored ($\zeta_1 = 0$), and the mass ratio of the PTMD was set to $\mu = 0.1$. The optimum parameters of the PTMD were designed from Eq. (10), which are $\beta_{\text{opt}} = 0.91$, $\zeta_{2\text{opt}} = 0.185$. The system responses with different initial displacements are obtained by numerically solving the nonlinear and linear governing equations, as expressed in Eqs. (3) and (4). Figures 2 and 3 show the dimensionless time histories for translation of the primary structure x, angular displacement of the PTMD θ, and the mechanical energy γ of the coupled system.

In Fig. 2, a small initial displacement of primary structure $x_0 = 0.1$ was adopted. It is shown that the displacements and mechanical energies of the system are in good agreement between the linear and the nonlinear results. However, the displacement responses and the mechanical energies of the coupled system obtained by the linear solution are not quite fitting with that obtained by the nonlinear solution when $x_0 = 1.6$ was adopted, as illustrated in Fig. 3. From Fig. 3b, the pendulum mass is firstly moved to the top position, namely $\theta = \pi$, when the dimensionless time is $\tau = 7.5$, which means that the unstable rotation phenomenon has happened. Then, the structural damping of the primary structure $\zeta_1 = 0.03$ is considered. The optimum parameters of the PTMD change to $\zeta_{2\text{opt}} = 0.189$ and $\beta_{\text{opt}} = 0.897$ in
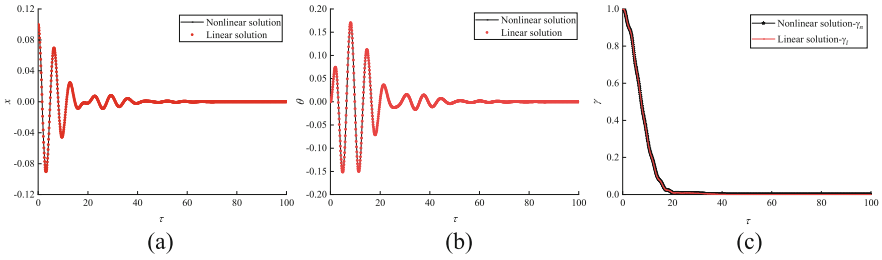
Fig. 2 Dimensionless time histories for $\mu = 0.1$, $\zeta_1 = 0$, $\zeta_{2\text{opt}} = 0.185$, $\beta_{\text{opt}} = 0.91$, $x_0 = 0.1$; (**a**) displacement of primary structure; (**b**) angular displacement of PTMD; (**c**) mechanical energy of the coupled system
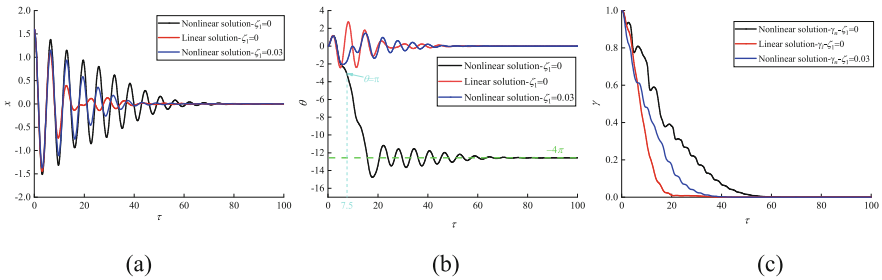
Fig. 3 Dimensionless time histories for $\mu = 0.1$, $\zeta_{2\text{opt}} = 0.185$, $\beta_{\text{opt}} = 0.91$, $x_0 = 1.6$; (**a**) displacement of primary structure; (**b**) angular displacement of PTMD; (**c**) mechanical energy of the coupled system

Eq. (10). It is shown that the structural damping enhances the stability of PTMD motion, as shown in Fig. 3b. The mechanical energies of the system under various initial displacements are illustrated in Fig. 4. It is shown that the decrement rate of mechanical energies of the coupled system obtained by the nonlinear solution varies with the changes of different initial displacements. However, the results obtained by the linear solution are independent to the changes of initial displacements.

3.2   Forced Vibration Analysis

In this section, the1 displacement responses of the coupled system for the forced vibration were investigated. Moreover, the optimum parameters of the PTMD were calculated by using Eq. (10). The structural damping is set to 0.005 and 0.03 to simulate low structural damping of steel structures and high structural damping of concrete structures. Table 1 shows the obtained results respectively solved by the linear and the nonlinear solutions for small and large dimensionless

Fig. 4 Effect of initial displacement condition of primary structure on mechanical energy in the system for $\mu = 0.1$, $\zeta_1 = 0.03$, $\zeta_{2opt} = 0.189$, $\beta_{opt} = 0.897$
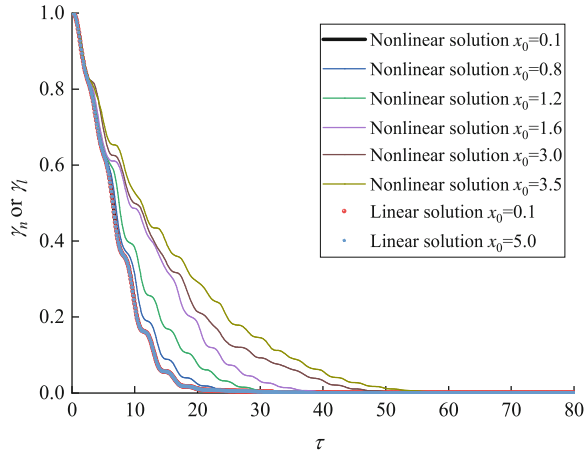
Table 1 Amplitude comparison under forced excitations

$\mu = 0.1$, $\zeta_1 = 0.03$, $\zeta_{2opt} = 0.189$, $\beta_{opt} = 0.897$

		Nonlinear solution		Linear solution	
F	ρ	x	θ	x	θ
0.01	0.85	0.190	0.004	3.707	0.072
	1.00	0.161	0.003	3.539	0.073
	1.15	0.142	0.023	3.006	0.049
0.10	0.85	1.437	0.278	3.707	0.719
	1.00	1.230	0.247	3.539	0.727
	1.15	1.134	0.183	3.007	0.493
0.30	0.85	2.755	1.240	3.707	2.158
	1.00	3.872	1.194	3.539	2.181
	1.15	2.303	0.824	3.007	1.479
$\mu = 0.05$, $\zeta_1 = 0.005$, $\zeta_{2opt} = 0.134$, $\beta_{opt} = 0.951$					
0.10	1.00	6.839	1.147	5.492	1.819
0.15	1.00	11.48	177.9	5.492	2.729

amplitudes of forced excitations. It is shown that the displacement responses of the coupled system are significantly different under the linear and nonlinear solutions and even the angular displacement of the PTMD is smaller than 0.01 rad. The pendulum nonlinearity can enhance the performance of the PTMD in controlling the displacement response of the primary structure when the dimensionless excitation amplitude is less than 0.3. However, the displacement response of the primary structure solved by the nonlinear solution is slightly larger than that solved by the linear solutions when the excitation amplitude $f = 0.3$ and excitation frequency ratio $\rho = 1$ are adopted (Fig. 5c).
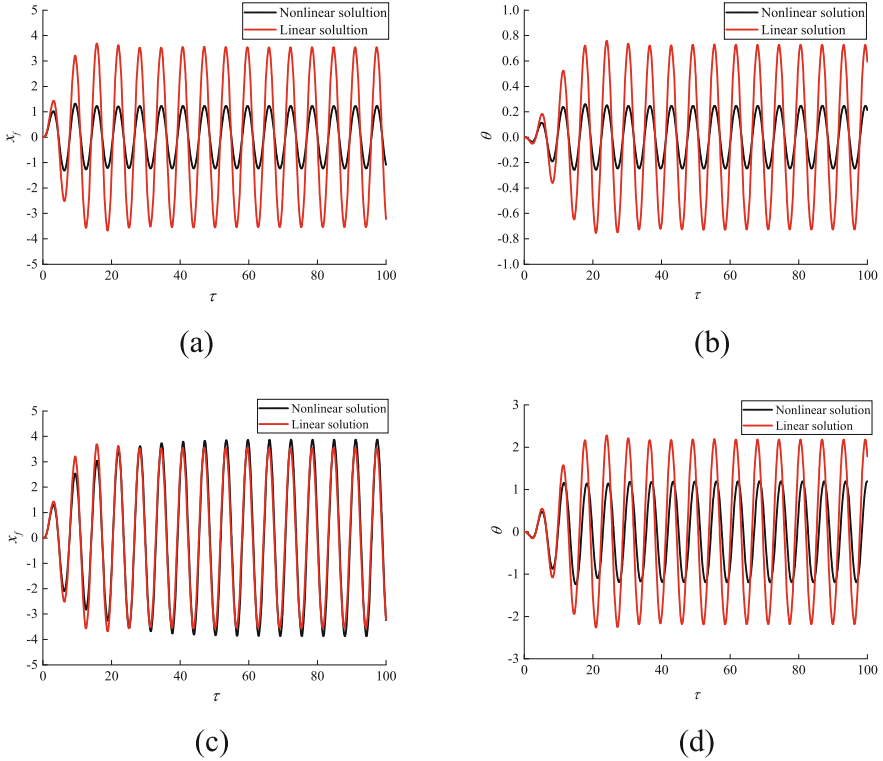
Fig. 5 Displacement responses of the coupled system for $\mu = 0.1$, $\zeta_1 = 0.03$, $\zeta_{2opt} = 0.189$, $\beta_{opt} = 0.897$, $\rho = 1.00$; (**a**) displacement of primary structure for $f = 0.1$; (**b**) angular displacement of PTMD for $f = 0.1$; (**c**) displacement of primary structure for $f = 0.3$; (**d**) angular displacement of PTMD for $f = 0.3$

4 Conclusions

This chapter employed a two-degree-of-freedom (2-DOF) coupled system simplified from a H-section hanger equipped with a PTMD to analyze the nonlinearity effects of the PTMD on vibration control of H-section hangers. The displacement responses and mechanical energy respectively obtained from the linear and nonlinear solutions are compared. The following conclusions can be drawn:

1. For the free vibration case, the displacement responses and the mechanical energy of the coupled system have no obvious differences when the linear and nonlinear results are compared at small initial displacement conditions of the primary structure, respectively. However, the system responses and mechanical energies are significantly different at the large initial displacement conditions of the primary structure.

2. For the forced vibration case, the steady-state responses of the coupled system solved by the nonlinear solution are smaller than that solved by the linear solution. However, in the cases of large excitation amplitudes, the steady-state responses of the coupled system solved by the nonlinear solution are larger than that solved by the linear solution.
3. A small structural damping of primary structure can significantly enhance the motion stability of the PTMD. Both nonlinearity of the PTMD and the structural damping of the primary structure should be considered in the design of PTMD.

References

1. Chen, Z.Q., Liu, M.G., Hua, X.G., Mou, T.M.: Flutter, galloping, and vortex-induced vibrations of H-section hangers. J. Bridg. Eng. **17**, 500–508 (2012)
2. Maher, F.J., Wittig, L.E.: Aerodynamic response of long H-sections. J. Struct. Div. **106**, 183–198 (1980)
3. Wang, Z.H., Xu, K., Zhao, Y.: Free torsional vibration analysis of coupled system with H-section hangers and horizontal wind-resistant cables in steel arch bridges. J. Vib. Eng. **30**, 620–629 (2017)
4. Ulstrup, C.C.: Aerodynamic lessons learned from individual bridge members. Ann. N. Y. Acad. Sci. **352**, 265–281 (1980)
5. Farid, M., Gendelman, O.V.: Tuned pendulum as nonlinear energy sink for broad energy range. J. Vib. Control. **23**, 373–388 (2017)
6. Manevich, A.I.: An oscillator-rotator system: vibrational maintenance of rotation, stationary synchronous regimes, stability, vibration mitigation. J. Sound Vib. **437**, 223–241 (2018)
7. Den Hartog, J.P.: Mechanical Vibration. McGraw-Hill, New York (1947)
8. Ioi, T., Ikeda, K.: On the dynamic vibration damped absorber of the vibration system. Bull. JSME. **21**, 64–71 (1978)

Resonance Behavior of the Non-Ideal System Which Contains a Snap-Through Truss Absorber

Yuri Mikhlin and Anton Onizhuk

Abstract Three-DOF system with a limited power-supply (or non-ideal system) having the von Mises girder as absorber is considered. Stationary resonance regimes of vibrations with snap-through motions around the unstable equilibrium position of the system are analyzed in two approximations of the mixed multiple scales/harmonic balance method. Namely, vibrations near the resonance 1:1 between the motor rotation frequency and the linearized sub-system frequency are analyzed. This analysis and numerical simulations confirm that the regime of snap-through motions guarantees an effective absorption of elastic vibrations. Besides, we can find other regimes which guarantee such absorption and the fast outcome from the resonance region.

1 Introduction

Systems with a limited power-supply (also the so-called non-ideal systems or NIS) are considered. In such systems the resonance interaction of the power-supply and elastic sub-system can be realized. This phenomenon is first observed by Sommerfeld in 1904 [14]. When it happens, large part of energy is going into increase of the elastic sub-system vibrations. Dynamics of NIS is first analytically described by Kononenko [8]. Then numerous investigations on this subject were published. Different aspects of the NIS dynamics are discussed in few books and overviews, in particular, in [3, 5, 7, 10].

Y. Mikhlin (✉)
Department of Applied Mathematics, National Technical University "KPI", Kharkov, Ukraine
e-mail: Yuri_Mikhlin@mail.ru; muv@kpi.kharkov.ua

A. Onizhuk
A. Podgorny Institute for Mechanical Engineering Problems, National Academy of Sciences, Kharkov, Ukraine

The use of absorbers allows to reduce amplitudes of the resonance elastic vibrations. A variety of vibration absorbers are also considered in the context of the systems with a limited power-supply, for example, in [3, 11]. In [12] a transfer from unstable vibration modes to stable ones is presented numerically for the non-ideal system coupled with a nonlinear oscillator as absorber under resonance conditions. Snap-through system called also the von Mises girder is considered as a vibration absorber in [1, 2]. Later dynamics of the 3-DOF NIS containing a motor, elastic oscillator, and the von Mises girder as absorber was studied in [6], where preferably numerical analysis of the system dynamics is made.

In this work a system containing the linear oscillator, the energy source with a limited power-supply, and the von Mises girder as absorber of elastic vibrations is considered, where main focus being on the large amplitude snap-through motions of the girder, and other vibration regimes which guarantee effective absorption of the elastic vibrations are considered too. The present paper aims to describe the snap-through motions as analytically, as well numerically. A mixed multiple scales/harmonic balance method (MSHBM) described by Luongo and Zulli in [9] is applied to obtain analytical results. Our task is to show first both an effective absorption of the elastic vibrations using the snap-through motions, and a possibility for escape from the resonance in the system. Moreover, we show that such effects can be obtained by other kinds of dynamical regimes.

The paper is organized as follows. Model under consideration and main equation of motions are described in Sect. 2. In Sect. 3 regimes of the snap-through motion with large girder amplitudes in region of the resonance of the motor rotation frequency and the first fundamental frequency are considered. Results of numerical analysis are shown and discussed in Sect. 4.

2   Principal Model

Resonance dynamics of a nonlinear system with a limited power-supply (Fig. 1) is considered here. The motor D acts on the elastic sub-system with mass M by the crankshaft of radius r. The mass M is connected to the shaft and rigid foundation by springs with stiffness c_1 and c_0. Besides, the system contains the Mises girder of the mass m as the nonlinear absorber which is attached to the sub-system and to the motionless ground by springs of the length l and stiffness c_2, c_3. The angle γ corresponds to the girder stable equilibrium state. A motion of the system is determined by the variables x, y, and φ, corresponding to motions of the linear oscillator, the girder, and the motor rotation, respectively.

Dimensionless parameters and time, defined in the Appendix, are introduced. Also the parameters of the system are rescaled using the small parameter $\varepsilon > 0$. The following normalized parameters are assumed to be small, namely the mass of the girder μ, stiffness of the girder springs k_2 and k_3, the dissipation coefficients β_1 and β_2, and the dimensionless radius of the shaft $\bar{r}$. The angle γ is assumed to be small too but it is not rescaled using the small parameter. Besides, it is assumed that

Fig. 1 The non-ideal system
under consideration
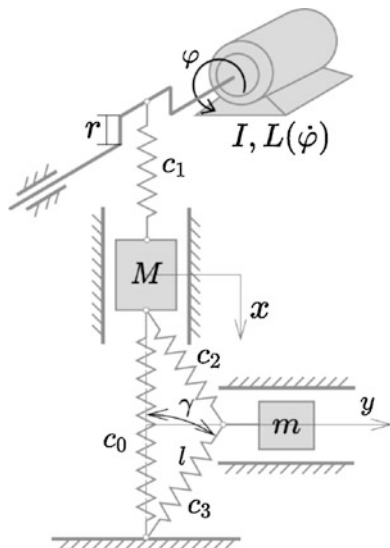
the vibration components as function of the angular velocity are small with respect
to the constant component. Now the equations of motion obtain the following form:

$$\ddot{u} + h_1 \dot{u} + (k_0 + 1)\, u + \varepsilon \overline{k_2} \left[(u - 1)\cos\gamma + \left(1 + \frac{w^2}{(1-u)^2} \right)^{-\frac{1}{2}} \right] = \varepsilon \overline{r}\sin\varphi \,,$$

$$\mu \ddot{w} + h_2 \dot{w} + w \left[\overline{k_{23}}\cos\gamma - \overline{k_2}\left((1-u)^2 + w^2 \right)^{-\frac{1}{2}} - \overline{k_3}\left(1 + w^2 \right)^{-\frac{1}{2}} \right] = 0 \,,$$

$$\tag{1}$$

$$\ddot{\varphi} - \varepsilon \rho \,(u - \varepsilon \overline{r}\sin\varphi)\cos\varphi = L(\dot{\varphi}) - H(\dot{\varphi}).$$

Here $L(\dot{\varphi})$ is the driving moment of the energy source, $H(\dot{\varphi})$ is the moment
of resistance to rotation. For simplification, the characteristic and the moment of
resistance are taken in the following form: $L(\dot{\varphi}) = \varepsilon K\,(q - \dot{\varphi})$, $H(\dot{\varphi}) = \varepsilon h \dot{\varphi}$.

Considering snap-through vibrations around the unstable equilibrium, we now
assume the following independent variable transformation: $u \rightarrow u + \varepsilon A$. Then,
using Taylor series where only terms up to third power inclusively are saved, we
have the following equations of motion near the zero equilibrium position:

$$\ddot{u} + \varepsilon h_1 \dot{u} + \omega_u^2 u = \varepsilon \overline{r}\sin\varphi + \varepsilon \overline{k_2} \left[\frac{1}{2}w^2 + w^2 u \right] + \varepsilon^2 \overline{k_2} A w^2 \,,$$

$$\mu \ddot{w} + h_2 \dot{w} - k_w w + \frac{1}{2}\overline{k_{23}}w^3 - \overline{k_2}(u + \varepsilon A)w - \overline{k_2}(u + \varepsilon A)^2 w = 0 \,, \tag{2}$$

$$\ddot{\varphi} = \varepsilon \left[\rho \,(u + \varepsilon A - \varepsilon \overline{r}\sin\varphi)\cos\varphi + Kq - (K + h)\dot{\varphi} \right] \,,$$

where $\omega_u^2 = 1 + k_0 + \varepsilon k_2$, $A = \frac{\overline{k_2}}{\omega_u^2}(1 - \cos \gamma)$, $k_w = \overline{k_{23}}(1 - \cos \gamma) + O(\varepsilon)$, $\overline{K_{23}} = \overline{K_2} + \overline{K_3}$.

3   Analysis of the Snap-Through Truss Motion

ODEs (2) are analyzed by the multiple scales method [10]. 1:1 resonance region is considered, namely, it means the resonance between the motor rotation frequency and the fundamental frequency of the elastic sub-system ω_u. Therefore a detuning parameter is introduced as $\omega_u^2 = (\dot{\varphi})^2 - \varepsilon \Delta$.

The following expansions of the variables in series by ε are applied:

$$u = u_0 + \varepsilon u_1 + \ldots, \quad w = w_0 + \varepsilon w_1 + \ldots, \quad \varphi = \varphi_0 + \varepsilon \varphi_1 + \ldots \qquad (3)$$

Terms of the expansions (3) are considered as functions of different time scales which are defined using the small parameter ε as

$$t_0 = t, \ t_1 = \varepsilon t, \ t_2 = \varepsilon^2 t, \ldots$$

$$\frac{\partial}{\partial t_i} = D_i; \ \frac{d}{dt} = D_0 + \varepsilon D_1 + \ldots; \ \frac{d^2}{dt^2} = D_0^2 + \varepsilon \, 2 D_0 D_1 + \ldots \qquad (4)$$

Substituting expansions (3) and (4) into (2) and collecting terms of the same order by ε, the following ODEs system is obtained in two approximations by ε:

$$\varepsilon^0: \ D_0^2 u_0 + (D_0 \varphi_0)^2 u_0 = 0, \qquad (5)$$

$$\mu D_0^2 w_0 + h_2 D_0 w_0 - k_w w_0 + \frac{1}{2}\overline{k_{23}} w_0^3 - \overline{k_2} u_0 w_0 + \frac{1}{2}\overline{k_2} u_0^2 w_0 = 0, \qquad (6)$$

$$D_0^2 \varphi_0 = 0, \qquad (7)$$

$$\varepsilon^1: \ D_0^2 u_1 + (D_0 \varphi_0)^2 u_1 = -\, 2 D_0 D_1 u_0 - h_1 D_0 u_0 - \overline{k_2}\left[\frac{1}{2}w_0^2 + u_0 w_0^2\right]$$
$$+ \Delta u_0 + \overline{r} \sin \varphi - 2 u_0 (D_0 \varphi_0)(D_1 \varphi_0 + D_0 \varphi_1), \qquad (8)$$

$$\mu D_0^2 w_1 + 2 D_0 D_1 w_0 + h_2 (D_0 w_1 + D_1 w_0) - k_w w_1 + \frac{3}{2}\overline{k_{23}} w_1 w_0^2$$
$$- \overline{k_2}(u_1 w_0 + u_0 w_1 + A w_0) + \frac{1}{2}\overline{k_2}(2 A u_0 w0 + u_0^2 w_1) = 0, \qquad (9)$$

$$D_0^2 \varphi_1 = -2 D_0 D_1 \varphi_0 + \rho u_0 \cos \varphi_0 + K q - (K + h) D_0 \varphi_0. \qquad (10)$$

Since the resonance 1:1 is considered here, only modes that can affect it are retained for solution of the (5)–(7). One has the following:

$$u_0 = C_1(t_1)e^{ip(t_1)t_0} + cc., \ w_0 = C_2(t_1)e^{ip(t_1)t_0} + cc., \ \varphi_0 = p(t_1)t_0. \quad (11)$$

Substituting (11) into (6) and balancing only e^{ip} terms the following relation is obtained:

$$-C_2\left(\mu p^2 + k_w\right) + \frac{3}{2}\overline{k_{23}}C_2^2\overline{C_2} - \overline{k_2}\left(C_1^2\overline{C_2} + 2C_1\overline{C_1}C_2\right) + ih_2pC_2 = 0. \quad (12)$$

Equation (12) provides an algebraic relation between complex amplitudes of the main oscillator and Mises girder in the first approximation by ε. In order to bring (12) into real numbers domain the complex variables C_1 and C_2 are presented as $C_1 = a_u e^{ib_u}$, $C_2 = a_w e^{ib_w}$ and real/imaginary parts are separated:

$$-\mu a_w p^2 - a_w k_w + a_w^3 \frac{3\overline{k_{23}}}{2} + a_w a_u^2 \overline{k_2} = a_w a_u^2 \overline{k_2} \cos(2b_u - 2b_w), \quad (13)$$

$$a_w p h_2 = a_w a_u^2 \overline{k_2} \sin(2b_u - 2b_w),$$

where a_u, a_w, b_u, b_w are real functions of t_1.

From Eq. (13) two relations between real oscillation amplitudes and phases can be obtained:

$$\left[k_w + \mu p^2 + 2\overline{k_2}a_u^2 - \frac{3}{2}\overline{k_{23}}a_w^2\right]^2 + [h_2 p]^2 = \left[\overline{k_2}a_u^2\right]^2,$$

$$\tan 2\xi = \frac{-h_2 p}{k_w + \mu p^2 + 2\overline{k_2}a_u^2 - \frac{3}{2}\overline{k_{23}}a_w^2}, \ \xi = b_u - b_w. \quad (14)$$

Expression for φ_1 and the first solvability condition (absence of secular terms) are now obtained from (10):

$$\varphi_1 = -\frac{\rho}{8p^2}C_1 e^{2it_0 p} + cc., \quad (15)$$

$$p' + (K + h_1)\,p - Kq - \frac{\rho}{2}\left(C_1 + \overline{C_1}\right) = 0. \quad (16)$$

Using (15) we can also present expression for u_1 and the second solvability condition from (8):

$$u_1 = \frac{\overline{k_2}}{2p^2}C_2\overline{C_2} - \frac{\overline{k_2}}{6p^2}C_2^2 e^{2ipt_0} + \frac{C_1}{16p^2}\left(-\overline{k_2}C_2^2 + i\rho C_1\right)e^{3ipt_0} + cc., \quad (17)$$

$$2\,(pC_1)' + (i\Delta + hp)\,C_1 + i\overline{k_2}\left(2C_1C_2\overline{C_2} + C_2^2\overline{C_1}\right) + \frac{1}{2}\left(\overline{r} - \rho C_1\overline{C_1}\right) = 0. \quad (18)$$

Then the same procedure of separation as was used above is applied to (18):

$$2 \left(a_u p\right)' + a_u p h + a_u a_w^2 \overline{k_2} \sin 2\xi + \frac{1}{2} \left(\overline{r} - a_u^2 \rho\right) \cos b_u = 0 \,,$$

$$2 a_u p {b_u}' + \Delta a_u + a_u a_w^2 \overline{k_2} \left(2 + \cos 2\xi\right) - \frac{1}{2} \left(\overline{r} - a_u^2 \rho\right) \sin b_u = 0 \,. \qquad (19)$$

These equations together with (14) and (16) form a system describing NIS under consideration in the first approximation of the multiple scales method.

4   Numerical Results

All numerical results are obtained using Julia programming language [4]. Besides, DifferentialEquations.jl framework [13] is used for ODE integration and Plots.jl package is used for drawing. On all figures the system without Mises girder is shown by the dark color, the system with one is shown by the light gray. Parameters used for plots are presented in the Appendix.

Obtained algebraic constraints between amplitudes and phases (14) are shown in Fig. 2 for some values of the motor angular velocity and oscillation frequency p. Up to two non-zero values of the girder oscillation amplitudes a_w are possible for some value of the main mass oscillation amplitude a_u. No stable regimes with snap-through motions are possible when there are no other solutions without trivial one for that value of a_u. Lowest possible value for girder amplitudes is exactly $\sqrt{4/3}$ times bigger than its stable position, then snap-through motions through all three equilibrium positions appear. In Fig. 3 integration of initial Eq. (1) is shown in comparison with integration of Eqs. (16), (19) together with constraints (14). We can see good correspondence of the analytical solution and checking numerical
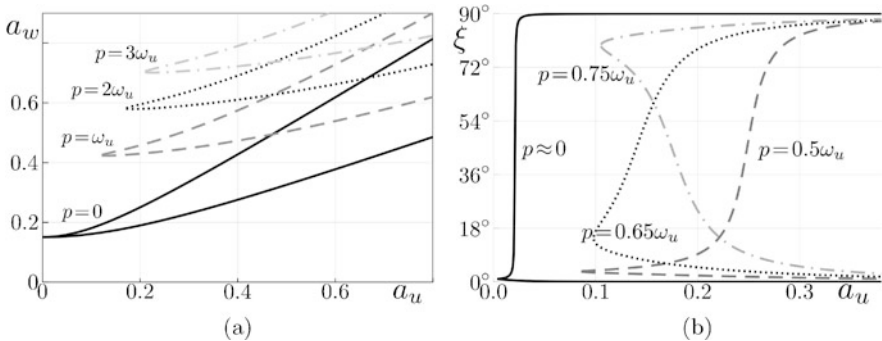
Fig. 2 Amplitude and phase difference relations for different p. Here $\omega_u = 1.4473$. (**a**) Amplitude a_w from a_u. (**b**) Phase difference ξ from a_u

Fig. 3 Numeric comparison of initial system and obtained in Sect. 3
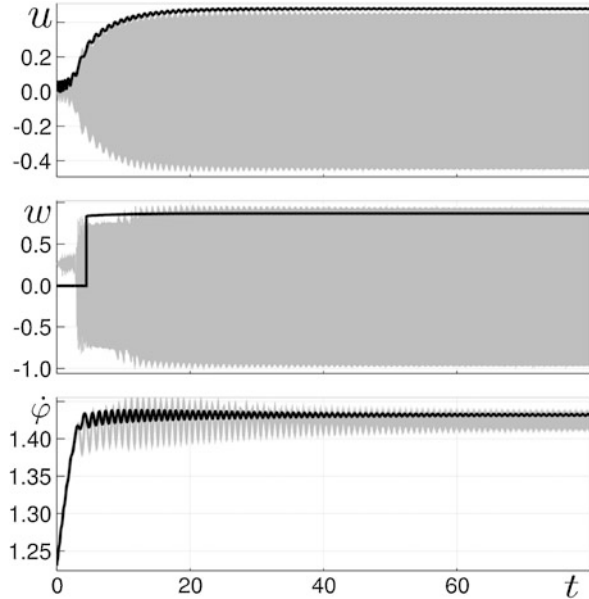
simulation. For each value of p only lower branch of amplitude constraint (see Fig. 2a) leads to vibration absorption regime, while upper leads to unrestricted growth.

Numerical analysis of the NIS confirms that the snap-through motions are effective for absorption of the elastic resonance vibrations. In Fig. 4 the snap-through vibration regime of absorption is shown. Vibrations of the elastic sub-system are more than 70% lower than in the system without the girder. However in the displayed regime resonance occurs on the frequency that is somewhat lower than the first resonance frequency.

In Fig. 5 it is shown that the Sommerfeld effect occurs for the system without girder. Its counterpart with the von Mises girder also gets stuck; however, when the amplitude of the girder motions grows, it soon switches to the regime of snap-through motions. Then amplitudes of the oscillator begin to fall down, and in a short interval of time the system gets pushed out of resonance. But the snap-through motions are not necessary for absorption regime appearance, as it is shown in Fig. 6. Note that the mass of the von Mises girder is equal to only 5% of the mass of the elastic sub-system.

5   Conclusions

Three-DOF NIS having the von Mises girder as absorber is considered. Analysis by the MSHBM and numerical simulation show that the regime of snap-though motion is very effective to absorb resonance elastic vibrations. Big part of the vibration
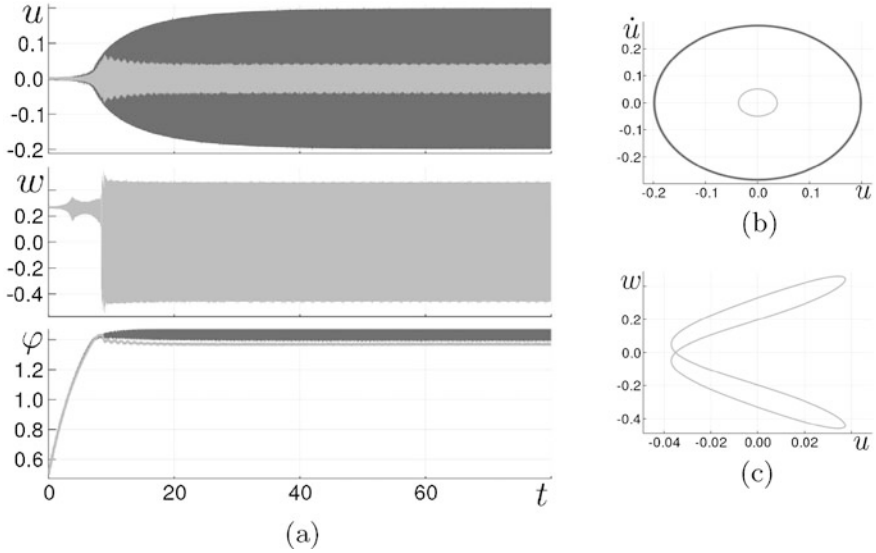
Fig. 4 Regime of absorption with snap-through motions. (**a**) Variables in time. (**b**) Phase plane.
(**c**) Configuration plane

Fig. 5 Escape from
resonance
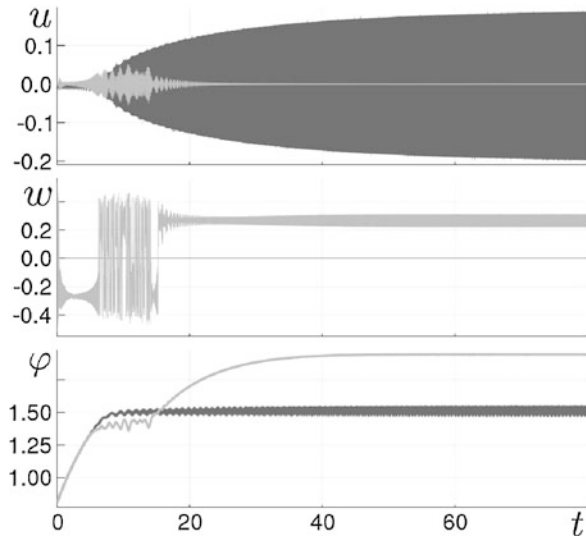
energy leaves to the snap-through motions even when the von Mises girder has small
mass. We can see here as absorption of elastic vibrations, as well an escape from
resonance. We can see also that other regimes can be effective for such absorption
and escape from the resonance too.
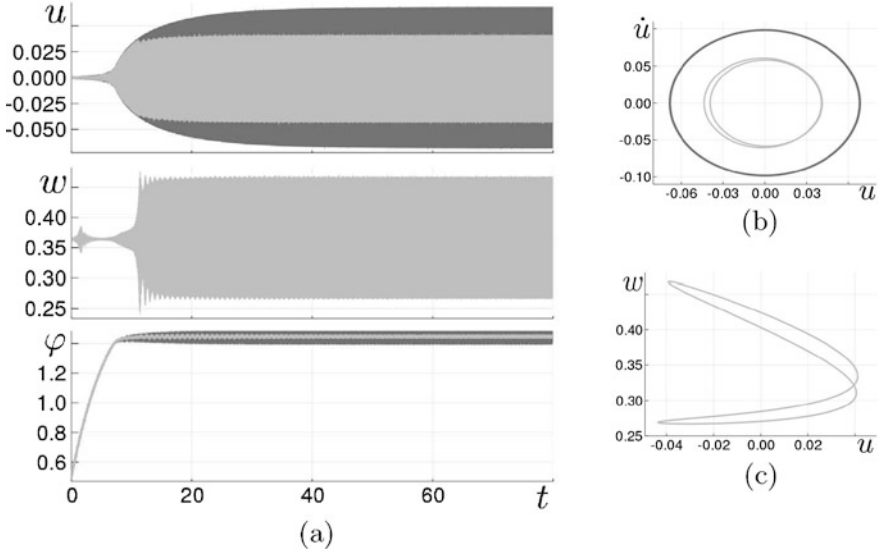
Fig. 6 Regime of absorption without snap-through motions. (**a**) Variables in time. (**b**) Phase plane. (**c**) Configuration plane

Appendix: Dimensionless Parameters and Parameter Values

The following relations between dimensional and dimensionless parameters are introduced and used in transition from Eqs. (1) to (2):

$$\frac{x}{l\cos\gamma} = u, \ \frac{y}{l\cos\gamma} = w, \ \frac{\overline{m}}{M} = \varepsilon\mu, \ \frac{r}{l\cos\gamma} = \varepsilon\overline{r},$$

$$\frac{\beta_1}{m\omega_l} = \varepsilon h, \ \frac{c_0}{c_1} = k_0, \ \frac{c_2}{c_1} = \varepsilon k_2,$$

$$\frac{c_3}{c_1} = \varepsilon k_3, \ \frac{k_i}{\cos\gamma} = \overline{k}_i, \ \frac{\beta_2}{m\omega_l} = \varepsilon h_2, \ \omega_l^2 = \frac{c_1}{M},$$

$$t = \frac{\tau}{\omega_l}, \ \frac{d}{dt} = \omega_l\frac{d}{d\tau}, \ \frac{M}{I}rl\cos\gamma = \rho$$

Default parameters (these are used unless specified other): $\gamma = \pi/12$, $I = 5.0$, $M = 1.0$, $c_0 = c_1 = 10^5$, $r = 0.04$, $b = 0.5$, $\beta_1 = \beta_2 = d = 0.1$.
Figures 2 and 3: $L = 3$, $m = 0.03 \times M$, $c_2 = c_3 = 0.095 \times c_1$.
Figure 4: $L = 10$, $I = 4.0$, $m = 0.01 \times M$, $c_2 = c_3 = 0.1 \times c_1$.
Figure 6: $\gamma = \pi/9$, $L = 30$, $I = 4.0$, $m = 0.05 \times M$, $c_2 = c_3 = 0.115 \times c_1$.
Figure 5: $L = 10$, $M = 2.6$, $m = 0.01 \times M$, $c_2 = c_3 = 0.3 \times c_1$.

References

1. Avramov, K.V., Mikhlin, Y.V.: Snap-through truss as a vibration absorber. J. Vib. Control. **10**, 291–308 (2004)
2. Avramov, K.V., Mikhlin, Y.V.: Snap-through truss as an absorber of forced oscillations. J. Sound Vib. **290**, 705–722 (2006)
3. Balthazar, J.M., et al.: An overview on the appearance of the Sommerfeld effect and saturation phenomenon in non-ideal vibrating systems (NIS) in macro and MEMS scales. Nonlinear Dyn. **93**(1), 19–40 (2018)
4. Bezanson, J., Edelman, A., Karpinski, S., Shah, V.B.: Fresh approach to numerical computing. SIAM Rev. **59**, 65–98 (2017). https://doi.org/10.1137/141000671
5. Cveticanin, L., Zukovic, M., Balthazar, J.M.: Dynamics of Mechanical Systems with Non-Ideal Excitation. Springer, Cham (2018)
6. De Godoy, W., et al.: A note on non-linear phenomena in a non-ideal oscillator, with a snap-through truss absorber, including parameter uncertainties. Proc. Inst. Mech. Eng. K J. Multi-body Dyn. **227**, 76–86 (2013)
7. Eckert, M.: The Sommerfeld effect: theory and history of a remarkable resonance phenomenon. Eur. J. Phys. **17**(5), 285–289 (1996)
8. Kononenko, V.O.: Vibrating Systems with Limited Power Supply. Iliffe Books, London (1969)
9. Luongo, A., Zulli, D.: Dynamic analysis of externally excited NES-controlled systems via a mixed multiple scale/harmonic balance algorithm. Nonlinear Dyn. **70**, 2049–2061 (2012). https://doi.org/10.1007/s11071-012-0597-6
10. Nayfeh, A.H., Mook, D.T.: Nonlinear Oscillations. Wiley, New York (1979)
11. Piccirillo, V., et al.: Non-linear dynamics of a thermomechanical pseudoelastic oscillator excited by non-ideal energy sources. Int. J. Non Linear Mech. **77**, 12–27 (2015)
12. Plaksiy, K.Y., Mikhlin, Y.V.: Resonance behavior of the limited power-supply system coupled with the nonlinear absorber. Mathe. Eng. Sci. Aerosp. **6**(3), 475–495 (2015)
13. Rackauckas, C., Nie, Q.: Differentialequations.jl–a performant and feature-rich ecosystem for solving differential equations in Julia. J. Open Res. Softw. **5**(1), 15 (2017). https://doi.org/10.5334/jors.151
14. Sommerfeld, A.: Beiträge zum dynamischen ausbau der festigkeitslehe. Physikal Zeitschr **3**, 266–286 (1902)

Experimental Dynamic Response of a Nonlinear Wire Rope Isolator

Andrea Salvatore, Biagio Carboni, Li-Qun Chen, and Walter Lacarbonara ⓘ

Abstract The steady-state dynamic response of a structure isolated by a nonlinear wire rope spring operating in the direction of gravity is experimentally studied. The isolated structure consists of two cantilever beams with a lumped mass at the tip. The force-displacement cycles provided by the isolator show a hysteretic behavior due to inter-wire friction and geometric nonlinearities. The restoring force is nonsymmetric exhibiting softening under compression and hardening under tension. The device rheological response is identified using experimental data and a suitable mechanical model. The frequency response curves (FRCs) for increasing levels of the vertical base excitation are obtained for the standalone device, the isolated and non-isolated structure. The expected softening trend of the isolation system and the increase of the displacement amplitude at low frequencies are ascertained both theoretically and experimentally. The comparison between the FRCs of the isolated and the non-isolated structure shows a severe reduction of the transmissibility coefficient in a broad frequency range. This work represents a first step towards the full modeling, validation of the reduced order model of the hysteretic isolator, and the isolated structure towards a full optimization of the device isolation performance.

Keywords Wire rope isolator · Transmissibility · Hysteresis · Vibration isolation · System identification

A. Salvatore (✉) · B. Carboni · W. Lacarbonara
Department of Structural and Geotechnical Engineering, Sapienza University of Rome, Rome, Italy
e-mail: a.salvatore@uniroma1.it

L.-Q. Chen
Shanghai Institute of Applied Mathematics and Mechanics, Shanghai University, Shanghai, China

89

1   Introduction

Wire ropes are commonly employed to sustain large axial loads. At the same time, they can be successfully exploited for applications in the field of structural vibration control. The first patented device based on steel wire ropes dates to the beginning of the last century and its scope consisted in the mitigation of galloping oscillations in cable electric transmission lines [1]. In recent years, several devices based on the hysteresis provided by wire rope assemblies have been proposed [2–7].

In this work, a nonlinear isolation system for reducing vertical vibrations is identified and experimentally investigated. The isolator is a so-called wire rope spring while the structure to be controlled is represented by two cantilevers with a tip mass undergoing bending motion. The nonlinear hysteretic behavior of the isolator is first characterized evaluating the equivalent stiffness and hysteretic damping at various displacement amplitudes and then identified through a suitable nonsymmetric hysteresis model. Subsequently, the test and the structure to be controlled are designed. Experimental FRCs of the isolated and non-isolated structures are finally obtained in order to estimate the transmissibility in the frequency bandwidth of interest.

2   The Isolator Response

The isolation system consists of a compact wire rope isolator (see Fig. 1). It is made of two metal plates joined by a stainless steel wire rope having a diameter of 4 mm (7×7 wire of 0.4 mm) [8]. The geometric nonlinearities of the cables induce an asymmetric hysteretic behavior. Hardening or softening is manifested under tension or compression, respectively. The device high deformability together with its high damping capacity makes it ideal for vibration control of machinery and other kinds of structures. Antonelli et al. investigated the hysteretic behavior of the device via quasi-static testing (Fig. 2) applying cyclic time histories with increasing amplitudes, namely (0, ± 2.5, ± 5, ± 7.5, ± 10, ± 12.5, ± 15) mm.

The equivalent stiffness and damping versus displacement are obtained at each quasi-static cyclic amplitude proving the softening behavior under compression and the softening-hardening behavior under tension with a decreasing trend in equivalent hysteretic damping (Fig. 3).

Starting from the modified asymmetric Bouc–Wen model of hysteresis proposed by Carboni et al. [9], a further generalization of the asymmetric constitutive response is proposed and implemented in this study. By employing the differential evolution algorithm [10], the model parameters that best fit the experimental quasi-static force–displacement cycles at different amplitudes are found (see Fig. 4).

Fig. 1 The compact wire
rope isolator

Fig. 2 Hysteretic loops
under cyclic tests
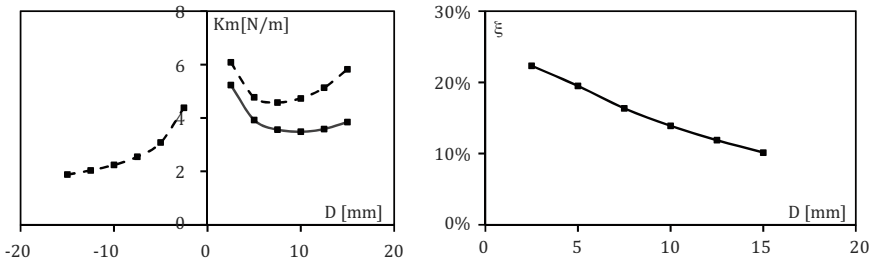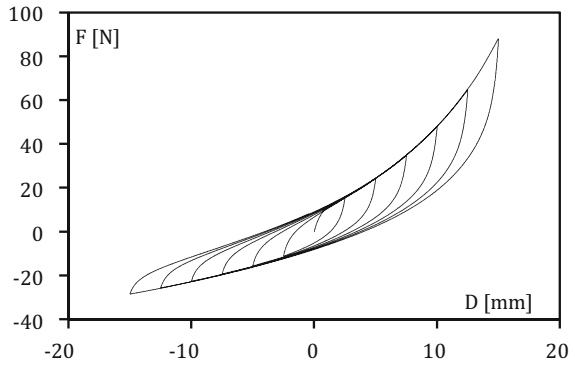
Fig. 3 (Left) Stiffness vs. displacement (tension and compression stiffness represented by the
dotted line, the average stiffness is indicated by the solid line) and (right) equivalent hysteretic
damping vs. displacement
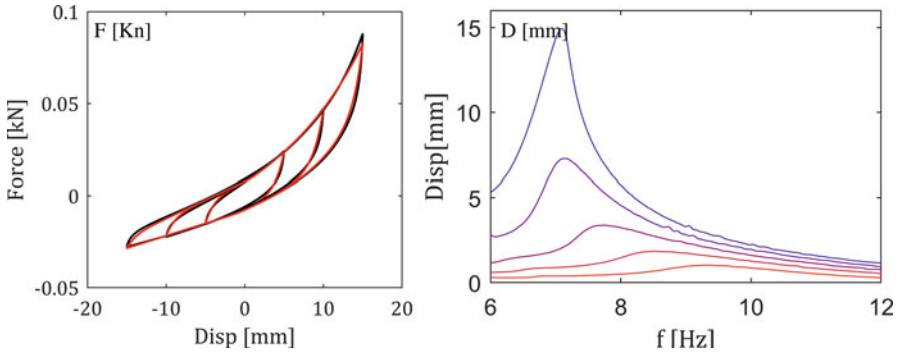
Fig. 4 (Left) Numerical (red) vs. experimental (black) force–displacement cycles and (right) numerically obtained FRCs for the device with a mass of 1 kg for different base accelerations (i.e., 0.25, red, 0.5, 0.75, 1.0, 1.25 g, blue)

Fig. 5 Test setup for (left) the non-isolated structure and (right) the isolated structure

3 Experimental Setup

The structure to control during the tests was designed starting with the stiffness of the device in order to obtain a frequency shift, between the non-isolated and the isolated structure, of about five times. The designed structure consists of two symmetric cantilever steel beams ($b = 30$ mm, $h = 2$ mm, $l = 7.5$ cm) with a tip mass of 0.24 kg for both beams. In order to evaluate the FRCs and the transmissibility over the investigated frequency range, for both the non-isolated and the isolated systems, shaker tests were carried out in frequency sweeps (i.e., sinusoidal input with constant amplitude and varying frequency) (Fig. 5).

The range of investigated frequencies was between 5 and 100 Hz with a logarithmic sweep of 0.5 oct/min. The test was repeated four times for both systems with different acceleration amplitudes. The accelerations of the masses (0.24 kg $\times$ 2) at the beam tips, of the mass mounted on the support (0.45 kg) and of the shaker head were acquired through four PCB piezotronic accelerometers.

Table 1 Base accelerations, stiffness constant

N_{test}	A_g [g]	a	ξ [%]
1	0.10	2.71	0.61
2	0.15	2.70	0.66
3	0.20	2.68	0.74
4	0.25	2.68	0.74

4 Dynamic Behavior of the Uncontrolled Structure

For the considered range of base motions, the non-isolated structure responds linearly, so the theoretical FRC curves can be obtained with acceptable approximation in closed form. The steady-state response in displacement, $x_{ss}(\Omega)$, and acceleration, $\ddot{x}_{ss}(\Omega)$, and the linear transfer function $H(\Omega)$ are given by: $x_{ss}(\Omega) = H(\Omega)\ \ddot{x}_g$, $\ddot{x}_{ss}(\Omega) = \Omega^2 H(\Omega)\ \ddot{x}_g$, $H(\Omega) = (m/k)/\sqrt{\left[1-(\Omega/\omega_n)^2\right]^2 + (2\xi\Omega/\omega_n)^2}$, where Ω is the excitation frequency and ω_n the frequency of the nth mode of the structure. The structural stiffness is that of a cantilever beam with a point load at the tip. By knowing the mass, the governing parameters are the elastic constant and the damping ratio, namely $k = a \cdot EI/l^3$ where the constant $a = 3$ for a perfect clamp; $\xi = c/(2m\omega_n)$ is the damping ratio expressed in terms of the viscous damping coefficient c which embodies the beam material damping and the boundary friction.

The frequency sweep tests were repeated for four different amplitudes, and for each amplitude, the stiffness and damping constant which better fit the experimental FRCs were found (see Table 1). The accelerations registered by the accelerometers were first filtered through the Savitzky–Golay filter [11] and then doubly integrated to obtain velocities and displacements. The results of the integration were filtered again by a high-pass filter to remove the integration drift. In the subsequent figures, the experimental FRCs (Fig. 6) and the trend of the transmissibility function (Fig. 7) are reported.

5 Experimental Response of the Isolated Structure

The same frequency sweep tests were repeated for four different excitation levels for the isolated structure. As in the previous tests, displacements of each mass can be obtained by double integration and filtering of the acquired accelerations. Figure 8 shows the comparison between the experimental FRCs in displacement and acceleration for the isolated (red) and non-isolated structures (black) for an input acceleration of 0.25 g.

A strong reduction of the maximum acceleration of the isolated system can be observed due to the high compliance (hence, low frequency) of the device. As expected, at low frequencies the displacement of the isolated structure is larger than that of the non-isolated structure. At the same time, the maximum displacement
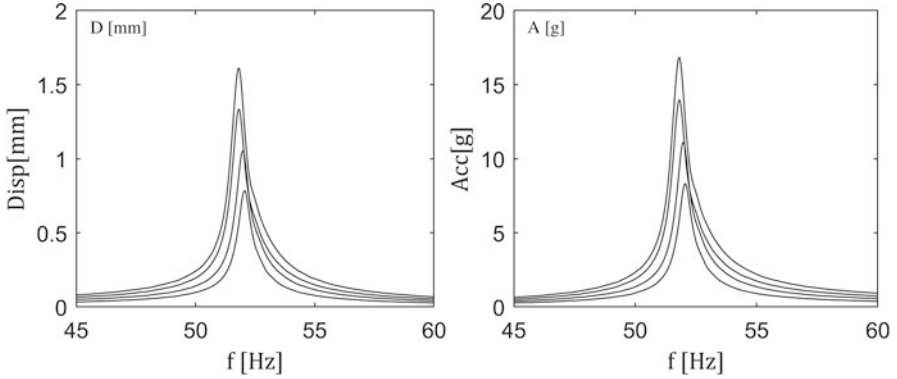
Fig. 6 Experimental FRCs in terms of (left) displacement and (right) acceleration for base accelerations of 0.1, 0.15, 0.2, 0.25 g
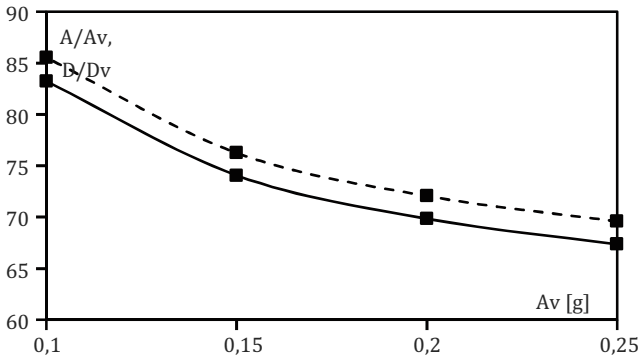
Fig. 7 Displacement (dotted) and acceleration and damping ratio for each test (cont.) transmissibility peak vs. acceleration amplitude

of the isolated structure (elongation of the isolator) is indeed much smaller than the maximum displacement of the non-isolated structure (flexural beam vibration), thanks to the energy dissipation provided by the device built-in hysteresis. Figure 9 represents the displacement and acceleration FRCs for the isolated structure for different excitation amplitudes (i.e., 0.25, 0.5, 0.75, 1 g). The first and the second resonance frequencies, about 14 and 24 Hz, are relative at the elongation modes of the isolator. The third mode, near 74 Hz, is the flexural mode of the beam. Furthermore, please note that the mass on the beam functions as a vibration absorber for the constraint mass at the frequency of 70 Hz, making its relative acceleration vanish.

By focusing on the frequency range of the two last modes, we can observe a softening trend on both (24 and 74 Hz) due to the softening geometric nonlinearities of the device (see Fig. 10).
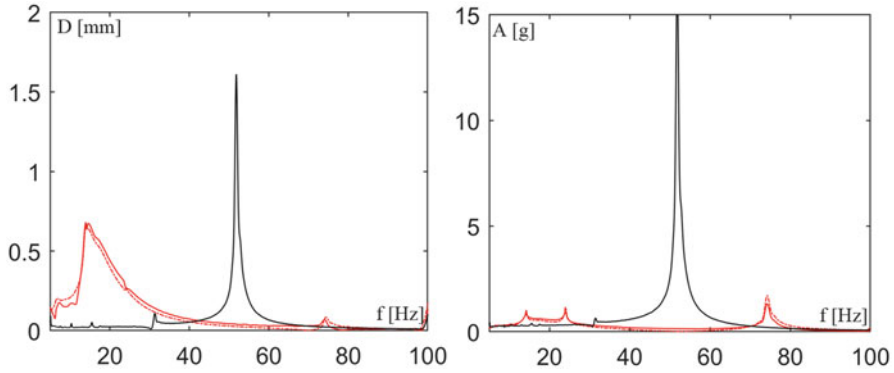
Fig. 8 Experimental FRCs of the uncontrolled structure (black line) vs. controlled structure (the red solid lines represent the response of the mass at the beam tip, while the red dashed lines indicate the response of the lumped mass on the isolator): (left) displacement and (right) acceleration
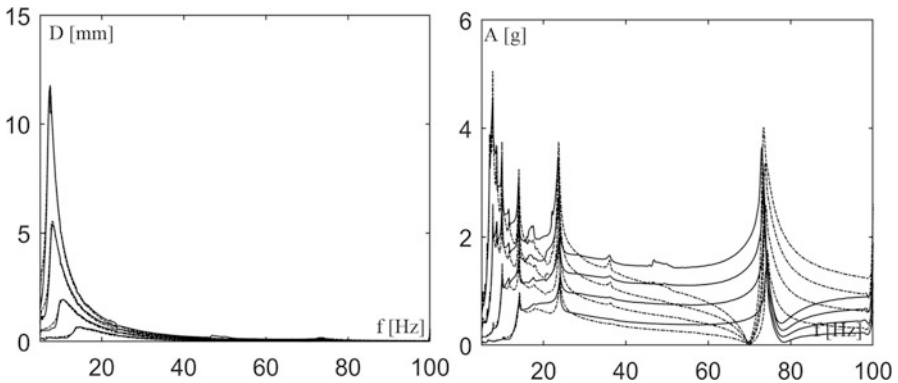
Fig. 9 (Left) Displacement FRC and (right) acceleration FRC of the isolated structure for different excitation amplitudes (i.e., 0.25, 0.5, 0.75, 1 g). The solid lines represent the response of the mass at the beam tip, while the black dashed lines indicate the response of the lumped mass on the isolator

The transmissibility is reduced by an order of magnitude over the entire frequency range examined (see Fig. 11). In fact, it goes from an average value of about 75 for both the acceleration and displacement factors to an average value of about 6. The transmissibility factor is evaluated for the third mode (74 Hz), which exhibits the maximum acceleration and the maximum displacement. The transmissibility factor shows a decreasing trend due to the softening behavior which causes a more pronounced decoupling between the structure and the ground for larger excitation amplitudes (see Fig. 12 left). By making use of considerations of balance of linear momentum, the restoring force of the isolator during the test is also estimated. Figure 12 (right) shows the force–displacement cycles at the resonance frequency of the isolator for four amplitudes. The agreement with the hysteretic
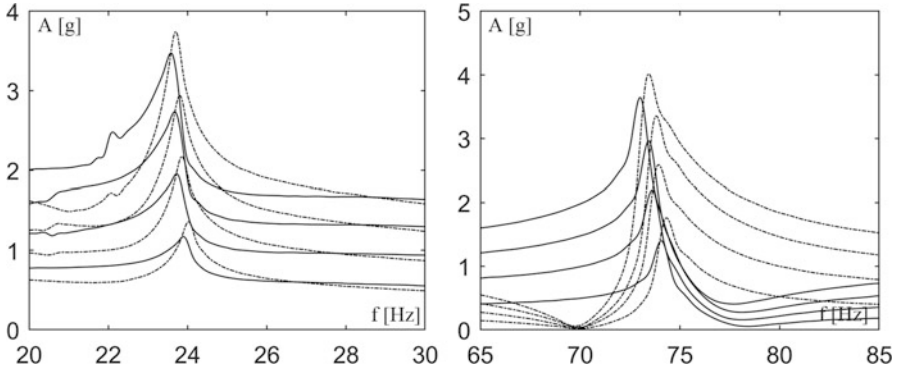
Fig. 10 Acceleration FRC near (left) the second mode and (right) the third mode of the isolated structure. Solid lines indicate the response of the mass on the beam and dotted lines denote the response of the mass on the isolator
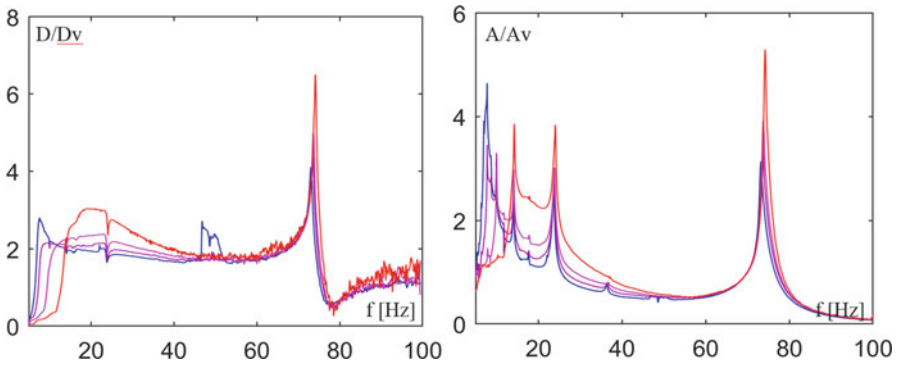
Fig. 11 (Left) Displacement transmissibility and (right) acceleration transmissibility vs. frequency of isolated structure for an excitation amplitude of 0.25 (red), 0.5, 0.75, 1.0 g (blue)

loops provided by the quasi-static cyclic tests confirms the hardening-softening asymmetric behavior. There is also a drift because of the system weight during the dynamic tests, differently from the static tests.

6 Conclusions

The performance of the investigated hysteretic, nonsymmetric wire rope isolator shows a strong reduction of the transmissibility in terms of both acceleration and displacement over a wide frequency range. The hysteretic restoring force provided by the wire ropes under compressional and tensile cyclic loads was identified, and it was shown to be suitable for vibration damping applications because of the large dissipation rate. This can mitigate the well-known drawback of isolation systems
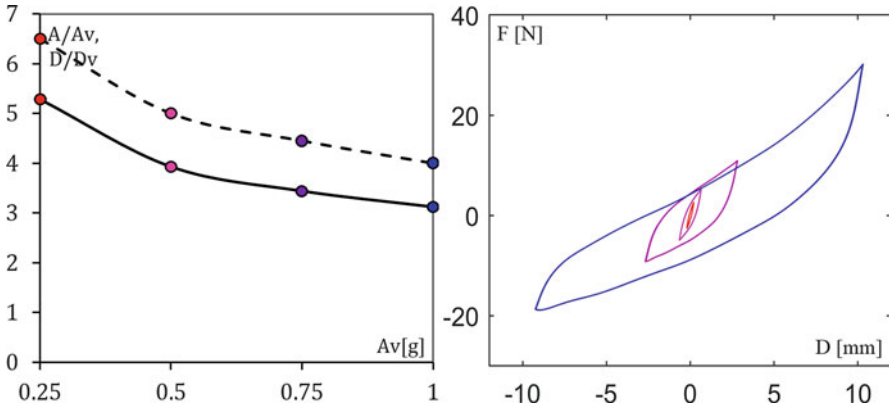
Fig. 12 (Left) Displacement (dotted line) and acceleration (solid line) transmissibility vs. acceleration amplitude and (right) force–displacement cycle of the device for the four test amplitudes

arising from the large compliance at low frequencies. However, the main problem with this type of devices for large-scale structural isolation is the relative size between the device and the structure to be controlled. The present chapter sets the initial steps of a wider experimental and theoretical work aimed at validating a reduced order nonlinear model capable of reproducing accurately the dynamic behavior of the device and the structure in order to achieve a wide nonlinear isolation system optimization.

References

1. George, H.: Stockbridge. Vibration damper. US Patent 1675931, 3 July 1928, Los Angeles
2. Tinker, M.L., Cutchins, M.A.: Damping phenomena in a wire rope vibration isolation system. J. Sound Vib. **157**, 718 (1992)
3. Demetriades, G.F., Constantinou, M.C., Reinhorn, A.M.: Study of wire rope systems for seismic protection of equipment in buildings. Eng. Struct. **15**, 321334 (1993)
4. Gerges, R.R., Vickery, B.J.: Parametric experimental study of wire rope spring tuned mass dampers. J. Wind Eng. Ind. Aerodyn. **91**, 13631385 (2003)
5. Gerges, R.R., Vickery, B.J.: Wind tunnel study of the across-wind response of a slender tower with a non-linear tuned mass damper. J. Wind Eng. Ind. Aerodyn. **91**, 10691092 (2003)
6. Carboni, B., Lacarbonara, W.: A nonlinear vibration absorber with pinched hysteresis: theory and experiments. J. Eng. Mech. **142**(5), 04016023 (2015)
7. Carboni, B., Lacarbonara, W.: Nonlinear dynamic characterization of a new hysteretic device: experiments and computations. Nonlinear Dyn. **83**(1–2), 23–39 (2016)
8. Compact Wire rope Isolator, ITT Enidine Inc., 7 Centre Drive Orchard Park
9. Carboni, B., Lacarbonara, W., Brewick, P.T., Masri, S.F.: Dynamical response identification of a class of nonlinear hysteretic systems. J. Intell. Mater. Syst. Struct. **29**(13), 2795–2810 (2018). https://doi.org/10.1177/1045389X18778792

10. Storn, R., Price, K.: Differential evolution—a simple and efficient heuristic for global optimization over continuous spaces. J. Glob. Optim. **11**, 341 (1997). https://doi.org/10.1023/A:1008202821328
11. Savitzky, A., Golay, M.J.E.: Smoothing and differentiation of data by simplified least-squares procedures. Anal. Chem. **36**(8), 1627–1639 (1964)

Optimization Strategies of Hysteretic Tuned Mass Dampers for Seismic Control

Antonio Boccamazzo, Biagio Carboni, Giuseppe Quaranta, and Walter Lacarbonara

Abstract The vibration damping capability of a hysteretic tuned mass damper (TMD) is investigated. Two optimization strategies, based on stationary and non-stationary excitations, are proposed. In the first instance, the base excitation is a harmonic acceleration and the cost function is the area subtended by the frequency response curves at selected amplitudes. In the second instance, the motion of the main mass caused by earthquake excitations is sought to be reduced for an ensemble of earthquakes. In both approaches the optimal parameters of the vibration absorber are obtained by employing a metaheuristic algorithm. Both methods provide optimal TMDs able to achieve significant reductions in structural displacement and acceleration.

Keywords Hysteretic tuned mass damper · Optimization · Seismic control

1 Introduction

Among the available technologies to mitigate structural vibrations, tuned mass dampers (TMDs) are especially attractive. The concept of tuned mass damper, first introduced by Frahm in 1909 [1], was originally conceived as an additional mass attached to the main structure with a linear spring; its performance was later improved when Ormondroyd and Den Hartog [2] introduced viscous damping. Since then, the concept of vibration absorber has been extensively studied in the literature from different standpoints. The majority of these studies have considered linear systems and harmonic inputs. For instance, Den Hartog [3] found the optimal TMD parameters in case of undamped main structures. Warburton [4] derived closed-form expressions of the optimal absorber parameters for undamped

---

A. Boccamazzo (✉) · B. Carboni · G. Quaranta · W. Lacarbonara
Department of Structural and Geotechnical Engineering, Sapienza University of Rome, Rome, Italy
e-mail: antonioboccamazzo@outlook.it

single-degree-of-freedom (SDOF) systems under harmonic and white noise random excitations.

The beneficial effects of TMDs in reducing structural vibrations have originated several efforts to extend their applicability in presence of random inputs and nonlinear systems. Indeed, the implementation of TMDs with nonlinear restoring forces has been proven to be especially promising in improving the absorber performances. Arnold [5] applied the Ritz averaging techniques to an absorber with a cubic spring and used a one-term approximation for the solution; Carter and Liu [6] studied an absorber system where both springs were nonlinear. Lacarbonara and Vestroni [7] proposed the use of a hysteretic TMD in the context of low-rise multi-storey buildings. Carboni and Lacarbonara [8] studied the steady-state response of TMDs featuring several types of hysteretic nonlinear restoring forces.

In spite of the large deal of researches (most of them numerically oriented) and despite the fact that TMDs are recognized as effective devices to mitigate wind-induced vibrations, their seismic effectiveness still remains an open issue. The main problem that deteriorates the TMD performance is the *detuning* effect, a frequency shift generally caused by structural damage that induces a reduction of structural stiffness and strength.

The main goal of the present study is to compare two distinct strategies to select the optimal hysteretic TMD parameters. In the first instance, named "Stationary", the amplitude of the frequency response curve (FRC) is minimized over a given frequency bandwidth. In the second instance, named "Nonstationary", the response of the main structure subject to seismic base excitations is sought to be minimized for an ensemble of earthquakes. The optimal TMD constitutive parameters are obtained using a differential evolution algorithm (DE). This method, originally proposed by Storn and Price [9], has been widely employed for both optimization and hysteresis identification [10]. Both approaches are shown to be effective since the optimized TMDs achieve a significant reduction of the seismic response of the structure.

2   Modeling Approach

The mechanical model of the main structure equipped with the TMD adopted in this study results into a two-degree-of-freedom (2-DOF) system. The structure is the scale five-storey building model investigated in [11]. The experimentally obtained natural frequencies and damping ratios are summarized in Table 1 as function of the 5th floor displacement amplitude (corresponding to the sway mode) and of the base acceleration magnitude [12].

The observed softening behavior, characterized by a decrease of the resonance frequency with the oscillation amplitude, is described by the Bouc–Wen (BW) model of hysteresis in which the restoring force is the sum of a linearly elastic part and a hysteretic part denoted by $k_e x$ and z, respectively. This model was first

Table 1 Lowest natural frequencies and associated damping ratios of the building for different displacement amplitudes and base accelerations

Acceleration [m/s^2]	Displacement [mm]	Frequency [Hz]	Damping ratio [%]
0.0018g	2	4.230	0.877
0.0081g	5	4.150	1.022
0.0191g	10	4.075	1.267
0.0244g	15	4.050	1.427
0.02715g	20	4.020	1.605

introduced by Bouc [13] and then extended by Wen [14]. The evolution of the hysteretic part is described by the first-order differential equation:

$$\dot{z} = [k_d - (\gamma + \beta sgn(\dot{x}z))]|z|^n \dot{x}, \tag{1}$$

where x represents the displacement of the main structure, while k_e and k_d are related to its stiffness (i.e., $k = k_e + k_d$ is the tangent stiffness and k_e is the post-elastic stiffness for $n \to \infty$), $\gamma \in R$ and $\beta \in R$ regulate the hysteresis loops shapes, and $n \in R^+$ rules the smoothness of the transition from elastic to elasto-plastic behavior.

The vibration absorber is described by a variant of the BW model proposed in [8] to include pinching effects observed in the experimental hysteresis loops. A pinching function $H(x)$ is introduced to modulate the tangent stiffness k at the origin according to $H(x) = 1 - \xi_H e^{x_2^2/x_H}$, where x_2 is the absorber displacement. This function depends on two parameters, namely $\xi_H \in [0, 1)$ and $x_H > 0$.

The equations of motion of the 2-DOF system read

$$
\begin{aligned}
m_1\ddot{x}_1 + k_{e1}x_1 + z_1 - k_{e2}x_2 - z_2 &= -m_1 a_g, \\
m_2\ddot{x}_2 + m_2\ddot{x}_1 + k_{e2}x_2 + z_2 &= -m_2 a_g, \\
\dot{z}_1 &= [k_{d1} - (\gamma_1 + \beta_1 sgn(\dot{x}_1 z_1))]|z_1|^n \dot{x}_1, \\
\dot{z}_2 &= [k_{d2}H(x) - (\gamma_2 + \beta_2 sgn(\dot{x}_2 z_2))]|z_2|^n \dot{x}_2,
\end{aligned}
\tag{2}
$$

where the subscripts 1 and 2 indicate the quantities related to the structure and TMD, respectively, while the overdot denotes differentiation with respect to time. The structural parameters are obtained by means of a system identification technique described in [12] and are reported in Table 2.

3 TMD Optimization: Stationary Case

In this section, the first TMD optimization procedure is presented. The goal is to mitigate the dynamic response of the primary structure subject to harmonic base

Table 2 The identified constitutive parameters of the BW model fitting the actual structure

k_{e1} $\left[\frac{\text{kN}}{\text{mm}}\right]$	k_{d1} $\left[\frac{\text{kN}}{\text{mm}}\right]$	γ_1 $\left[\frac{\text{kN}^{1-n}}{\text{mm}}\right]$	β_1 $\left[\frac{\text{kN}^{1-n}}{\text{mm}}\right]$	n_1 $[-]$
0.356	0.058	0.312	0.076	1.000

Table 3 Weights for different optimizations, the base acceleration $\ddot{x}_g$ is in [m/s^2]

Optimization	0.0018g	0.0081g	0.0191g	0.02715g
Low excitation	1	1	1	0
High excitation	0	0	1	1

excitations. Since the excitation is a stationary process, here and henceforth the strategy is called "Stationary."

The proposed method seeks to minimize the area subtended by the FRCs within a frequency bandwidth of interest around the frequency of the mode to control. The optimization method is based on the use of the DE. By means of this approach it is possible to consider simultaneously multiple excitation amplitudes. The function to maximize, varying the TMD design parameters, is the vibration reduction factor $R_1 = 1 - CF_1$ in which

$$CF_1 = \frac{\sum_{i=1}^{N} \alpha_i \int_{f_{\text{inf}}}^{f_{\text{sup}}} FRF_{i,\text{Cont}}(f, A_i) \, df}{\sum_{i=1}^{N} \alpha_i \int_{f_{\text{inf}}}^{f_{\text{sup}}} FRF_{i,\text{Uncont}}(f, A_i) \, df} \tag{3}$$

where FRF$_i$ denotes the displacement amplitude of the FRC for the ith excitation amplitude A_i, N is the number of considered excitation amplitudes, and α_i is a weight function introduced to penalize certain amplitudes. As a matter of fact, without weighting the FRCs with respect to the amplitude, this method tends automatically to minimize the highest excitation amplitude that gives the largest contribution to the cost function.

The TMD optimization is performed for the system described by Eq. (2). The hysteretic TMD is optimized by assuming a mass ratio (i.e., the ratio between the TMD and the main system mass) equal to 1% whereas n is set equal to 1. The remaining variables k_{e2}, k_{d2}, γ_2, β_2, ξ_H, and x_H need to be optimized. Four levels of ground motion severity are considered and two different optimizations are carried out. The weights for these optimizations are reported in Table 3. The optimization referred to as "Low excitation" considers the three lowest excitation magnitudes, while the second referred to as "High excitation" considers the third (intermediate) and fourth (strongest) amplitudes. As expected, in Fig. 1 it can be seen an equal peak behavior for the highest oscillation amplitude in the "High excitation" case, while for the "Low excitation" case the equal peak is achieved for lower accelerations.
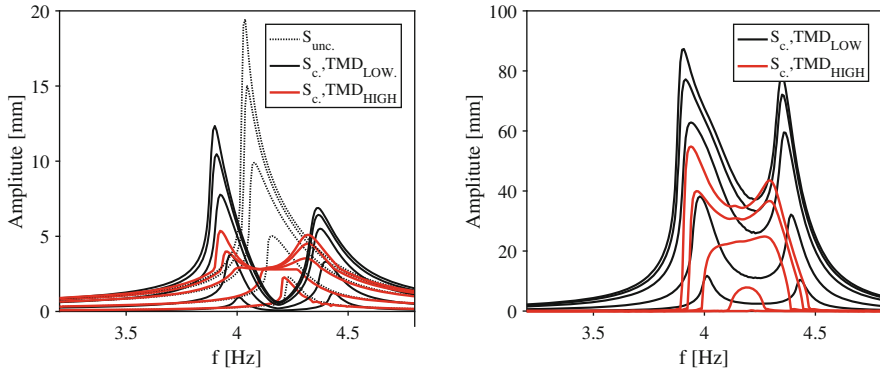
Fig. 1 FRCs for the uncontrolled structure and for the controlled structure (left) and for the absorber (right). The curves, from the lowest to the highest, are obtained for base accelerations set to $0.0018g$, $0.0081g$, $0.0191g$, $0.0244g$, $0.02715g$, respectively

4 TMD Optimization: Nonstationary Case

The second optimization strategy tries to minimize directly the displacement of the primary structure subject to an ensemble of seismic base excitations. Since the signals are nonstationary processes, this strategy is referred to as "Nonstationary."

The mass ratio μ and n are set to 1% and 1, respectively, while the remaining parameters (k_{e2}, k_{d2}, γ_2, β_2, ξ_H, x_H) are selected by means of the DE algorithm. The objective function to maximize is the vibration reduction factor $R_2 = 1 - CF_2$ in which

$$CF_2 = \frac{\sqrt{\frac{1}{N} \sum_{k=1}^{N} |x_{k,\text{Cont}}|^2}}{\sqrt{\frac{1}{N} \sum_{k=1}^{N} |x_{k,\text{Uncont}}|^2}}, \tag{4}$$

where $x_{k,\text{Uncont}}$, and $x_{k,\text{Cont}}$ are the root mean square (RMS) of the uncontrolled and controlled main structure displacement for the kth earthquake. In order to take into account the averaged values of the RMS displacement, according to the Italian Design Code [15], N is set equal to 7.

For each earthquake, the RMS of the main structure displacement is computed in the unprotected and protected scenarios (only structure and structure equipped with the TMD, respectively). We consider the RMS instead of the peak displacement because the latter does not give enough information about the cumulative damage. Artificial seismic ground motions are considered. The parameters used for generating spectrum-compatible ground acceleration signals are the following: $a_g = 0.363g$, $F_0 = 2.466$, $T_c^* = 0.389s$, and the soil is chosen to be of type A. These earthquakes correspond to the collapse prevention limit state (according to the Italian Building Code [15]); indeed, strong ground motions are considered to
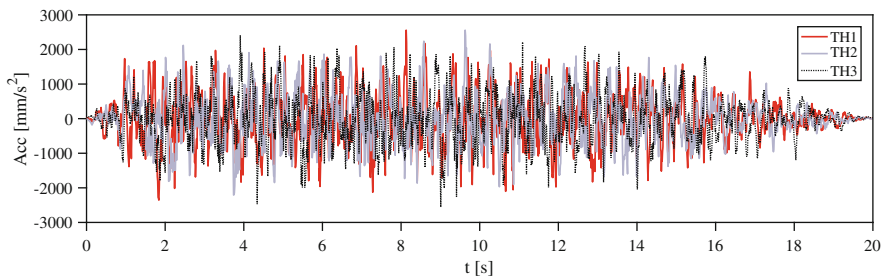
Fig. 2 Sample time histories of the base acceleration

Table 4 Comparison between the seismic effectiveness of the hysteretic TMD optimized according to the stationary (S) and nonstationary (NS) strategies in terms of RMS of the main structure displacement (D) and acceleration (A), TH labels the artificial seismic ground motion record

Strategy	RMS	TH 1	TH 2	TH 3	TH 4	TH 5	TH 6	TH 7	TH 8	TH 9	TH 10	CF2
S	D	0.24	0.24	0.30	0.52	0.32	0.04	0.14	0.14	0.06	0.32	0.259
S	A	0.25	0.25	0.32	0.53	0.33	0.07	0.15	0.18	0.08	0.33	0.275
NS	D	0.41	0.41	0.37	0.58	0.39	0.23	0.18	0.20	0.03	0.42	0.357
NS	A	0.42	0.42	0.37	0.58	0.40	0.25	0.19	0.24	0.05	0.42	0.367

emphasize the main structure frequency shift. Three of the seven artificial time histories chosen as base excitation are shown in Fig. 2.

5 Numerical Simulations and Optimizations Comparison

The two optimization strategies are here compared. For this purpose, a new set of 10 artificial ground motions are generated to closely match an elastic response spectrum in the period range of interest for the site of L'Aquila (Italy). The characteristic parameters for the elastic response spectrum according to the Italian Design Code [15] are $a_g = 0.261g$, $F_0 = 2.364$, $T_c^* = 0.347s$, type A soil and the generated earthquakes correspond to the life safety limit state. The reductions in terms of RMS of the main structure displacement and acceleration are reported in Table 4. A comparison in terms of displacement and acceleration time histories is shown in Fig. 3 and in terms of FRFs curves in Fig. 4. The slightly larger reduction attained by means of the nonstationary optimization is appreciable in Fig. 3. For both optimization strategies, the antiresonance located at the resonance frequency of the structure is observable in Fig. 4. This shows that the optimized hysteretic TMDs, changing their resonant frequencies, are able to match the nonlinear behavior of the main structure and, in this way, can mitigate the detrimental effects of detuning. Indeed, these devices provide a greater RMS displacement reduction than linear TMDs, as discussed in [12].
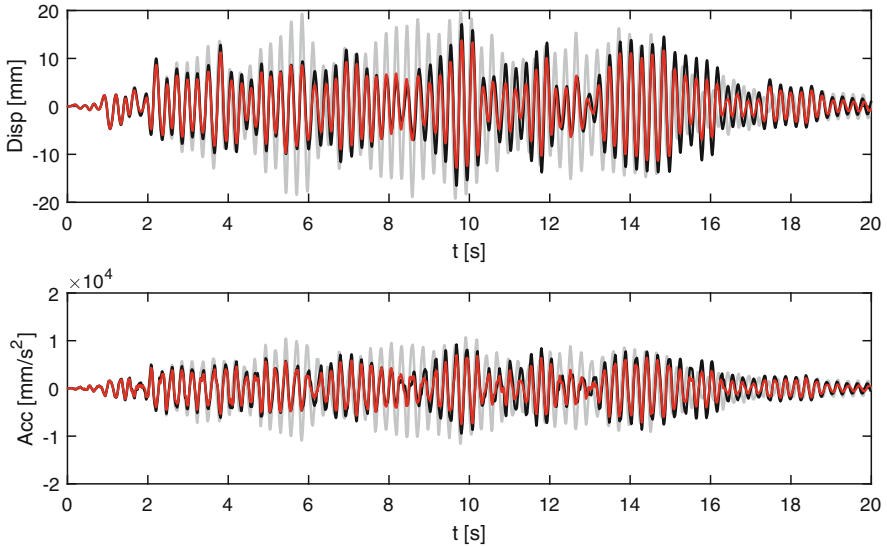
Fig. 3 Displacement (up) and acceleration (down) obtained for the uncontrolled structure (gray) and for the structure controlled via hysteretic TMD optimized according to stationary (black) and nonstationary (red) approaches for TH 2
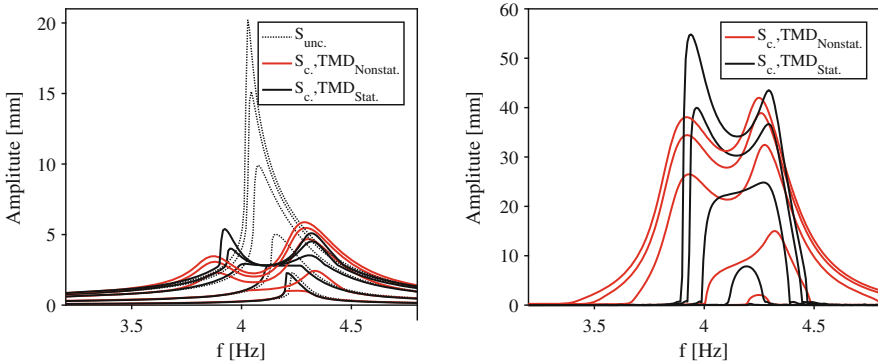
Fig. 4 FRCs for the main structure (left) and vibration absorber (right) for the uncontrolled structure (black dotted) and the controlled structure via the hysteretic TMD optimized according to the stationary (red solid) and nonstationary (black solid) approach

6   Conclusions

In this work, the capability of hysteretic TMDs in reducing the nonlinear response of a structural system under stationary and nonstationary excitations is discussed. It is shown that a hysteretic TMD with only 1% mass ratio can reduce the RMS displacement by an average of 30%. Two different strategies to obtain the absorber

parameters are explored. The first approach, named Stationary, is based on the reduction of the FRFs curves obtained for different excitation amplitudes. The second one, named Nonstationary, makes use of acceleration time histories. Both approaches lead to significant reduction of the main system response, thereby confirm the effectivness of the considered hysteretic TMD. As expected, the mitigation obtained by optimizing the TMD parameters through the nonstationary approach is more evident, since earthquake signals together with their nonstationary signatures are directly involved, and it is time-saving because it avoids calculating the entire FRF. The overall reduction of the area subtended by the FRF is a valid and equivalent optimization approach, which can thus be conveniently exploited using a semi-analytical solution. In addition, it is more general and can be employed when there exists great uncertainty about the excitation signals.

References

1. Frahm, H.: Device for damping vibrations of bodies. U.S. Patent No. 989958 (1911)
2. Ormondroyd, J.: The theory of the dynamic vibration absorber. Trans. ASME Appl. Mech. **50**, 9–22 (1928).
3. Den Hartog, J.P., Pieter, J.: Mechanical Vibrations. Courier Corporation, North Chelmsford (1985)
4. Warburton, G.B.: Optimum absorber parameters for minimizing vibration response. Eartq. Eng. Struct. **9**(3), 251–262 (1981)
5. Arnold, F.R.: Steady-state behavior of systems provided with nonlinear dynamic vibration absorbers. J. Appl. Mech. **22**(1), 487–492 (1955)
6. Carter, W.J., Liu, F.C.: Steady-state behavior of nonlinear dynamic vibration absorber. J. Appl. Mech. **28**(1), 67–70 (1961)
7. Lacarbonara, W., Vestroni, F.: Feasibility of a vibration absorber based on hysteresis. In: Proceedings of Third World Congress on Structural Control, Como (2002)
8. Carboni, B., Lacarbonara, W.: Dynamic response of nonlinear oscillators with hysteresis. In: ASME 2015 International Design Engineering Technical Conferences and Computers and Information in Engineering Conference. American Society of Mechanical Engineers, New York (2015)
9. Storn, R., Kenneth P.: Differential evolution–a simple and efficient heuristic for global optimization over continuous spaces. J. Glob. Optim. **11**(4), 341–359 (1997)
10. Quaranta, G., Monti, G., Marano, G.C.: Parameters identification of Van der Pol–Duffing oscillators via particle swarm optimization and differential evolution. Mech. Syst. Signal Process. **24**(7), 2076–2095 (2010)
11. Carboni, B., Lacarbonara, W.: Nonlinear vibration absorber with pinched hysteresis: theory and experiments. J. Eng. Mech-ASCE **142**(5), 04016023 (2016)
12. Boccamazzo, A., Carboni, B., Quaranta, G., Lacarbonara, W.: Optimized hysteretic TMD for seismic control of a nonlinear steel structure. In: ASME 2018 International Design Engineering Technical Conferences and Computers and Information in Engineering Conference. American Society of Mechanical Engineers, New York (2018)
13. Bouc, R.: Forced vibrations of mechanical systems with hysteresis. In: Fourth Conference on Nonlinear Oscillations, Prague (1967)
14. Wen, Y.-K.: Method for random vibration of hysteretic systems. J. Eng. Mech. **102**(2), 249–263 (1976)
15. DM 14/01/2008: Italian Technical Norms for Constructions (2008)

Part II
Control of Nonlinear Systems

Sliding Mode Control of Nonlinear Systems Under Nonstationary Random Vibrations via an Equivalent Linearization Method Using Block Pulse Functions

Amir Younespour and Shaohong Cheng

Abstract This chapter proposes a sliding mode control (SMC) method for nonlinear systems subjected to stationary and nonstationary excitations. The equivalent linearization (EL) method is commonly used as an effective tool in seeking approximate solutions to nonlinear systems, and SMC has numerous successful applications in the field of nonlinear system control due to its robustness in handling uncertainties in dynamic systems. In the current study, the nonlinear system is first linearized by a proposed block pulse (BP) function-based equivalent linearization method, then a continuous form of SMC method is developed to control the linearized nonlinear system. Numerical simulations reveal that compared to other existing methods, the proposed BP function-based EL method can predict the nonlinear system responses more accurately at lower computational cost, and the chattering-free SMC approach can effectively improve the performance of a nonlinear system when subjected to various types of random excitations including seismic load.

Keywords Equivalent linearization · Sliding mode control · Block pulse functions

1 Introduction

Natural phenomena such as wind and earthquake would exert random excitations on structures and induce nonlinear responses. Studying nonlinearity in dynamic systems and mitigating vibrations with various control systems to improve their performance have drawn much attention of researchers in the past few decades. The key to obtain a favorable system performance is to select a proper control

A. Younespour (✉) · S. Cheng
Department of Civil and Environmental Engineering, University of Windsor,
Windsor, ON, Canada
e-mail: younespa@uwindsor.ca

strategy. As a nonlinear control method, the sliding mode control (SMC) approach is proved to be a robust control theory in controlling nonlinear processes under highly uncertain external excitations. The ability of SMC to handle variable structure characteristics has made it a more flexible method and possible to switch between different control laws. It has been successfully applied to various linear and nonlinear systems, including the single-input-single-output (SISO) and the multi-input-multi-output (MIMO) systems, the large-scale systems, and the stochastic systems [1].

On the other hand, the mathematical treatment of nonlinear systems is challenging, and there is no universal solution available [2]. Among various methods dealing with nonlinear systems, the equivalent linearization (EL) method is the most popular one. Since 1970s, the block pulse (BP) functions have been widely studied and used as a rudimentary set of functions for signal characterizations in controlled systems. They can provide more accurate approximation with less mathematical computations and are useful tools in identifying and controlling dynamic systems [3–5]. Thus, introducing BP functions as the orthogonal functions into the EL method could considerably reduce the computational cost and accurately approximate the response of the nonlinear systems subjected to nonstationary external excitations.

The method proposed in this chapter employs the idea of SMC to improve the performance of the nonlinear systems linearized by the BP function-based EL method. To avoid the undesirable characteristic of "chattering" in SMC, in the proposed approach, a continuous form of the SMC method is developed. Therefore, when combining with the BP function-based EL method, the proposed approach would be robust in dealing with system nonlinearities and uncertainties in various types of nonstationary excitations. Both the stationary and nonstationary excitations of a Duffing oscillator and a single-degree-of-freedom (SDOF) setup spring are considered. To validate the accuracy of the proposed approach in determining the linearization coefficients, other existing linearization methods are exploited. Further, the linear quadratic regulator (LQR) method is used to evaluate the performance of the proposed SMC method.

2 Equivalent Linearization Methodology Based on Orthogonal Functions

The equation of motion of an SDOF system with displacement and velocity dependent nonlinearity can be expressed as

$$\ddot{x}(t) + 2\beta\dot{x}(t) + \omega^2 x(t) + g\left[x(t), \dot{x}(t)\right] = w(t) \tag{1}$$

where $\beta = \xi\omega$, ξ and ω are respectively the damping ratio and frequency of the linear system; $x(t)$, $\dot{x}(t)$, and $\ddot{x}(t)$ are respectively the displacement, velocity, and

acceleration vectors; $g\left[x(t), \dot{x}(t)\right]$ is a nonlinear function of the displacement and velocity; and $w(t)$ is the excitation which is assumed to be a zero-mean random excitation. Using the EL method, Eq. (1) becomes

$$\ddot{x}(t) + 2\beta_{\text{eq}}\dot{x}(t) + \omega_{\text{eq}}^2 x(t) = w(t) \tag{2}$$

where β_{eq} and ω_{eq} are the coefficients of linearization found by the EL method. When the excitation to the original system is a Gaussian function, if we assume the response of the nonlinear system is also Gaussian, then β_{eq} and ω_{eq} can be calculated by the simplified method proposed in [6], i.e.,

$$2\beta_{\text{eq}} = 2\beta + E\left[\frac{\partial g(x, \dot{x})}{\partial \dot{x}}\right]; \, \omega_{\text{eq}}^2 = \omega^2 + E\left[\frac{\partial g(x, \dot{x})}{\partial x}\right] \tag{3}$$

where $E[\cdot]$ is the mathematical expectation. For nonstationary evaluation, the equivalent damping and frequency are functions of time. For a system with initial stability (i.e., $x(0) = \dot{x}(0) = 0$) and by assuming that these coefficients are constant in stationary analysis, the time domain response of the system in Eq. (2) can be expressed by the Duhamel' integral, and the mean square of the displacement response is [7]:

$$E\left[x^2\right] = \iint\limits_{-\infty}^{\infty} h(t - \tau_1) E\left[w(\tau_1) w(\tau_2)\right] h(t - \tau_2) d\tau_1 d\tau_2 \tag{4}$$

In order to solve this integral, we use the BP operational matrix, which, for any arbitrary functions such as $f(t)$ and $l(t) \in [0, T)$, is defined as

$$\mathcal{B}\left\{\int_0^T f(\tau) l(t - \tau) d\tau\right\} \cong \frac{q}{2}\boldsymbol{F}^T \boldsymbol{J_L} \cong \frac{q}{2}\boldsymbol{L}^T \boldsymbol{J_F} \tag{5}$$

where $\boldsymbol{J_L}$ and $\boldsymbol{J_F}$ are the convolution operational matrices [5]. Substituting the operational matrices into Eq. (3) determines the linearization coefficients β_{eq} and ω_{eq} as constant values. However, with reference to Eq. (3), the equivalent damping and frequency are time dependent in the nonstationary random process. Although the assumption of using the constant stationary limits with large duration for these coefficients is common, an iterative solution process is introduced to enhance the accuracy of the solutions [8, 9].

In the current study, the proposed linearization approach utilizes the operational rules of the BP functions to calculate the mean square response of the linearized system, which allows to increase the efficiency of the EL method, particularly for nonlinear systems under any general type of nonstationary random excitations such as wind and seismic loading.

3 Concept of Sliding Mode Control Method

The basic strategy in sliding mode control is to design a suitable control law to force the system to move toward a steady state, i.e., a predefined switching surface called the sliding surface, and remain on it. The SMC design procedure includes designing a suitable sliding surface and formulating a control law to meet the reaching and sliding phases. The variable structure characteristic of the SMC allows it to purposely change the structure by a switching feedback law to track the desired state.

The dynamic equation of motion for a n-degree-of-freedom system derived from the proposed equivalent linearization method (Eq. (2)) while including a control force vector $U(t)$ is written in the state space form as

$$\dot{z}(t) = AZ(t) + B_u U(t) + B_r W(t) \tag{6}$$

with

$$A = \begin{bmatrix} 0 & I \\ -M^{-1}(K + K_{eq}) & -M^{-1}(C + C_{eq}) \end{bmatrix}, \quad B_u = \begin{bmatrix} 0 \\ M^{-1}B \end{bmatrix},$$

$$B_r = \begin{bmatrix} 0 \\ M^{-1}\phi \end{bmatrix}, \quad z(t) = \begin{Bmatrix} x(t) \\ \dot{x}(t) \end{Bmatrix}$$

where M, C, and K are the $n \times n$ mass matrix, damping matrix, and elastic stiffness matrix of the considered system, respectively. C_{eq} and K_{eq} are respectively the $n \times n$ equivalent matrices and A is a $2n \times 2n$ plant matrix of the system. B and B_u are $n \times r$ and $2n \times r$ dimensional location matrices of control force, respectively. $U(t)$ is a r-vector denoting the control law obtained from SMC algorithm. B_r is a $2n \times 1$ vector of excitation orientation, and $Z(t)$ includes the degree-of-freedom displacements and velocities called $2n \times 1$ dimensional state vector. $W(t)$ is a $n \times 1$ nonstationary zero-mean Gaussian random excitation vector.

It is supposed to design a suitable switching control law $U(t)$ to force the system-state trajectories move on the specified sliding surface in the state space for all subsequent time and slide toward the steady point. Choosing a suitable sliding surface equation $S(x(t))$ helps the system slide on it toward and reach $x = 0$ within a limited time. Thus, $S = 0$ would represent a linear differential equation whose unique solution is $x = 0$ [10].

The sliding surface is chosen to be a linear function of the system states

$$S(x(t)) = PZ = \begin{bmatrix} p_1 & p_2 & \cdots & p_n \end{bmatrix} \left\{ x(t)_1 \cdots x(t)_n \ \dot{x}(t)_1 \cdots \dot{x}(t)_n \right\}^T \tag{7}$$

where $x_i = x_1, \ldots, x_n$ and $\dot{x}_i = \dot{x}_1, \ldots, \dot{x}_n$ are the system states and $p_i = p_1, \ldots, p_n$ are the coefficients of the sliding surface equation which are determined by minimizing a quadradic performance index [11].

Considering the dynamics while in the sliding mode as

$$\dot{S}(x(t)) = P\dot{Z} \tag{8}$$

and solving the above equation with respect to Eq. (6) while neglecting $W(t)$, an expression of U called the equivalent control U_{eq} can be obtained as:

$$U_{eq} = -(PB_u)^{-1}PAZ \tag{9}$$

However, in order to keep S at zero during the subsequent time, the control law needs to be selected such that out of S [10]:

$$\frac{1}{2}\frac{d}{dt}S^2 \leq 0 \tag{10}$$

Taking the derivative and using the state equation of motion in Eq. (6), it yields

$$S^T\dot{S} = S^T P\dot{Z}$$

$$= S^T P (Az + B_u U + B_r W)$$

$$= S^T P \left[AZ - B_u(PB_u)^{-1} PAZ - B_u\delta\left(S^T PB_u\right)^T + B_r W \right]$$

$$= S^T P \left[-B_u\delta\left(S^T PB_u\right)^T \right] + S^T PB_r W$$

$$= -\delta\left(S^T PB_u\right)^2 + S^T PB_r W$$

$$= -\delta\left(S^T PB_u\right)^2 \left[1 - \frac{S^T PB_r W}{-\delta(S^T PB_u)^2} \right] \tag{11}$$

where δ is the sliding margin $(r \times r)$ diagonal matrix with diagonal elements. Assuming $\|B_r W\| \leq d$ and considering $\delta \geq \frac{d}{\|B_u\|}$, Eq. (11) satisfies the condition in Eq. (10). Thus, the control law is obtained as

$$U = -(PB_u)^{-1} PAZ - \delta\left(S^T PB_u\right)^T = U_{eq} - \delta\left(S^T PB_u\right)^T \tag{12}$$

By substituting Eq. (12) into Eq. (6), the state trajectories would drive toward the sliding surface $S = 0$, and it is expected that the dynamic responses of the system would decrease satisfactorily.

4 Evaluation of the Proposed Equivalent Linearization Method

4.1 SDOF Nonlinear Duffing Oscillator

We first consider SDOF Duffing oscillator systems. The Duffing oscillator has been successfully used to model a wide range of physical processes of which the response has nonlinear dynamic nature. In the current section, the proposed BP-function-based EL method is applied to study the behavior of an SDOF Duffing oscillator. The system equation of motion has the form of [12]:

$$\ddot{x}(t) + 2\beta\dot{x}(t) + \omega^2\left[x(t) + \gamma x^3(t)\right] = w(t) \tag{13}$$

where γ is a positive real constant representing the strength of the nonlinearity and $w(t)$ is the excitation. The exact value of the mean-square displacement response, $E[x^2]$, of Eq. (13) is evaluated as [5]:

$$E\left[x^2\right]_{exact} = \frac{\int_{-\infty}^{\infty} x^2 exp\left[\frac{4\xi\omega}{2\pi S_0\sigma^2}\left(\frac{1}{2}\omega^2 x^2 + \frac{1}{4}\gamma x^4\right)\right]dx}{\int_{-\infty}^{\infty} exp\left[\frac{4\xi\omega}{2\pi S_0\sigma^2}\left(\frac{1}{2}\omega^2 x^2 + \frac{1}{4}\gamma x^4\right)\right]dx} \tag{14}$$

where S_0 is a constant power spectrum and σ is the excitation intensity.

In this example, we only consider the stationary excitations, the excitation force function of which is a Gaussian white noise process. The sampling rate of the considered random excitation is 0.01 s. The mean-square response of the SDOF Duffing oscillator is evaluated by the proposed orthogonal-function-based EL method under the assumptions of $S_0 = 0.15$, $\omega = 2$, and $\xi = 0.05$ for two different nonlinearity strength of $\gamma = 0.1$ and 1.0. The standard EL method (i.e., with the stationary constant value and no iteration) and the iteration method proposed by Orabi and Ahmadi [8] are also applied to analyze the response of the studied Duffing oscillator. The results obtained from the above three different approaches are portrayed in Fig. 1, along with the exact value of variances determined by Eq. (14).

It can be seen from Fig. 1 that the system responses determined by the standard EL method, the iterative EL method [8], and the proposed BP-function-based EL method are always smaller than the exact solution, especially when the system has relatively stronger nonlinearity. However, when compared with the former two methods, the responses determined by the proposed approach show better agreement with the exact solution.
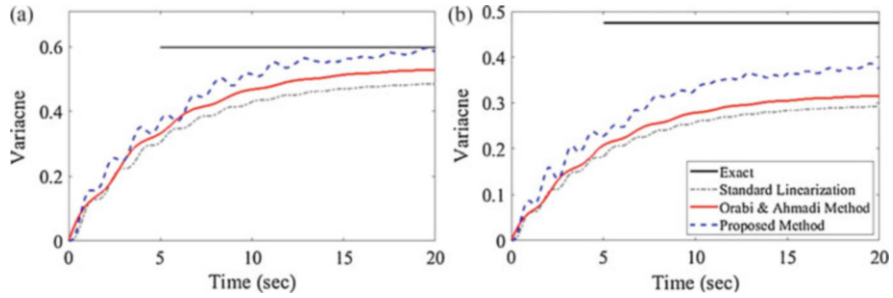
Fig. 1 Mean square displacement response due to stationary excitation. (**a**) $\gamma = 0.1$; (**b**) $\gamma = 1.0$

4.2 SDOF Nonlinear System with a Setup Spring

The nonlinear setup spring system consists of a concentrated mass m, which is connected to a setup spring and a linear viscous damper. The system equation of motion has the form of

$$\ddot{x}(t) + 2\beta\dot{x}(t) + \omega^2\left[x(t) + \gamma\,\text{sgn}(x)\right] = w(t) \tag{15}$$

where γ is a positive real constant that corresponds to nonlinearity strength and $w(t)$ is a non-white noise function. In this example, the proposed method is applied to evaluate the response of a setup spring under the nonstationary excitation defined by Eq. (16)

$$f(t) = \sum_{j=1}^{m} t a_j \exp\left\{-\beta_j t\right\} \cos\left(\omega_j t + \theta\right) \tag{16}$$

where a_j, β_j, and ω_j are constant system parameters, and θ is a random variable uniformly distributed over $[0, 2\pi]$. The forcing function in Eq. (16) was proposed by Bogdanoff et al. [13] as a model to describe ground acceleration induced by earthquake. If we assume $\mu_1 = 0.1$ and $\omega_1 = 1$, the system parameters in Eq. (16) would become $a_j = 1$, $\omega_j = j\omega_1$, $\beta_j = \mu_1\omega_j$.

Under this set of system parameters, the mean-square response of the setup spring is evaluated for $\omega = 5$, $\xi = 0.05$ and two different values of nonlinearity strength. For the nonstationary excitation, the sampling rate and the positive integer m are taken as 0.01 s and 2000, respectively. The results are shown in Fig. 2 for two different nonlinearity strength of $\gamma = 1.0$ and $\gamma = 10$. Again, Fig. 2 depicts clearly that the results yielded from the proposed BP-function-based EL method agree well with those obtained by Orabi and Ahmadi's method. In addition, compared to latter, they have better agreement with those determined by the Monte Carlo (MC) simulation. The examples illustrated in Sects. 4.1 and 4.2 suggest that the proposed approach is applicable to an SDOF nonlinear system subjected to either stationary or nonstationary excitations.
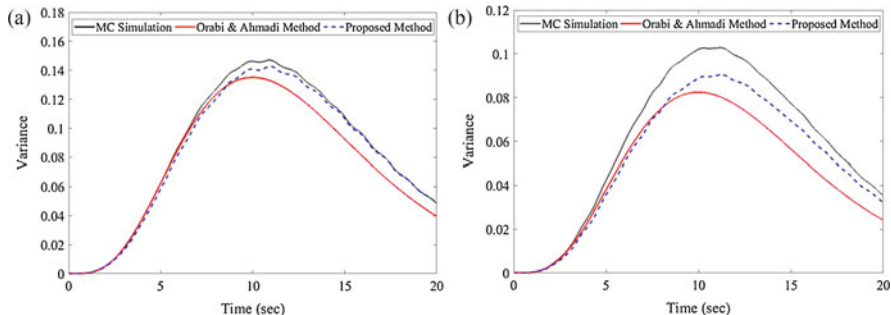
Fig. 2 Mean square displacement response due to nonstationary excitation (**a**) $\gamma = 1.0$; (**b**) $\gamma = 10$

5 Evaluation of Sliding Mode Control Method

In this section, in order to demonstrate the efficiency of the proposed control method in reducing the dynamic response, the SDOF Duffing oscillator system subjected to nonstationary loading is considered. The SMC control law is applied to the dynamic equation of motion to alleviate the responses to a satisfactory level. Using the proposed EL method, the dynamic equation of motion is written as Eq. (13), where the equivalent natural frequency and system damping ratio are 3.88 rad/s and 0.05, respectively. A set of real earthquake data, consisting of North-South acceleration records of the El Centro earthquake (1940), is considered as the nonstationary excitation. Following the method discussed in [11], the sliding surface is obtained by minimizing the quadratic performance index with a diagonal weighting matrix Q, $Q_{11} = 5.3$, $Q_{22} = 0.05$. Thus, the sliding surface equation is obtained as $S(x) = 10.3x + \dot{x}$.

For comparison, the LQR method is also utilized to control the dynamic response of the studied SDOF Duffing oscillator system. Thus, using the weighting matrix Q identical to that used for the sliding surface and considering a sliding margin $\delta_1 = 1.75 \ m^2/s^3$ for calculating the control law in Eq. (12), the uncontrolled and controlled responses of the SDOF system using SMC and LQR methods are illustrated in Fig. 3.

In addition, the root mean square of the control forces for both methods are also illustrated in Fig. 4. It is clear that the considered weighting matrix can yield the same control force; however, the proposed SMC method is more efficient in mitigating the system response.

6 Conclusions

In the current study, a vibration control method for nonlinear systems subjected to stationary and nonstationary excitations has been proposed, of which the sliding mode control method is applied to nonlinear systems linearized by the BP function-
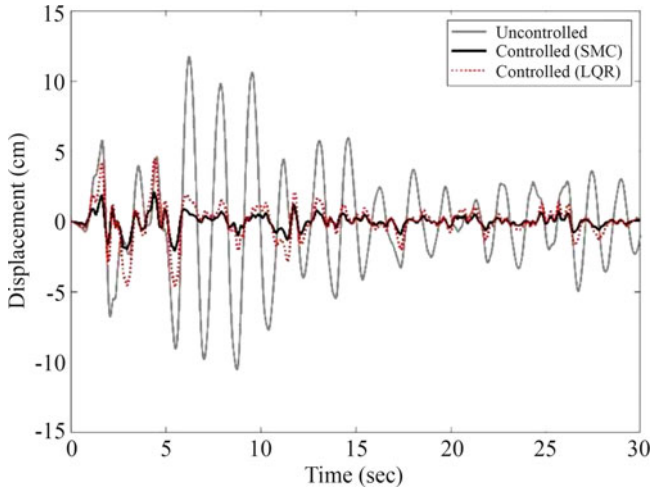
Fig. 3 Uncontrolled and controlled responses of a SDOF Duffing oscillator using SMC and LQR methods under El Centro earthquake
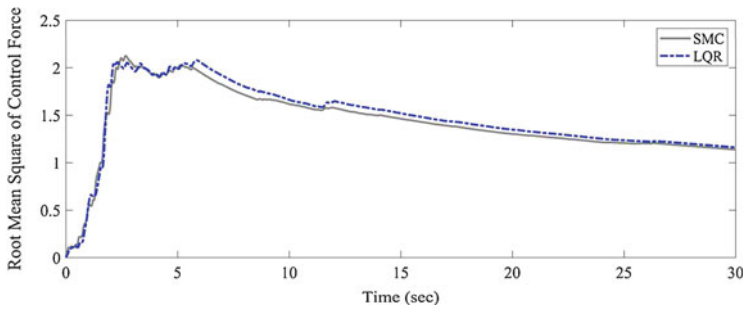
Fig. 4 RMS of control forces for SMC and LQR methods

based EL method. Results show that compared to other existing EL methods, the system responses predicted by the proposed BP function-based EL method are in better agreement with the exact solution and also the method is computationally more efficient. In addition, it was found that using the same level of control effort, the proposed chattering free SMC method can mitigate dynamic vibration of nonlinear systems more efficiently.

References

1. Edwards, C., Spurgeon, S.: Sliding Mode Control: Theory and Applications. Taylor & Francis, London (1998)
2. Qiao, F., Zhu, Q., Winfield, A.F., Melhuish, C.: Adaptive sliding mode control for MIMO nonlinear systems based on fuzzy logic scheme. Int. J. Autom. Comput. **1**, 51–62 (2004)

3. Pacheco, R., Valder Jr., S.: On the identification of non-linear mechanical systems using orthogonal functions. Int. J. NonLinear Mech. **39**, 1147–1159 (2004)
4. Ghaffarzadeh, H., Younespour, A.: Block pulse transform method for linearization of nonlinear SDOF systems. Nonlinear Eng. **4**, 77–82 (2015)
5. Younespour, A., Cheng, S., Ghaffarzadeh, H.: An equivalent linearization method for nonlinear systems under nonstationary random excitations using orthogonal functions. Struct. Eng. Mech. **66**, 139–149 (2018)
6. Atalik, T.S., Utku, S.: Stochastic linearization of multi-degree-of-freedom non-linear systems. Earthq. Eng. Struct. Dyn. **4**, 411–420 (1976)
7. Lutes, L., Sarkani, S.: Random Vibrations: Analysis of Structural and Mechanical Systems. Elsevier, Jordan Hill, Oxford (2004)
8. Orabi, I., Ahmadi, G.: An iterative method for non-stationary response analysis of non-linear random systems. J. Sound Vib. **119**, 145–157 (1978)
9. Iwan, W., Yang, I.: Application of statistical linearization techniques to nonlinear multidegree-of-freedom systems. J. Appl. Mech. **39**, 454–450 (1972)
10. Slotine, J., Li, W.: Applied Nonlinear Control. Prentice Hall, Englewood Cliffs, NJ (1991)
11. Utkin, V., Yang, I.: Methods for construction of discontinuity planes in multidimensional variable structure systems. Avtomat. i Telemekh. **10**, 72–77 (1978)
12. Kovacic, I., Brennan, M.J.: The Duffing Equation: Nonlinear Oscillators and Their Behaviour. Wiley, Hoboken, NJ (2011)
13. Bogdanoff, J., Goldberg, J.E., Bernard, M.C.: Response of a simple structure to a random earthquake-type disturbance. Bull. Seismol. Soc. Am. **51**, 293–310 (1961)

Experimental Dynamic Response of a SDOF Oscillator Constrained by Two Symmetrically Arranged Deformable and Dissipative Bumpers Under Harmonic Base Excitation

Giulia Stefani (ID)**, Maurizio De Angelis** (ID)**, and Ugo Andreaus** (ID)

Abstract During strong earthquakes, base isolated systems (buildings, bridges, strategic facilities, equipment, etc.) can impact against the surrounding moat wall because of the deformation of the isolator if the available separation distance is limited. A possible mitigation measure is the interposition of shock absorbers. The aim of this work is to illustrate some of the results of an experimental laboratory campaign concerning the study of the dynamic response of a single-degree-of-freedom (SDOF) oscillator excited by a harmonic base acceleration and symmetrically constrained by two unilateral deformable and dissipative constraints (bumpers). Three different peak values of table acceleration, four amplitudes of the total gap between mass and bumpers, and four types of bumpers were considered. Among the various aspects investigated, particular attention was paid to the study of pseudo-resonance curves of maximum absolute acceleration and excursion of the SDOF oscillator and to the characterization of the hysteresis zone.

Keywords Shaking table tests · Two-sided impact · Hysteresis area

1 Introduction

Base isolation represents one of the most applied passive control strategies to mitigate the dynamic response of both new and existing structures against earthquakes [1, 2]. The aim of base isolation is to uncouple the motion of the structure from that of the ground by introducing some type of support that isolates it from the shaking ground, thus limiting the energy input into the system and protecting it from damaging [3]. Flexibility of base isolation increases the fundamental vibration

G. Stefani (✉) · M. De Angelis · U. Andreaus
Department of Structural and Geotechnical Engineering, "Sapienza" University of Rome, Rome, Italy
e-mail: giulia.stefani@uniroma1.it; maurizio.deangelis@uniroma1.it; ugo.andreaus@uniroma1.it

period of the structure, which is expected to experience large displacements relative to the ground, concentrated in the isolation system. In case of strong earthquakes, these large displacements can damage the isolation system or can lead to poundings with adjacent structures or surrounding moat wall if the available seismic gap is not sufficient [4, 5]. The problem of pounding does not only concern buildings but also other systems, such as bridges and equipment. Rigaud and Perret-Liaudet [6] studied experimental and numerical dynamic responses of a preloaded vibro-impacting Hertzian contact under sinusoidal excitation and investigated the evolution of the experimental downward jump frequency vs. input amplitude in order to identify the nonlinear damping law during intermittent contact. With reference to pounding between base-isolated structures, Andreaus and De Angelis [7] conducted a numerical study to investigate the dynamic response of a nonlinear SDOF oscillator excited by a harmonic base acceleration and constrained by two symmetrically arranged nonlinear unilateral bumpers. This study allowed the authors to highlight typical aspects that characterize the dynamics of impacting systems and to outline possible scenarios within the system response. Based on the obtained results, subsequent campaigns of experimental tests were carried out [8, 9]. In the preliminary experimental study presented in [8], three peak values of table acceleration were applied, one amplitude of the total gap was considered, and one type of bumper was employed. Additional gap sizes and bumper types were considered in the subsequent campaign [9]. The experimental dynamic responses with and without bumpers were compared, and the main characteristics of the dynamics with impact (jump phenomenon, resonance frequency, force-displacement cycles, phase portraits, force and time of contact, coefficient of restitution, and energy dissipated by the bumpers during the impact) were identified.

The aim of this work is to illustrate some of the results of a parametric laboratory campaign of experimental tests, performed using a shaking table, that is linked to a previous preliminary and exploratory campaign of tests conducted in preceding laboratory activities [8, 9]. This campaign concerns the study of the dynamic response of a SDOF oscillator. Three different peak values of table acceleration, four amplitudes of the total gap between mass and bumpers, and four types of bumpers were considered. Among the various aspects investigated, in this work pseudo-resonance curves (PRCs) of maximum absolute acceleration and excursion of the SDOF oscillator were analyzed in depth. Particular attention was paid to the characterization of the hysteresis region between the PRCs obtained under forward and backward frequency sweeps and the variation of the hysteresis region depending on the considered parameters, namely peak table acceleration, gap clearance, and bumper stiffness. The nondimensional parameters governing the equation of motion of the SDOF oscillator excited by a harmonic base excitation will also play an important role in the case of earthquake ground motion. Although seismic excitation has much broader frequency content than harmonic motion, it can be assumed that when a structure is subjected to seismic excitation, large portion of its response may be characterized by a quasi-resonant state at its effective fundamental

period of vibration. The chapter is organized as follows: in Sect. 2, the experimental setup and the performed tests are described; in Sect. 3, some of the results obtained are shown and discussed; and in Sect. 4, the main conclusions are illustrated.

2 Experimental Setup

The physical model consists of a rigid body that can be treated as a lumped mass ($M = 500$ kg), an elastomeric high damping rubber bearing isolator (damper), and a couple of elastomeric shock absorbers (bumpers). The bumpers are symmetrically mounted on steel stands which are bolted onto the base plate. The mass is composed of six plates of mild steel jointed by bolts. The damper is centrally connected to the lower layer of the mass; the distance between bumpers and mass (gap) can be varied by adjusting the screws at the fronts of the stands; the mass is supported by four spherical bearings, rotating within unidirectional guides (Fig. 1). The series of experimental investigations has considered two distinct configurations: the absence (No Bumpers, NB) and the presence (Yes Bumpers, YB) of bumpers, under the same type of excitation. In the second case, the system has two possible states: a situation when the mass is not in contact with the bumper, denoted as *flight*, and another situation when the mass is in contact with the bumper, denoted as *contact*. In the following, some of the results obtained in the presence of bumpers (YB) will be illustrated.

Four different amplitudes of the total gap G (defined as the sum of right and left gaps, as shown in Fig. 1a) between mass and bumpers were considered: $G1 = 15$ mm, $G2 = 20$ mm, $G3 = 25$ mm, $G4 = 30$ mm. Four different bumpers B ($B1$, $B2$, $B3$, $B4$), obtained from three types of cross-section, were employed (Fig. 2). Two bumpers ($B1$ and $B2$) have the same cross-section (Fig. 2a) but different contact length L.

Three different peak values of table acceleration A were imposed ($A1 = 0.03$ g, $A2 = 0.04$ g, $A3 = 0.05$ g, where g is the gravity's acceleration). The system was excited by a stepwise forward ($f = 0.5$–5.0 Hz) and backward ($f = 5$–0.5 Hz) sine
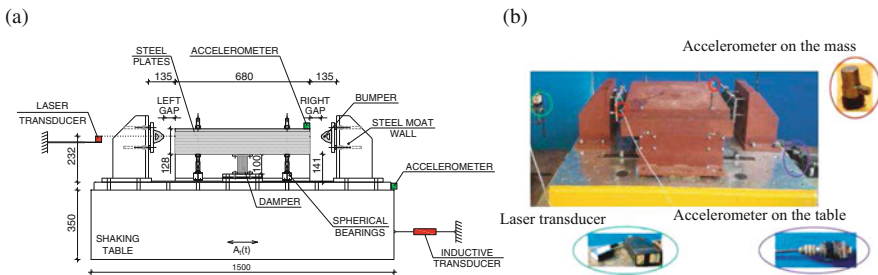
Fig. 1 Experimental setup: (**a**) schematic view; (**b**) side view
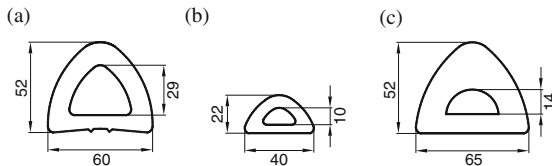
Fig. 2 Bumper sections: (**a**) *B*1 and *B*2: MB 60 × 52 mm, *B*1: $L = 100$ mm, *B*2: $L = 400$ mm; (**b**) *B*3: MB 40 × 22 mm, $L = 400$ mm; (**c**) *B*4: AP 65 × 52 mm, $L = 400$ mm

Fig. 3 Stepwise forward and backward sine sweep in displacement control ($f = 0.5$–5.0–0.5 Hz, $\Delta f = 0.1$ Hz, $A = A3 = 0.05$ g)
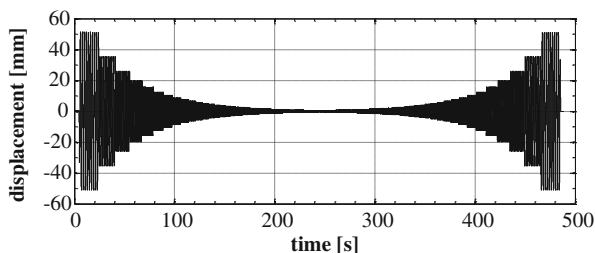
sweep in displacement control (step $\Delta f = 0.1$ Hz), in order to impose a given peak acceleration to the table, with a sufficient number of cycles to reach steady state; the attainment of the steady-state condition was checked by verifying the convergence to the limit cycle in both planes of phase portraits (relative velocity vs. relative displacement) and hysteresis loops (absolute acceleration vs. relative displacement). A sine sweep in displacement control, corresponding to *A*3, is shown in Fig. 3, for illustrative purposes.

3 Results of the Experimental Tests

The measured parameters are the absolute acceleration of the mass and the excursion of the relative displacement of the mass with respect to the shaking table. The acceleration of the mass was measured by an accelerometer positioned on the mass. The relative displacement of the mass was calculated as the difference between the absolute displacement of the mass, measured by a laser transducer, and the absolute displacement of the table, measured by an inductive transducer (Fig. 1a).

3.1 Pseudo-Resonance Curves

Among the different results obtained processing the experimental data, for each combination bumper-gap-peak table acceleration (*B–G–A*), forward (in the following figures indicated with the letter f), and backward (in the following figures

indicated with the letter b) PRCs of normalized maximum absolute acceleration $\alpha = A_{max}/A$ and normalized excursion $\eta = (D_{max} - D_{min})/G$ of the SDOF oscillator were represented. D_{max} and D_{min} are the maximum (positive) and the minimum (negative) relative displacement of the mass, respectively. The values of maximum acceleration and excursion were evaluated at steady state of each sub-frequency range both on the forward and on the backward sweep (see Fig. 3). A value of $\alpha > 1$ indicates that the acceleration of the mass is greater than the acceleration of the table. Since the excursion was normalized with respect to the total gap G, a value of η less than 1 indicates that the mass does not touch the bumpers, the limit value 1 indicates that the mass grazes the bumpers but does not deform them, and finally, a value of η greater than 1 indicates that the mass has beaten and deformed the bumpers. The symbol ν represents the normalized frequency, that is the excitation frequency normalized with respect to the pseudo-resonance value relative to the configuration in the absence of bumpers (NB) for $A = 0.1\ g$, that is, $f_R \approx 1.0$ Hz, which corresponds to a shear deformation of the damper equal to about 100%. In Fig. 4, for illustrative purposes, the forward (red solid line) and backward (blue dashed line) PRCs of the normalized maximum absolute acceleration α (Fig. 4a) and normalized excursion η (Fig. 4b), corresponding to the combination $B4$-$G2$-$A2$, are depicted. Compared to the linear case, the PRCs are bent to the right due to the hardening caused by impact against the bumpers.

By increasing the excitation frequency (forward sweep, red arrows), the amplitude of the response increases until a bifurcation (point A) to a smaller amplitude orbit occurs, associated with the absence of impact; at this point, for a slight increase in ν, the response shows a sudden downward jump to lower values (point B) and then continues to decrease slowly (no impact). If the exciting frequency is decreased (backward sweep, blue arrows), the amplitude of the response increases slowly until a bifurcation (point C) to a larger amplitude orbit occurs, associated with the
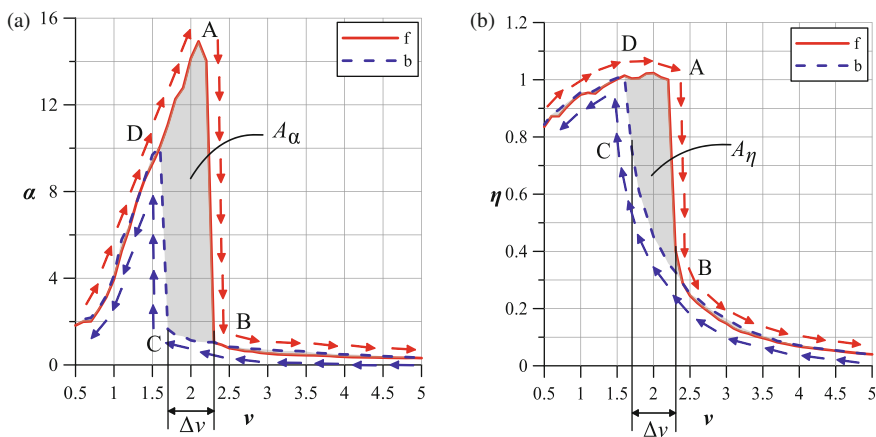
Fig. 4 PRCs ($B4$-$G2$-$A2$) of normalized: (**a**) maximum absolute acceleration; (**b**) excursion

occurrence of impact; at this point, for a slight decrease in ν, the response shows a sudden upward jump to higher values (point D) and then continues to decrease as ν decreases (in the presence of impact). The upward jump is less evident in the PRC of the excursion (Fig. 4b); this is due to the physical limitation of the displacement of the mass produced by the bumper which accentuates the bending of the curve. In the interval of amplitude $\Delta\nu$, between the downward and upward jump frequencies, for each value of ν there are three steady-state solutions, one of which is unstable and thus not experimentally realizable, whereas the other two stable solutions correspond respectively to large- and small-amplitude oscillations [10]. This leads to the jump phenomenon. The multivalued amplitudes are consequence of the bending of the response curve. The hysteresis region (shaded area), comprised between the downward and upward jump frequencies, in the interval $\Delta\nu$, is also represented in Fig. 4. This area gives a measure of the nonlinear unstable behavior of the considered dynamic system. Its extension is influenced by many parameters such as the peak table acceleration A, the gap between mass and bumpers G, and the type of bumper considered B. In Figs. 5 and 6, the forward (solid lines) and backward (dashed lines) PRCs of normalized maximum absolute acceleration α and normalized excursion η, respectively, are depicted for different values of the peak table acceleration A (Figs. 5a and 6a, for the pair $B4$-$G2$), total gap clearance G (Figs. 5b and 6b for the pair $B4$-$A2$), and bumper stiffness B (Figs. 5c and 6c, for the pair $G2$-$A2$). It can be observed that as the acceleration A increases (Figs. 5a and 6a), the PRCs tend to be bent more and more to the right, and thus the downward jump frequency increases, while the upward jump frequency increases at a much smaller extent. Consequently, the amplitude of the range $\Delta\nu$ increases.

As the total gap G increases (Figs. 5b and 6b), the downward jump frequency decreases, while the upward jump frequency does not vary significantly, as already observed. Consequently, the amplitude of the range $\Delta\nu$ decreases. As the bumper stiffness B increases (passing from $B1$ to $B4$ in Figs. 5c and 6c), the downward jump frequency increases, while the upward jump frequency does not vary significantly. Consequently, the amplitude of the range $\Delta\nu$ increases. The presence of ridges
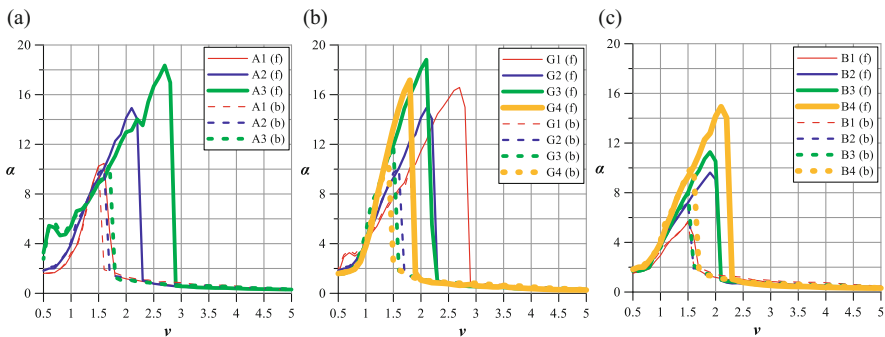
Fig. 5 PRCs of normalized maximum absolute acceleration α for different values of: (**a**) A ($B4 - G2$); (**b**) G ($B4 - A2$); (**c**) B ($G2 - A2$)
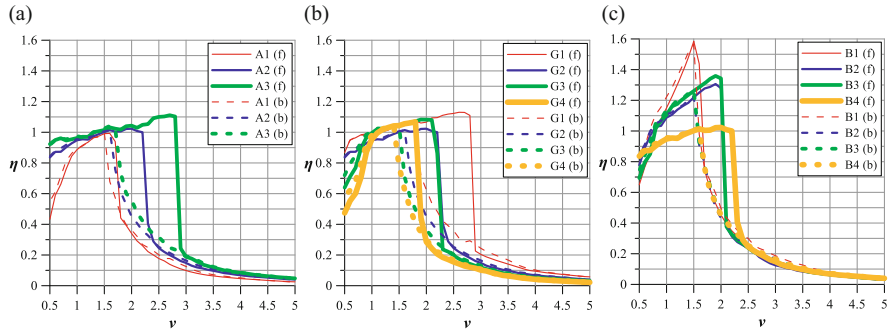
Fig. 6 PRCs of normalized excursion η for different values of: (**a**) A ($B4 - G2$); (**b**) G ($B4 - A2$); (**c**) B ($G2 - A2$)

at low frequencies was also noted in some cases, and multi-periodic orbits were observed in the corresponding phase portraits, as already highlighted in [7]. However, this topic, which deserves to be studied in more detail, will not be further treated in this work. In the absence of the bumpers (free flight), the PRCs are bent to the left due to the soft restoring force of the damper, and, as the peak table acceleration increases, the pseudo-resonance frequency decreases.

3.2 Characterization of the Hysteresis Area

In this work, among the different aspects investigated, the characterization of the hysteresis area and the identification of the parameters that influence its extension were studied. To characterize the extension and shape of this region, we chose to consider the area and the width of the frequency range $\Delta \nu$. The hysteresis area was calculated by computing the approximate integral of α and η via the trapezoidal method between the downward and upward jumps. In Fig. 7 the area of the hysteresis region, calculated from the acceleration (A_α, Fig. 7a) and excursion (A_η, Fig. 7b) PRCs, and the frequency range $\Delta \nu$ (Fig. 7c) are depicted, for each bumper, as a function of a dimensionless parameter δ_0 that represents the total gap normalized with respect to the maximum excursion at resonance without bumpers (free flight). A value $\delta_0 = 0$ indicates that the bumpers are attached to the mass, a value $\delta_0 = 1$ indicates that the mass grazes the bumpers but does not deform them, while a value between 0 and 1 indicates that the mass beats and deforms the bumpers; the mass is in the free-flight condition for $\delta_0 > 1$. Since the maximum excursion at resonance without bumpers depends on the peak table acceleration, the dimensionless parameter δ_0 allows to take into account, in a synthetic way, both the A and G variations. Consequently, each value of δ_0 corresponds to a specific pair gap–peak table acceleration. In the experimental tests, different values of δ_0 were obtained by fixing the gap and varying the peak table acceleration.
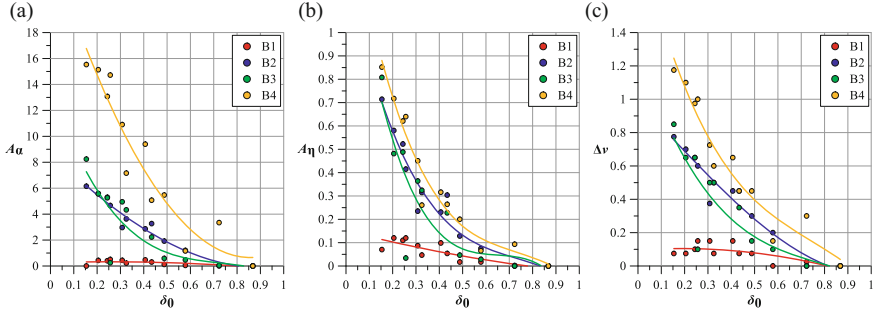
Fig. 7 Summary graphs: (**a**) A_α vs. δ_0; (**b**) A_η vs. δ_0; (**c**) $\Delta\nu$ vs. δ_0

Although there is a certain dispersion of experimental data, some considerations can be made. The trends depicted in Fig. 7a–c are qualitatively similar. It can be observed that, as δ_0 decreases from 1 to 0, that is bringing the bumpers near to the mass, both the area (A_α and A_η) and $\Delta\nu$ increase, with a more significant increase, the more rigid the bumper is. Another observation that can be made is that, if δ_0 tends to 0, that is the bumpers are sticking to the mass, the curves diverge from each other, whereas if δ_0 tends to 1, that is the bumpers are grazing the mass, all the curves tend to zero. In this work, we chose to characterize the hysteresis area through its area A_α (or A_η) and the frequency range $\Delta\nu$. In this way, it is possible to bring the original area back to a simpler and equivalent rectangular area with base $b = \Delta\nu$ and height $h = A_\alpha$ (or A_η)$/\Delta\nu$, which can be useful to make further investigations. Reasoning in terms of equivalent area could possibly be related to different parameters' range (tall, $h > b$; wide, $h < b$, rectangular or square area).

4   Conclusions

In this work, the experimental dynamic response of a SDOF oscillator excited by a harmonic base excitation and symmetrically constrained by two unilateral deformable and dissipative bumpers was investigated. The experimental tests were conducted using a shaking table and considering different combinations of peak table acceleration, total gap amplitude and bumper stiffness. Only steady-state dynamic response was studied by means of PRCs of normalized maximum absolute acceleration and normalized excursion of the SDOF oscillator. The hysteresis region between the forward and backward PRCs was investigated and characterized. The analysis of the experimental results showed that its extension (characterized through its area A_α and A_η and the amplitude of the frequency range $\Delta\nu$) is influenced by the variation of the investigated parameters. The trends of A_α, A_η, and $\Delta\nu$ were plotted against the dimensionless parameter δ_0, which takes into account the ratio between the gap width and the maximum excursion in free-flight condition. As δ_0

decreases from 1 to 0, both the area and the instability frequency range increase with increasing stiffness of the bumper. Moreover, if δ_0 tends to 0, the curves diverge from each other, whereas if δ_0 tends to 1, all the curves tend to zero.

References

1. Soong, T.T., Dargush, G.F.: Passive Energy Dissipation Systems in Structural Engineering. Wiley, New York (1997)
2. Housner, G.W., Bergman, L.A., Caughey, T.K., Chassiakos, A.G., Claus, R.O., Masri, S.F., Skelton, R.E., Soong, T.T., Spencer, B.F., Yao, J.T.P.: Structural control: past, present, and future. J. Eng. Mech. **123**(9), 897–971 (1997)
3. Naeim, F., Kelly, J.M.: Design of Seismic Isolated Structures: From Theory to Practice. Wiley, Chichester (1999)
4. Polycarpou, P.C., Komodromos, P.: On poundings of a seismically isolated building with adjacent structures during strong earthquakes. Earthq. Eng. Struct. Dyn. **39**(8), 933–940 (2010)
5. Polycarpou, P.C., Komodromos, P.: Earthquake-induced poundings of a seismically isolated building with adjacent structures. Eng. Struct. **32**(7), 1937–1951 (2010)
6. Rigaud, E., Perret-Liaudet, J.: Experiments and numerical results on non-linear vibrations of an impacting Hertzian contact. Part 1: harmonic excitation. J. Sound Vib. **265**, 289–307 (2003)
7. Andreaus, U., De Angelis, M.: Nonlinear dynamic response of a base-excited SDOF oscillator with double-side unilateral constraints. Nonlinear Dyn. **84**(3), 1447–1467 (2016)
8. Andreaus, U., Baragatti, P., De Angelis, M., Perno, S., A preliminary experimental study about two-sided impacting SDOF oscillator under harmonic excitation. J. Comput. Nonlinear Dyn. **12**(6), 061010-1–061010-10 (2017)
9. Andreaus, U., Baragatti, P., De Angelis, M., Perno, S.: Shaking table tests and numerical investigation of two-sided damping constraint for end-stop impact protection. Nonlinear Dyn. **90**(4), 2387–2421 (2017)
10. Nayfeh, A.H., Mook, D.T.: Nonlinear Oscillations. Wiley, New York (1979)

Active Sling Load Stabilization

Austin Morock, Andrea Arena, Mary Lanzerotti, Jacob Capps, Blake Huff, and Walter Lacarbonara (ORCID)

Abstract A control strategy for stabilization of single-point sling loads and hoists is proposed. Nonlinear oscillations of an elastically suspended mass are described by a suitable nonlinear dynamic model that incorporates delayed position feedback for active stabilization of both sling loads and hoist. Helicopter maneuvers are described by assigned trajectories of the mass suspension point to model oscillations of the payload. For the sling load case, stability analysis is performed to estimate optimal control gains. For the hoist case, a genetic algorithm is adopted to estimate optimal control parameters. The controlled system is simulated via time integration of the nonlinear equations of motion.

Keywords Sling load · Hoist · Active stabilization · Delayed position feedback

1 Introduction

There is a need for reliable stabilization systems that can effectively control lightly damped, low-mass sling load oscillations. Several models are proposed for the control problem of containers and slung loads [1–7]. The aim of this work is to develop a stabilization system for a low-mass sling load or hoist based on active vibration control devices schematically represented in Fig. 1 [1, 8–10]. Hoisting an

A. Morock
Department of Civil and Mechanical Engineering, United States Military Academy (USMA), West Point, NY, USA
e-mail: austin.morock@westpoint.edu

A. Arena (✉) · W. Lacarbonara
Department of Structural and Geotechnical Engineering, Sapienza University of Rome, Rome, Italy
e-mail: andrea.arena@uniroma1.it; walter.lacarbonara@uniroma1.it

M. Lanzerotti · J. Capps · B. Huff
USMA, Department of Physics and Nuclear Engineering, West Point, NY, USA

Fig. 1 Schematic representation of the helicopter with hoist and adopted fixed frame
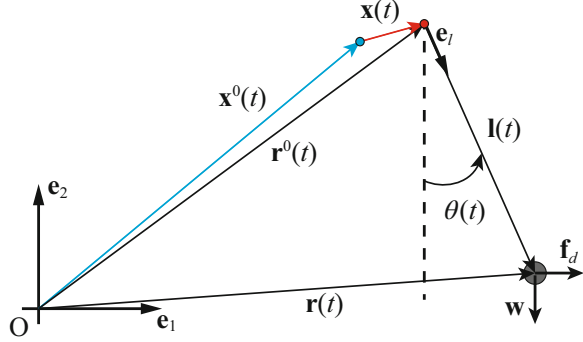
individual in 90 s may be taken as a worst case scenario implying a need for fast and precise control, as required in several rescue missions.

2 Modeling Approach

A fixed Cartesian frame (O, $\mathbf{e}_1$, $\mathbf{e}_2$) with $\mathbf{e}_1$ and $\mathbf{e}_2$ collinear with the horizontal and the vertical directions, respectively, is shown in Fig. 1. Vector $\mathbf{r}^0(t) = r_1^0(t)\mathbf{e}_1 + r_2^0(t)\mathbf{e}_2$ is adopted to describe the motion of the payload suspension point. The latter is given by two contributions, namely $\mathbf{x}^0(t)$ (helicopter trajectory) and $\mathbf{x}(t)$ (motion of the payload suspension point relative to the helicopter). The position of the payload with respect to its suspension point is given by $\mathbf{l}(t) = l(t)\mathbf{e}_l$, where $\mathbf{e}_l$ is the direction of the cable. At time t, the position of the payload is described by $\mathbf{r}(t) = \mathbf{r}^0(t) + \mathbf{R}^\top \cdot \mathbf{l}(t)$, where the 2×2 orthonormal matrix $\mathbf{R}$ describes the finite rotations, indicated by the angle $\theta(t)$, undergone by the hoisting sling with components $R_{11} = R_{22} = \cos\theta$, $R_{12} = -R_{21} = \sin\theta$. The payload with weight $\mathbf{w} = -M g \mathbf{e}_2$ is subjected to the disturbance force $\mathbf{f}_d = f_d\mathbf{e}_1$ provided by the horizontal component of the downwash generated by the helicopter blades [11]. After obtaining expressions for the potential and kinetic energies, including motion of the suspension point, the equation of motion of the one-degree-of-freedom (1 dof) mechanical system is obtained by differentiating the Lagrangian function with respect to the generalized coordinate $\theta(t)$ and its velocity $\dot{\theta}(t)$ and equating to the Lagrangian component $F_\theta = \mathbf{f}_d \cdot \partial_\theta \mathbf{r}(t)$ of the disturbance force, where $\cdot$ represents the dot product, and ∂_θ indicates partial differentiation with respect to θ, such that

$$M l^2(t)\ddot{\theta} + 2\zeta\omega_p M l^2(t)\dot{\theta} + 2M l(t)\dot{l}(t)\dot{\theta} + M g l(t)\sin\theta$$
$$+2\zeta\omega_p M l(t)\left(\dot{r}_1^0\cos\theta + \dot{r}_2^0\sin\theta\right) + M l(t)\left(\ddot{r}_1^0\cos\theta + \ddot{r}_2^0\sin\theta\right) = f_d l(t)\cos\theta.$$
(1)

The proposed mechanical model incorporates a delayed feedback control system in which the suspension point (i.e., the point where the sling attaches to the helicopter) is moved in the horizontal direction. The time-delayed position and

velocity feedback terms are introduced in the expressions of the components $\dot{x}_1(t)$ and $\dot{x}_2(t)$ of the time rate-of-change of $\dot{\mathbf{x}}(t)$, such that,

$$\dot{x}_1(t) = K_1 l_0 \omega_p \sin \theta(t - \tau) + K_2 l_0 \omega_p \sin \frac{\dot{\theta}(t - \tau)}{\omega_p}; \quad \dot{x}_2(t) = 0, \qquad (2)$$

where τ is the time delay, and K_1 and K_2 are the control gains.

3 The Case of Sling Load Transportation

Figure 2 shows a typical maneuver performed when carrying a sling load with fixed cable length (i.e., $l(t) = l_0$). The helicopter accelerates forward from rest to a steady hover, moves to forward flight, decelerates, and terminates in a hover.

Preliminary stability analyses were performed by solving the eigenvalue problem associated with the linearized equations of motion in Eq. (1) incorporating the feedback control terms given by Eq. (2). Stability charts for $K_2 = -0.05$ and $K_2 = -0.025$ shown in Fig. 3 (here blue dots indicate stable regions while red dots indicate unstable regions) are used to select the optimal control gains.

Figure 4 shows the results of time integrations, in terms of the oscillation angle θ, for the sling load with fixed cable length $l_0 = 20$ m. The figure shows the uncontrolled case (black curves) and feedback controlled case (blue curves, for $\tau = 3.58856$ s, $K_1 = -0.5$ and $K_2 = -0.025$ taken from the stability charts depicted in Fig. 3b) for the support vertical motion. The effectiveness of the active control scheme to perform fast reduction of the payload oscillations can be appreciated in both simulations for free oscillations (left side) and oscillations during a simulated helicopter maneuver (right side) with fixed cable length.

4 The Hoist Case of Retrieving a Low-Mass Payload

The situation in which a hoist retrieves within 90 s a low-mass (i.e., 299 kg) payload positioned 88 m below the helicopter is here investigated. For this simulation, the helicopter is standing at a fixed position (i.e., $\mathbf{x}^0(t) = \mathbf{o}$), and the payload is retrieved at a cable winding speed constant at the value of 1.778 m/s, during the first part of the cable retrieval (i.e., for $0 \leq t \leq 47.7$ s), while during the last three meters as the cable approaches the helicopter, the winding speed is reduced to the value of 0.0508 m/s (i.e., for $47.7 \leq t \leq 90$ s). This implies a cable length varying linearly in time from a maximum length of 88 m to a minimum length of 1 m as shown in Fig. 5 for the uncontrolled case (black line) and controlled case (blue line). For the case modeled in this section, the wind speed is assumed to take on a constant value of 5 m/s during the entire time the cable is being retrieved, corresponding to a disturbance force f_d of approximately 20 N. The wind speed at the low mass initial location can be estimated from [11].
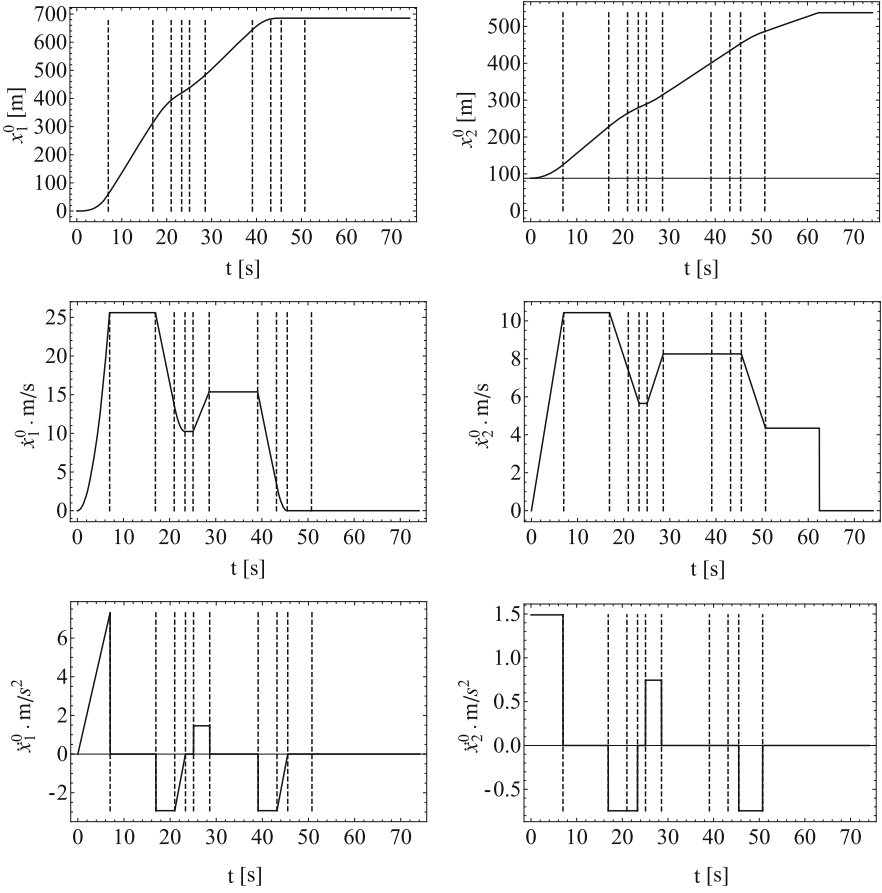
Fig. 2 Helicopter maneuver showing the $\mathbf{e}_1$—(lower left) and $\mathbf{e}_2$—component of the acceleration (lower right). Integration provides the $\mathbf{e}_1$—(middle left) and $\mathbf{e}_2$—component of the velocity (middle right) and $\mathbf{e}_1$—(upper left) and $\mathbf{e}_2$—component of the position (upper right)
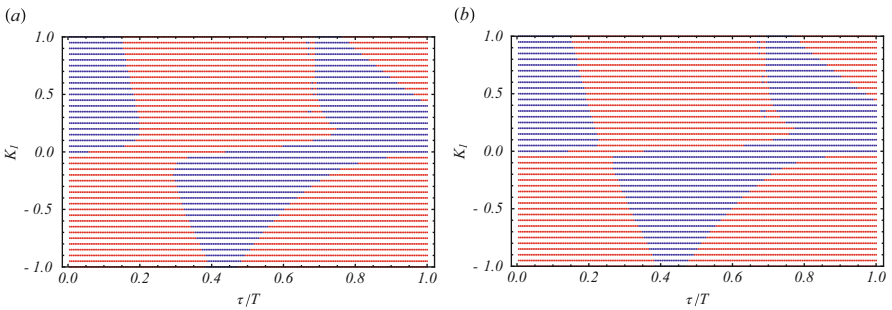
Fig. 3 Stability charts for the selected values of K_2: (a) $K_2 = -0.05$ and (b) $K_2 = -0.025$
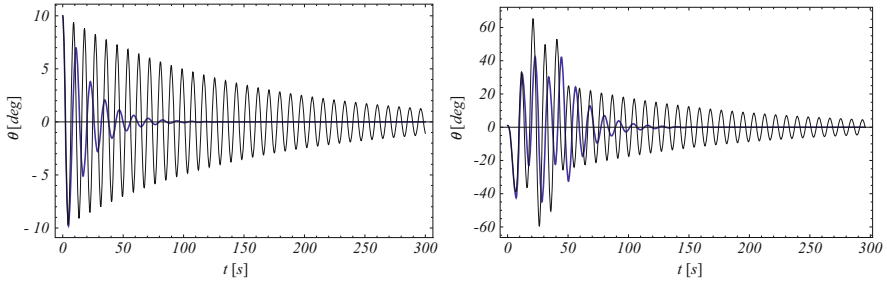
Fig. 4 Uncontrolled (black lines) vs. controlled (blue lines) oscillations of sling load: (left) free oscillations and (right) simulated helicopter maneuver
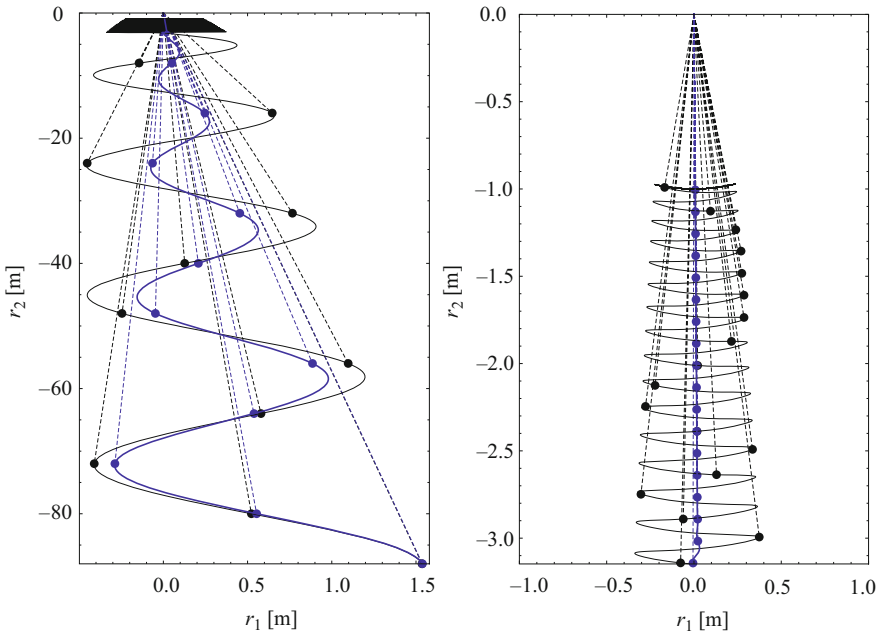
Fig. 5 Payload position relative to the helicopter for the full length of the hoist (left) and final three meters of hoist (right). Black and blue circles indicate selected positions of the payload across its uncontrolled and controlled motion, respectively, while the dashed lines indicate the corresponding cable configuration

4.1 Feedback Control Parameters Optimization

In the hoist case, the cable length is varying in time and so is the payload oscillation frequency. Consequently, the stability regions of the control parameters change together with the cable length; therefore, to find a set of optimal control parameters, a global optimization search is needed. In this work we adopt a global optimization

method based on a genetic algorithm, the so-called differential evolution (DE) algorithm [12]. The approach consists of generating a pool of n three-dimensional parameters vectors (including the gains K_1 and K_2 and the time delay τ) from uniform probability distributions to ensure that the parameters span the space equally and respect the constraint $\tau > 0$. Time integration of the controlled system reproducing the entire retrieving maneuver is then performed for each set of vectors, and the maximum oscillation angle (i.e., θ_{max}) is calculated for each simulation. The DE algorithm then perturbs a randomly selected vector chosen from among $n - 1$ vectors of the first generation and provides a new mutated parameters vector (i.e., a trial vector); θ_{max}^{tri} is then calculated for the generated trial parameters vector and compared with the maximum angle θ_{max}^{tar} evaluated for the parameters vector (namely the target vector) excluded in the generation of the trial vector. If $\theta_{max}^{tri} < \theta_{max}^{tar}$, the trial vector survives; otherwise, the target vector is selected for creating the new generation of parameters vectors which best perform in terms of control. The algorithm proceeds by providing new generations of parameters vectors up to the achievement of a fitness objective, here assumed to be $\theta_{max} < 5°$. The optimal parameters provided by this DE-based optimization procedure are represented by the vector $[K_1, K_2, \tau] = [0.0921, -0.00992, 0.02478]$.

4.2   Numerical Results

Numerical simulations performed for the uncontrolled system show that during the retrieving maneuver, the payload undergoes a maximum oscillation angle of $\theta \approx 15°$ which turns out to be unacceptable in practical applications. For the controlled system, Fig. 6 shows that the feedback control with the optimal parameters calculated through the DE algorithm bounds and damps the payload oscillations during the entire maneuver.

A sensitivity analysis was carried out to study the robustness of the control system. The effectiveness of the feedback control and stability of the system was

Fig. 6 Time history of the oscillation angle $\theta(t)$ during the payload motion (top) showing uncontrolled response (black line) and controlled case (blue line)
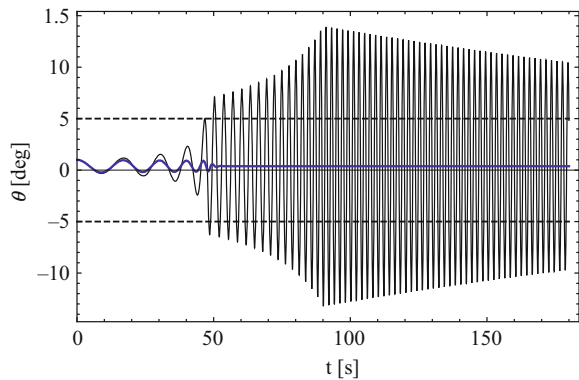
Fig. 7 Time histories of the oscillation angle $\theta(t)$ during the payload motion varying the optimal control parameters: 50% increase of K_1 (top), 50% increase of K_2 (center), and 50% increase of τ (bottom) for uncontrolled case (black line) and controlled case (blue line)
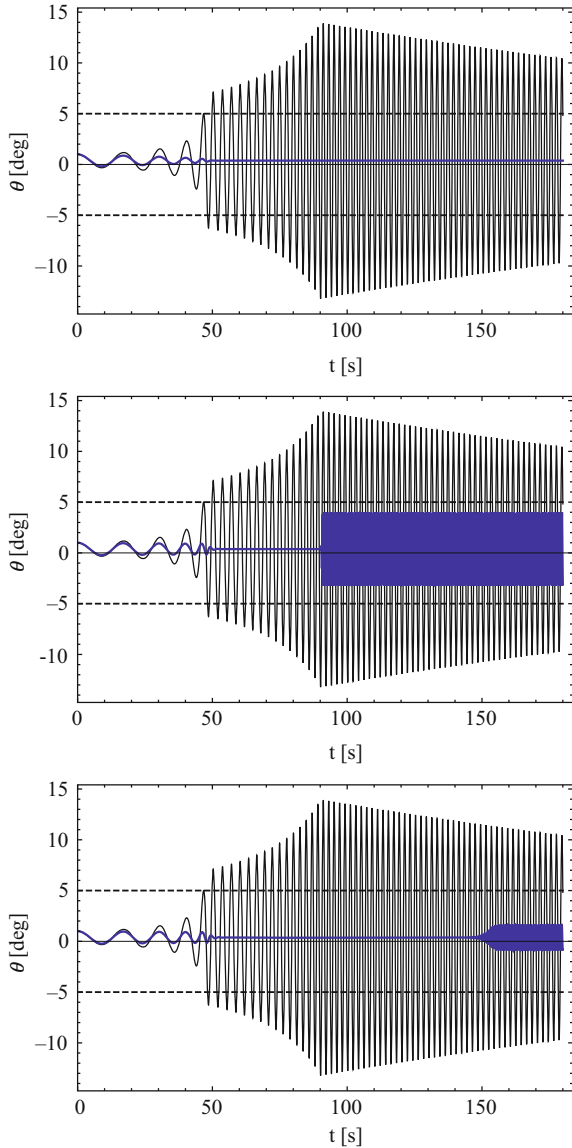
studied by varying the gains K_1 and K_2 and the time delay τ within ±50% of their optimal values. Figure 7 shows that the most sensitive parameters are K_2 and τ whose detuning from their optimal values may lead to the loss of efficiency of the control system.

5 Conclusions

The proposed active feedback control method is shown to be an effective approach for reducing payload oscillations arising from typical helicopter maneuvers. The delayed-feedback control approach may be effectively used to reduce oscillations in sling loads and hoists. Further testing and modeling will be carried out to include a 3D model of the actual controller and a small-scale testing of the control feedback in a drone or advanced computer model. Future work will also estimate the downwash velocity and motion of the helicopter.

References

1. Liu, D. T.: In-flight stabilization of externally slung helicopter loads. USAAMRDL Technical Report 73-5. Northrop Corporation, Electronics Div., Hawthorne (1973)
2. Papanek, M.: Coast guard: Sector Humboldt Bay crews rescue stranded hiker near Klamath Sunday. News Channel (2018). Available: https://www.ntd.tv/2018/06/28/coast-guard-rescues-stranded-hiker-from-bottom-of-300-foot-cliff-in-california/.KRCR
3. Arena, A., Casalotti, A., Lacarbonara, W., Cartmell, M.P.: Dynamics of container cranes: three-dimensional modeling, full-scale experiments, and identification. Int. J. Mech. Sci. **93**, 8–21 (2015)
4. Arena, A., Lacarbonara W., Cartmell, M.P.: Nonlinear interactions in deformable container cranes. P. I. Mech. Eng. C-J. Mec. **230**(1), 5–20 (2016)
5. Cicolani, L.S., Kanning, G.: Equations of Motion of Slung Load Systems with Results for Dual Life. NASA Technical Memorandum 102246. National Aeronautics and Space Administration, Washington, p. 39 (1990)
6. Gera, J., Farmer, Jr., S.W.: A Method of Automatically Stabilizing Helicopter Sling Loads. NASA Technical Note TN D-7593. NASA, Washington (1974)
7. Cicolani, L.S., Ivler, C., Ott, C., Raz, R., Rosen, A.: Rotational stabilization of cargo container slung loads. J. Am. Helicopter Soc. **60**, 042006-1-042006 (2015)
8. Masoud, Z.N., Nayfeh A.H.: Sway reduction on container cranes using delayed feedback controller. Nonlinear Dynam. **34**, 347–358 (2003)
9. Arena, A., Lacarbonara, W., Casalotti, A.: Payload oscillations control in harbor cranes via semi-active vibration absorbers: modeling, simulations and experimental results. Procedia Eng. **199**, 501–509 (2017)
10. Henry, R.J., Masoud, Z.N., Nayfeh, A.H., Mook, D.T.: Cargo pendulation reduction on ship-mounted cranes via boom-luff angle actuation. J. Vib. Control. **7**, 1253–1264 (2001)
11. Anderson J.: Fundamentals of Aerodynamics. McGraw-Hill, New York (2001)
12. Storn, R., Price, K.: Differential evolution a simple and efficient heuristic for global optimization over continuous spaces. J. Global Optim. **11**, 341–359 (1997)

Multi-Objective Optimization of Active Vehicle Suspension System Control

Dong Jing, Jian-Qiao Sun, Chuan-Bo Ren, and Xiu-hua Zhang

Abstract In this chapter, a multi-objective optimal design of delayed acceleration feedback control of an active vehicle suspension system under random excitations is investigated. The simple cell mapping (SCM) method is used to obtain solutions of the multi-objective optimization problem (MOP). The continuous time approximation (CTA) method is applied to analyze the delayed system. Stability is imposed as a constraint for MOP. Three conflicting objective functions are considered. The Pareto set and Pareto front of the optimal feedback control design for the vehicle suspension system are presented. Numerical results have found that the Pareto optimal solutions provide effective control performance of the suspension.

Keywords Active vehicle suspension system · Delayed acceleration feedback control · Multi-objective optimization · Simple cell mapping

1 Introduction

Active vehicle suspension technology has received much attention from the research community for several decades. Suspension system is an assembly of spring and damper that connect the wheels and vehicle body. When a vehicle moves over a bump or pothole, the vertical excitation can transfer to the vehicle body from the road through the suspension. The suspension is designed to isolate the vehicle from the road disturbances [1, 2]. Active and semi-active controls are introduced to

D. Jing (✉) · C.-B. Ren
School of Transportation and Vehicle Engineering, Shandong University of Technology, Zibo, Shandong, China
e-mail: jingvenzhi@163.com

J.-Q. Sun
School of Engineering, University of California Merced, Merced, CA, USA

X.-h. Zhang
Department of Electrical Engineering, Shandong Vocational College of Industry, Zibo, Shandong, China

further improve the performance of the vehicle suspension. This chapter considers a delayed relative acceleration feedback control for active suspensions.

The quarter-car model is commonly used to help design the suspension system, which shares many features with the vehicle suspension system [3, 4]. Semi-active suspension systems with magneto-rheological (MR) and electro-rheological (ER) dampers have been popular [5]. Active suspensions are frequently studied including the ones with feedback optimal controls [6], sliding mode controls [7], and passive optimal controls [8]. We should point out that the literature on passive, semi-active, and active suspensions is vast. The readers interested in the complete review of the literature can find review articles online.

Time delay has been widely considered in vibration control design. Active tuned vibration absorbers with time delay were studied by Olgac and colleagues [9–13]. The positive feedback proportional control using large time delays is reported in [14]. Proper design of feedback controls for active vibration absorbers generally requires a compromise between usually conflicting objectives. Examples include minimizing peak levels of the frequency response, flattening the frequency response over a frequency range, and minimizing the control effort [15]. The work reported in this chapter is an extension of the research in [15].

Multi-objective optimization of passive and active systems has attracted much attention [6, 16, 17]. This chapter presents a multi-objective optimal control of active suspension system with delayed relative acceleration feedback. The simple cell mapping (SCM) method is applied to solve for the MOP [18–21]. The continuous time approximation (CTA) method [22, 23] is used to obtain the response of the delayed system and to analyze the stability and statistics of the responses.

2   The Suspension Model

A vehicle represents a complex vibration system with many degrees of freedom. Common vehicle models include quarter car, half car, and full vehicle models. Quarter-car models have been extensively used for investigating the dynamics of a car suspension, which shares many features with the vehicle suspension system. Figure 1 shows a simplified two-degree-of-freedom quarter-car model of an active suspension system.

The equations of motion of a quarter car are given as follows:

$$m\ddot{x}_1 - c_2(\dot{x}_2 - \dot{x}_1) - k_2(x_2 - x_1) + c_1(\dot{x}_1 - \dot{x}_0) + k_1(x_1 - x_0) + u(t) = 0,$$
$$M\ddot{x}_2 + c_2(\dot{x}_2 - \dot{x}_1) + k_2(x_2 - x_1) - u(t) = 0$$

$$(1)$$

where $u(t) = G[\ddot{x}_1(t - \tau) - \ddot{x}_2(t - \tau)]$ is an active control force consisting of a delayed relative acceleration feedback; M is the sprung mass of the vehicle body; m is the unsprung mass of the wheel; k_1 and c_1 stand for the equivalent coefficients

Fig. 1 A two-degree-of-freedom vehicle suspension system model
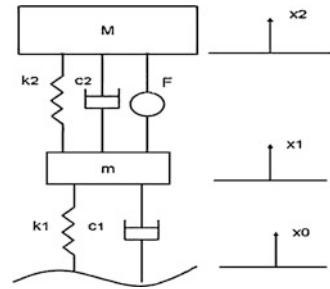
of stiffness and damping of the wheel tire; k_2 and c_2 are the stiffness and damping coefficieints of the suspension system; x_0 denotes the road random roughness; x_1 is the wheel displacement; x_2 is the vehicle body displacement; G is the feedback gain; and τ is the time delay. In this work, we set $c_1 = 0$ due to the damping of the wheel tire is too small. With the acceleration feedback, the delay differential equation of the system is of neutral type.

Define a state vector as $[x_1, \ x_2, \ \dot{x}_1, \ \dot{x}_2]$. The equations of motion can be written in state space form as

$$y = A_0 y + A_t \dot{y}(t - \tau) + G_0 W(t) \tag{2}$$

where

$$A_0 = \begin{bmatrix} 0 & 0 & 1 & 0 \\ 0 & 0 & 0 & 1 \\ -\frac{k_1}{m} - \frac{k_2}{m} & \frac{k_2}{m} & -\frac{c_2}{m} & \frac{c_2}{m} \\ \frac{k_2}{M} & -\frac{k_2}{M} & \frac{c_2}{M} & -\frac{c_2}{M} \end{bmatrix}, \tag{3}$$

$$A_\tau = \begin{bmatrix} 0 & 0 & 0 & 0 \\ 0 & 0 & 0 & 0 \\ 0 & 0 & -\frac{G}{M} & \frac{G}{M} \\ 0 & 0 & \frac{G}{M} & -\frac{G}{M} \end{bmatrix}, \quad G_0 = \begin{bmatrix} 0 \\ 0 \\ \frac{k_1}{m} \\ 0 \end{bmatrix} \tag{4}$$

and $W(t) = k_1 x_0$ is modeled as the Gaussian white noise having the zero mean and the correlation given by

$$E[W(t)W(t+T)] = 2D\delta(T) \tag{5}$$

In the multi-objective design of the feedback control, we shall make use of the system response in both the frequency and time domains.

2.1 Spectral Response

The frequency response matrix of the suspension system is given by

$$H(\omega) = \left[i\omega I - A_0 - i\omega A_\tau e^{-i\omega\tau} \right]^{-1} \tag{6}$$

We can obtain the exact solution of the PSD matrix of the state vector $y(t)$. The PSD matrix of the system response is given by [24]

$$S_{yy}(\omega) = H^*(\omega) G_0 S_{ww}(\omega) G_0^T H^T(\omega) \tag{7}$$

where $H^*(\omega)$ denotes the complex conjugate of the matrix $H(\omega)$.

2.2 Time Domain Response

The dimension of the state space where the state vector $(y(t), y(t - s), 0 < s \leq \tau)$ is defined is infinite. To obtain the response of the system, we apply the continuous time approximation (CTA) method by discretizing the delayed part of the state vector on the mesh $\Omega = \{\tau_i, i = 0, 1, \cdots, M\}$ of $M + 1$ points in $[0, \tau]$ such that $0 = \tau_0 < \tau_1 < \cdots < \tau_{M-1} < \tau_M = \tau$. We define an extended state vector

$$Y(t) = [y_1(t), y_2(t), y_3(t) \ y_3(t - \tau_1), \ldots,$$
$$y_3(t - \tau_M), y_4(t), y_4(t - \tau_1), \cdots, y_4(t - \tau_M)]^T \tag{8}$$

We can show that the extended state vector satisfies a differential equation without time delay. The time domain response and frequency response of $Y(t)$ can be obtained with the conventional analytical and numerical tools.

The accuracy of the CTA as a function of the discretization level M and the ability of the method to predict the eigenvalues and time domain responses are studied in [22, 23]. The theoretical foundation of the method for predicting the right-most eigenvalue of linear time-invariant systems with time delay is well documented in a book by Bellen and Zennaro [25].

3 Multi-Objective Optimization

The multi-objective optimization problem for designing the delayed feedback control can be stated as follows.

Consider the minimization of a vector-valued function.

$$\frac{\min}{k \in Q} \{F(k)\} \tag{9}$$

where $F = [f_1(k), \cdots, f_p(k)]$ is the map that consists of the p objective functions and $f_i : Q \to R^1, k \in Q \subset R^q$ is a q-dimensional vector of design parameters. The domain $Q \subset R^q$ can in general be expressed in terms of inequality and equality constraints.

In this study, we have the design parameters as

$$k = [G, \tau] \tag{10}$$

where G is the feedback gain, and τ is the feedback time delay. The design space is to be described later.

In this chapter, the following three objective functions are considered.

The first objective function is the peak value of the PSD function of the displacement response of the vehicle body

$$f_1(k) : S_{XX}^{\max} = \frac{\max}{\omega \in R^1} S_{x_2 x_2}(\omega) \tag{11}$$

The second objective function is the following integration of the power spectral density (PSD) function $S_{x_2 x_2}(\omega)$ of the displacement response of the vehicle body

$$f_2(k) : \overline{S}_{XX} = \int_{\omega_1}^{\omega_2} S_{x_2 x_2}(\omega) \, d\omega \tag{12}$$

where ω_1 and ω_2 denote the frequencies corresponding to the two resonant peaks of the PSD function.

The third objective function represents the input energy of the delayed feedback control given by

$$f_3(k) : \overline{S}_{uu} = \int_0^\infty S_{uu}(\omega) \, d\omega \tag{13}$$

where $S_{uu}(\omega)$ is the power spectral density function of the delayed feedback control.

Here, $\overline{S}_{XX}$ would be in conflict with $\overline{S}_{uu}$ and $S_{XX}^{\max}$, while the relationship between $\overline{S}_{uu}$ and $S_{XX}^{\max}$ can be more complicated from the physics point of view.

The simple cell mapping (SCM) method is used to solve the above MOP. The cell mapping methods describe system dynamics with cell-to-cell mappings by discretizing both the state space and time [18–21].

In this chapter, the SCM method is used to obtain the Pareto optimal solutions for the delayed feedback control design. For more details of the SCM method for MOP, the reader is referred to the references cited above.

4   Numerical Results

We consider the multi-objective optimal control of active suspension system with the delayed relative acceleration feedback. The design space for the parameters $k = [G, \tau]$ is chosen as follows:

$$Q = \left\{ k \in R^2 | G \in [0, 200], \quad \tau \in \left[0, 2.0\right], \quad \text{subject to Re} \left(\lambda(k)\right)_{\max} < -\varepsilon \right\}$$
(14)

where $\text{Re}(\lambda(k))_{\max}$ represents the largest real part of the eigenvalues of the extended state matrix obtained with the CTA method, and $\varepsilon > 0$ is a small positive number to provide the robustness of stability. The parameters of the vehicle suspension system are $m = 30$, $M = 330$, $c_1 = 0$, $c_2 = 6000$, $k_1 = 30,000$, $k_2 = 1500$, and $\varepsilon = 0.0001$. The discretization of the time delay for the CTA method is $M = 8$. The number of divisions of both the design parameters is chosen to be 50. The computations of the example are conducted in Matlab on a laptop PC.

The Pareto set and Pareto front of the multi-objective optimal design of the active suspension are shown in Figs. 2 and 3. The Pareto set presents a variety of multi-objective optimal feedback control designs compromising the three objectives.

Figure 4 shows the response PSD of the vehicle body and the wheel with and without the delayed acceleration feedback control when the peak value $f_1(k)$ of the PSD function of the displacement response of the vehicle body is the smallest. This is one extreme design in the framework of MOP.

Figure 5 shows the response PSD of the vehicle body with and without the delayed acceleration feedback control in three cases: (1) when the integration $f_2(k)$ of the PSD function of the displacement response of the vehicle body is the smallest; (2) when the input energy $f_3(k)$ of the control is the smallest, and (3) when the three objective functions are compromised. The control design is known as the knee point.
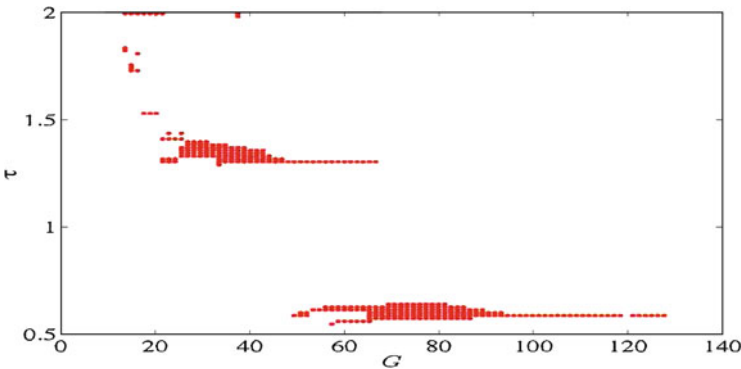
Fig. 2   The Pareto set in the design space for the delayed acceleration feedback control
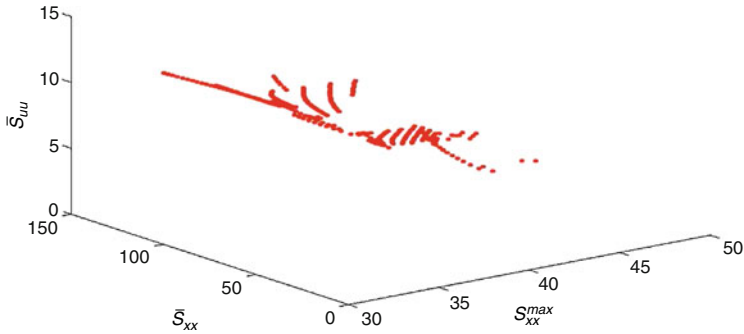
Fig. 3 The Pareto front in the objective space for the delayed acceleration feedback control
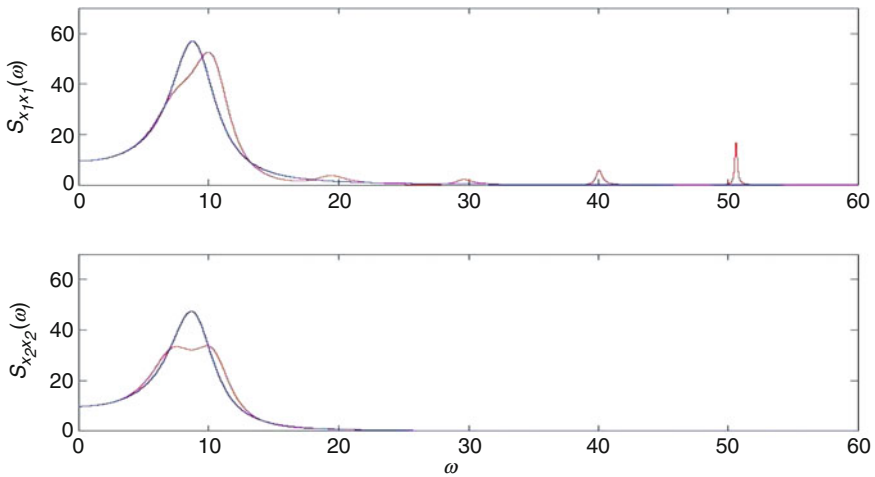
Fig. 4 The response PSD of the vehicle body with and without the delayed feedback control when the peak value of the PSD function of the displacement response of the vehicle body is the smallest

The results presented in the figures indicate that the multi-objective optimal designs of the feedback gain and the delay deliver a range of performances of the suspension and therefore offer engineers more choices in their tuning of the active suspension for vehicles.

5 Concluding Remarks

This chapter presents a multi-objective optimal control design method of an active suspension system with delayed relative acceleration feedback. The Pareto set provides the multi-objective optimal designs representing various compromises of the control objectives, and hence gives engineers more choices in their tuning of the active suspension system for vehicles.
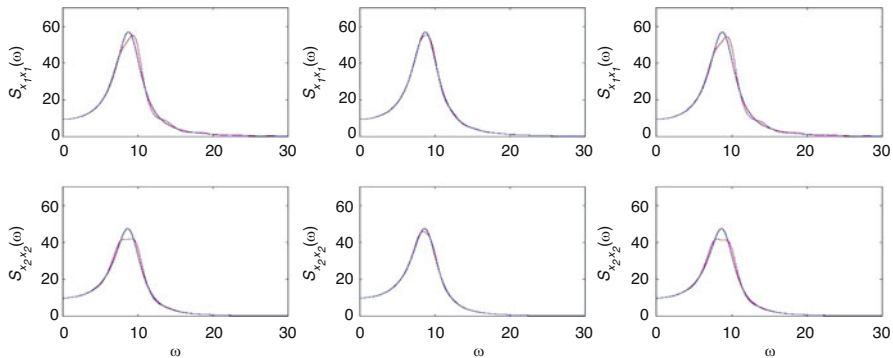
Fig. 5 The response PSD of the vehicle body with and without the delayed feedback control (**a**) shows the response PSD of the vehicle body with and without the delayed feedback control when the integration of the PSD function of the displacement response of the vehicle body is the smallest, (**b**) the input energy of the delayed feedback control is the smallest, (**c**) the three objective functions are compromised

References

1. Yao, J.L., Shi, W.K., Zheng, J.Q., Zhou, H.P.: Development of a sliding mode controller for semi-active vehicle suspensions. J. Vib. Control. **19**(8), 1152–1160 (2013)
2. Xiao, L., Zhu, Y.: Sliding-mode output feedback control for active suspension with nonlinear actuator dynamics. J. Vib. Control. **21**(14), 2721–2738 (2015)
3. Snamina, J., Kowal, J., Orkisz, P.: Active suspension based on low dynamic stiffness. Acta Phys. Polon. A. **123**(6), 1118–1122 (2013)
4. Kim, C., Ro, P.I.: A sliding mode controller for vehicle active suspension systems with non-linearities. Proc. Inst. Mech. Eng, Pt D J. Autom. Eng. **212**(2), 79–92 (1998)
5. Yao, G., Yap, F., Chen, G., Li, W., Yeo, S.: Mr Damper and its application for semi-active control of vehicle suspension system. Mechatronics. **12**(7), 963–973 (2002)
6. Gao, H., Lam, J., Wang, C.: Multi-objective control of vehicle active suspension systems via load-dependent controllers. J. Sound Vib. **290**(3), 654–675 (2006)
7. Sam, Y.M., Osman, J.H., Ghani, M.R.A.: A class of proportional-integral sliding mode control with application to active suspension system. Syst. Control Lett. **51**(3), 217–223 (2004)
8. Goga, V., Kľúčik, M.: Optimization of vehicle suspension parameters with use of evolutionary computation. Proc. Eng. **48**, 174–179 (2012)
9. Olgac, N., Elmali, H., Hosek, M., Renzulli, M.: Active vibration control of distributed systems using delayed resonator with acceleration feedback. J. Dyn. Syst. Meas. Control. **119**(3), 380–389 (1997)
10. Renzulli, M.E., Ghosh-Roy, R., Olgac, N.: Robust control of the delayed resonator vibration absorber. IEEE Trans. Control Syst. Technol. **7**(6), 683–691 (1999)

11. Olgac, N., Elmali, H.: Analysis and design of delayed resonator in discrete domain. J. Vib. Control. **6**(2), 273–289 (2000)
12. Jalili, N., Olgac, N.: A sensitivity study on optimum delayed feedback vibration absorber. J. Dyn. Syst. Meas. Control. **122**(2), 314–321 (2000)
13. Jalili, N., Olgac, N.: Identification and retuning of optimum delayed feedback vibration absorber. J. Guid. Control Dynam. **23**(6), 961–970 (2000)
14. Udwadia, F.E., Phohomsiri, P.: Active control of structures using time delayed positive feedback proportional control designs. Struct. Control Health Monit. **13**(1), 536–552 (2006)
15. Huan, R.-H., Chen, L.-X., Sun, J.-Q.: Multi-objective optimal design of active vibration absorber with delayed feedback. J. Sound Vib. **339**, 56–64 (2015)
16. Maciejewski, I.: Control system design of active seat suspensions. J. Sound Vib. **331**(6), 1291–1309 (2012)
17. Brown, M., Smith, R.E.: Directed multi-objective optimization. Int. J. Comput. Syst. Signals. **6**(1), 3–17 (2005)
18. Hsu, C.S.: A theory of cell-to-cell mapping dynamical systems. J. Appl. Mech. **47**(4), 931–939 (1980)
19. Hernández, C., Naranjani, Y., Sardahi, Y., Liang, W., Schütze, O., Sun, J.-Q.: Simple cell mapping method for multi-objective optimal feedback control design. Int. J. Dyn. Control. **1**(3), 231–238 (2013)
20. Hernández, C., Sun, J.-Q., Schütze, O.: Computing the set of approximate solutions of a multi-objective optimization problem by means of cell mapping techniques. In: EVOLVE—A Bridge Between Probability, Set Oriented Numerics, and Evolutionary Computation IV, pp. 171–188. Springer, Berlin (2013)
21. Naranjani, Y., Hernández, C., Xiong, F.-R., Schütze, O., Sun, J.-Q.: A hybrid algorithm for the simple cell mapping method in multi-objective optimization. In: EVOLVE—A Bridge Between Probability, Set Oriented Numerics, and Evolutionary Computation IV, pp. 207–223. Springer, Berlin (2013)
22. Sun, J.-Q.: A method of continuous time approximation of delayed dynamical systems. Commun. Nonlinear Sci. Numer. Simul. **14**(4), 998–1007 (2009)
23. Sun, J.-Q.: Random vibration analysis of time-delayed dynamical systems. Probab. Eng. Mech. **29**, 1–6 (2012)
24. Sun, J.-Q.: Stochastic Dynamics and Control. Elsevier, Amsterdam (2006)
25. Bellen, A., Zennaro, M.: Numerical Methods for Delay Differential Equations. Oxford University Press, London (2013)

Control Quality Assessment of Nonlinear Model Predictive Control Using Fractal and Entropy Measures

Paweł D. Domański and Maciej Ławryńczuk

Abstract Industry faces the winds of change with the new era of Industry 4.0 paradigm. Systems require flexible and stringent operation on the edge of technological limitations. Process and control quality are closely coupled affecting simultaneously the overall plant performance within such an environment. Nonlinear model predictive control (MPC) is considered as the top quality control strategy used in the most challenging tasks. Control quality assessment of nonlinear MPC is required to supervise and maintain its operation. This work discusses efficiency of control quality non-Gaussian and nonlinear measures applied to nonlinear MPC of a polymerization reactor benchmark.

1 Introduction

Control systems often perform inefficiently. It happens due to the insufficient daily maintenance, process fluctuations, instrumentation failures, inappropriate control structure, poor tuning, varying operating regimes, shortage of experienced personnel, unknown disturbances, human interventions, etc. The tools to assess loop quality are required driving the research on evaluation of the approaches and measures supporting control performance assessment (CPA).

The task of CPA started with the first works on the controllers benchmarking [1]. Research in this area got further interest and popularity with the introduction of the minimum variance measures [2]. Minimum variance benchmark has soon evolved towards other benchmarks, such as the linear quadratic Gaussian (LQG) controller, the proportional integral derivative (PID) controller, and MPC [3]. During the last

P. D. Domański · M. Ławryńczuk (✉)

Institute of Control and Computation Engineering, Warsaw University of Technology, Warsaw, Poland

e-mail: P.Domanski@ia.pw.edu.pl; M.Lawrynczuk@ia.pw.edu.pl

years standard benchmarking methods have been extended with other methods that might be called alternative, using notions of entropy [4], fractals, and Hurst exponent [5]. CPA addresses various control philosophies, such as univariate feedback and feedforward control, unstable and nonminimum phase systems, multivariate multiple-input single-output (MISO), and multiple-input multiple-output (MIMO) cases, varying set-point and cascaded control with further works on MPC [6].

This work addresses the CPA analysis of nonlinear MPC [7] applied to the nonlinear process benchmark. Many different structures of the predictive control technique have attracted CPA research for years. First works applied knowledge-based system for the dynamic matrix control (DMC) algorithm [6]. Further works followed the benchmarking path [8, 9] and model based approaches [10, 11]. Statistical approach was proposed in [12, 13]. The DMC algorithm was assessed in different configurations, i.e., as a single controller or the supervisory level over PID [14, 15].

The nonlinearities require specific quality assessment approach. Review of real process industry data shows that the majority of the considered variables exhibits nonlinear, non-stationary, and non-Gaussian behavior. These facts are reflected by the fat-tailed and/or fractional order [16] properties of the data originating from industrial processes. Following, this work considers not only standard measures, such as Gaussian standard deviation, mean square and absolute error indexes, but also robust measures of Huber standard deviation, least median square error (LMS), scale factor of the α-stable distribution [17], Hurst exponent [18], differential and rational entropies [19]. As the classical PID and simple MPC algorithms have been previously analyzed [20], this work extends the research towards nonlinear MPC control impacted by fat-tailed disturbances. The analysis points out that proposed non-Gaussian methods, i.e., stable distribution dispersion factor, Hurst exponent, or entropy have much higher detectability and robustness against tail fatness of the embedded process disturbances than classical mean square or Gaussian indexes.

2 Problem Formulation

Alternative CPA methods address practical aspects frequently met in process industry. In the last years, many attempts to the nonlinear data analysis not based on the Gaussian assumption have been proposed. Stable statistics, fractal, and entropy measures are the leaders in these approaches [17, 20]. Such methods are appropriate for nonlinear control quality assessment, which MPC often exhibits.

2.1 Fractal Methods for CPA

The Hurst exponent was proposed for CPA and tested for the single-input single-output (SISO) PID control loop [5]. Complex process dynamics frequently brings about multiple scaling exponents in the same range of scales. Observation of

industrial control loops data shows that crossover and multiple scales appear frequently. Thus, the analysis should not be only limited to the single Hurst exponent, but also consider multiple exponents and crossovers. The rescaled range R/S plots are used to investigate multi-persistence. Such analysis reveals dichotomy of scaling behavior that is not predicted by existing simulation models, but detected empirically.

2.2 Entropy Measures

Ideally, it is assumed that the control error signal should not be fluctuating. Hence, its distribution shape should be as narrow as possible. Such shape depicts that uncertainty of the related variable is small, corresponding with the small entropy value. Entropy has been already used in the CPA as control benchmark [4]. Thus, it is natural to investigate the opportunities that are offered by the entropy properties itself. Two different definitions of the continuous-type entropy can be validated ($\gamma\,(x)$ denotes variable distribution, $x \in \mathbb{R}$): the differential entropy

$$H_{\text{diff}} = -\int_{-\infty}^{\infty} \gamma\,(x)\ln\gamma\,(x)\,\mathrm{d}x \tag{1}$$

and the rational entropy

$$H_{\text{rat}} = -\int_{-\infty}^{\infty} \gamma\,(x)\log\left(\frac{\gamma\,(x)}{1+\gamma\,(x)}\right)\mathrm{d}x. \tag{2}$$

2.3 Nonlinear MPC Control

In MPC the values of the process inputs are optimized successively on-line at each sampling instant. The differences between the required set-point trajectory and the predicted values of the process outputs are minimized over the prediction horizon. The algorithm has two important advantages: it can be applied to complex processes with many inputs and outputs and constraints may be imposed on process variables during optimization. Simple linear models are used for prediction in classical MPC algorithms. Unfortunately, in case of nonlinear processes such models cannot be used since they give inaccurate prediction and perform badly in MPC. In the most advanced MPC algorithms nonlinear models are used. On-line successive linearization of a nonlinear model is used to obtain a computationally simple quadratic optimization tasks [7].

3   Simulations

Nonlinear polymerization reactor [21] is used as the simulation benchmark. The initiator flow rate, the monomer flow rate, and the number average molecular weight are process input, disturbance, and output, respectively. Industrial disturbances are seldom Gaussian. Hence, the α-stable noise, exhibiting heavy-tails, is used to address these effects. The following four types of the disturbance signal are considered to check the impact of the tail heaviness on control quality detection:

r00:   normal with small variance generated as α-stable noise: $\alpha = 2.0$, $\gamma = 0.01$,
r20:   normal with large variance generated as α-stable noise: $\alpha = 2.0$, $\gamma = 0.1$,
r16: α-stable noise with the same variance: $\alpha = 1.6$, $\gamma = 0.1$,
r12: α-stable noise with the same variance: $\alpha = 1.2$, $\gamma = 0.1$.

Other two probability distribution function (PDF) factors are set to zero, i.e., $\beta = \delta = 0.0$). Nine scenarios of MPC settings are tested:

Scen0:   the ideal model and tuning parameters: the prediction horizon $N = 10$, the control horizon $N_u = 3$, the weighting coefficient $\lambda = 0.5$,
Scen1:   too short horizons: $N = 2$, $N_u = 1$, ($\lambda = 0.5$),
Scen2:   too long the prediction horizon: $N = 20$ ($N_u = 3$, $\lambda = 0.5$),
Scen3:   too small the weighting coefficient: $\lambda = 0.05$ ($N = 10$, $N_u = 3$),
Scen4:   too large the weighting coefficient: $\lambda = 50$ ($N = 10$, $N_u = 3$),
Scen5:   ideal tuning, but the model with too small gain: $K = 0.5K^{nom}$ (K^{nom} is the nominal gain),
Scen6:   ideal tuning, but the model with too large gain: $K = 2K^{nom}$,
Scen7:   combination of Scen1 and Scen5,
Scen8:   combination of Scen1 and Scen6.

The analysis is performed using the methodology discussed in [20]. It starts with the evaluation of the control error. Time trends for selected (Scen0, Scen1, Scen3, and Scen4) control errors are sketched in Fig. 1. Time series reflect representative
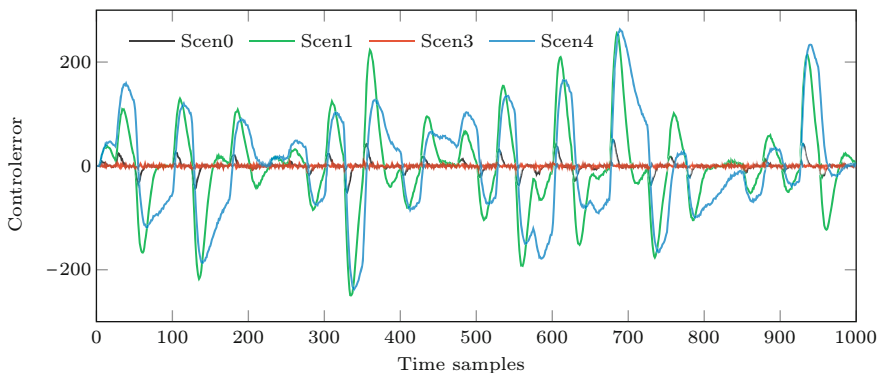
Fig. 1 Time series for selected scenarios with the disturbance variant r00

features. Scen1 leads to poor control, Scen3 results in very good control, while in contrary Scen4 gives sluggish controller behavior. The trends enable to calculate main integral measures of integral square error (ISE), integral absolute error (IAE), and least median square (LMS).

Next, Figs. 2 and 3 depict two example histograms for the scenarios Scen0 and Scen1, respectively, with the disturbance variant r00. Two features that affect further analysis are observed. Firstly, significant fat tails are present. Secondly, worse control quality observed in Scen1 increases both histogram broadness and tail heaviness. More interesting is the fact that despite normal disturbance the control error is no longer Gaussian. It exhibits significant tails introduced by the closed loop operation in the set-point tracking control mode. This observation is somehow in contrary to the popular understanding. A possible explanation is according to the central limit theorem. It is assumed that with the increased number of empirical observations $n \rightarrow \infty$ the distribution should converge towards Gaussian PDF. Unfortunately, it is impossible to find out where one is on the convergence path, which may result in fat tails [22].

Finally, the fractal R/S analysis is carried out and the persistence measures in the form of the Hurst exponent are evaluated. Two examples (the same as for

Fig. 2 Histogram for the scenario Scen0 and the disturbance variant r00
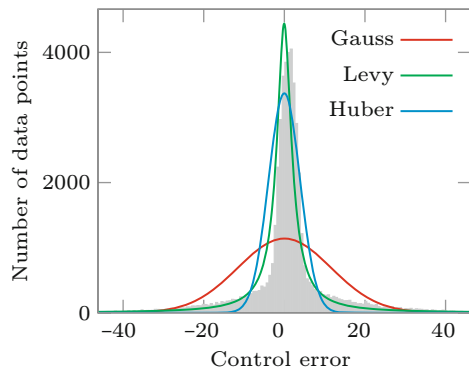
Fig. 3 Histogram for the scenario Scen1 and the disturbance variant r00
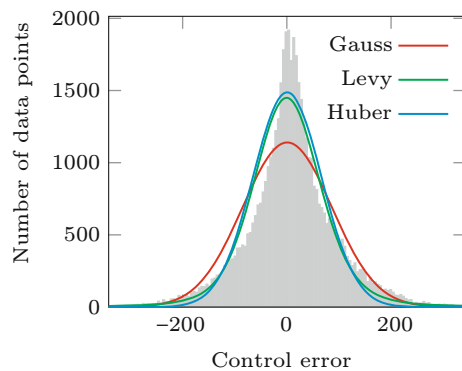
the histograms) are sketched in Figs. 4 and 5 for the scenarios Scen0 and Scen1, respectively, with the disturbance variant r00.

There are two first sight observations. The value of the short memory Hurst exponent which reflects loop dynamics is $H_1 \backsim 0.75$, which is rather quite far away from the literature expectations [5], but it has been already observed in real data. This subject requires further investigation, but one of the hypotheses is that it might be affected by process or data granulation. Nonetheless, the relative relationship between optimal control Scen0 and bad sluggish behavior of the Scen1 is well visible as the $H_1^{\text{Scen0}} < H_1^{\text{Scen1}}$.

Further analysis uses all the data collected for all selected scenarios run for all considered disturbance variants. The first observation is that all the considered indexes are able to detect control quality changes. The detectability for the considered measures is visualized for two examples of the ISE index in Fig. 6 and for the α-stable scale factor γ in Fig. 7. The graphs present relative values for the indexes according to the optimal one in each disturbance variant. One would like to expect that all the bars in each scenario should be of a similar height. It is observed that for classical indexes ISA, IAE, σ_{Gauss} this condition is not fulfilled, while other

Fig. 4 R/S plot for the scenario Scen0 and the disturbance variant r00
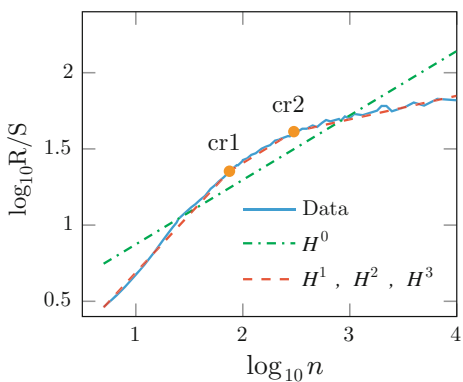
Fig. 5 R/S plot for the scenario Scen1 and the disturbance variant r00
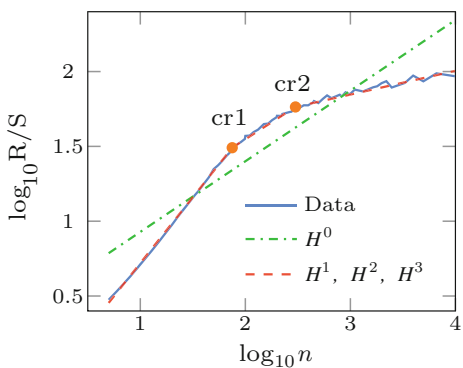
Fig. 6 Detection with the ISE index
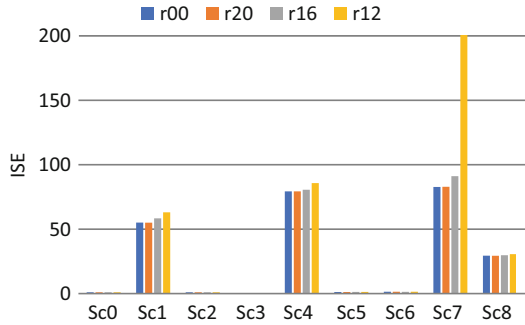
Fig. 7 Detection with the index γ
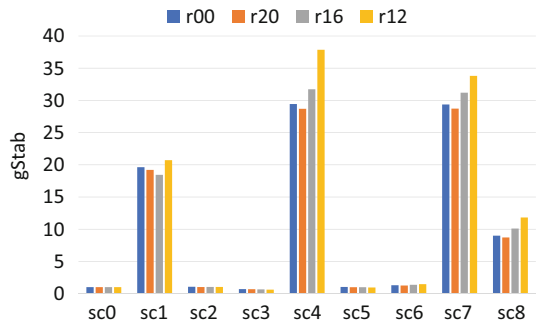
measures behave closer to the expectations. It is mostly visible for α-stable scale factor γ and robust standard deviation σ_{Huber}. The goal should be the ability to detect analog loop properties similarly.

Although all the measures are able to detect imperfect control, they cannot point out the character of poor control. It is achievable with the Hurst exponent (Fig. 8). Hurst exponent relative changes against the optimal one (Scen0) are in close relation to the real loop behavior. It is a constructive feature of the Hurst exponent as it is able to point out the reason and a solution for the loop tuning.

Finally, sensitivity of the measures to the tail index (measured by stability factor α) is analyzed. Figure 9 presents the relative change for each index against disturbance variants for optimal Scen0 and Fig. 10 the same relationship for bad control of Scen1 (normal standard deviation σ_{Gauss} is denoted as sgauss, the α-stable scale factor γ is denoted as gstab, the robust measure in form of the scale M-estimator with logistic psi-function σ_{Huber} is denoted as shuber). ISE, σ_{Gauss}, and both entropies are highly sensitive to the tail index. IAE is more robust, while LMS, γ, and σ_{Huber} indexes are fully robust to the fat tails.
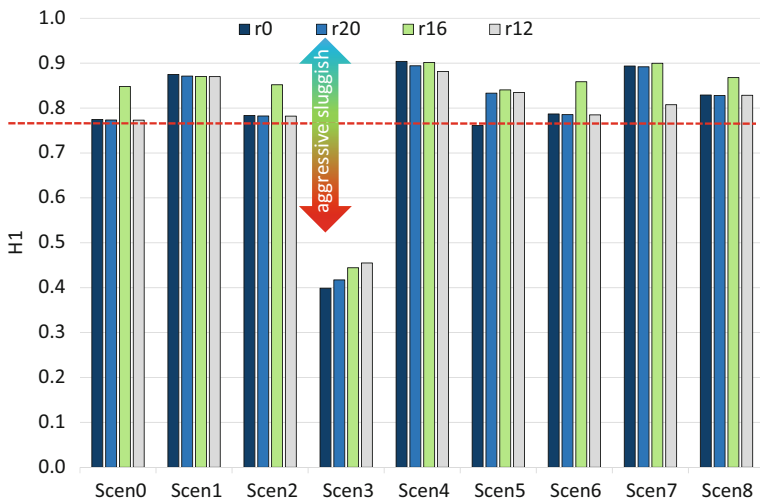
Fig. 8 Detection with the index H_1

Fig. 9 The impact of fat tails for the scenario Scen0
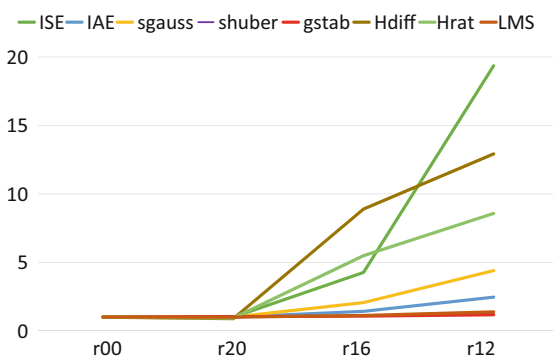
Fig. 10 The impact of fat tails for the scenario Scen1
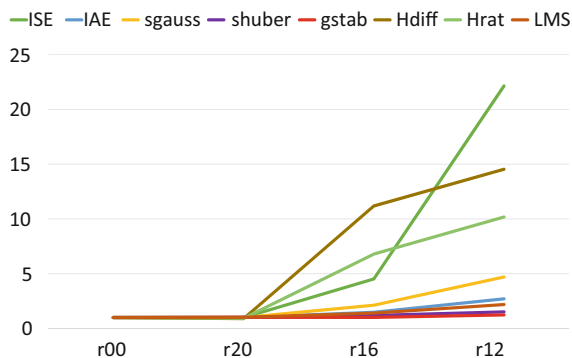
4 Conclusions

The analysis of the nonlinear MPC simulations results brought a few main observations. First of all, the control error signal, which is the basis for the CPA, exhibits fat tails despite the normal character of disturbances. All considered indexes are able to detect degradation of control quality, although they are unable to show how far the MPC tuning parameters are from the optimal ones. Moreover, they are unable to point out the reason for mistuning, i.e., control sluggishness or aggressiveness. Hurst exponent, as the only one, is able to show the character of poor control (sluggishness versus aggressiveness). It is shown that α-stable dispersion γ, robust standard deviation σ_{Huber}, and LMS are the most reliable and robust against the fat tails. On the other hand, MSE and normal standard deviation are sensitive to the fat tails, disabling the assessment.

References

1. Åström, K.J.: Computer control of a paper machine–an application of linear stochastic control theory. IBM J. **11**, 389–405 (1967)
2. Harris, T.: Assessment of closed loop performance. Can. J. Chem. Eng. **67**, 856–861 (1989)
3. Jelali, M.: Control Performance Management in Industrial Automation: Assessment, Diagnosis and Improvement of Control Loop Performance. Springer, London (2013)
4. Meng, Q.W., Fang, F., Liu, J.Z.: Minimum-information-entropy-based control performance assessment. Entropy **15**, 943–959 (2013)
5. Srinivasan, B., Spinner, T. Rengaswamy, R.: Control loop performance assessment using detrended fluctuation analysis (DFA). Automatica **48**, 359–1363 (2012)
6. Schäfer, J., Cinar, A.: Multivariable MPC system performance assessment, monitoring, and diagnosis. J. Process Control **14**, 113–129 (2004)
7. Ławryńczuk, M.: Computationally Efficient Model Predictive Control Algorithms: A Neural Network Approach. Springer, Cham (2014)
8. Sotomayor, O.A.Z., Odloak, D.: Performance assessment of model predictive control systems. IFAC Proc. Vol. **39**, 875–880 (2006)
9. Zhao, C., Zhao, Y., Su, H., Huang, B.: Economic performance assessment of advanced process control with LQG benchmarking. J. Process Control **19**, 557–569 (2009)
10. Carelli, A.C., da Souza Jr, M.B.: GPC controller performance monitoring and diagnosis applied to a diesel hydrotreating reactor. IFAC Proc. Vol. **42**, 976–981 (2009)
11. Sun, Z., Qin, S.J., Singhal, A., Megan, L.: Performance monitoring of model-predictive controllers via model residual assessment. J. Process Control **23**, 473–482 (2013)
12. Badwe, A.S., Gudi, R.D., Patwardhan, R.S., Shah, S.L., Patwardhan, S.C.: Detection of model-plant mismatch in MPC applications. J. Process Control **19**, 1305–1313 (2009)
13. Chen, J.: Statistical Methods for Process Monitoring and Control. McMaster University, Hamilton (2014)
14. Danesh Pour, N., Huang, B., Shah, S.L.: Performance assessment of advanced supervisory-regulatory control systems with subspace LQG benchmark. Automatica **46**, 1363–1368 (2010)
15. Khan, M., Tahiyat, M., Imtiaz, S., Choudhury, M.A.A.S., Khan, F.: Experimental evaluation of control performance of MPC as a regulatory controller. ISA Trans. **70**, 512–520 (2017)
16. Liu, K., Chen, Y.Q., Domański, P.D., Zhang, X.: A novel method for control performance assessment with fractional order signal processing and its application to semiconductor manufacturing. Algorithms **11**, 90 (2018)

17. Domański, P.D., Ławryńczuk, M.: Assessment of the GPC control quality using non-Gaussian statistical measures. Int. J. Appl. Math. Comput. Sci. **27**, 291–307 (2017)
18. Domański, P.D.: Non-Gaussian and persistence measures for control loop quality assessment. Chaos: An Interdisciplinary J. Nonlinear Sci. **26**, 043105 (2016)
19. Chen, L.J., Zhang, J., Zhang, L.: Entropy information based assessment of cascade control loops. In: Proceedings of the International Multi Conference of Engineers and Computer Scientists, IMECS (2015)
20. Domański, P.D., Ławryńczuk, M.: Assessment of predictive control performance using fractal measures. Nonlinear Dyn. **89**, 773–790 (2017)
21. Maner, B.R., Doyle, F.J., Ogunnaike, B.A., Pearson, R.K.: Nonlinear model predictive control of a simulated multivariable polymerization reactor using second-order Volterra models. Automatica **32**, 1285–1301 (1996)
22. Taleb, N.N.: Real-World Statistical Consequences of Fat Tails: Papers and Commentary, Technical Incerto Collection. STEM Academic, Rockville (2018)

Impact of the Controller Algorithm on the Effect of Motor Vehicle Steering During a Lane-Change Manoeuvre

Mirosław Gidlewski (iD)**, Leszek Jemioł** (iD)**, and Dariusz Żardecki** (iD)

Abstract The automation of the lane-change manoeuvre by using an active steering system is a fundamental problem of the automation of controlling a vehicle driven at a high speed. The algorithm of controlling the steering system during the lane change as proposed herein is the result of optimizing the control process by means of a reference model for the dynamics of vehicle motion with various degrees of simplification. The algorithm includes the determination of time-optimal reference curves describing the control input signal (a "bang-bang" type reference signal of the steering wheel angle) and the vehicle's linear and angular "responses" describing its trajectory. The predefined vehicle trajectory signals are implemented in a regulation process based on two Kalman's regulators, which ensure the follow-up process to be optimized in terms of the "linear-quadratic problem". The regulation loops can be switched on in different modes. Simulation test results, reflecting the functioning of such a control system with using various reference signal models and various regulators' operation modes, prove the direction of the engineering works to be correct.

Keywords Controller algorithm · Lane-change models · Simulation studies

M. Gidlewski (✉)
Automotive Industry Institute (PIMOT), Warsaw, Poland

University of Technology and Humanities (UTH), Radom, Poland
e-mail: miroslaw.gidlewski@uthrad.pl

L. Jemioł
University of Technology and Humanities (UTH), Radom, Poland

D. Żardecki
Automotive Industry Institute (PIMOT), Warsaw, Poland

Military University of Technology (WAT), Warsaw, Poland

157

1   Introduction

Numerous research centres are engaged in works on systems to automate the road manoeuvres of motor vehicles. The manoeuvres performed with high speeds (e.g., obstacle avoidance or overtaking) are particularly difficult for automation because of the requirement to control an object whose dynamics is non-linear, unstable and sensitive to parameter changes and whose trajectory is subject to tight limitations. Usually, road manoeuvres may be treated as a sequence of elementary lane changes. Therefore, the automation of the lane change is a fundamental problem of the automation of steering a motor vehicle.

The algorithms of controlling the steering wheel angular motion during the lane-change manoeuvre are usually based on the concept of tracking system, where the controller includes a generator of reference signals defining the vehicle motion in the road plane and regulators correcting the control signal so that the actual vehicle trajectory is close to the reference (prescribed) trajectory. In many publications, an assumption is made a priori that the reference vehicle trajectory is to be a heuristic composition of smooth elementary functions, e.g., sinusoid segments [1–4]. Similarly, the regulator algorithm forms are a priori assumed, e.g., as PID or MPC [5–7]. In authors' works, both algorithms of the reference signal generator and correcting regulators have been the results of a formal optimization carried out with using simplified reference models of vehicle motion lateral dynamics. Of course, such conceptual control system has to be verified in extensive simulation investigations by using a very detail model of vehicle motion as a virtual object of a control. These works have been reported in many authorial publications, e.g. [8–10].

The set point signals generated can be based on reference models with various degrees of simplifications. Also various regulation loop switching-on modes can be used in the algorithm of the controller. These research threads are subjects of this chapter which presents fragments of unpublished simulation investigations.

2   Controller Algorithms

The process of changing the lane by a car travelling at a constant speed on a straight road can be described using three variables: one "input signal"—steering system wheel angle $\delta_H(t)$ and two "output signals"—position of the centre of vehicle mass relative to the centre line of the road (lateral shift) $Y(t)$ and angular position of the vehicle body relative to centre line of the road (yaw angle) $\psi(t)$. The course $\delta_H(t)$ that minimizes the manoeuvring time should generally be of the "bang-bang" type, and the control process can be divided into two successive phases, i.e., transposition and stabilization. This concept (Fig. 1) is in line with experiences of drivers and can be confirmed by the control theory relating to time-optimized systems. It should be noted that when an obstacle suddenly arises, the driver turns the steering wheel

Fig. 1 The general concept of "bang-bang"-type steering (here the most sharp form of the steering signal) and time decomposition of lane change control [8]
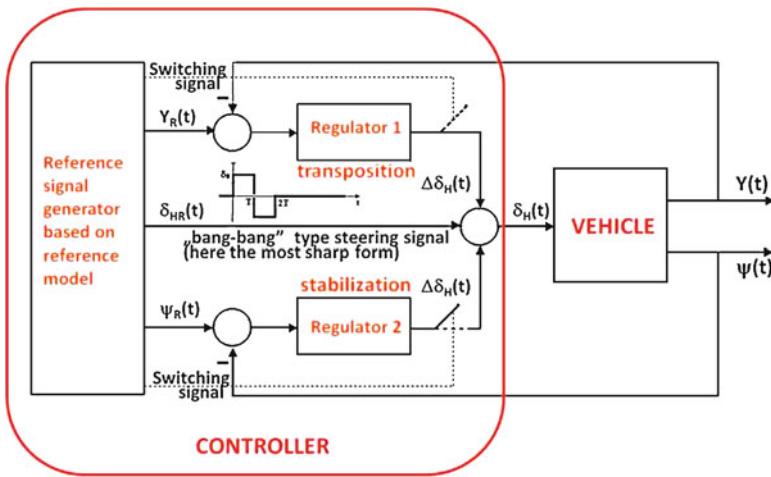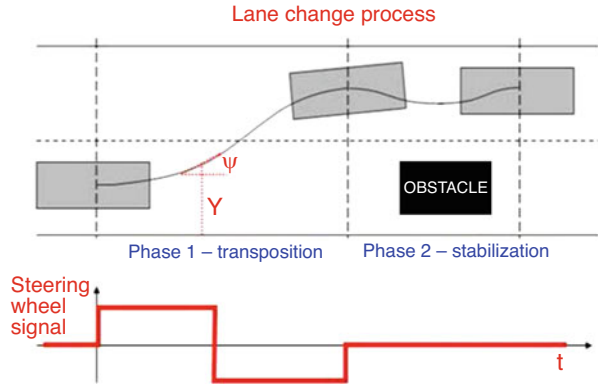
Fig. 2 Block diagram of the automatic control system [9]

violently, first looking for the good lateral displacement of the vehicle and ultimately improving the angular position of the vehicle.

The structure of the authors' control system resulting from this general concept is expressed in a block diagram (Fig. 2).

The reference signals—the steering wheel angle $\delta_{HR}(t)$ as well as its responses—the lateral displacement $Y_R(t)$ and vehicle yaw angle $\Psi_R(t)$ are planned and generated on the basis of an assumed reference model describing the lateral vehicle dynamics. Because the reference model must be efficient for online computations, its mathematical form must be simplified enough (here linearized "bicycle model" expressed by transfer functions). Note also that formal optimization of $\delta_{HR}(t)$ due to minimization of the time of the lane change process requires extremely reduced model. In this case, using Pontriagin's maximum principle, $\delta_{HR}(t)$ is calculated in the most sharp "bang-bang" type form describable analytically by adopted

parameters of the car and the lane-change. Of course, to get satisfactory input and output signals $\delta_H(t)$, $Y(t)$, $\psi(t)$ in a real vehicle controlled, the reference signal $\delta_{HR}(t)$ needs a correction by signals $\Delta\delta(t)$ from two regulators based on error signals $Y_R(t) - Y(t)$ (regulator 1) and $\Psi_R(t) - \Psi(t)$ (regulator 2). For analytical synthesis of the regulators' algorithms, the control task should be formulated to the SISO (single-input single-output) object. So, according to this concept, the $\Delta\delta(t)$ correction signal comes from only one regulator, and the regulation loops are switched on sequentially: in the transposition phase—the regulator 1 to minimize the error $Y_R(t) - Y(t)$, and then in the stabilization phase—the regulator 2 to minimize the error $\Psi_R(t) - \Psi(t)$. Such a decomposition of the regulation task seems to be not only in line with experience of drivers but is very beneficial for synthesis effective regulators' algorithms. Using Kalman's control theory of optimal linear-quadratic systems associated with SISO models, we obtain algorithms in fully analytical forms whose parameters depend on the parameters of the reference model.

The concept of synthesis of controller's algorithms (reference signal generator for $\delta_{HR}(t)$, $Y_R(t)$, $\Psi_R(t)$, as well as both regulators for $\Delta\delta(t)$) is expressed in Fig. 3. Details are presented in Ref. [8].

A special feature of the developed controller algorithm is an analytical linking of its parameters with the parameters of the reference model and lane-change description. So, by changing the parameters like Y_0, V, $\ldots$, the controller can change its parameters like δ_0, T, $\ldots$ automatically.

Some detail assumptions of the algorithm shown in Fig. 3 which have been introduced to simplify its analytical synthesis can be modified very easily. Two modifications are presented in this chapter:

1. Modification of the reference model in the signal generator:

    Here, the model extremely reduced (where the transmittances $G_{Y\delta}(s)$ and $G_{\psi\delta}(s)$ contained only integrating members with gains) is replaced by the linearized "bicycle model" (with $G_{Y\delta}(s)$ and $G_{\psi\delta}(s)$ more developed).
2. Modification of the method of switching control loops:

    Here, some earlier activation of regulator 2 is allowed and/or to shorten or extend an operating time of the regulator 1. In this case, correction action can be described as follows (see also Fig. 4):

$$\delta_H(t) = \delta_{HR}(t) + \Delta\delta_{H1}(t) \cdot f_1(t) + \Delta\delta_{H2}(t) \cdot f_2(t) \tag{1}$$

$$\Delta\delta_{H1}(t) = L^{-1} \left(R_1(s) \left(Y_R(s) - Y(s) \right) \right) \tag{2}$$

$$\Delta\delta_{H2}(t) = L^{-1} \left(R_2(s) \left(\psi_R(s) - \psi(s) \right) \right) \tag{3}$$

$$f_1(t) = 1(t) - 1\,(t - T_1) \tag{4}$$

INITIAL MODEL (standard approach):
    Classic "bicycle model" equations (in local coordinates (x,y))
    + Transformation equations (to global coordinates (X,Y))

Linearization
Laplace transformation
Transfer functions $G_{Y\delta}(s)$, $G_{\psi\delta}(s)$

REFERENCE MODEL - Reduced transfer functions

REFERENCE SIGNAL GENERATOR based on reduced transfer functions

CONTROL SYSTEM based on reduced transfer functions

$$\delta_H(s)=p\cdot\delta(s), \quad \delta(s)=\delta_R(s)+\Delta\delta(s)$$

For transposition state (t≤2T) $\Delta\delta(s)=Reg_1(s)(Y_R(s) - Y(s))$
                                        $Y_R(s)= G_{Y\delta}(s)\cdot\delta_R(s)$
For stabilization state (t>2T) $\Delta\delta(s)=Reg_2(s)(\psi_R(s) - \psi(s))$
                                        $\psi_R(s)= 0$

$Reg_1(s)$, $Reg_2(s)$ – transfer functions of Kalman's regulators (their structures
and parameters result from reference model)

Fig. 3 The concept of the lane-change control system synthesis [10]

$$f_2(t) = 1\,(t-T_2) \tag{5}$$

where

$\Delta\delta_{H1}(t)$, $\Delta\delta_{H2}(t)$—signals from the regulators 1 and 2

Fig. 4 Interpretation of functions $f_1(t), f_2(t)$
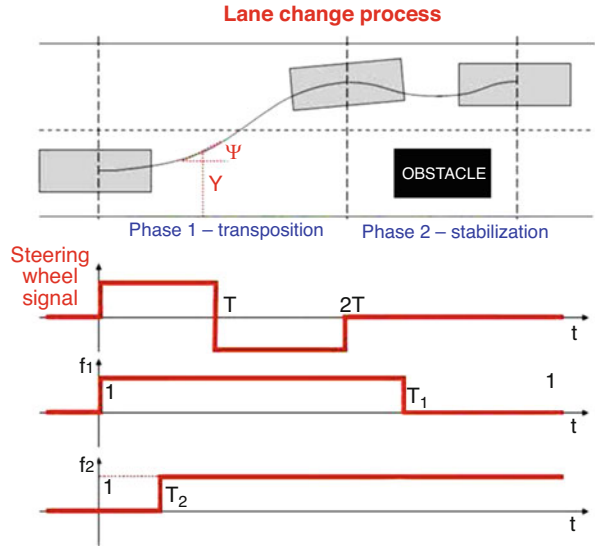
$f_1(t), f_2(t)$—control functions expressing switching on/off of regulation loops
$1(t)$—Heaviside function
T_1, T_2—time parameters

These two modifications require simulation investigation. Representative results
are presented in Sect. 3.

3 Simulation Investigations

The examination of the control system proposed was based on simulation tests
where the controller model controlled a model describing in detail the motion of
a real motor vehicle during a lane-change manoeuvre. The virtual steered object
used in the tests was an authorial 3D multi-body non-linear mathematical model
of the dynamics of motion of a two-axle motor truck of medium load capacity,
with 20 degrees of freedom. Prior to the simulations, the model was thoroughly
experimentally verified during both rig and road tests, carried out in various
conditions, extremely difficult inclusive. Since the simulation tests were to result
in thorough assessment of the impact of changes in model parameters on the vehicle
motion, the calculations were repeated for many datasets describing the controller,
vehicle, and road conditions (including those defined as "difficult"). To deepen the
comparative analysis of the simulation results for different variants of the data,
special integral indicators were introduced. The general idea of simulation-based
investigations has been illustrated in Fig. 5.
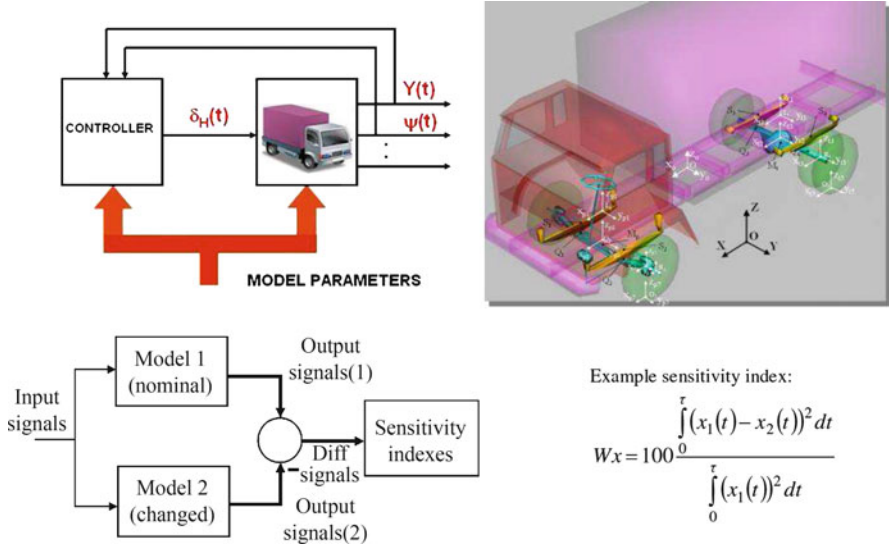
Fig. 5 The concept of sensitivity studies based on simulation investigations

By changing model equations or parameters, we can observe their influence on the results of simulations. The method is very useful for validating our lane-change control system. In this case, the models "1" and "2" are activated by the same signal $\delta_{HR}(t)$ from the reference signal generator. Here the most important indexes are $W_{\delta H}$, W_Y and W_ψ.

Simulation investigations presented in this chapter concern the two types of modifications of the controller algorithm. Representative results of simulation are shown in Fig. 6. Here the modifications of the method of switching control loops concern the situation when regulators work "in series" ($T_1 = T_2$) and $T_1, T_2 \subset \{1.2T, 1.5T, 2T\}$.

In these tests the parameters of the virtual lorry are identical. The simulated lane-change manoeuvre refers to quit difficult traffic conditions ($V = 70$ km/h, friction coefficient $\mu = 0.3$). Also, parameters of the reference signal $\delta_{HR}(t)$ ($\delta_{H0} = 54.7^o$, $T = 1.01$ s) as well as parameters of regulators are unchanged.

Example values of the indexes presented in Table 1 have been calculated on the assumption that Model 1 (nominal) corresponds to the simplest version of the controller (when the signal generator reference model is based on the most reduced model) while Model 2 (changed) corresponds to the more sophisticated model of the controller (when the reference signals are generated on the linearized bicycle model). The calculations have been repeated for $T_1, T_2 \subset \{1.2T, 1.5T, 2T\}$), ($T_1 = T_2$).
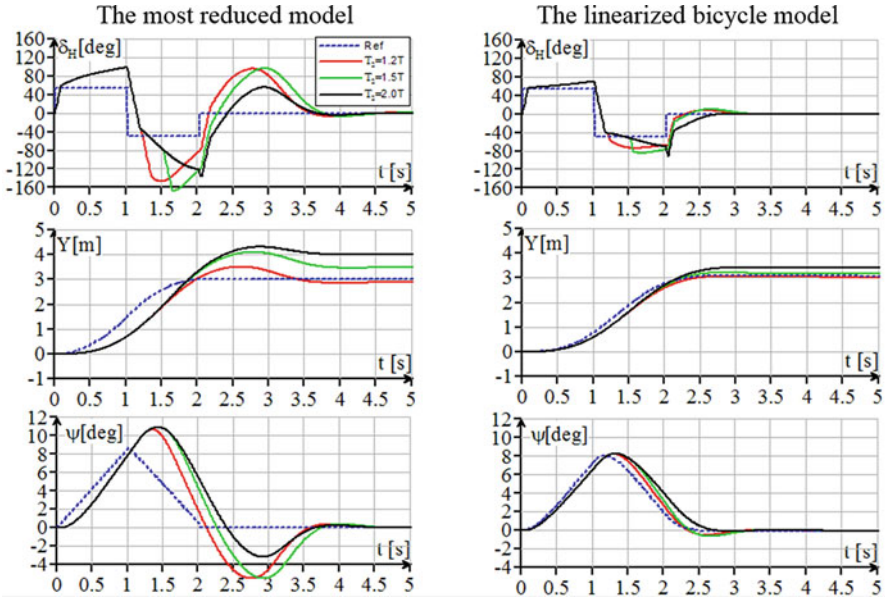
Fig. 6 Example of result simulations

Table 1 Values of sensitivity indexes for different T_2

T_2	$W_{\delta H}$ (%)	W_Y (%)	W_Ψ (%)
1.2 T	33.1	1.2	20.5
1.5 T	32.3	3.2	18.8
2.0 T	21.2	3.4	10.4

4   Conclusions

The investigation results show the complexity of the dynamic properties of the vehicle and confirm the advantages of the automatic control solutions adopted. The regulators used in the controller, correcting the reference "bang-bang" control signal generated, were confirmed to be effective. For the reference curves obtained from the extremely simplified vehicle model, the time and distance of avoiding the obstacle by the truck were shorter, but with excessive steering wheel turning angle and velocity applied by the regulator. In the case of such a reference model, the instant of switching on the regulator in the stabilization loop is important for the vehicle trajectory. The use of the more complicated vehicle model for the generation of reference signals resulted in a minor growth in the time and distance needed for avoiding the obstacle, but the steering wheel rotation was far less intensive, its velocity and angle values were far lower than those obtained for the extremely simplified model, and the vehicle trajectory was stabilized almost immediately. The impact of the instant of switching on the regulator was insignificant in this case. Modifications of the switching on/off procedures seem to be important when the reference model has the most reduced form.

References

1. Anderson, S.J., Peters, S.C., Pilutti, T.E., Iagnemma, K.: An optimal-control-based framework for trajectory planning, threat assessment, and semi-autonomous control of passenger vehicles in hazard avoidance scenarios. Int. J. Veh. Autonom. Syst. **8**(2), 190–216 (2010)
2. Katrakazas, C., Quddus, M., Chen, W.-H., Deka, L.: Real-time motion planning methods for autonomous on-road driving: state-of-the-art and future research directions. Transport. Res. Pt C Emerg. Technol. **60**, 416–442 (2015)
3. Korzeniowski, D., Ślaski, G.: Method of planning reference trajectory of a single change maneuver with Bezier curve. IOP Conference Series: Materials Science and Engineering, vol. 148 (2016), Paper Number 012012
4. Moshchuk, N., Chen, S-K., Zagorski, C., Chatterjee, A.: Path planning for collision avoidance maneuver. Proceedings of the ASME 2013 International Mechanical Engineering Congress and Exposition IMECE'2013 San Diego, California, USA (2013)
5. Gao, Y., Lin, T., Borrelli, F., Tseng, E., Hrovat, D.: Predictive control of autonomous ground vehicles with obstacle avoidance on slippery roads. Dyn. Syst. Control Conf. (2010)
6. Liu, K., Gong, J., Chen, S., Chen, H.: Model predictive stabilization control of high-speed autonomous ground vehicles considering the effect of road topography. Appl. Sci. **8**(5), 822 (2018)
7. Park, J.M., Kim, D.W., Yoon, Y.S., Kim, H.J., Yi, K.S.: Obstacle avoidance of autonomous vehicles based on model predictive control. Proc. Inst. Mech. Eng. Pt D J. Autom. Eng. **223**, (2009)
8. Gidlewski, M., Żardecki, D.: Automatic control of steering system during lane change. Proceedings of 24th ESV International Technical Conference, Gothenburg, Sweden (2015). Paper No 15-0106. http://nhtsa.gov/ESV
9. Gidlewski, M., Żardecki, D.: Linearization of the lateral dynamics reference model for the motion control of vehicles. Mech. Res. Commun. **82**, 49–54 (2017)
10. Gidlewski, M., Jemioł, L., Żardecki, D.: Selected problems of automatic obstacle avoiding. Published IOP Conference Series: Materials Science and Engineering, vol. 421 (2018), Paper Number 032009

Fractional Order Impedance Control

**Guangrong Chen, Sheng Guo, Bowen Hou, Junzheng Wang,
and Xiangyang Wang**

Abstract This paper proposes a novel fractional order impedance control. An integral item is added into the traditional impedance model to eliminate the tracking error and the idea of fractional order is introduced to make the orders of inertia, damping, and stiffness are no longer only integers to achieve more significant compliant performance. Simulation results validate the advantages and proposed impedance control can be employed to absorb, hold, and dissipate system energy. It provides an insight for robot dynamic interaction, bouncing, and jumping control.

Keywords Fractional order · Impedance control · Compliance control · Stability analysis

1   Introduction

Impedance control is an effective way to detail with robotic environmental interaction [1]. But as for the traditional impedance model, a second-order system [2], there exists a tracking error in robotic end-effector, which results in a bad track performance of robots in handling tasks. In this paper, an integral item is added to eliminate the tracking error.

It has been studied that fractional order PID can achieve more significant control performance than traditional PID [3]. In order to improve the compliant performance, the traditional impedance model is transferred to fractional order

G. Chen (✉) · S. Guo · X. Wang
Robotics Research Center, Beijing Jiaotong University, Beijing, China
e-mail: cgr2012@foxmail.com

B. Hou
Beijing Engineering and Technology Research Center of Rail Transit Line Safety and Disaster Prevention, Beijing, China

J. Wang
State Key Laboratory of Intelligent Control and Decision of Complex Systems, School of Automation, Beijing Institute of Technology, Beijing, China

impedance model by setting the orders of inertia, damping, and stiffness as fractions by taking the advantages of fractional order [4].

In fact, a robotic leg can be equivalent to a hopper [5]. For simple, a vertical hopper actuated by hydraulic cylinder was taken as a research subject here.

2 System Model

The system model is shown in Fig. 1. The vertical hopper simulation model, vertical hopper model, and vertical hopper equivalent model are shown in Fig. 1a, b, and c, respectively. M is the lumped mass of the system; L is total length of hydraulic bouncing system; L_c is the length of cylinder; L_s is the length of spring; L_f is the length of foot; H is the falling height; K_s is the stiffness of passive spring, which can be taken as the stiffness of environment ($\frac{K_e K_s}{K_e + K_s}$) for the cylinder when the touch terrain is rigid, which means $K_e = \infty$; x is the motion displacement of lumped mass; K_c, D_c is the actual stiffness and damping of the active hydraulic cylinder system, respectively; F_c is the control force produced by hydraulic cylinder; F_e is the contact impact force, which almost equals to the force F_s produced by passive spring and $F_s = K_s \Delta L_s$, where ΔL_s represents the compression of passive spring caused by contact impact.

3 Fractional Order Impedance Control

3.1 Fractional Order

The overall structure of a FOPID controller is given as

$$C_{\text{FOPID}} = K_P + K_I s^{-\lambda} + K_D s^{\mu}. \tag{1}$$

Fig. 1 The system model. (**a**) The vertical hopper simulation model. (**b**) The vertical hopper model. (**c**) The vertical hopper equivalent model

(a)   (b)   (c)
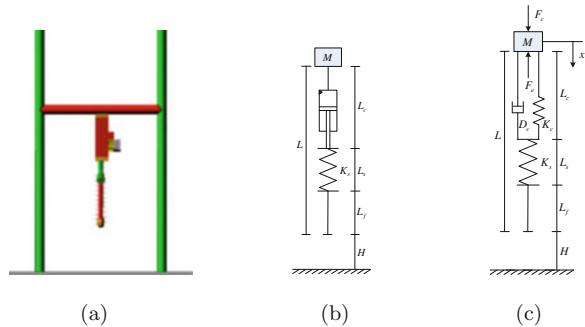
Compared with PID controllers, there are two more tuning parameters: λ and μ, in FOPID scheme ($PI^\lambda D^\mu$). λ and μ are positive and real numbers. In fact, they have been added to the classical PID controllers to make a compromise between the advantages and disadvantages of the integer-order integral and derivative parts, and make the controller design more flexible. Since this paper focuses on fractional order, the details about parameters tuning and stability analysis of FOPID, which can be found in [4], are omitted here.

3.2 Impedance Control

The diagram of position/force based active compliance controller is illustrated in Fig. 2, where $\mathbf{x}_d \in \mathbb{R}^n$ is desired displacement; $\mathbf{x} \in \mathbb{R}^n$ is actual displacement; $\mathbf{x}_r \in \mathbb{R}^n$ is required displacement; $\mathbf{x}_e \in \mathbb{R}^n$ is displacement caused by the environment. The impedance model Z_f is utilized to shape the relationship between contact force $\mathbf{F}_e$ and corresponding nominal position modifications or output of target admittance $\Delta \mathbf{x}_f \in \mathbb{R}^n$. There exists an inner position loop and an outer compliance loop in the impedance controller.

The desired impedance $Z_f(s)$ is usually adopted in the form of second-order linear system (spring-damping-inertia system) [2, 6]:

$$Z_f(s) = \frac{1}{\mathbf{M}s^2 + \mathbf{D}s + \mathbf{K}},$$ (2)

where $\mathbf{K}, \mathbf{D}, \mathbf{M} \in \mathbb{R}^{n \times n}$ are diagonal positive-define matrices and characterize the desired stiffness, damping, and inertia, respectively.

3.3 A Novel Fractional Order Impedance Control

For further research, a special and useful example of $Z_f(s)$ in (2) (the proposed novel fractional order impedance model) for legged robots is addressed as
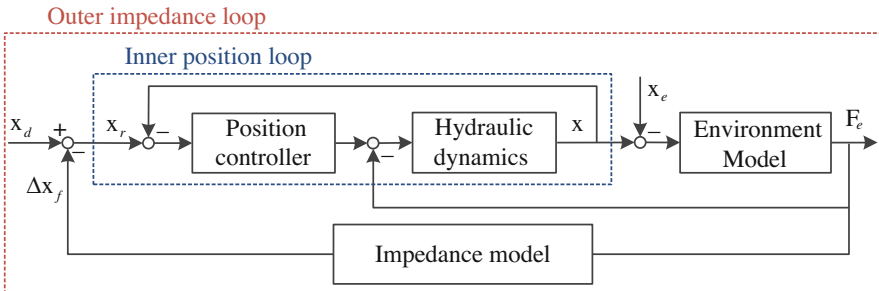
Fig. 2 The diagram of position/force based active compliance controller

$$\frac{\Delta x(s)}{F_e(s)} = \frac{D_{f_1}s^{d_{f_1}} + K_f + I_{f_1}s^{-i_{f_1}}}{D_{x_2}s^{d_{x_2}} + D_{x_1}s^{d_{x_1}} + K_x + I_{x_1}s^{-i_{x_1}} + I_{x_2}s^{-i_{x_2}}}, \tag{3}$$

where all the coefficients and orders are larger than 0 and belong to real numbers (no longer only integers). Specially, $0 < d_{x_1} < 1.5 \leqslant d_{x_2} \leqslant 2.5$, $0 < i_{x_1} < 1.5 \leqslant i_{x_2} \leqslant 2.5$. By comparison, D_{x_2}, D_{x_1}, and K_x are the set impedance-like inertia, damping, stiffness as in (2). The integral item in (3) is utilized to eliminate (denominator) or increase (numerator) the tracking error in traditional impedance model. The derivative item in the numerator of (3) is used to determine the total energy of the system (dissipating or absorbing).

4 Simulation Analysis

4.1 The Influence of Each Parameter

Co-simulations are done between Adams software and Matlab. There are two main problems in designing a FOPID controller experimentally: (1) an approximation method is required to realize the fractional-order differentiators and integrators and (2) an optimization algorithm is needed for the control parameters tuning based on the experimental data. The first problem can be solved by referring to [3, 4]. Through comparing six different values in one of the 14 parameters in a given model, analyzed effects are shown in Fig. 3.

The functions of parameters in the choosing model are concluded as follows (6 classical models are shown):

Model 1 ($\frac{1}{D_{x_1}s^1+10}$) The D_{x_1} is the traditional damping in (2). A large D_{x_1} can dissipate the system energy and reduce the oscillations, but it will increase the contact force in turn.

Model 2 ($\frac{1}{0.6s^{d_{x_1}}+10}$) When d_{x_1} gets closer to 1.5, the damping-like $D_{x_1} = 0.6$ begins to behave inertia-like, which results in growing contact force and oscillations before coming into a stable state. When d_{x_1} gets closer to 0, $D_{x_1} = 0.6$ begins to behave like a stiffness so that the system energy cannot be dissipated well and no stable state can be reached. When $d_{x_1} \in [0.9, 1.1]$, a good transition can be obtained.

Model 3 ($\frac{1}{0.002s^2+0.6s^1+10+I_{x_1}s^{-1}}$) The novelty is that a suitable I_{x_1} can be utilized to eliminate the tracking error. A small I_{x_1} has a long convergence time, while a large one will cause oscillations before coming into a stable state.

Model 4 ($\frac{1}{0.002s^2+0.6s^1+10+40s^{-i_{x_1}}}$) The i_{x_1} mainly affects the transition of contact force and tracking error with little effect on their values. When i_{x_1} gets closer to 0, I_{x_1} behaves like a stiffness. When i_{x_1} gets closer to 1.5, an overshoot/oscillation forms.
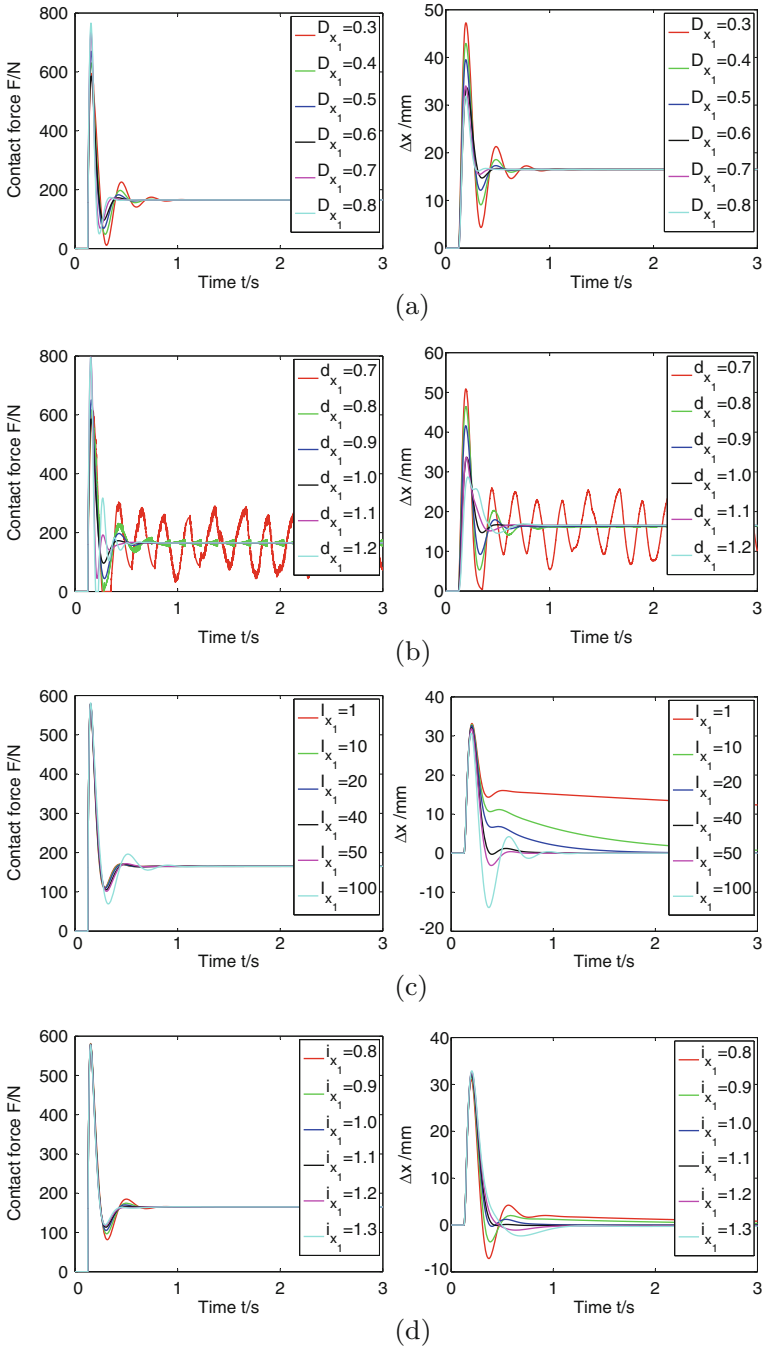
Fig. 3 The influences of parameters in (3): (**a**) Model 1: $\frac{1}{D_{x_1}s^1+10}$. (**b**) Model 2: $\frac{1}{0.6s^{d_{x_1}}+10}$. (**c**) Model 3: $\frac{1}{0.002s^2+0.6s^1+10+I_{x_1}s^{-1}}$. (**d**) Model 4: $\frac{1}{0.002s^2+0.6s^1+10+40s^{-i_{x_1}}}$. (**e**) Model 5: $\frac{D_{f_1}s^1+1}{0.002s^2+0.6s^1+10}$. (**f**) Model 6: $\frac{0.001s^{d_{f_1}}+1}{0.002s^2+0.6s^1+10}$

(e)

(f)
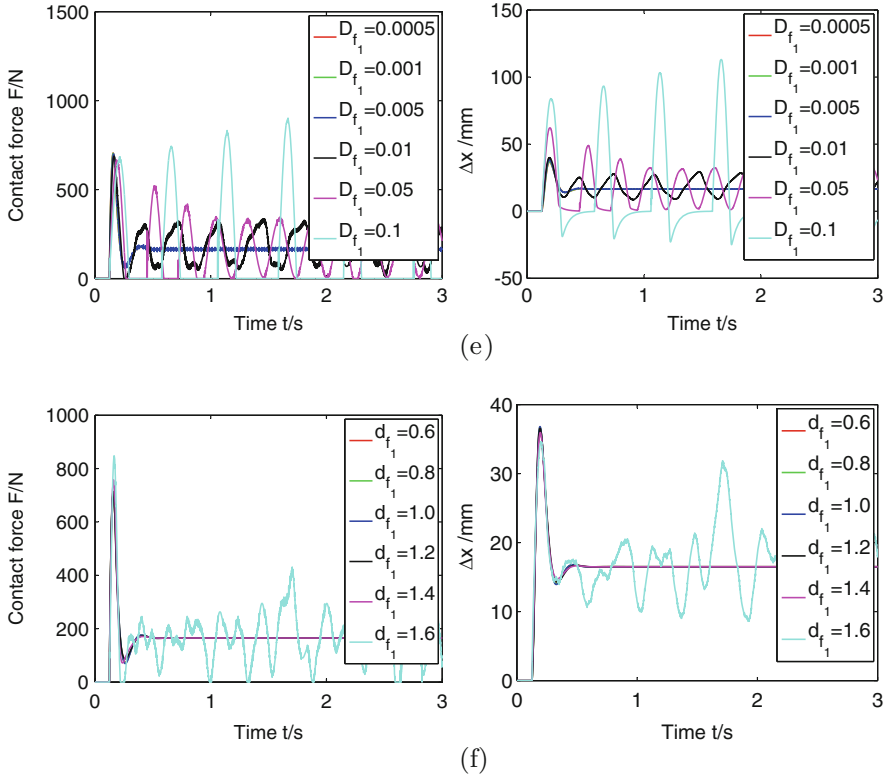
Fig. 3 (continued)

Model 5 ($\frac{D_{f_1}s^1+1}{0.002s^2+0.6s^1+10}$) When D_{f_1} grows, oscillations occur. The energy is added into system so that the system begins to bouncing up with the growing D_{f_1}. The dissipated energy is fixed by the chosen damping 0.6, while the added energy depends on D_{f_1}.

Model 6 ($\frac{0.001s^{d_{f_1}}+1}{0.002s^2+0.6s^1+10}$) When d_{f_1} gets closer to 0, $D_{f_1} = 0.001$ begins to behave like $K_f = 1$. When d_{f_1} grows, undesired oscillations occur.

From above simulation results, compared with traditional impedance control, the proposed novel fractional order impedance control has little effect on reducing contact impact F_e, but it can improve the transition process of force/position response efficiently and decrease the tracking error $\Delta x = x_d - x$ gradually.

4.2 Comparative Simulations

Simulations were done in a free falling situation. Figure 4a and b is the traditional ($\frac{1}{0.6s^1+10}$) and fractional order ($\frac{1}{0.002s^{1.9}+0.6s^{0.95}+10+40s^{-1.1}}$) impedance model, respectively. They are all energy dissipating impedance model and proposed fractional order impedance control with an added integral item could eliminate the tracking error and achieve more significant compliance behavior. Figure 4c and d is the energy holding ($\frac{1}{0.6s^{0.7}+10}$) and absorbing ($\frac{0.1s^1+1}{0.002s^2+0.6s^1+10}$) impedance model, which provides guides for robots bouncing height control and jumping control, respectively.

In order to know why more significant complaint behavior can be achieved in the proposed novel fractional order impedance control, the further research of comparative simulations are implemented in Fig. 4 and the calculated stiffness and damping of impedance models are shown in Fig. 5. In Fig. 5a, it is easy to see that the calculated stiffness and damping are almost the same to the given ones $K_x = 10\,\text{N/mm}$, $D_{x_1} = 0.6\,\text{N/(mm/s)}$ in traditional impedance model. In Fig. 5b, the calculated stiffness and damping are variable in impact phase in fractional order impedance control. The result validates references [7, 8] and is the reason why more significant complaint behavior can be achieved. Besides, the calculated stiffness and damping values would decrease to be negative in compressing phase and increase to be positive again in rebounding phase. As thus, the energy could be dissipated more efficiently. In Fig. 5c, the calculated damping does not change a lot in the energy holding impedance model, but the calculated stiffness increases in compressing phase and decreases in rebounding phase and the whole system energy is held so that the bouncing height could be kept. In Fig. 5d, the calculated stiffness still increases in compressing phase and decreases in rebounding phase in the energy absorbing
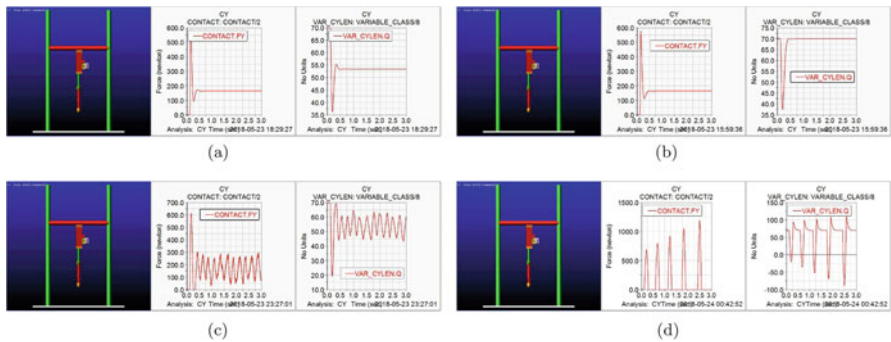
Fig. 4 Comparative simulations. (**a**) Traditional impedance model: $\frac{1}{0.6s^1+10}$ https://youtu.be/h5uBiMIziJU. (**b**) Fractional order impedance model: $\frac{1}{0.002s^{1.9}+0.6s^{0.95}+10+40s^{-1.1}}$ https://youtu.be/UMgfV7xIIxk. (**c**) Energy holding impedance model: $\frac{1}{0.6s^{0.7}+10}$ https://youtu.be/g4LbhrrdmJI. (**d**) Energy absorbing impedance model: $\frac{0.1s^1+1}{0.002s^2+0.6s^1+10}$ https://youtu.be/DE9X5q4W3dI

Fig. 5 Calculated stiffness and damping. (**a**) Traditional impedance model: $\frac{1}{0.6s^1+10}$. (**b**) Fractional order impedance model: $\frac{1}{0.002s^{1.9}+0.6s^{0.95}+10+40s^{-1.1}}$. (**c**) Energy holding impedance model: $\frac{1}{0.6s^{0.7}+10}$. (**d**) Energy absorbing impedance model: $\frac{0.1s^1+1}{0.002s^2+0.6s^1+10}$

impedance model, but the calculated damping always decreases from positive to negative to inject energy into the system so that the system starts to jump. Note that the calculated stiffness and damping are based on the assumption that they are the same in the neighboring two control cycles and do not change in the flight phase.

4.3   The Criterion of Choosing and Tuning Parameters

Firstly, the chosen parameters in (3) should guarantee the system stability. Assume the position servo controller (inner position loop in Fig. 2) is stable. If the proposed novel fractional order impedance model in (3) is stable, the whole system will be stable. Our previous published work [4] can be employed to ensure the stability of proposed novel fractional order impedance model.

Secondly, the parameters in (3) are chosen and tuned to make sure the contact force is as small as possible. Meanwhile, the required/unrequired tracking error should have a good transition or be eliminated. Model 4 could be a good reference.

Finally, the detailed procedure of choosing and tuning parameters in (3) refers to Sect. 4.1. Specially, $D_{x_1}, d_{x_1}, K_x, I_{x_1}, i_{x_1}, D_{f_1}, d_{f_1}, K_f$ play more important roles among the 14 parameters in (3) and should be determined firstly.

5 Conclusions

In this paper, a novel fractional order impedance control was proposed by combining an integral item and fractional order into the traditional impedance control. The research of this paper provides an insight for the compliance control for legged robots. The main contributions are concluded as follows:

– An integral item is added into the traditional impedance model to eliminate the tracking error caused by the compliant behavior.
– The idea of fractional order is introduced to make the orders of inertia, damping, and stiffness are no longer only integers so that more significant compliant performance can be achieved.
– The proposed novel fractional order impedance control is validated by comparative simulations in a hydraulic bouncing system.

References

1. Chen, G., Wang, J., Wang, S., Zhao, J., Shen, W.: Compliance control for a hydraulic bouncing system. ISA Trans. **79**, 232–238 (2018)
2. Part, S.: Impedance control: an approach to manipulation. J. Dyn. Syst. Meas. Control. **107**, 17 (1985)
3. Oustaloup, A., Levron, F., Mathieu, B., Nanot, F.M.: Frequency-band complex noninteger differentiator: characterization and synthesis. IEEE Trans. Circuits Systems I Fund. Theory Appl. **47**(1), 25–39 (2000)
4. Zhao, J., Wang, J., Wang, S.: Fractional order control to the electro-hydraulic system in insulator fatigue test device. Mechatronics **23**(7), 828–839 (2013)
5. Raibert, M.H., Brown Jr, H.B., Chepponis, M.: Experiments in balance with a 3D one-legged hopping machine. Int. J. Robot. Res. **3**(2), 75–92 (1984)
6. Koivumäki, J., Mattila, J.: Stability-guaranteed impedance control of hydraulic robotic manipulators. IEEE/ASME Trans. Mechatron. **22**(2), 601–612 (2017)
7. Shen, Z., Seipel, J.: Animals prefer leg stiffness values that may reduce the energetic cost of locomotion. J. Theor. Biol. **364**, 433–438 (2015)
8. Shen, Z., Seipel, J.: The leg stiffnesses animals use may improve the stability of locomotion. J. Theor. Biol. **377**, 66–74 (2015)

Analysis of Quadcopter Dynamics During Programmed Movement Under External Disturbance

Izabela Krzysztofik (ID) **and Zbigniew Koruba** (ID)

Abstract This chapter presents the quadcopter dynamics and controls during programmed movement under external disturbance such as wind gusts and projectile blasts. To ensure high precision in maintaining the line of sight at a required position, the authors proposed a new control method based on a combination of three regulators: a classic PID controller, a robust sliding controller and a modified linear quadratic controller. Effectiveness of the developed control method was examined due to the precision of the set motion. Selected results of the simulation studies are presented graphically.

Keywords Quadcopter · Programmed movement · Modified LQR · Sliding mode controller

1 Introduction

This chapter analyses the quadcopter (QUAV) dynamics and controls during programmed movement under external disturbance such as wind gusts and projectile blasts. It should be highlighted that the QUAV in question offers an advantage of being able to remain in a hover position for a specific period of time.

The laser target indication system (LTIS) will therefore not require its own control system and thus be much simplified, for its control is reduced to adjusting the angle between the target line of sight (TLOS) and the QUAV longitudinal axis. The LTIS function is therefore exercised by the drone itself, which is equipped with an automatic pilot, an infrared sensor for detecting thermal radiation emitted by ground targets (a tank, a combat vehicle, etc.) and a laser target indicator. In the target search mode, the drone is set in programmed movement, which provides for scanning the ground surface along its longitudinal axis which is fitted with an infrared sensor and laser target indicator. When a heat signal from a target is received, the drone

I. Krzysztofik (✉) · Z. Koruba
Kielce University of Technology, Kielce, Poland
e-mail: pssik@tu.kielce.pl; ksmzko@tu.kielce.pl
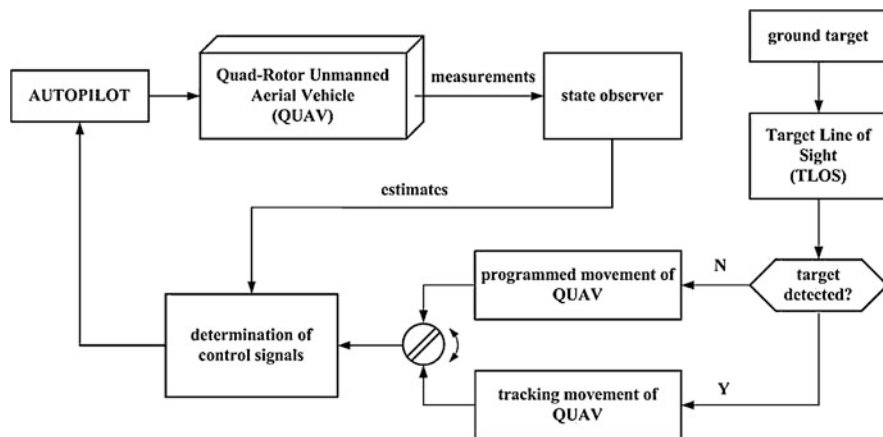
Fig. 1 Algorithm for QUAV control during detection and laser illumination of a ground target

moves to a hover position and starts illuminating the target with laser impulses, thus rendering it as a possible object of attack [1, 2].

The studies used a full, non-linear model of the quadcopter's dynamics. It should be emphasized that in the absence of knowledge of the initial conditions and some variables of the state of the drone, the model was linearized using Jacobian, i.e. a state matrix with non-stationary parameters. Thanks to this, we can use a dynamic regulator in autonomous drone movement.

To ensure high precision in maintaining the TLOS at a required position, the authors proposed a new control method based on a combination of three regulators: a classic PID [3] controller, a robust sliding mode controller (SMC) [4, 5], and a modified linear-quadratic controller [6], in the following way: the sliding controller was determined for the linear coordinates *x, y, z* of the drone position, while the PID controller and LQR for the angular coordinates ϕ, θ, ψ of the drone position.

A simplified operating diagram of the target detection, tracking and laser indication system from a QUAV is shown in Fig. 1.

2 Control Algorithm

The QUAV position is controlled with the speed of the motors Ω_i [7]. Six control signals are defined: U_1—height control, U_2—roll channel control, U_3—pitch channel control, U_4—yaw channel control and two auxiliary signals for *x* and *y* position control: U_x and U_y [3]. The quadcopter control algorithm is as follows. Pre-set controls U_{z1} as well as U_x and U_y are established. Based on them, roll and pitch angles are determined:

$$\phi_z = m \left(U_x \sin \psi - U_y \cos \psi \right) / U_{z1} \tag{1}$$

$$\theta_z = m \left(U_x \cos \psi + U_y \sin \psi \right) / U_{z1} \tag{2}$$

Then, pre-set controls U_{z2}, U_{z3} and U_{z4} are determined. With the pre-set control values known, one can determine the desired rotational speed values for the drone's rotors:

$$\Omega_1^2 = \frac{1}{4b} U_{z1} - \frac{1}{2b} U_{z3} + \frac{1}{4d} U_{z4} \tag{3}$$

$$\Omega_2^2 = \frac{1}{4b} U_{z1} - \frac{1}{2b} U_{z2} - \frac{1}{4d} U_{z4} \tag{4}$$

$$\Omega_3^2 = \frac{1}{4b} U_{z1} + \frac{1}{2b} U_{z3} + \frac{1}{4d} U_{z4} \tag{5}$$

$$\Omega_4^2 = \frac{1}{4b} U_{z1} + \frac{1}{2b} U_{z2} - \frac{1}{4d} U_{z4} \tag{6}$$

Finally, with the rotational speed values known, one can determine the vector $\mathbf{U}$ components:

$$\begin{bmatrix} U_1 \\ U_2 \\ U_3 \\ U_4 \end{bmatrix} = \begin{bmatrix} b \left(\Omega_1^2 + \Omega_2^2 + \Omega_3^2 + \Omega_4^2 \right) \\ b \left(\Omega_2^2 - \Omega_4^2 \right) \\ b \left(\Omega_1^2 - \Omega_{43}^2 \right) \\ d \left(\Omega_1^2 - \Omega_2^2 + \Omega_3^2 - \Omega_4^2 \right) \end{bmatrix} \tag{7}$$

where m—drone weight; b—thrust coefficient; d—drag coefficient; ψ—yaw angle.

The control laws for the sliding mode controller are established as follows [8]:

$$U_{zi} = -k_i \tan h \left(\lambda_i e_i + \dot{e}_i \right) \tag{8}$$

where

$i = x, y, 1, 2, 3, 4$; λ_i—positive constants; k_i —sliding gains
$e_x = x - x_z$; $\dot{e}_x = \dot{x} - \dot{x}_z$; $e_y = y - y_z$; $\dot{e}_y = \dot{y} - \dot{y}_z$; $e_1 = z - z_z$; $\dot{e}_1 = \dot{z} - \dot{z}_z$;
$e_2 = \phi - \phi_z$; $\dot{e}_2 = \dot{\phi} - \dot{\phi}_z$; $e_3 = \theta - \theta_z$; $\dot{e}_3 = \dot{\theta} - \dot{\theta}_z$; $e_4 = \psi - \psi_z$; $\dot{e}_4 = \dot{\psi} - \dot{\psi}_z$

In order to establish the optimum control, the following functional is formulated:

$$I_{\mathrm{rot}} = \int_0^\infty \left(\mathbf{x}_{\mathrm{rot}}^T \mathbf{Q}_{\mathrm{rot}} \mathbf{x}_{\mathrm{rot}} + \mathbf{u}_{\mathrm{rot}}^T \mathbf{R}_{\mathrm{rot}} \mathbf{u}_{\mathrm{rot}} \right) \tag{9}$$

The law of control $\mathbf{u}_{\text{rot}}$ is represented by the following formula [9]:

$$\mathbf{u}_{\text{rot}} = -\mathbf{K}_{\text{rot}} \left(\mathbf{x}_{\text{rot}} - \mathbf{x}_{\text{rot}}^z \right) \qquad (10)$$

where $\mathbf{x}_{\text{rot}}$—the vector of true variables of the quadcopter state; $\mathbf{x}_{\text{rot}}^z$—the vector of the desired values of the quadcopter state variable.

The gain matrix $\mathbf{K}_{\text{rot}}$ is determined with the *lqr* function present in Matlab [10]:

$$\mathbf{K}_{\text{rot}} = lqr\left(\mathbf{J}, \mathbf{B}, \mathbf{Q}, \mathbf{R}\right) \qquad (11)$$

where the state matrix $\mathbf{A}$ is replaced with the system Jacobian, $\mathbf{B}$ is the control matrix and $\mathbf{Q}$ and $\mathbf{R}$ are weight matrices reduced to diagonal forms and selected experimentally.

The Jacobian $\mathbf{J}$ is determined on the basis of nonlinear equations that describe the quadcopter's movement

$$\mathbf{J}_{\text{rot}} = \begin{bmatrix} \left.\frac{\partial g_1}{\partial x_{\text{rot}1}}\right|_{x_1^z} & \cdots & \left.\frac{\partial g_1}{\partial x_{\text{rot}6}}\right|_{x_6^z} \\ \vdots & \ddots & \vdots \\ \left.\frac{\partial g_6}{\partial x_{\text{rot}1}}\right|_{x_1^z} & \cdots & \left.\frac{\partial g_6}{\partial x_{\text{rot}6}}\right|_{x_6^z} \end{bmatrix} \qquad (12)$$

where functions $g_1, g_2, g_3, g_4, g_5, g_6$ represent the right sides of the non-linear state equations that describe the quadcopter's dynamics model.

3 Numerical Simulation Results

Simulation studies were conducted in the Matlab/Simulink environment for the quadcopter control during programmed circular movement in the presence of external disturbance. The parameters of PID and SMC regulators were selected using the *fmincon* function available in the Matlab software. The weight matrices $\mathbf{Q}$ and $\mathbf{R}$ were selected in the manner described in [11]. The following quadcopter movement parameters were assumed [3]:

$m = 0.65$ [kg]; $b = 3.13 \cdot 10^{-5}$ [Ns^2]; $d = 7.5 \cdot 10^{-7}$ [Nms^2]
$l = 0.23$ [m]—arm length
$J_r = 6.0 \cdot 10^{-5}$ [kgm^2]—rotor's moment of inertia
$I_x = 7.5 \cdot 10^{-3}$ [kgm^2], $I_y = 7.5 \cdot 10^{-3}$ [kgm^2], $I_z = 1.3 \cdot 10^{-32}$ [kgm^2]—moments of inertia relative to respective axes of the drone-related coordinate system

The values of the sliding mode controller factors are set to:
$\lambda_x = 1.1, k_x = 2.9$
$\lambda_y = 1.3, k_y = 3.2$
$\lambda_1 = 8.8, k_1 = 28.2$

The values of the PID controller factors are:

$k_{p2} = 0.45, k_{d2} = 0.36$
$k_{p3} = 0.45, k_{d3} = 0.36$
$k_{p4} = 0.12, k_{d4} = 0.12$

Disturbances acting on linear coordinates of drone position were considered. They were adopted in harmonic form with large amplitudes of 0.5 for x and y coordinates and 2.5 for z coordinate.

The graphs in Figs. 2, 3 and 4 clearly show that the appearance of external disturbances causes significant deviations of the quadcopter position from the set point. The selected regulator works properly, because the drone quickly reaches the set values. Figures 5, 6 and 7 show that the developed control system works effectively when disturbances occur as well as the moment when a drone's flight

Fig. 2 Actual and pre-set quadcopter flight trajectory in space
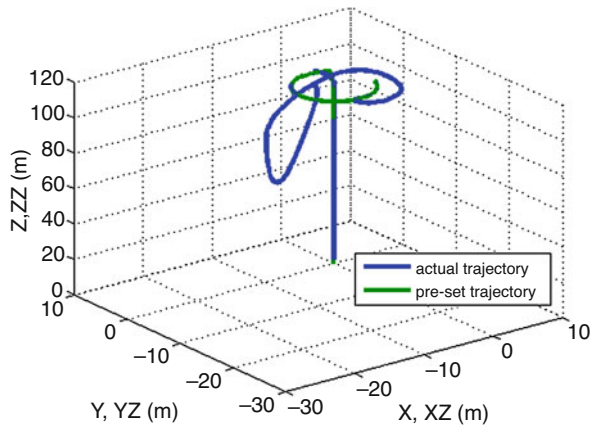
Fig. 3 Time-dependent variations of the actual coordinate x (blue) and pre-set coordinate x_z (green) for the quadcopter position in space
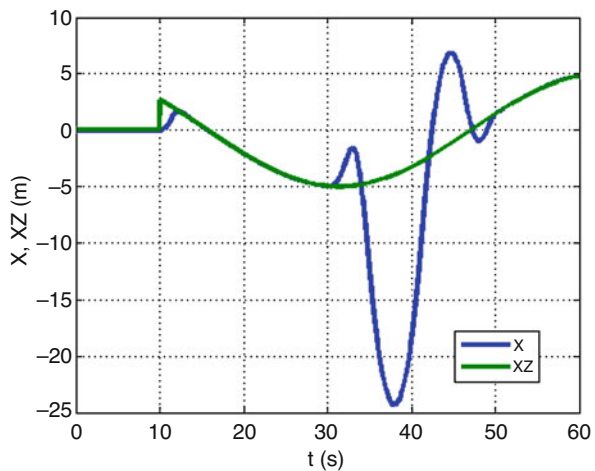
Fig. 4 Time-dependent
variations of the actual
coordinate y (blue) and
pre-set coordinate y_z (green)
for the quadcopter position in
space
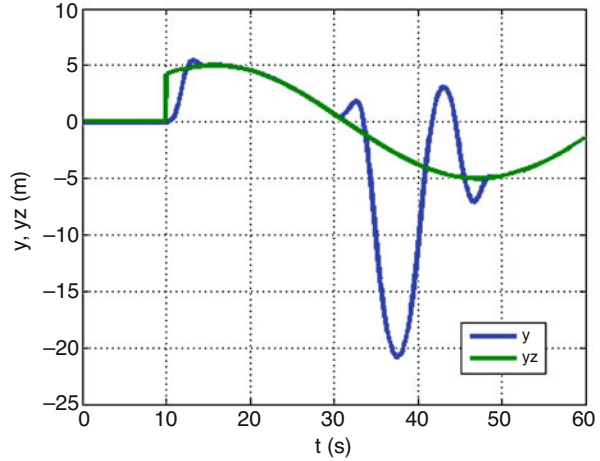
Fig. 5 Time-dependent
variations of the quadcopter
roll angle: actual ϕ (blue),
pre-set ϕ_z (red) and ϕ
obtained for LQR (green)
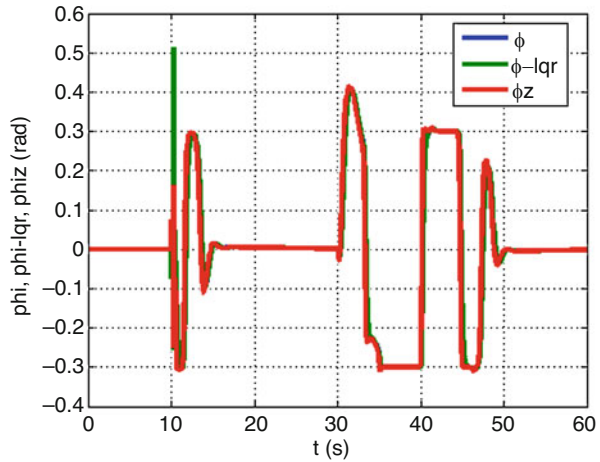
changes from an ascending flight to a circle flight (target searching). In turn, Fig. 8
presents that the z position of the quadcopter is not affected by disturbance. During
the whole drone's flight, the rotational speeds achieve feasible values as shown in
Fig. 9.

In conclusion, external disturbances cause significant deviations of the quad-
copter from the pre-set trajectory (Figs. 2, 3 and 4). However, it should be noted
that despite the large disturbance, the drone quickly returns to the set position.
Therefore, the presented test results clearly show that the drone control system is
good at dealing with external disturbances, despite the fact that it is very sensitive
to them. This is particularly evident in Figs. 5 and 6.
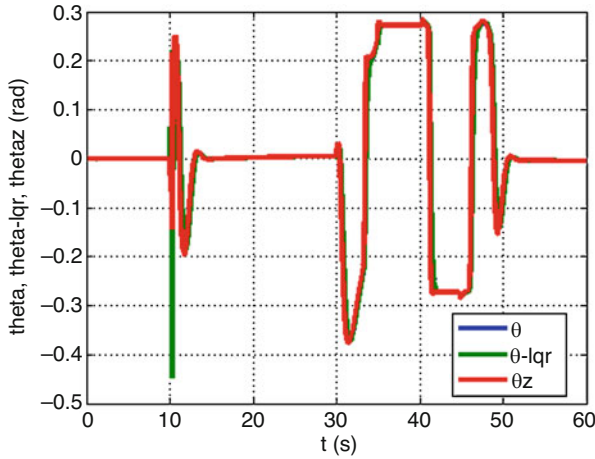
Fig. 6 Time-dependent variations of the quadcopter pitch angle: actual θ (blue), pre-set θ_z (red) and θ obtained for LQR (green)

Fig. 7 Time-dependent variations of the quadcopter yaw angle: actual ψ (blue), pre-set ψ_z (red) and ψ obtained with LQR (green)
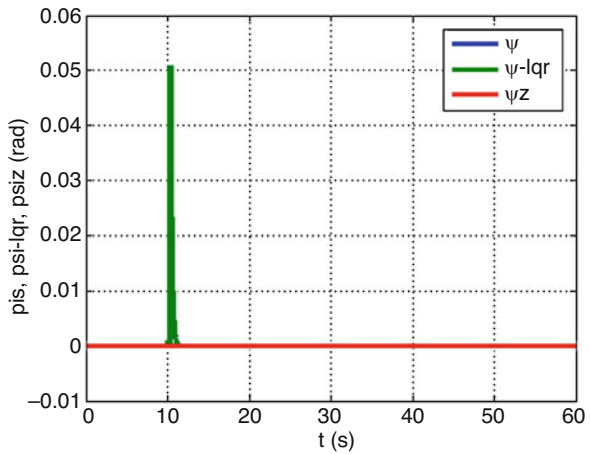
4   Conclusions

This chapter examined the effectiveness of the proposed new control system based on a combination of three regulators: PID, SMC and modified LQR to ensure a stable position of the drone in its motion on a pre-set trajectory during tracking of the ground target, under the prevailing disturbances (gusts of wind, explosions of projectiles).

Where the initial conditions and certain state variables were unknown, the authors conducted a linearization of the model with the use of a non-stationary state

Fig. 8 Time-dependent variations of the actual coordinate z (blue) and pre-set coordinate z_z (green) for the quadcopter position in space
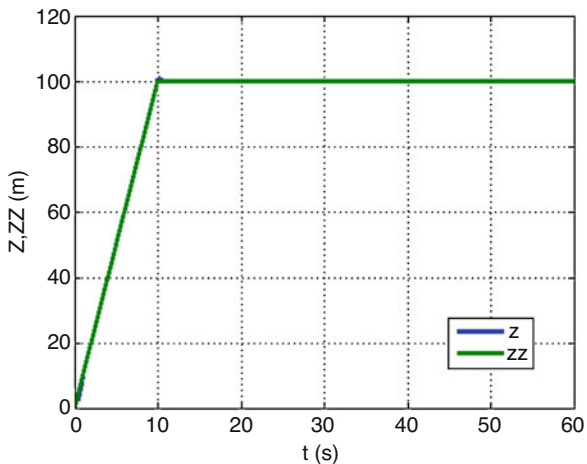
Fig. 9 Time-dependent variations of rotational speed of the motors
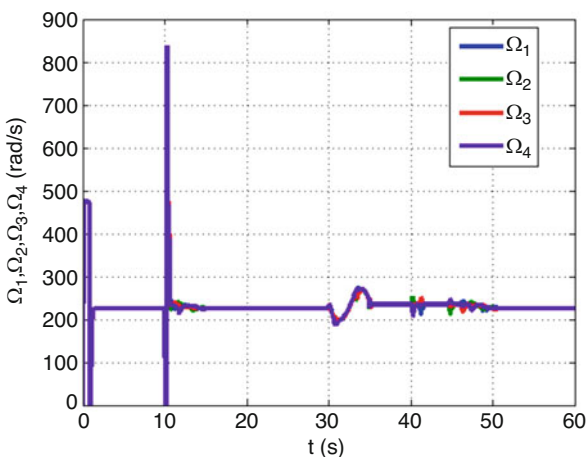
matrix in the form of the Jacobian. This makes the LQR an adaptive regulator that improves the drone's flight stability.

The authors conducted a series of tests of control efficiency for each of the above-mentioned regulators separately. However, initial simulations demonstrated that the highest efficiency in ensuring the target tracking and laser illumination accuracy from the drone's deck was provided by a control system composed of the LQR, SMC and PID.

References

1. Krzysztofik, I., Koruba, Z.: Mathematical model of movement of the observation and tracking head of an unmanned aerial vehicle performing ground target search and tracking. J. Appl. Math. **2014**, 934250., 11 pages (2014)
2. Gapinski, D., Krzysztofik, I.: The process of tracking an air target by the designed scanning and tracking seeker. In: Proceedings of the 2014 15th International Carpathian Control Conference (ICCC), pp. 129–134. Velke Karlovice, Czech Republic (2014)
3. Hasseni, S., Abdou, L.: Decentralized PID control by using GA optimization applied to a Quadrotor. J. Autom. Mobile Robot. Intell. Syst. **12**, 33–44 (2018)
4. Bouabdallah, S., Siegwart, R.: Backstepping and sliding-mode techniques applied to an indoor micro Quadrotor. In: Proceedings of the 2005 IEEE International Conference on Robotics and Automation, pp. 2259–2264, Barcelona, Spain (2005)
5. Krzysztofik, I., Koruba, Z.: Application of the sliding controller for the gyroscope system of the anti-aircraft missile. In: Fuis, V. (ed.) Engineering Mechanics 2017, pp. 530–533. Institute of Thermomechanics, Czech Academy of Sciences, Prague (2017)
6. Koruba, Z., Krzysztofik, I.: A control with the use of LQR modified method in the gyroscope system of target tracking. In: Fuis, V. (ed.) Engineering Mechanics 2017, pp. 486–489. Institute of Thermomechanics, Czech Academy of Sciences, Prague (2017)
7. Bresciani, T.: Modelling, identification and control of a Quadrotor Helicopter. Master Thesis, Lund University (2008)
8. Utkin, V.I.: Sliding mode control: mathematical tools, design and applications. In: Nonlinear and Optimal Control Theory, pp. 289–347. Springer-Verlag, Heidelberg (2008)
9. Lewis, F.L., Vrabie, D.L., Syrmos, V.L.: Optimal Control. Wiley, Hoboken, NJ (2012)
10. Tewari, A.: Modern Control Design with Matlab and Simulink. Wiley, Chichester (2002)
11. Awrejcewicz, J., Koruba, Z.: Classical Mechanics. Applied Mechanics and Mechatronics, vol. 30. Springer, New York (2012)

Nonlinear Model of Quadrotor Dynamics During Observation and Laser Target Illumination

Zbigniew Koruba (iD) and **Izabela Krzysztofik** (iD)

Abstract This chapter presents a nonlinear mathematical model of movement dynamics of a quadrotor unmanned aerial vehicle (QUAV). The model takes into account specific properties of QUAV control and introduces auxiliary virtual controls. The authors have proposed deployment of this type of QUAV to flights on programmed routes aimed at search, detection, observation and laser illumination of ground targets, both stationary and moving. Furthermore, it presented kinematic relationships of the programmed movement and mutual movement of the drone and ground target. Also, the authors examined operating efficiency of the PID controller in ensuring the drone's stability in a hover position and its movement along a pre-set trajectory during tracking under kinematic disturbance from the drone's deck.

Keywords Quadrotor dynamics · Non-linear dynamics · Observation and tracking

1 Introduction

In recent years, quadrotor unmanned aerial vehicles have become a very popular unmanned platform which finds various applications and is still at the stage of intensive research. At present, they are used for *inter alia* making video footage of collective events, monitoring of transport infrastructure, supporting rescue operations and monitoring of air pollution. In this chapter, the authors propose to use this type of quadrotor unmanned aerial vehicle (QUAV) for laser indication of ground targets, both stationary and moving. The quadrotor flights on a programmed route searching for a target, and upon receiving a heat signal, it starts illuminating the target with laser impulses [1]. A full non-linear mathematical model of quadrotor flight dynamics has been prepared [2, 3]. The authors took into account auxiliary controls of the position in the horizontal plane, i.e. towards the *x* and *y* axes [4].

Z. Koruba · I. Krzysztofik (✉)
Kielce University of Technology, Kielce, Poland
e-mail: ksmzko@tu.kielce.pl; pssik@tu.kielce.pl

The dynamics and navigation of the QUAV are known and widely described in the subject literature. However, the analysis of drone navigation methods during tracking and ground target observation is not well-known. For this reason, the original element and main contribution of this work is the development of the QUAV guidance kinematics on a specific point in space and tracking, as well as laser illumination of the ground target. This is the starting point for further research on the possibility of cooperation of the QUAV with an autonomous land vehicle, looking for ground targets covered by terrain obstacles (hills, buildings, etc.). It should be emphasised that we also have in mind the take-off and landing of the quadrotor from and to the deck of the land vehicle.

2 Nonlinear Mathematical Model of Movement of the Quadrotor

The position of the QUAV in the earth-fixed inertial frame is established with three linear coordinates x, y, z and three angles ϕ, θ, ψ. Figure 1 shows the QUAV configuration with rotational speeds, forces and moments generated by the four motors.

The angular velocity vector ω in the fixed frame is defined as follows:

$$\omega = \begin{bmatrix} \omega_x \\ \omega_y \\ \omega_z \end{bmatrix} = \begin{bmatrix} \dot{\phi} - \dot{\psi} \sin \theta \\ \dot{\theta} \cos \phi + \dot{\psi} \sin \phi \cos \theta \\ -\dot{\theta} \sin \phi + \dot{\psi} \cos \phi \cos \theta \end{bmatrix}. \tag{1}$$

The following forces and moments acting on the QUAV have been taken into consideration:

The total motor thrust

Fig. 1 QUAV-related coordinate system
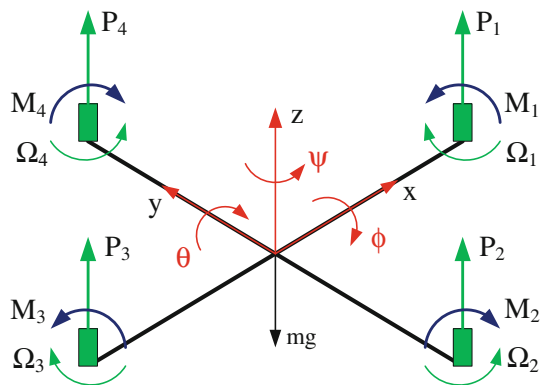
$$P = \sum_{i-1}^{4} P_i = b \left(\Omega_1^2 + \Omega_2^2 + \Omega_3^2 + \Omega_4^2 \right), \tag{2}$$

where b is the thrust coefficient and Ω_i are rotational speeds of the motors.

The torque resulting from the difference in the thrust generated by motors 2 and 4:

$$M_\phi = bl \left(\Omega_4^2 - \Omega_2^2 \right), \tag{3}$$

where l is the length of the arms.

The torque resulting from the difference in the thrust generated by motors 1 and 3:

$$M_\theta = bl \left(\Omega_3^2 - \Omega_1^2 \right). \tag{4}$$

The torque resulting from the difference in thrusts generated by respective motor pairs (1,3) and (2,4):

$$M_\psi = \sum_{i-1}^{4} M_i = d \left(\Omega_1^2 + \Omega_3^2 - \Omega_2^2 - \Omega_4^2 \right), \tag{5}$$

where d is the drag coefficient.

Gyroscopic moments:

$$M_\phi^g = J_r \dot{\theta} \left(\Omega_1 + \Omega_3 - \Omega_2 - \Omega_4 \right), \tag{6}$$

$$M_\theta^g = J_r \dot{\phi} \left(\Omega_1 + \Omega_4 - \Omega_1 - \Omega_3 \right), \tag{7}$$

where J_r represents the rotor moment of inertia.

Applying the Euler–Lagrange formalism, the authors derived the following full non-linear mathematical model of the quadr movement [2, 5]:

$$\begin{bmatrix} \ddot{x} \\ \ddot{y} \\ \ddot{z} \\ \ddot{\phi} \\ \ddot{\theta} \\ \ddot{\psi} \end{bmatrix} = \begin{bmatrix} U_1 \left(\cos \psi \sin \theta \cos \phi + \sin \psi \sin \phi \right) / m \\ U_1 \left(\sin \psi \sin \theta \cos \phi - \cos \psi \sin \phi \right) / m \\ U_1 \cos \theta \cos \phi / m - g \\ \left[(I_y - I_z) \dot{\psi} \dot{\theta} - J_r \dot{\theta} \Omega_r + l U_2 \right] / I_x \\ \left[(I_z - I_x) \dot{\psi} \dot{\phi} + J_r \dot{\phi} \Omega_r + l U_3 \right] / I_y \\ \left[(I_x - I_y) \dot{\theta} \dot{\phi} + U_4 \right] / I_z \end{bmatrix}, \tag{8}$$

where

$\Omega_r = \Omega_1 + \Omega_3 - \Omega_2 - \Omega_4$

I_x, I_y, I_z—QUAV moments of inertia

U_1, U_2, U_3, U_4—controls

The control vector U is established according to the following formula:

$$\begin{bmatrix} U_1 \\ U_2 \\ U_3 \\ U_4 \end{bmatrix} = \begin{bmatrix} b\left(\Omega_1^2 + \Omega_2^2 + \Omega_3^2 + \Omega_4^2\right) \\ b\left(\Omega_4^2 - \Omega_2^2\right) \\ b\left(\Omega_3^2 - \Omega_1^2\right) \\ d\left(\Omega_1^2 + \Omega_3^2 - \Omega_2^2 - \Omega_4^2\right) \end{bmatrix}. \tag{9}$$

3   Movement Kinematics Model of the QUAV and Target

While searching for a ground target, the drone moves in a programmed movement which enables it to scan the earth surface along its longitudinal axis. Upon target detection, the drone moves to a hover position and starts illuminating the target with laser impulses, thus rendering it as a possible object of attack [6].

Reaching a mobile point in space with pre-set coordinates $P[x_p(t), y_p(t), z_p(t)]$ and the initial position of the drone at point $D[x_{do}, y_{do}, z_{do}]$ as well as tracking and laser illumination from a constant height H_{do} (hover) of point C having coordinates $C[x_c(t), y_c(t), z_c(t)]$ (ground target) are implemented in accordance with the algorithm described in the following Eqs. (10)—(19).

Guidance equations:

$$\frac{dx_d}{dt} = V_{dx}(t) = V_d \frac{r_{dx}(t)}{r_d(t)}, \tag{10}$$

$$\frac{dy_d}{dt} = V_{dy}(t) = V_d \frac{r_{dy}(t)}{r_d(t)}, \tag{11}$$

$$\frac{dz_d}{dt} = V_{dz}(t) = V_d \frac{r_{dz}(t)}{r_d(t)}, \tag{12}$$

where

$$r_{dx}(t) = x_p(t) - x_d(t), \quad r_{dy}(t) = y_p(t) - y_d(t), \quad r_{dz}(t) = z_p(t) - z_d(t).$$

The mutual distance between points D and P:

$$r_d(t) = \sqrt{\left(x_p(t) - x_d(t)\right)^2 + \left(y_p(t) - y_d(t)\right)^2 + \left(z_p(t) - z_d(t)\right)^2}. \tag{13}$$

The drone's tracking of a mobile point moving on the ground surface from a pre-set height $H_d = \text{const} = H_{do}$:

$$\frac{dx_d(t)}{dt} = V_{dx}(t) = V_d \frac{r_{dx}(t)}{r_d(t)}, \tag{14}$$

$$\frac{dy_d}{dt} = V_{dy}(t) = V_d \frac{r_{dy}(t)}{r_d(t)}, \tag{15}$$

$$\frac{dz_d}{dt} = V_{dz}(t) = 0, \tag{16}$$

$$r_d(t) = \sqrt{(x_c(t) - x_d(t))^2 + (y_c(t) - y_d(t))^2 + H_{do}^2}, \tag{17}$$

$$r_{dx}(t) = x_c(t) - x_d(t), \quad r_{dy}(t) = y_c(t) - y_d(t), \quad r_{dz}(t) = H_{do}. \tag{18}$$

During laser illumination of a ground target from a constant height H_{do}, the drone should be controlled, so that the mutual distance between points D and C is constant, i.e., $r_d(t) = \text{const} = r_{do}$. Consequently,

$$\frac{dr_d(t)}{dt} = 0 \leftrightarrow \frac{dx_d(t)}{dt} = \frac{dx_c(t)}{dt}, \quad \frac{dy_d(t)}{dt} = \frac{dy_c(t)}{dt}, \quad \frac{dz_d(t)}{dt} = 0,$$

$$\sqrt{(x_c(t) - x_d(t))^2 + (y_c(t) - y_d(t))^2 + H_{do}^2} = r_{do},$$

$$x_d = x_c, \quad y_d = y_c, \quad z_d = H_{do}. \tag{19}$$

4 Quadrotor Control Algorithm

The QUAV position is controlled with rotational speed of the motors Ω_i. Six control signals are defined: U_1—height control, U_2—roll channel control, U_3—pitch channel control, U_4—yaw channel control and two auxiliary signals for x and y position control: U_x, U_y [4, 7].

The control laws for the PID controller were defined as follows [8, 9]:

$$U_x = k_{px}e_x + k_{dx}\dot{e}_x, \tag{20}$$

$$U_y = k_{py}e_y + k_{dx}\dot{e}_y, \tag{21}$$

$$U_{z1} = k_{p1}e_1 + k_{d1}\dot{e}_1 + k_{i1} \int e_1 \, dt. \tag{22}$$

Then, the desired values of angles ϕ_z and θ_z were found to be:

$$\phi_z = \frac{m\left(U_x \, \sin \, \psi - U_y \, \cos \, \psi\right)}{U_{z1}}, \tag{23}$$

$$\theta_z = \frac{m\left(U_x \, \cos \, \psi + U_y \, \sin \, \psi\right)}{U_{z1}}, \tag{24}$$

$$U_{z2} = k_{p2}e_2 + k_{d2}\dot{e}_2 + k_{i2} \int e_2 \, dt, \tag{25}$$

$$U_{z3} = k_{p3}e_3 + k_{d3}\dot{e}_3 + k_{i3} \int e_3 \, dt, \tag{26}$$

$$U_{z4} = k_{p4}e_4 + k_{d4}\dot{e}_4 + k_{i4} \int e_4 \, dt, \tag{27}$$

where

$e_x = x_z - x; \dot{e}_x = \dot{x}_z - \dot{x}; e_y = y_z - y; \dot{e}_y = \dot{y}_z - \dot{y},$
$e_1 = z_z - z; \dot{e}_1 = \dot{z}_z - \dot{z}; e_2 = \phi_z - \phi; \dot{e}_2 = \dot{\phi}_z - \dot{\phi},$
$e_3 = \theta_z - \theta; \dot{e}_3 = \dot{\theta}_z - \dot{\theta}; e_4 = \psi_z - \psi; \dot{e}_4 = \dot{\psi}_z - \dot{\psi}$
$k_{px}, k_{py}, k_{p1}, k_{p2}, k_{p3}, k_{p4}$ —the regulator gain coefficients
$k_{dx}, k_{dy}, k_{d1}, k_{d2}, k_{d3}, k_{d4}$ —the regulator damping coefficients
$k_{i1}, k_{i2}, k_{i3}, k_{i4}$—the regulator coefficients of integral parts

Supplying the above drone controls to formula (9), one can determine the desired values of rotational speeds of the respective rotors:

$$\Omega_1^2 = \frac{1}{4b}U_{z1} - \frac{1}{2b}U_{z3} + \frac{1}{4b}U_{z4}, \tag{28}$$

$$\Omega_2^2 = \frac{1}{4b}U_{z1} - \frac{1}{2b}U_{z2} - \frac{1}{4d}U_{z4}, \tag{29}$$

$$\Omega_3^2 = \frac{1}{4b}U_{z1} + \frac{1}{2b}U_{z3} + \frac{1}{4d}U_{z4}, \tag{30}$$

$$\Omega_4^2 = \frac{1}{4b}U_{z1} + \frac{1}{2b}U_{z2} - \frac{1}{4d}U_{z4}. \tag{31}$$

The rotational speed values thus determined are supplied to Eq. (9) and then to Eq. (8).

5 Results

Let us examine the process of movement of the drone from a point in space to the point at the pre-set height $H_{do} = 100$ [m] exactly above and at a constant distance from a target moving on the ground surface. In order to verify the correctness of the algorithm for navigation (guidance) and ground target tracking and laser illumination described herein, simulations were carried out assuming the following system parameters [4]:

$m = 0.65$ [kg]; $l = 0.23$ [m]; $b = 3.13 \cdot 10^{-5}$ [Nms^2]; $d = 7.5 * 10^{-7}$ [Nms^2],
$J_r = 6.0 \cdot 10^{-5}$ [kg m^2]; $\omega_{max} = 500$ $\left[\text{rad}/\text{s}\right]$; $V_d = \left[\text{m}/\text{s}\right]$; $d = 7.5 \cdot 10^{-5}$ [Nms^2],
$I_x = 7.5 \cdot 10^{-3}$ [kg m^2]; $I_y = 7.5 \cdot 10^{-3}$ [kg m^2]; $I_z = 1.3 \cdot 10^{-2}$ [kg m^2],
$\Omega_1 = 250$ $\left[\text{rad}/\text{s}\right]$; $\Omega_2 = 250$ $\left[\text{rad}/\text{s}\right]$; $\Omega_3 = 250$ $\left[\text{rad}/\text{s}\right]$; $\Omega_4 = 250$ $\left[\text{rad}/\text{s}\right]$,
The initial position of the drone is set to: $x_{do} = 0$; $y_{do} = 0$; $z_{do} = 0$
while the initial position of the target is: $x_{co} = 0$; $y_{co} = 0$; $z_{co} = 0$
The velocity components of the target are: $V_{cx} = 5$ $\left[\text{m}/\text{s}\right]$; $V_{cy} = 5$ $\left[\text{m}/\text{s}\right]$; $V_{cz} = 0$ $\left[\text{m}/\text{s}\right]$

On the other hand, the values of parameters of the drone's PID controller are set to:

$k_{p1} = 11.8$, $k_{d1} = 10.8$, $k_{i1} = 0.9$; $k_{p2} = 0.65$, $k_{d2} = 0.46$,
$k_{p3} = 0.45$, $k_{d3} = 0.36$; $k_{p4} = 0.12$, $k_{d4} = 0.12$,
$k_{px} = 8.8$, $k_{dx} = 8.9$, $k_{ix} = 3.0$; $k_{py} = 8.8$, $k_{dy} = 8.9$, $k_{iy} = 3.0$.

The parameters of the PID controller were selected using the *fmincon* function available in Matlab. Some test results are shown in Figs. 2, 3, 4, 5, 6, and 7.

Figures 2, 3, 4, and 5 show that the drone movement fairly accurately reproduces the set trajectory, thus thanks to this, the target can be tracked and precisely illuminated with a laser. The control moments (Fig. 6) and rotational speeds (Fig. 7) achieve required values.
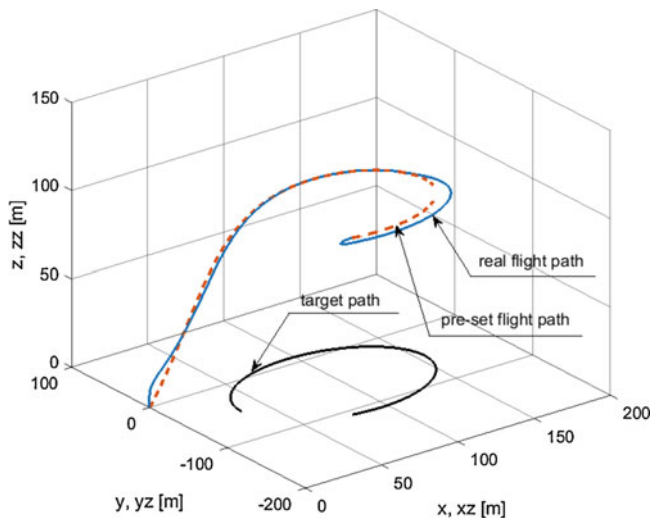
Fig. 2 The process of mutual movement of the drone and target during tracking and laser illumination of the ground target

Fig. 3 Time-dependent variations of the actual coordinate x and pre-set coordinate x_z
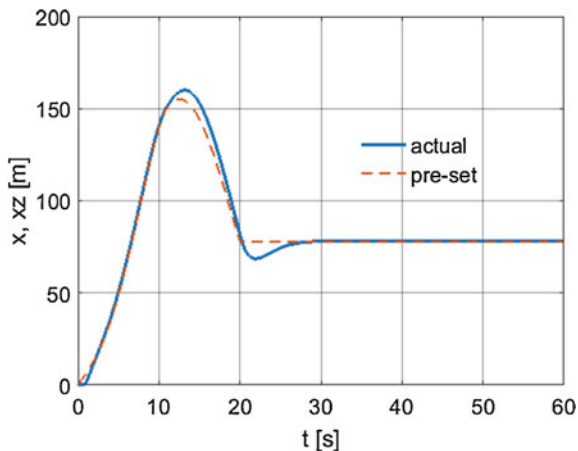
6 Conclusions

In this chapter, the authors conducted a theoretical study regarding the possible application of an unmanned mini rotorcraft for tracking and laser illumination of a stationary and moving ground target such as a tank, infantry fighting vehicle or an artillery and missile launcher. The full nonlinear mathematical model of the UAV

Fig. 4 Time-dependent variations of the actual coordinate y and pre-set coordinate y_z
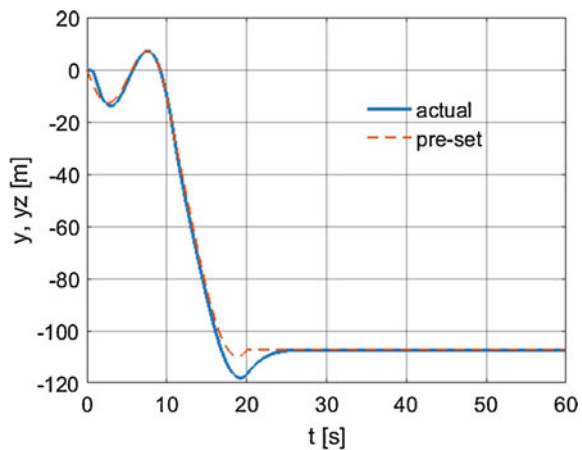
Fig. 5 Time-dependent variations of the actual coordinate z and pre-set coordinate z_z
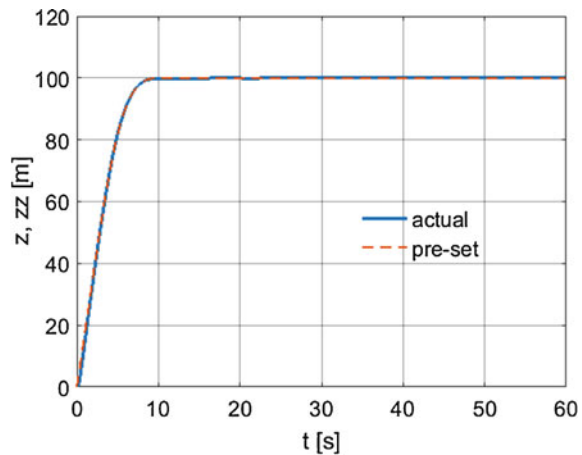
Fig. 6 Time-dependent variations of the drone's calculated controls
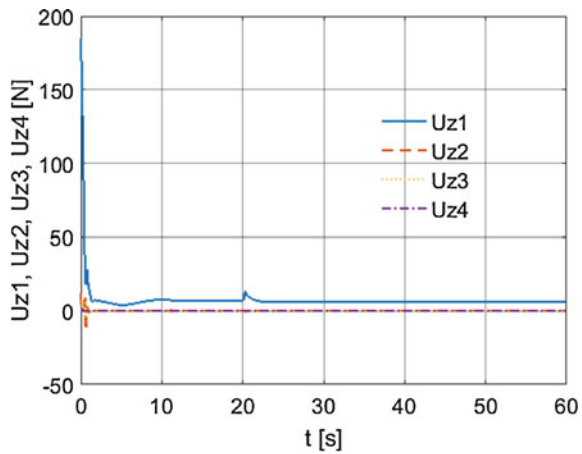
Fig. 7 Time-dependent
variations of rotational speeds
of the drone's motors
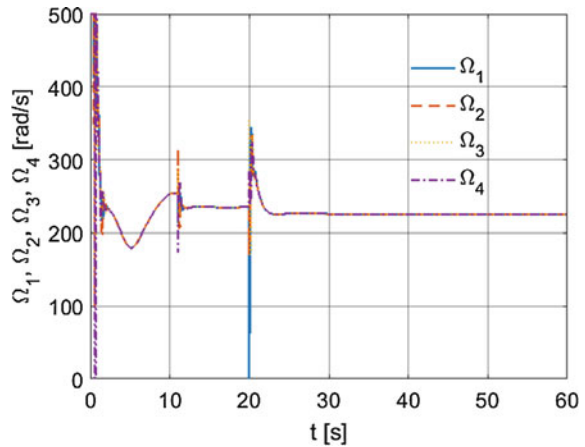
movement developed herein provides ground to conduct a comprehensive examination of the drone's dynamics during search and subsequent laser illumination of the target.

The authors examined the operating efficiency of the PID controller in ensuring the drone's stability in a hover position and its movement along a pre-set trajectory during tracking under kinematic disturbance from the drone's deck. Initial simulations demonstrated that the drone control algorithm proposed herein functions correctly and ensures the laser target illumination capability.

References

1. Gapiński, D., Krzysztofik, I., Koruba, Z.: Analysis of the dynamics and control of the modified optical target seeker used in anti-aircraft rocket missiles. J. Theor. Appl. Mech. **52**(3), 629–639 (2014)
2. Bouabdallah, S.: Design and control of quadrotors with application to autonomous flying. PhD dissertation, EPFL (2007)
3. Bresciani, T.: Modelling, identification and control of a quadrotor helicopter. Master thesis, Lund University (2008)
4. Hasseni, S., Abdou, L.: Decentralized PID control by using GA optimization applied to a quadrotor. J. Autom. Mobile Robot. Intell. Syst. **12**, 33–44 (2018)
5. Naidoo, Y., Stopforth, R., Bright, G.: Quad-rotor unmanned aerial vehicle helicopter modelling & control. Int. J. Adv. Robot. Syst. **8**(4), 139–149 (2011)
6. Krzysztofik, I., Koruba, Z.: Mathematical model of movement of the observation and tracking head of an unmanned aerial vehicle performing ground target search and tracking. J. Appl. Math. **2014**, 934250, 11 pages (2014)
7. He, Z., Zhao, L.: A simple attitude control of quadrotor helicopter based on Ziegler-Nichols rules for tuning PD parameters. Sci. World J. **2014**, 280180, 13 pages (2014)
8. Zuo, Z.: Trajectory tracking control design with command-filtered compensation for a quadrotor. IET Control Theory Appl. **4**(11), 2343–2355 (2010)
9. Lewis, F.L., Vrabie, D.L., Syrmos, V.L.: Optimal Control. Wiley, Hoboken (2012)

Reduced-Order Modeling Friction for Line Contact in a Turbine Blade Damper System

Dongwu Li, Chao Xu, Muzio Gola, and Daniele Botto

Abstract Under-platform damper is used to attenuate resonant response and further prevent high cycle fatigue failure of turbine blades. The aim of this work is to improve the representation of contact interfaces in modeling an asymmetrical under-platform damper. A new reduced-order contact model with a lumped parameter form is proposed, which is based on a modification of the classical Iwan model. This model can explicitly consider the normal contact pressure on line contact. In modeling process, a method to relate the physical Hertzian normal contact pressure with the probability density function (PDF) of slider sliding force for continuous Iwan model is developed. Experimental results from a laboratory asymmetrical under-platform damper test rig are employed to validate the proposed model. For comparison, different normal contact pressure distributions are considered. The out-of-phase motion of the damper is numerically investigated, and the results show that the proposed model can give an accurate prediction of the damper's nonlinear mechanics behavior.

Keywords Turbomachinery · Under-platform damper · Friction contact · Iwan model

1 Introduction

To prevent high cycle fatigue failure due to resonant vibration, dry friction dampers are often used. They are positioned on the underside of two adjacent platforms of blades and pressed by centrifugal force during rotation. Vibration energy in blades can be largely dissipated due to the contact friction between the damper and

D. Li · C. Xu (✉)
School of Astronautics, Northwestern Polytechnical University, Xi'an, China
e-mail: chao_xu@nwpu.edu.cn

M. Gola · D. Botto
Department of Mechanical and Aerospace Engineering, Politecnico di Torino, Torino, Italy
e-mail: daniele.botto@polito.it

platforms. The analysis and optimization of dampers are not an easy task because complex nonlinear mechanics behaviors occur on contact interfaces [1–3].

The ability to model frictional contact on these interfaces and to predict the nonlinear dynamic response of the blade system is essential. Specifically, a reduced-order contact model with fewer parameters is desired for the aim of simplifying analysis and optimization task. From this point, Griffin [1] investigated numerically resonant response of a turbine blade based on a Coulomb friction model which is characterized by a gross slip force and tangential contact stiffness. Subsequently, Yang et al. [4] developed a gross slip model to further consider the effect of variable normal load. Since then, this model has been widely used in modeling of friction contact in blade damper systems due to mathematic simplicity.

When a contact surface is subjected to a high normal load or low amplitude of tangential relative motion, gross slip may not happen. In this case, micro-slip dominates hysteresis friction behavior. To reproduce the micro-slip motion, Menq et al. [5] developed a continuous frictional model and found that incorporating the effect of micro-slip can give a better prediction of system resonant response. Ciğeroğlu et al. [6] presented a distributed parameter micro-slip model, which can model the varying normal contact load and separation. Gastaldi et al. [7] proposed a reduced-order micro-slip model using an array of Yang's macro-slip models, which was used to analyze the mechanics of under-platform dampers. Recently, Li et al. [8] developed a modified Iwan model including variable normal load and analyzed mechanics behavior of an asymmetrical damper. However, the assumption of contact pressure distribution is not suitable for curved-flat contact.

In this chapter, to improve the performance of predicting energy dissipation of asymmetrical under-platform dampers, a reduced-order micro-slip model is proposed. The model can physically consider Hertzian normal contact in the Iwan model. The first part of this work will focus on the derivation of the proposed contact model and show the effect of contact pressure distribution on the model. In the second part, the experimental results from a laboratory asymmetrical under-platform damper test rig will be employed to validate the proposed model. A dedicated contact parameter extraction procedure will be devised to obtain friction coefficient and contact stiffness. Moreover, the effect of different PDF forms will be discussed.

2   The Proposed Reduced-Order Iwan Model

2.1   Modifying Iwan Model to Consider Hertzian Contact Pressure

Iwan model [9] is a phenomenological friction model which can reproduce tangential stick/micro/macro-slip motions and be easily integrated into dynamic analysis code for complex jointed structures. The original Iwan model consists of an infinite number of Jenkins elements in a parallel form. The tangential friction force is defined as

$$T(x) = \int_0^{k_t x} f^* \varphi\left(f^*\right) df^* + k_t x \int_{k_t x}^{\infty} \varphi\left(f^*\right) df^*, \tag{1}$$

where $T(x)$ is tangential force, k_t is tangential stiffness, x is relative displacement, f^* is critical slipping force, and $\varphi(f^*)$ is pre-assumed PDF. The first integral denotes slip state, while the second denotes stick state.

To achieve physical modeling line contact between blade platform and damper, the relation between PDF of critical sliding force and contact pressure is developed in this work. For linear contacts, the pressure distribution $p(s)$ can be obtained by Hertzian contact theory,

$$p(s) = p_0\sqrt{1 - (s/a)^2}, \quad (-a \leq s \leq a), \tag{2}$$

where p_0 and a denote the maximum contact pressure and contact half-length, respectively. The total normal load is defined by the integral of the pressure distribution, $N_0 = \int_0^a p(s)ds$. Corresponding central pressure can be derived, $p_0 = 4N_0/\pi a$.

A projection of contact pressure from spatial distribution to Jenkins elements is built to introduce physical pressure distribution into Iwan model. Correspondingly, contact pressure distribution on each Jenkins element can be derived,

$$p(i) = p_0\sqrt{(2i/n) - (i/n)^2}, \quad (0 < i \leq n), \tag{3}$$

where $p_0 = 4N_0/(\pi n)$, i is the number of Jenkins element and n the total number of elements. According to Coulomb law of friction, critical slipping force distribution on Jenkins element can be obtained from Eq. (3) by assuming a constant friction coefficient μ, i.e.

$$f_i^*/n = (4\mu N_0/\pi n)\sqrt{(2i/n) - (i/n)^2}, \quad (0 < i \leq n). \tag{4}$$

To get the density function $\varphi(f^*)$ of critical slipping force, its probability distribution function $\rho(f^*)$ must be constructed first. From Eq. (4), it can be found that $\rho(f^*)$ is a joint distribution function of i. Solving Eq. (4), the expression of i can be easily derived,

$$i = n - \sqrt{n^2 - \left(\pi n f^*/4\mu N_0\right)^2}. \tag{5}$$

Then the probability distribution function $\rho(f^*)$ is an integral of PDF $\varphi(i)$ of the number of Jenkins element,

$$\rho\left(f^*\right) = \int_0^{n - \sqrt{n^2 - (\pi n f^*/4\mu N_0)^2}} \varphi(i)di = 1 - \sqrt{1 - \left(\pi n f^*/4\mu N_0\right)^2}, \tag{6}$$

where $\varphi(i) = 1/n$ which is a uniform density function. Density function $\varphi(f^*)$ of critical sliding force is the derivative of $\rho(f^*)$,

$$\varphi\left(f^*\right) = \frac{\mathrm{d}\rho\left(f^*\right)}{\mathrm{d}f^*} = \frac{\pi^2 f^*}{4\mu N_0 \sqrt{(4\mu N_0)^2 - (\pi f^*)^2}}. \tag{7}$$

Then substituting Eq. (7) into Eq. (1) and considering gross slip, the tangential force can be obtained,

$$T(x) = \frac{2\mu N_0}{\pi} a \cot \sqrt{\left(\frac{4\mu N_0}{\pi k_t x}\right)^2 - 1} + \sqrt{\left(\frac{k_t x}{2}\right)^2 - \left(\frac{\pi k_t^2 x^2}{8\mu N_0}\right)^2}. \tag{8}$$

When contact interface suffers from a tangential cyclic load, the curve that plots the tangential friction force versus relative displacement forms a hysteresis loop. The expression of the hysteretic loop can be deduced according to Masing rule [9].

2.2 Effect of Pressure Distribution on Tangential Hysteresis Friction

This subsection studies the effect of contact pressure distribution on tangential hysteresis friction by comparing among three typical distribution forms of contact pressure which are uniform, linear, and Hertzian, respectively, as shown in Fig. 1a. A group of quasi-static numerical simulations are carried out to get hysteresis loops. This simulation assumes that one of the contact points is fixed and imposes a tangential cyclic displacement on the other one. Then the tangential friction force transmitted through contact point is calculated using Eq. (8) and Masing rule. Parameters of this numerical example include: the tangential stiffness $k_t = 1 \times 10^7$ N/m, the friction coefficient $\mu = 0.5$, the normal load $N_0 = 100$ N, and the harmonic tangential displacement $x = 10 \sin(2\pi t)$ µm. Figure 1b shows
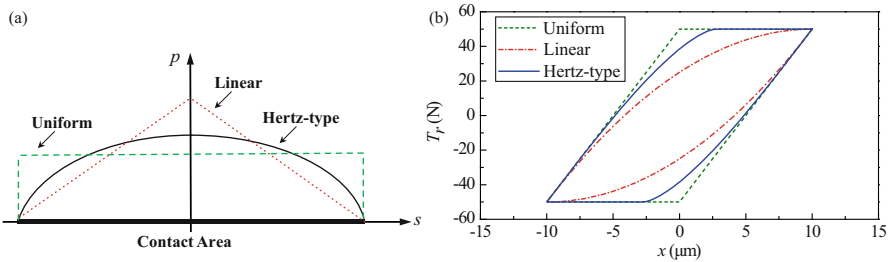
Fig. 1 (**a**) Three distribution forms of contact pressure, (**b**) hysteresis loops

simulated hysteresis loops for the above three distributions. The model with uniform pressure distribution is the first one reaching slip state with increasing relative displacement and has the maximum energy dissipation. The damping predicted by the Hertzian distribution model is moderate, compared with the other two. The linear distribution model is the last one to reach slip state and has minimum predicted damping which is 30% lower than that of the first one. Therefore, it can be concluded that contact pressure distribution has an important effect on prediction results.

On blade damper contact surface, normal load is variable and intermittent separation is possible for some dampers. To extend the proposed model to include the representation of normal load variation and intermittent separation, a unilateral linear spring with detachment is applied. Similar process can be found in ref. [8].

3 Experimental Validation in an Underplatform Damper Test Rig

3.1 Review of an Asymmetric Damper

A laboratory "crossed curve-flat damper" was designed in ref. [10], which includes a cylinder-to-flat contact on the left side and a flat-to-flat contact on the right side, as shown in Fig. 2. The damper is placed between the two platforms by centrifugal force (CF). The friction forces transmitted from the left blade to the right one through the damper are measured by two load cells placed orthogonally, shown in Fig. 2b. The relative displacements between the two blades are measured using two laser Doppler vibrometers. This test rig can reproduce two main representative blade motions: Out of Phase (OoP), imposing a horizontal relative motion between the platforms, and In Phase (IP), a vertical relative motion. The IP motion has been studied in ref. [8]; therefore, in this chapter, only OoP motion is studied, which can be regarded as a supplement.
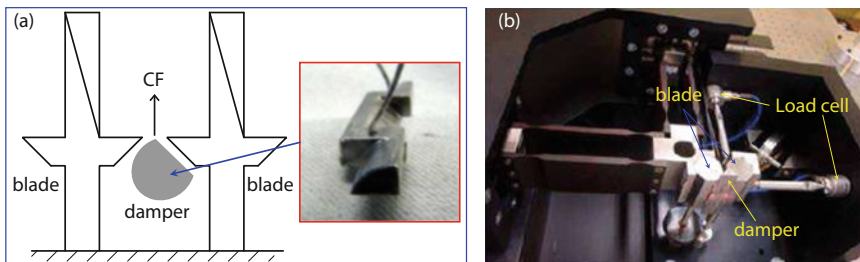
Fig. 2 (**a**) The turbine blade damper model, (**b**) experimental setup in ref. [10]

3.2 Model Parameters Estimation Approach

To validate the proposed model, a group of measured results for micro-slip are selected. In this case, piezo-actuator nominal displacement was a cosine motion with 10 μm amplitude, and the frequency was set to 5 Hz. The deadweight mass simulating the centrifugal force was 4.65 kg.

The 450th measured cycle (90s) is taken as an example to show the contact parameters estimation procedure and validate the proposed model. First, friction coefficients are estimated according to experimental data. Figure 3a depicts the ratios of tangential force over normal force on two surfaces. In this case the flat contact surface experiences a gross slip motion at the stages s2–s3 and s4–s1 because the ratio of tangential over normal force is approximately invariant. While for the curved surface, the ratio keeps variable during a period. Therefore, the ratio on the flat surface in gross slip state is regarded as corresponding friction coefficient. The obtained friction coefficient averages the ratios at stage s2–s3 and s4–s1, $\mu_R = 0.21$.

From experimental results, it just can be known that the friction coefficient on the curved surface is larger than the highest ratio, $\mu_L > 0.34$. Reference [10] concluded that friction coefficient has a decisive effect on the range of the force in the hysteresis loop. Therefore, the friction coefficient μ_L on the curved surface can be estimated by matching the relative height of numerical hysteresis loop with that of experiment. The contact stiffness values obtained in IP motion are employed for the OoP case to implement initial numerical simulation. Figure 3b illustrates numerical hysteresis loops for different friction coefficients on the curved surface and shows that the relative height of horizontal force gradually increases with increasing μ_L. Matching the relative range of horizontal force with the experimental counterpart, an optimal friction coefficient can be selected, $\mu_L = 0.36$.

After estimating friction coefficients, the values of contact stiffness will be estimated. When the input displacement is very small, the surface is in stick state, and the relation between relative displacement and force on surfaces can be regarded
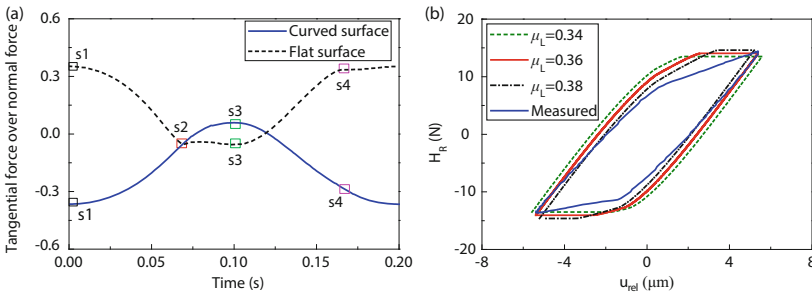
Fig. 3 (a) The experimental tangential force over normal force on each surface at the 450th cycle, (b) hysteresis loops for selecting friction coefficient on curved surface

as linear. Therefore, the relation between contact stiffness and measured variables can be derived according to the equilibrium equations of the system, which can be found in ref. [8].

Figure 4a depicts the measured vertical force V_R versus the horizontal force H_R. The initial slopes of this curve in loading and unloading average at $V_R/H_R = 0.154$. Figure 4b depicts the measured horizontal force H_R versus horizontal relative displacement u_{rel}, and the average initial slope of the curve V_R/w_{rel} equals 4.516×106 N/m. Based on experiments and a classical genetic algorithm, a dedicated contact stiffness estimation procedure is developed. The objective function is min $\{|A_{num-exp}/A_{exp}|\}$, where $A_{num-exp}$ denotes the difference of enclosed areas between simulated and experimental cycles. The design variables are δ_R and δ_L. The bar chart in Fig. 5a depicts optimized results and displays variation of $|A_{num\_exp}|/A_{exp}$ with sampling generation. It shows that the relative error gradually decreases with sampling generation and reaches a steady state with the minimum error after evolution of nine generations. Contact parameters are listed in upper right corner of Fig. 5a. The parameters, δ_R and δ_L, denote a proportional relationship between tangential and normal stiffness.
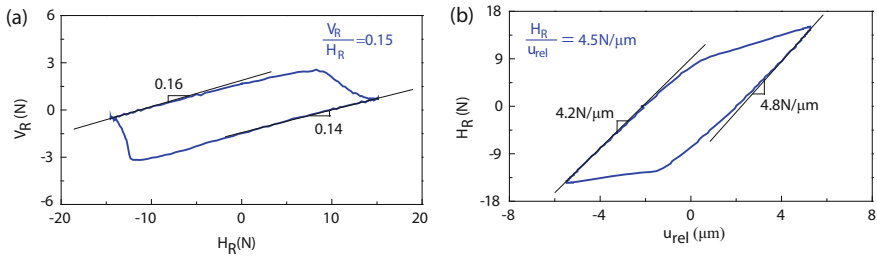
Fig. 4 (**a**) Measured vertical force V_R versus measured horizontal force H_R, (**b**) measured horizontal force H_R versus horizontal relative platforms displacement u_{rel}
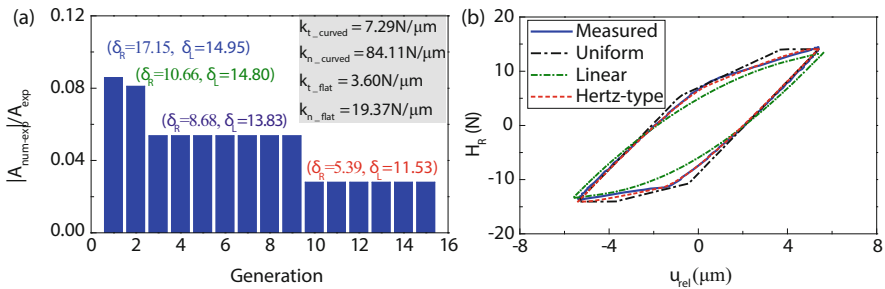
Fig. 5 (**a**) Random sampling for the determination of contact stiffness, (**b**) comparison of numerical simulations with experiments

Table 1 Energy dissipation and equivalent elastic stiffness

	Experiment	Uniform	Linear	Hertz type
Area (μJ)	91.1	102.3	80.5	90.4
K_R(N/μm)	1.4553	1.4761	1.3666	1.4549

3.3 Numerical Results and Discussions

Contact parameters tuned above are employed to implement numerical simulations which are compared with experimental results to validate the proposed model. Iwan models with uniform and linear contact pressure distributions are also studied to find the effect of pressure distribution on dynamic response of the blade damper system. Figure 5b depicts the numerical and experimental hysteresis loops in OoP case. The numerical loop simulated by the Hertzian distribution model matches well with the experimental counterpart. The amplitude of relative displacement predicted by the linear distribution model is larger than those by the other models, while the horizontal force is lower. The linear distribution model is easy to handle. The hysteresis loop predicted by uniform distribution model encloses more area than that of the other loops. To compare these results more obviously, some characteristic variables are extracted from the dynamic response of the damper.

Table 1 lists areas enclosed by hysteresis loops and K_R to give more evidences for model validation and comparison. Here, K_R represents equivalent elastic stiffness in this case, which can be derived by a truncated Fourier term of horizontal force divided by input displacement [8]. Obviously, the relative differences of these two characteristic variables between experiment and simulation by the developed model is less than 1%, which validates the model well. Therefore, a conclusion can be drawn that the proposed model considering Hertz-type pressure distribution can realize a high accuracy prediction for cylindrical contact surface in blade damper system. The uniform distribution model predicts maximum energy dissipation, as mentioned above, and the relative difference reaches +12.3%. The linear pressure distribution model has a conservative prediction of energy dissipation with a −11.6% relative difference. The prediction of equivalent elastic stiffness by linear pressure distribution model behaves softer than the other two, with a −6.1% relative difference.

4 Conclusions

In this work, the original Iwan model is modified to include the effect of Hertzian contact pressure. The relation between contact pressure distribution and the PDF of the slider sliding force of the Iwan model is built. Quasi-static analyses are conducted to compare the hysteresis loops predicted by models with different pressure distribution forms. The results show that the relative difference of energy dissipation caused by pressure distribution can reach 30% in some cases.

A laboratory asymmetrical damper test is used to validate the effectiveness of the proposed model. A corresponding parameter estimation procedure is developed to characterize friction contact. Comparison of numerical simulations with the experimental results shows that the proposed model has good prediction capability for the contact mechanics of the asymmetric under-platform damper.

References

1. Griffin, J.H.: Friction damping of resonant stresses in gas turbine engine airfoils. J. Eng. Power. **102**, 329–333 (1980)
2. Petrov, E.P., Ewins, D.J.: Advanced modelling of underplatform friction dampers for analysis of bladed disk vibration. J. Turbomach. **129**(1), 143–150 (2007)
3. Panning, L., Popp, K., et al.: Asymmetrical underplatform dampers in gas turbine bladings: theory and application. In: Paper No. GT2004-53316, ASME Turbo Expo (2004)
4. Yang, B.D., Chu, M.L., Menq, C.H.: Stick–slip–separation analysis and non-linear stiffness and damping characterization of friction contacts having variable normal load. J. Sound vib. **210**(4), 461–481 (1998)
5. Menq, C.H., Bielak, J., Griffin, J.H.: The influence of micro-slip on vibratory response, part I: a new micro-slip model. J. Sound Vib. **107**(2), 279–293 (1986)
6. Ciğeroğlu, E.A., Menq, N., H, C.: A micro-slip friction model with normal load variation induced by normal motion. Nonlinear Dyn.**50**, 609–626 (2007)
7. Gastaldi, C., Gola, M.M.: On the relevance of a micro-slip contact model for under-platform dampers. Int. J. Mech. Sci. **115**, 145–156 (2016)
8. Li, D., Xu, C., et al.: A modified Iwan model for micro-slip in the context of dampers for turbine blade dynamics. Mech. Syst. Signal Process. **121**, 14–30 (2019)
9. Iwan, W.D.: A distributed-element model for hysteresis and its steady-state dynamic response. J. Appl. Mech. **33**, 893–900 (1966)
10. Liu, T.: Investigation of under-platform damper kinematics and dynamics. PhD thesis, Politecnico di Torino (2013)

Finite-Time Control of Omnidirectional Mobile Robots

Mirosław Galicki

Abstract In the present work, a new task space nonsingular terminal sliding mode (TSM) manifold defined by nonlinear integral equation of the first order with respect to the task tracking error and a variant of the computed torque method are introduced to control a four mecanum wheeled mobile robot (FMWMR). By fulfilment of a reasonable assumption regarding the estimate of the actuation matrix, the proposed control scheme is shown to be finite-time stable despite uncertain dynamic equations and (globally) unbounded disturbances acting on the FMWMR. Moreover, the proposed control law provides (instantaneous) optimal solution. The numerical simulation results illustrate both the performance of the proposed scheme and simultaneously its minimizing property for some practically useful objective function.

Keywords Mobile robots · Trajectory tracking · Finite-time control

1 Introduction

In recent years, an interest in a special class of omnidirectional wheeled mobile robots has increased due to their particular abilities. The four mecanum wheeled mobile robots (FMWMR) belong to such class of vehicles which are mathematically described by holonomic dynamic systems. FMWMRs can move in sideways and even along curved trajectories (paths) without changing their orientation. These advantages make it possible to accomplish complicated tasks such as materials (objects) handling or safe manoeuvring in parts stockrooms, which require, by their nature, high precision and stability of the performance. However, due to the use of redundant number of separate actuators with respect to the trajectory tracking task, the control of FMWMRs becomes complicated. In addition, a

M. Galicki (✉)
University of Zielona Góra, Zielona Góra, Poland
e-mail: M.Galicki@ibem.uz.zgora.pl

controller to be designed for the FMWMR should accurately and stably track desired trajectory expressed in task coordinates despite uncertain dynamics and (globally) unbounded unknown external disturbances. Due to the challenging nature of the aforementioned control design problems, many researchers have proposed different types of controllers. In such a context, one can distinguish a few algorithms of controlling the FMWMR, which only partially meet the expectations of modern controllers. The control techniques offered in works [1–5] present robust [1–3] and/or adaptive [4, 5] algorithms that are capable of trajectory tracking. However, the approaches from [1–3] require full knowledge of dynamic equations and are not optimal in any sense. Work [4] involves adaptive term multiplied by the regression matrix that seems to be both complex to implement and time consuming and work [5] requires the knowledge of the nominal dynamics whose construction may not be a trivial task. In the present work, a new task space non-singular terminal sliding mode (TSM) manifold of the first order is introduced to control FMWMR. The main drawback of the standard first-order sliding modes is mostly related to the undesirable chattering effect [6]. In order to eliminate (or to alleviate) the chattering, the robust sliding mode controllers based on the higher-order sliding techniques have been used [7, 8], which cannot be applied to discontinuous disturbances (e.g. the Coulomb or Stribeck terms) and/or to continuous and everywhere non-differentiable disturbances (e.g. to a Brownian motion). Based on the non-singular first-order TSM manifold introduced, we propose a new robust model-free controller acting in the task (Cartesian) space. By fulfilment of a reasonable assumption regarding the estimate of the actuation matrix, the proposed control scheme is shown to be finite-time stable despite uncertain dynamic equations and (globally) unbounded disturbances. On the other hand, works [1–3] require full knowledge of FMWMR dynamics. Moreover, as opposed to other exiting approaches (see, e.g., [1–4]) utilizing the sliding variables, the proposed control law provides (instantaneous) optimal solution. Furthermore, adaptive control algorithm given in [5] is not also optimal and neglects external disturbances. In order to eliminate the undesirable chattering effect, we propose herein a continuous control law based on the use of a known technique of boundary layer, which is also shown to possess in our case (non-linear sliding manifold as well as uncertain non-diagonal actuation matrix) a desirable property of ultimate uniform boundedness. The paper is organized as follows. Formulation of the finite-time optimal control of FMWMR is presented in Sect. 2. Section 3 sets up a class of task space robust controllers solving the trajectory tracking problem in a finite time. Section 4 presents computer simulation of the trajectory tracking. Finally, some concluding remarks are drawn in Sect. 5.

2 Problem Formulation

Consider a four mecanum wheeled mobile robot (FMWMR) whose dynamic equations, expressed in task coordinates, are given below [1–3]

$$\ddot{x} = A(x)u + F(x, \dot{x}) + D(t, x, \dot{x}), \tag{1}$$

where $x = (x_{1,c}, x_{2,c}, \theta)^T$ is the vector of task coordinates; $(x_{1,c}, x_{2,c})$ denotes location of the mass centre with respect to a global coordinate system and θ stands for orientation of the mobile platform; $A(x)$ is 3×4 non-singular actuation matrix; $F(x, \dot{x})$ represents, in general, vector of viscous damping forces; $u = (u_1, u_2, u_3, u_4)^T$ stands for vector of controls and $D(t, x, \dot{x})$ denotes external disturbing signal. In further considerations, D is assumed to be a locally bounded Lebesgue measurable mapping which is upper estimated as follows:

$$||D(t, x, \dot{x})|| \leq \alpha(t, x, \dot{x}), \tag{2}$$

where α is a non-negative and locally bounded Lebesgue measurable function. Let us observe that dynamic system (1) represents a redundant mechanism with respect to vector of controls u. Consequently, from the practical point of view, it is particularly desirable to generate robot trajectory $x = x(t)$, $t \geq 0$ in such a way as to minimize an objective function $\mathcal{F}$. We employ a simple and practically useful optimization criterion for redundancy resolution with the following cost function:

$$\mathcal{F}(u) = \frac{1}{2}\langle u, \ u\rangle, \tag{3}$$

where $\langle, \ \rangle$ denotes scalar product of vectors. The aim is to find control $u = u(t)$ which (instantaneously) minimizes performance index (3) and simultaneously robot trajectory $x = x(t)$, corresponding to u, exactly follows a given desired trajectory $x_d(t) \in \mathbb{R}^3$. Mapping $x_d(\cdot)$ is assumed in further analysis to be at least twice continuously differentiable, i.e. $x_d(\cdot) \in C^2[0, \infty)$. Let us define the task tracking error e as $e = x - x_d$. Utilizing the task error e, the finite-time control problem of the FMWMR may now be formally expressed as follows:

$$\lim_{t \to T} e(t) = 0, \qquad \lim_{t \to T} \dot{e}(t) = 0, \tag{4}$$

where $0 \leq T < \infty$ stands for a finite time of convergence of $x(t)$ to $x_d(t)$ and $e(t) = \dot{e}(t) = 0$ for $t \geq T$. Based on expressions (1)–(4) and the Lyapunov stability theory, a controller solving the robotic task (4) will be proposed in the next Section.

3   (Instantaneously) Optimal Control of FMWMR

For purpose of further considerations, some properties of dynamic equations (1) are given below. Utilizing inequality (2), the norm of the sum of uncertain term $F(x, \dot{x})$ and unknown disturbing signal $D(t, x, \dot{x})$ may be upper estimated as follows

$$||F(x, \dot{x}) + D(t, x, \dot{x})|| \leq w_1(||\dot{x}|| + 1) + \alpha(t, x, \dot{x}), \tag{5}$$

where w_1 is a given positive coefficient (construction parameter of the FMWMR). If $\alpha(t, x, \dot{x})$ is unknown constant function, i.e. $\alpha(t, x, \dot{x}) = \alpha_{\max} = \text{const}$ then expression (5) may be simplified in the following way:

$$||F(x, \dot{x}) + D(t, x, \dot{x})|| \leq w_2(||\dot{x}|| + 1), \tag{6}$$

where $w_2 = w_1 + \alpha_{\max}$. In order to propose the controller solving the robotic task (4), we introduce the following non-singular non-linear terminal sliding vector variable $s = (s_1, s_2, s_3)^T \in \mathbb{R}^3$, defined in task coordinates as follows:

$$s = \dot{e} + \int_0^t \left(\lambda_0 e^{\alpha_1} + \lambda_1 (\dot{e})^{\alpha_2} \right) d\tau, \tag{7}$$

where $\alpha_1 = \frac{a}{b}$; a, b are positive odd numbers, $a < b < 2a$, $\alpha_2 = \frac{2\alpha_1}{1+\alpha_1}$; λ_0, λ_1 stand for controller gains. Let us note that for a particular case, i.e. $\alpha_1 = \alpha_2 = 1$, expression (7) presents a classic linear PID sliding manifold. In further analysis, a useful lemma will be given [9].

Lemma 1 *If $s(t) = 0$ for $t \geq T \geq 0$ then task errors $(e, \dot{e})$ of (7) stably converge to the origin $(e, \dot{e}) = (0, 0)$ in a finite time.*

Let $\hat{A}(x)$ be a non-singular non-adaptive matrix, which estimates uncertain non-singular actuation matrix $A(x)$. Moreover, $\hat{A}(x)$ is assumed to fulfil the following practically reasonable inequality:

$$||\hat{A}(x) - A(x)||_F \leq \frac{\rho}{||\hat{A}^\#||_F}, \tag{8}$$

where $0 \leq \rho < 1$ denotes the accuracy of the approximation; $|| \cdot ||_F$ stands for the Frobenius (Euclidean) matrix norm; $\hat{A}^\#$ is the Moore–Penrose pseudo-inverse of $\hat{A}$. Based on (3) and (5)–(8), we propose the following simple control law of FMWMR solving the kinematic task (4):

$$u(t, x, s) = \begin{cases} -c\hat{A}^\# \frac{s}{||s||}(\mathcal{R} + c') & \text{for } s \neq 0 \\ 0 & \text{otherwise,} \end{cases} \tag{9}$$

where c, c' denote controller gains to be specified further on; $\mathcal{R} = w_1(||\dot{x}|| + 1) + \alpha + ||\lambda_0 e^{\alpha_1} + \lambda_1 (\dot{e})^{\alpha_2} - \ddot{x}_d||$ (or $\mathcal{R} = w_2(||\dot{x}|| + 1) + ||\lambda_0 e^{\alpha_1} + \lambda_1 (\dot{e})^{\alpha_2} - \ddot{x}_d||$ for $\alpha = \alpha_{\max} = \text{const}$). The aim is to provide conditions on controller gains λ_0, λ_1, c and c', which guarantee fulfilment of equalities (4). Applying the Lyapunov stability theory, we now derive the following result.

Theorem 1 *If λ_0, λ_1, $c' > 0$ and $c > \frac{1}{1-\rho}$ then control scheme (1), (9) guarantees stable convergence in a finite time of the task tracking errors $(e, \dot{e})$ to the origin $(e, \dot{e}) = (0, 0)$. Moreover, control u (instantaneously) minimizes performance index (3).*

Proof Consider the following Lyapunov function candidate:

$$V = \frac{1}{2}\langle s, s \rangle. \tag{10}$$

Computing the time derivative of (10) and taking into account definition (7) results in the following expression:

$$\dot{V} = \langle s, \ddot{e} + \lambda_0 e^{\alpha_1} + \lambda_1 (\dot{e})^{\alpha_2} \rangle. \tag{11}$$

Based on (1) and definition of e, one obtains that

$$\ddot{e} = A(x)u + F(x, \dot{x}) + D(t, x, \dot{x}) - \ddot{x}_d. \tag{12}$$

Inserting the right-hand side of (12) into (11) results in the formula given below

$$\dot{V} = \langle s, A(x)u \rangle + \langle s, F(x, \dot{x}) + D(t, x, \dot{x}) - \ddot{x}_d + \lambda_0 e^{\alpha_1} + \lambda_1 (\dot{e})^{\alpha_2} \rangle. \tag{13}$$

Let us reformulate (13) to the following equivalent useful form:

$$\dot{V} = \langle s, \hat{A}(x)u \rangle + \langle s, (A(x) - \hat{A}(x))u \rangle + \langle s, F(x, \dot{x}) + D(t, x, \dot{x}) - \ddot{x}_d + \lambda_0 e^{\alpha_1}$$
$$+ \lambda_1 (\dot{e})^{\alpha_2} \rangle. \tag{14}$$

Our aim is to minimize criterion function (3) subject to the following equality constraint:

$$\hat{A}(x)u = -c\frac{s}{||s||}(\mathcal{R} + c'). \tag{15}$$

As is easy to see, the solution to (instantaneous) optimization problem (3), (15) takes the form of control (9). Let us upper estimate the last scalar product in (14). On account of inequalities (5)–(6), we have

$$\langle s, F(x, \dot{x}) + D(t, x, \dot{x}) - \ddot{x}_d + \lambda_0 e^{\alpha_1} + \lambda_1 (\dot{e})^{\alpha_2} \rangle \leq ||s||\mathcal{R}. \tag{16}$$

The next step is to replace u in (14) by the right-hand side of (9) and to utilize relationship (16). The result is the following inequality:

$$\dot{V} \leq -c\left\langle s, \hat{A}\hat{A}^{\#}\frac{s}{||s||}(\mathcal{R} + c')\right\rangle - \left\langle s, (A - \hat{A})c\hat{A}^{\#}\frac{s}{||s||}(\mathcal{R} + c')\right\rangle + ||s||\mathcal{R}. \tag{17}$$

On account of (8), we have

$$\dot{V} \leq -||s||c'c(1 - \rho) + ||s||\mathcal{R}(1 - c + c\rho). \tag{18}$$

Based on the assumption of Theorem 1 for c and the fact that $\rho \in [0, 1)$ (see the comment immediately below relation (8)), the last term of the right-hand side of inequality (18) is non-positive, i.e. $||s||\mathcal{R}(1 - c + c\rho) \leq 0$. Hence,

$$\dot{V} \le -||s||c'c(1 - \rho). \tag{19}$$

On account of the fact that $cc'(1-\rho) > 0$, inequality (19) proves that TSM manifold $s = 0$ is stably attainable in a finite time less or equal to $\sqrt{\frac{2V(0)}{cc'(1-\rho)}}$. Finally, from Lemma 1, it follows that origin $(e, \dot{e}) = (0, 0)$ can be attained in a finite time.

A few remarks may be made regarding the control law (9) and Theorem 1.

- Remark 1. Let us note that non-singular sliding variable s has useful property for a typical regulation task with $\dot{e}(0) = 0$, which implies $s(0) = 0$. In such a case, from (19) and (10), it follows that $V(t) = 0$ and consequently $s(t) = 0$ for $t \ge 0$ (TSM manifold $s = 0$ is attainable for $t = 0$).
- Remark 2. The term $\frac{s}{||s||}$ in controller (9) will cause undesirable chattering effect in a small neighbourhood of $s = 0$. In order to eliminate the chattering, a known boundary layer technique of control law may now be utilized as follows:

$$u(t, x, s, \epsilon) = \begin{cases} -c\hat{A}^{\#} \frac{s}{||s||}(\mathcal{R} + c') & \text{for } ||s|| \ge \epsilon \\ -c\hat{A}^{\#} \frac{s}{\epsilon}(\mathcal{R} + c') & \text{otherwise,} \end{cases} \tag{20}$$

where ϵ is a user-specified arbitrarily small positive real number. Let $e = e(t, \epsilon)$ and $\dot{e} = \dot{e}(t, \epsilon)$ be the solutions of control problem (1), (7) and (20). Although boundary layer control is a well-known technique, its desired property of uniform ultimate boundedness has been established for linear sliding variables s, e, $\dot{e}$ and diagonal actuation matrices of non-zero diagonal components (or of constant signs) in [10] as well as for dynamic systems fulfilling the so-called matching conditions with known actuation matrices in work, e.g. [11], respectively. On the other hand, expression (7) is a non-linear differential equation with respect to $e = e(t, \epsilon)$ and $\dot{e} = \dot{e}(t, \epsilon)$. Moreover, $A(x)$ is uncertain non-diagonal actuation matrix. Consequently, the classic results regarding the ultimate uniform boundedness of $e = e(t, \epsilon)$ and $\dot{e} = \dot{e}(t, \epsilon)$ may not, in general, apply in our case. Hence, based on the recent results from our work [9], we may conclude that task errors $e = e(t, \epsilon)$, $\dot{e} = \dot{e}(t, \epsilon)$ converge uniformly with respect to time t ($t \ge T$) to the origin $(e, \dot{e}) = (0, 0)$ as $\epsilon \to 0$, i.e. $e(t, \epsilon)$, $\dot{e}(t, \epsilon) \to 0$ as $\epsilon \to 0$.
- Remark 3. Let us note that controller (9) or (20) depends on construction parameter w_1 or w_2 whose determination may not be easy task in practice. Let $\hat{w}_2$ be an estimate of unknown parameter w_2 (without loss of generality and for shortening the analysis, we consider only the case of completely unknown and bounded disturbing signal D, i.e. $\alpha(t, x, \dot{x}) = \alpha_{\max}$). If this is the case, we propose the following adaptive version of control law (9):

$$u(t, x, s, \hat{w}_2) = \begin{cases} -c\hat{A}^{\#} \frac{s}{||s||}(\hat{\mathcal{R}} + c') & \text{for } s \ne 0 \\ 0 & \text{otherwise,} \end{cases} \tag{21}$$

where $\hat{\mathcal{R}} = \hat{w}_2(||\dot{x}|| + 1) + ||\lambda_0 e^{\alpha_1} + \lambda_1(\dot{e})^{\alpha_2} - \ddot{x}_d||$ and

$$\dot{\hat{w}}_2 = \frac{c(1 - \rho)}{k_{w_2}}||s||(||\dot{x}|| + 1), \tag{22}$$

k_{w_2} stands for positive adaptive gain. We are now in position to give the following theorem.

Theorem 2 *If assumptions regarding λ_0, λ_1, c' and c of Theorem 1 are satisfied and $\hat{w}_2$ is computed from (22) then control scheme (21)–(22) guarantees stable convergence in a finite time of task errors $(e, \dot{e})$ to the origin $(e, \dot{e}) = (0, 0)$. Moreover, controller (21)–(22) instantaneously minimizes criterion function (3).*

Proof The proof of Theorem 2 with Lyapunov function candidate $V = \frac{1}{2}||s||^2 + \frac{k_{w_2}}{2}\tilde{\alpha}^2$, where $\tilde{\alpha} = \hat{w}_2 - w_2$, is a small modification of the proof of Theorem 1. Therefore, it is omitted.

4   Computer Simulations

The aim of this section is to demonstrate the performance of one of the controllers given by expressions (9), (20), (21)–(22). From the practical point of view, it seems both interesting and reasonable to test continuous (chattering free) controller (20) with $\alpha(t, x, \dot{x}) = \alpha_{\max}$. Moreover, both a quantitative and qualitative comparison of our control law to other well-known control algorithms is also carried out. For this purpose, we utilize a dynamic model of FMWMR presented, e.g., in works [1–3]. In computer simulations, the SI units are used. The components of the nominal dynamic equations take the following values (see [1–3]): mass of the mobile platform $m = 6$; moment of inertia of the platform $I = 0.0945$; radius of the wheel $R = 0.05$; length of the mobile platform $2L = 0.22$; width of the mobile platform $2W = 0.36$; coefficients of viscous friction $\beta_{x_1} = \beta_{x_2} = \beta_\theta = 0.02$. The exact form of actuation nominal matrix $A(x)$ and vector $F(x, \dot{x})$ are given in [1–3]. Initial configuration $x(0)$ and velocity $\dot{x}(0)$ are equal to $x(0) = (0, 0, 0)^T$, $\dot{x}(0) = (0, 3, 0)$, respectively. Our rough estimates for controller (20) are chosen as $w_2 = 0.7$, $\rho = 0.15$. The estimate of uncertain actuation matrix $A(x)$ equals

$$\hat{A}(x) = A(x) + \begin{bmatrix} 0.9 & -0.6 & 0.9 & -0.6 \\ -0.6 & -0.9 & 0.6 & -0.9 \\ -14 & 14 & 14 & -14 \end{bmatrix}. \tag{23}$$

The task is to track a desired trajectory (flower trajectory) expressed by the following equation:

$$x_d(t) = (10\sin(0.3t - \pi)\sin(0.2t - \pi), \ 10\sin(0.3t - \pi)\cos(0.2t - \pi), \ 0)^T. \tag{24}$$

Moreover, our aim is to show that (instantaneously) optimal controller (20) is robust against disturbance signal $D \neq 0$. For this purpose, the discontinuous bounded term D of the form $D = (0, 0, 0)^T$ for $t \in [0, 7]$, $D = (0, 1, 1)^T$ for $t \in (7, 10]$, $D = (0, 0, 0)^T$ for $t \in (10, 20]$, $D = (0.5, 0, 0)^T$ for $t \in (20, 26]$, $D = (0, 0, 0)^T$ for $t \in (26, 40]$, $D = (0, 0.5 \sin(2t), 0)^T$ for $t \in (40, 60]$, $D = (0, 0.5 \sin(2t), 0.5 \sin(2t))^T$ for $t \geq 60$ has been added to dynamic equations. In order to attain the convergence of task error e less than 10^{-3}, the following numerical values of gain coefficients are taken: $\lambda_0 = 10$; $\lambda_1 = 5$; $c' = 1$; $c = 1.2$, $\alpha_1 = \frac{3}{5}$ and $\epsilon = 0.1$, respectively. The results of the simulation are given in Figs. 1 and 2, which indicate a good tracking performance of controller (20) (see Fig. 1). The corresponding torques u are depicted in Fig. 2. The peaks in Figs. 1 and 2 are result of acting the discontinuous disturbance signal D.

Fig. 1 Task errors e versus time
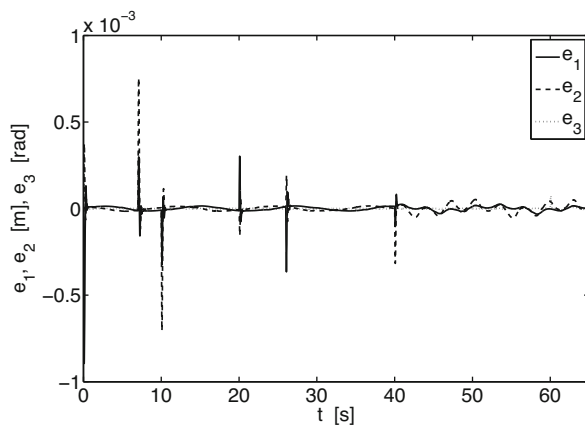
Fig. 2 Controls u versus time
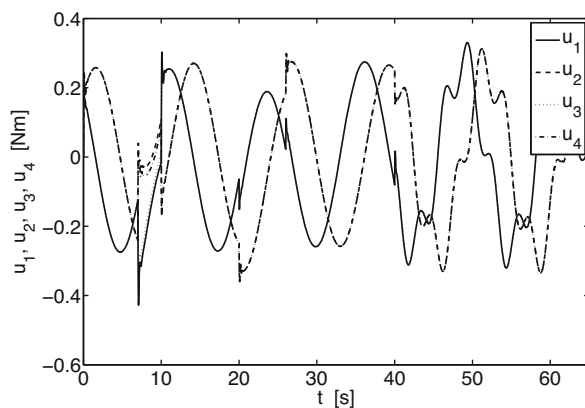
5 Conclusions

A new class of robust and optimal task space controllers for FMWMRs has been proposed. Applying the Lyapunov stability theory, control strategies (9), (21)–(22) are shown to be finite-time stable. Although our controllers need knowledge about the system equation of the FMWMR, the approach is able to handle uncertainties in dynamics and disturbances occurring in the holonomic system. Let us observe that our controller seems to be superior to the flatness-based control from work [1] in the accuracy of the trajectory tracking. Moreover, the control scheme given by Eq. (20) results also in significantly smaller torques than those obtained in [1] for the same desired trajectory. It is also worth to note that optimal control law (20) utilizes only estimated actuation matrix $\hat{A}(x)$ while control algorithms from works [1–3] require the full knowledge of dynamic equations. Finally, the values of controller gains in [1–3] are found by means of off-line time consuming optimization procedure while coefficients λ_0, λ_1, c and c' are directly given from Theorem 1.

References

1. Sahoo, S.R., Chiddarwar, S.S., Alakshendra, V.: Intuitive dynamic modelling and flatness-based nonlinear control of a mobile robot. Simulation (2017). https://doi.org/10.1177/0037549717741192
2. Alakshendra, V., Chiddarwar, S.S.: Adaptive robust control of Mecanum-wheeled mobile robot with uncertainties. Nonlinear Dyn. **87**(4), 2147–2169 (2017)
3. Alakshendra, V., Chiddarwar, S.S.: A robust adaptive control of mecanum wheel mobile robot: simulation and experimental validation. In: IEEE/RSJ International Conference on Intelligent Robots and Systems (IROS), Daejeon, pp. 5606–5611 (2016)
4. YaChao, Y., ChiCheng, C.: Robust adaptive trajectory control for an omnidirectional vehicle with parametric uncertainty. Trans. Can. Soc. Mech. Eng. **37**(3), 405–413 (2013)
5. Lin, L.-C., Shih, H.-Y.: Modeling and adaptive control of an omni-mecanum-wheeled robot. Intell. Control. Autom. **4**(2), 166–179 (2013)
6. Fridman, L.: Singularly perturbed analysis of chattering in relay control systems. IEEE Trans. Autom. Control **47**(12), 2079–2084 (2002)
7. Defoort, M., Floquet, T., Kokosy, A., Perruquetti, W.: Higher order sliding modes in collaborative robotics. In: Lecture Notes in Control and Information Sciences Book Series (LNCIS), vol. 412, pp. 409–437 (2017)
8. Galicki, M.: Finite-time control of robotic manipulators. Automatica **51**, 49–54 (2015)
9. Galicki, M.: Constraint finite-time control of redundant manipulators. Int. J. Robust Nonlinear Control **27**(4), 639–660 (2016)
10. Slotine J.J., Li, W.: Applied nonlinear control. Prentice Hall, Upper Saddle River (1991)
11. Brogliato, B., Neto A.T.: Practical stabilization of a class of nonlinear systems with partially known uncertainties. Automatica **31**(1), 145–150 (1995)

Fast Moving of a Population of Robots Through a Complex Scenario

Leandro Nesi, Dario Antonelli, Gianluca Pepe, and Antonio Carcaterra

Abstract Swarm robotics uses a large number of coordinated autonomous robots, or agents, to accomplish one or more tasks, using local and/or global rules. Individual and collective objectives can be designed for each robot of the swarm. Generally, the agents' interactions exhibit a high degree of complexity that makes it impossible to skip nonlinearities in the model. In this chapter, both a collective interaction using a modified Vicsek model where each agent follows a local group velocity and the individual interaction concerning internal and external obstacle avoidance are implemented. The proposed strategies are tested for the migration of a unicycle robot swarm in an unknown environment, where the effectiveness and the migration time are analyzed. To this aim, a new optimal control method for nonlinear dynamical systems and cost functions, named Feedback Local Optimality Principle—FLOP, is applied.

Keywords Swarm robotic · Swarm migration · Adaptive velocity strategy

1 Introduction

Swarm robotics is aimed at using the coordination of many robots. It is generally inspired by the observation of the natural world, such as a flock of birds, ant colonies, and school of fishes. The study of collective animal behavior is still a source of inspiration for scientists and engineers, who, by imitating biological processes, seek solutions to complex problems.

Among many, the study and analysis of the migration and transport of swarm of robots are of interest. Through the study of stigmergy [1], it is possible to identify

L. Nesi · D. Antonelli · G. Pepe · A. Carcaterra (✉)
Department of Mechanical and Aerospace Engineering, Sapienza University of Rome, Rome, Italy
e-mail: leandro.nesi@uniroma1.it; dario.antonelli@uniroma1.it; gianluca.pepe@uniroma1.it; antonio.carcaterra@uniroma1.it

the interaction processes that give rise to intelligent cooperative systems, capable of performing complicated collective operations.

In nature, agents follow very simple rules, and even without the need for centralized control, global behavior emerges, unknown to the individual agents, who can find efficient methods of transport and migration. One of the first efficient collective transport is given by the Vicsek particle model in which each agent follows a collective group velocity [2, 3]. This model is widely used to imitate the movement of shoals of fish and swarms of birds that manage to move in a coordinated way, following environmental stimuli. Based on this model, many studies have been developed concerning the coordinated collective transport of robots [3–6]. In particular, the generalization of the Vicsek model to robot movement concerns two types of models: (a) a first class does not involve anti-collision rules allowing for collisions between robots [5] and (b) a second class uses sophisticated sensors and communication hardware that make the swarm collision-free [6].

In this chapter, the used communication template presents simplifications with respect to a fully all-to-all connected system, balancing short-range and long-range transmission of information within the swarm. This gives the possibility to equip the robots with exteroceptive sensors present on the market in such a way as to analyze the state of the agents around them and implement the actions provided by the control strategy. Furthermore, appropriate control logics introduce effective anti-collision rules between agents. For this reason, a method of analyzing information from neighboring agents is proposed, which combines the most significant aspects of the simplified analysis of the first neighbors only and the complete global analysis. The proposed navigation system of a swarm of robots is divided into two main categories: collective exploration and coordinated motion. Here, unicycle robots [7] move in an unknown environment and navigate without internal collisions with other agents, trying to migrate from a start to a target zone using the information provided by the neighbors' agents to reduce the migration time. These different tasks are achieved by using innovative feedback controls developed by authors, named Feedback Local Optimality Principle (FLOP) and Variational Feedback Controls (VFC) [8–10]. The FLOP method controls linear and nonlinear dynamical systems, through the introduction of a nonlinear penalty in the cost function. This permits to apply simultaneously the collective exploration and the coordinated motion strategies. The environment is made by lowlands and hills, as the case, for example, of sand dunes. Robots are subjected to attractive and repulsive forces dependent on the terrain orography. The distributed control uses only local velocity information to drive the members of the swarm in a small region where the signal velocity is captured. The agents follow a nonlinear control strategy where each of them is tracking a target velocity resulting in a directional averaging operation. This process is mimicking the behavior of ant colonies in which the information travels with pheromones permitting to move around obstacles of various types together with a high migration speed.

This chapter intends to show the ability of the FLOP method to control a large population of cooperative agents to complete the exploration within an unknown scenario.

The FLOP logic has the advantage of operating in pure feedback, ensuring a local minimum result. The present method, although does not reach the global minimum of the cost function, exhibits large computational advantages when compared to predictive control strategies. This has been already tested in complex systems like autonomous drive terrestrial and marine vehicles [8, 11].

2 Resume of FLOP theory

Feedback Local Optimality Principle, or FLOP [8, 9], is based on the variational approach aimed at the minimization or maximization of a given functional J. The Lagrangian multiplier technique is used to include in the optimization process a differential constraint. In fact, the two pillars of the variational approach are the cost function $E(\boldsymbol{x}, \boldsymbol{u})$, the base to build the cost functional J, and the dynamical evolution of the system represented by the differential nonlinear equation $\dot{\boldsymbol{x}} = \boldsymbol{f}(\boldsymbol{x}, \boldsymbol{u})$, with $\boldsymbol{x}, \boldsymbol{u}$ the input and the control vectors, respectively. The constrained optimization is introduced by the Lagrangian multiplier $\boldsymbol{\lambda}$ as follows:

$$
\begin{aligned}
J &= \int_0^T \mathcal{L}\left(\dot{\boldsymbol{x}}, \boldsymbol{x}, \boldsymbol{u}, \boldsymbol{\lambda}\right) dt \\
\mathcal{L}\left(\dot{\boldsymbol{x}}, \boldsymbol{x}, \boldsymbol{u}, \boldsymbol{\lambda}\right) &= E\left(\boldsymbol{x}, \boldsymbol{u}\right) + \boldsymbol{\lambda}^T\left(\dot{\boldsymbol{x}} - \boldsymbol{f}\left(\boldsymbol{x}, \boldsymbol{u}\right)\right)
\end{aligned}
\tag{1}
$$

where the optimization is performed over the entire time interval $[0, T]$. The FLOP method introduces a different optimality criterion, switching from a global to a local principle. With this aim, the original functional is split into N sub-integrals:

$$
J = \sum_{i=1}^{N} J_i = \sum_{i=1}^{N} \int_{\mathrm{LB}_i}^{\mathrm{UB}_i} \mathcal{L}\left(\dot{\boldsymbol{x}}, \boldsymbol{x}, \boldsymbol{u}, \boldsymbol{\lambda}\right) dt
\tag{2}
$$

The general optimization problem expressed by Eq. (1) requires to find the minimum cost function J^*. FLOP, splitting the general problem in subintervals, finds a local minimum result $\overline{J}^*$ where the following inequality is true:

$$
J^* \leq \overline{J}^* = \sum_{i=1}^{N} \min J_i
\tag{3}
$$

Equation (1), when subjected to the local optimality criterion, and using the first-order Euler discretization technique, produces a set of three equations:

$$
\begin{aligned}
\frac{\partial E}{\partial \boldsymbol{x}}\Big|_{\mathrm{LB}_i} - \left(\boldsymbol{\lambda}^T \frac{\partial \boldsymbol{f}}{\partial \boldsymbol{x}}\right)\Big|_{\mathrm{LB}_i} + \frac{\boldsymbol{\lambda}_{\mathrm{LB}_i}}{\Delta \tau} &= 0, \\
\frac{\partial E}{\partial \boldsymbol{u}}\Big|_{\mathrm{LB}_i} - \left(\boldsymbol{\lambda}^T \frac{\partial \boldsymbol{f}}{\partial \boldsymbol{u}}\right)\Big|_{\mathrm{LB}_i} &= 0, \qquad \forall i \in [1, N] \\
\frac{\boldsymbol{x}_{\mathrm{UB}_i} - \boldsymbol{x}_{\mathrm{LB}_i}}{\Delta \tau} &= \boldsymbol{f}\left(\boldsymbol{x}_{\mathrm{LB}_i}, \boldsymbol{u}_{\mathrm{LB}_i}\right)
\end{aligned}
\tag{4}
$$

The continuous counterpart of Eq. (4) leads to an augmented form to the Pontryagin's formulation:

$$
\begin{aligned}
&\frac{\partial E}{\partial x} - \lambda^T \frac{\partial f}{\partial x} - \dot{\lambda} = 0, \\
&\frac{\partial E}{\partial u} - \lambda^T \frac{\partial f}{\partial u} = 0, \\
&\dot{x} = f(x, u, t), \\
&\dot{\lambda} = G\lambda
\end{aligned}
\qquad \forall t \in [0, T]
\tag{5}
$$

Equation (5) represents the basis of the FLOP solution technique. Matrix G is assumed as $G = -\left(\frac{N}{T}\right)I = -\frac{1}{\Delta\tau}I$, and its form is related to the size of N subintervals. The FLOP method introduces the hypothesis of affine system dynamics, i.e., $f = \phi(x) + Bu$ is linear in the control vector u, but it can be nonlinear in the state vector x. The remarkable result, in this case, is that an explicit feedback control $u(x)$ is determined in the form:

$$
\begin{aligned}
&J = \int_0^T \tfrac{1}{2} u^T R u + g(x) + \lambda^T (\dot{x} - (\phi(x) + Bu))\, dt, \\
&\dot{x} = \phi(x) + Bu, \\
&u = R^{-T} B^T \left[\nabla_x \phi(x)^T - \frac{I}{\Delta\tau}\right]^{-1} \nabla_x g(x)
\end{aligned}
\tag{6}
$$

in which no special assumption is required about the function $g(x)$.

3 System Dynamics and Cost Function

The single agent, represented on the left of Fig. 1, is intended as a unicycle model [7], and its dynamics are expressed by:
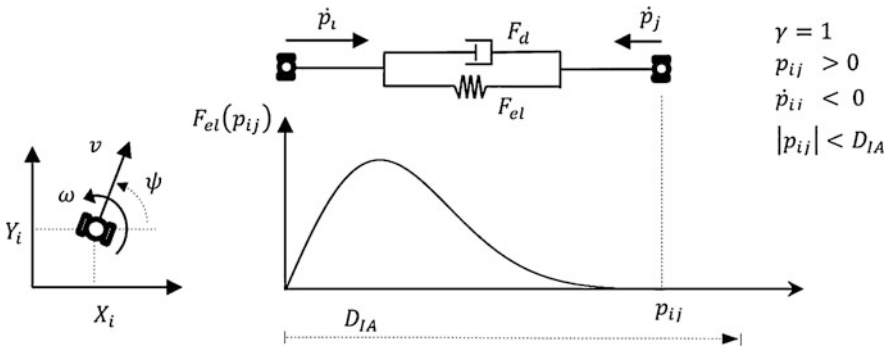
Fig. 1 Schematic representation of the unicycle model and internal avoidance strategy

$$\begin{bmatrix} \dot{X} \\ \dot{Y} \\ \dot{\psi} \\ \dot{v} \\ \dot{\omega} \end{bmatrix} = \boldsymbol{M}^{-1} \begin{bmatrix} v \cos(\psi) \\ v \sin(\psi) \\ \omega \\ f_{\mathrm{T}} - c_1 v - \nabla_X h(X, Y) \sin(\psi) + \nabla_Y h(X, Y) \cos(\psi) \\ f_{\mathrm{M}} - c_{\mathrm{r}} \omega \end{bmatrix} \qquad (7)$$

where $\boldsymbol{M} = \mathrm{diag}\,[1; 1; 1; m; I]$. X, Y, ψ, v, ω, m, I, c_1, c_r and $h(X, Y)$ are the spatial coordinates of each agent, the heading orientation, the longitudinal speed, the rotational speed, the mass, the rotational inertia, the two-speed resistance coefficients (longitudinal and rotational), and the potential function representing the unknown environment, respectively. In this example, the robots are controlled by the thrust force f_{T} and the yaw moment f_{M}. $\nabla_X h(X, Y)$, $\nabla_Y h(X, Y)$ represents the external gravity force. Moreover, defining the vector state as $\boldsymbol{x} = [\boldsymbol{x}_1, \ldots, \boldsymbol{x}_N]$, the control vector $\boldsymbol{u} = [\boldsymbol{u}_1, \ldots, \boldsymbol{u}_N]$ for the N-robots system, and considering for the ith robot $\boldsymbol{x}_i = [X_i; Y_i; \psi_i; v_i; \omega_i]$ and $\boldsymbol{u}_i = [f_{T_i}; f_{M_i}]$ is simple to organize the full nonlinear dynamic system as:

$$\dot{\boldsymbol{x}} = \boldsymbol{\phi}(\boldsymbol{x}) + \boldsymbol{B}\boldsymbol{u} \qquad (8)$$

The cost function is expressed as:

$$E(\boldsymbol{x}, \boldsymbol{u}) = \frac{1}{2}\boldsymbol{u}^T \boldsymbol{R}\boldsymbol{u} + g(\boldsymbol{x}) \qquad (9)$$

where $g(\boldsymbol{x}) = g_{\mathrm{CE}}(\boldsymbol{x}) + g_{\mathrm{CM}}(\boldsymbol{x})$, and these two terms represent the collective exploration and the cooperative motion task, respectively. The collective exploration task regarding every single agent: every agent has the information to migrate from one zone to another by having an assigned target location $\boldsymbol{x}_T$ and must avoid all other agents through an internal avoidance rule. The coordinated motion strategy has the aim to increase the performance of the migration of the swarm, by giving to each agent some information of the velocities of its surrounding agents, as illustrated later.

The collective exploration provides two effects:

Rendezvous: all agents must reach the assigned location $\boldsymbol{x}_T$. This task is here often referred also as Go to Target:

$$g_{\mathrm{T}}(\boldsymbol{x}) = (\boldsymbol{x} - \boldsymbol{x}_T)^T \boldsymbol{Q}_T (\boldsymbol{x} - \boldsymbol{x}_T) \qquad (10)$$

Internal avoidance: each agent must not collide with any of the other agents, here written as $g_{\mathrm{IA}}(\boldsymbol{x})$. The internal avoidance penalty function is written as the sum of two terms, one for the relative positions between agents $\boldsymbol{p}_{ij} = \boldsymbol{p}_j - \boldsymbol{p}_i$ and one for their respective velocities $\dot{\boldsymbol{p}}_{ij} = \dot{\boldsymbol{p}}_j - \dot{\boldsymbol{p}}_i$ with $\boldsymbol{p}_i = [X_i, Y_i]$ the ith agent coordinates:

$$g_{\mathrm{IA}}\left(\boldsymbol{x}\right) = \sum_{i=1}^{N_{\mathrm{drones}}} \sum_{\substack{j=1 \\ j \neq i}}^{N_{\mathrm{drones}}} \left(\frac{K_{\mathrm{IA}}}{\sqrt{2\pi |\boldsymbol{\Sigma}_{\mathrm{IA}}|}} \exp - \left[\left(\boldsymbol{p}_{ij} \right)^T \boldsymbol{\Sigma}_{\mathrm{IA}}^{-1} \left(\boldsymbol{p}_{ij} \right) \right] + \gamma \, \dot{\boldsymbol{p}}_{ij}^T \boldsymbol{Q}_{IA} \dot{\boldsymbol{p}}_{ij} \right)$$

$$\gamma = \tfrac{1}{2} \left(1 + \tanh \left(-k_{p1} \left(\boldsymbol{p}_{ij} \cdot \dot{\boldsymbol{p}}_{ij} \right) \right) \tanh \left(-k_{p2} \left(\left\| \boldsymbol{p}_{ij} \right\| - D_{\mathrm{IA}} \right) \right) \right)$$

(11)

The first addend of the g_{IA} is a Gaussian function, and its gradient is depicted in the right of Fig. 1, where the repulsive elastic force F_{el} between agents is represented. The Gaussian parameters $\boldsymbol{\Sigma}_{\mathrm{IA}}$, $|\boldsymbol{\Sigma}_{\mathrm{IA}}|$, K_{IA}, i.e., the variance–covariance matrix, its determinant, and a gain factor respectively are studied, so that the maximum F_{el} is high enough to avoid any kind of crash between agents. The second addend is a quadratic potential function of the relative speed $\dot{\boldsymbol{p}}_{ij}$.

Its gradient represents a dissipation force F_{d} that is activated and deactivated as a function of gamma. In particular (see example in Fig. 1), the dissipation force is turned on when two agents find themselves at a distance closer than D_{IA} and have a relative speed that identifies a collision given by the sign of the scalar product of $\boldsymbol{p}_{ij} \cdot \dot{\boldsymbol{p}}_{ij}$. Tuning positive parameters k_{p1}, k_{p2} permit to obtain a smooth slope for γ.

The cooperative motion here introduced provides an adding term, which expresses the ability of every single drone to go to the area near him with the highest average speed in the direction of the target, and its cost function is written by $\boldsymbol{s}_i = [\psi_i, v_i, \omega_i]$ as:

$$g_{\mathrm{CM}}\left(\boldsymbol{x}\right) = \sum_{i=1}^{N_{\mathrm{drones}}} \left(\boldsymbol{s}_i - \boldsymbol{s}_i^* \right)^T \boldsymbol{Q}_{\mathrm{CM}} \left(\boldsymbol{s}_i - \boldsymbol{s}_i^* \right)$$

(12)

where $\boldsymbol{s}_i^*$ is determined by the strategy proposed below. The ith agent can observe a portion of the surrounding environment, called $\mathcal{S}_i$. $\mathcal{S}_i$ is assumed as a sector of the circle of radius R_{max}, centered at the agent position, and delimited by the two lines associated with the angles α_0 and α_{END} measured with respect to the x-axis of the ith agent. $\mathcal{S}_i$ is further divided into N_{zones} sub-sectors or zones, named Z_k ($k = 1, N_{\mathrm{zones}}$), so that each zone is a sector of angle $\hat{\alpha} = \frac{\alpha_{\mathrm{END}} - \alpha_0}{N_{\mathrm{zones}}}$. In $\mathcal{S}_i$, the agent searches for all the agents currently within Z_k, the number of which is denoted by J_k. For each agent j therein, its velocity component in the direction of the target $v_{jk, T}$ is observed. Here, the chosen direction of the target is along the Y direction. If r_{ijk} is the distance of the jth agent within Z_k from the ith observer agent, the weighing numbers are defined:

$$w_{ijk} = -r_{ijk} + R_{\mathrm{max}}$$

(13)

The weighted velocity $V_{ik, T}$ is estimated by the ith observer for the zone Z_k as:

$$V_{ik,T} = \frac{\sum_{j=1}^{J_k} w_{ijk} v_{jk,T}}{\sum_{j=1}^{J_k} w_{ijk}}$$

(14)

Fig. 2 Coordinated motion strategy for the ith agent
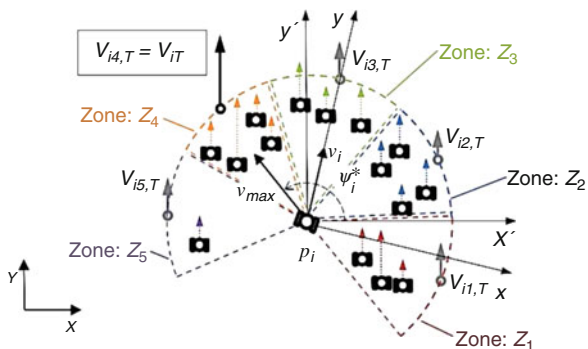
and the highest value within the sector is selected as:

$$V_{i,T} = \max \{ V_{ik,T} \} \quad \forall k \in [1, N_{\text{zones}}] \tag{15}$$

Once the sector with the highest velocity is found, the agent steers its velocity in the direction of the bisector of the zone k_* with the highest velocity.

In Fig. 2 the coordinated motion strategy is represented if the target is positioned along the vertical axes. In the case depicted in Fig. 2, the highest weighted velocity is in the zone Z_4, so $k_i^* = 4$. The angle of the desired maximum velocity v_{max} is $\psi_i^* = \alpha_0 + \left(k_i^* - \frac{1}{2} \right) \hat{\alpha}$, so s_i^* in (12) becomes:

$$s_i^* = [\psi_i^*; v_{\text{max}}; 0] \tag{16}$$

4 FLOP Application for Coordinated Motion Strategy

In this section, the benefits of the discussed strategy on the migration of robot swarms are discussed. Simulations are performed with and without the velocity-based strategy. Different simulations in the same environment (Fig. 3) are performed through the FLOP control: first, the number of robots N is assigned. Then, many simulations are generated by varying the initial conditions of the swarm. The mean of the arrival time in the target area of the last entering agent is kept with and without using the velocity-based strategy. The simulations are then repeated for different numbers of agents, from 1 to 40, as shown on the left in Fig. 4. Finally, the probability density function (PDF) of the arrival time for $N = 85$ for 60 simulations is shown on the right of Fig. 4. The arrival time and the success of the strategy is strongly dependent on the number of obstacles. The collective motion strategy is not expected to have more success in the individual strategy in the case of a low
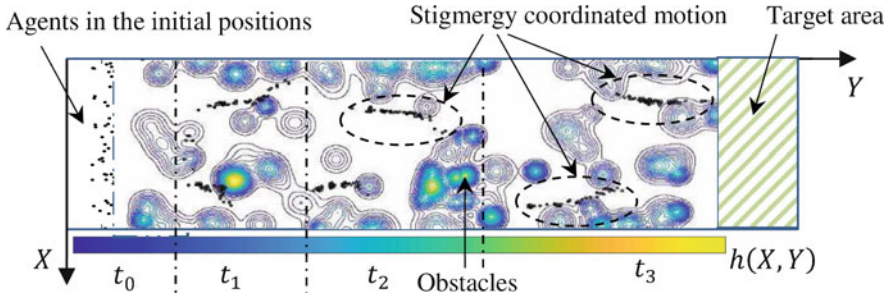
Fig. 3 Map of the environment
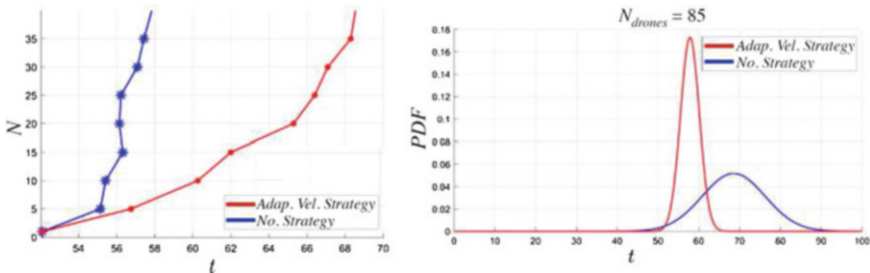
Fig. 4 Arrival time for $N = [1, 40]$ (left); PDF of the arrival time of the last of 85 agents in 60 simulations (right)

number of obstacles. In Fig. 3 some screenshots for different t_i time windows of one simulation are shown.

As can be seen in Fig. 4, the proposed strategy provides a remarkable decrease in the arrival time with a lower variance for the last agent.

5 Conclusions

In this chapter, the application of an innovative feedback control named Feedback Local Optimality Principle for the coordinated motion strategy of a robot swarm is presented. The strategy is based on the Vicsek model, but it changes some paradigms to add internal avoidance and to localize the interaction between agents of the swarm. The FLOP application to the proposed strategy gives promising results in terms of the total time of the migration. Further developments will be the subject of future investigations, as for example the correlation between the migration time and the number of obstacles in the environment.

References

1. Lewis, T.G.: Cognitive stigmergy: a study of emergence in small-group social networks. Cogn. Syst. Res. **21**, 7–21 (2013)
2. Vicsek, T., Czirk, A., Ben-Jacob, E., Cohen, I., Shochet, O.: Novel type of phase transition in a system of self-driven particles. Phys. Rev. Lett. **75**(6), 1226–1229 (1995)
3. Ginelli, F.: The Physics of the Vicsek model. Eur. Phys. J. Spec. Top. Rev. **225**(11–12), 2099–2117 (2016)
4. Martinez, R., Alarcon, F., Rodriguez, D.R., Aragones, J.L., Valeriani, C.: Collective behavior of Vicsek particles without and with obstacles$_*$. Eur. Phys. J. E. **41**(8), 91 (2018)
5. Mayya, S., Pierpaoli, P., Nair, G., Egerstedt, M.: Localization in densely packed swarms using interrobot collisions as a sensing modality. IEEE Trans. Robot. **35**(1), 21–34 (2019)
6. Zhao, H., Liu, H., Leung, Y.W., Chu, X.: Self-adaptive collective motion of swarm robots. IEEE Trans. Autom. Sci. Eng. **15**(4), 1533–1545 (2018). Art no. 8393468
7. Indiveri, G.G. Kinematic time-invariant control of a 2D nonholonomic vehicle. In: Proceedings of the 38th IEEE Conference on Decision and Control (Cat. No. 99CH36304), pp. 2112–2117 (1999)
8. Antonelli, D., Nesi, L., Pepe, G., Carcaterra, A.: Mechatronic control of the car response based on VFC. In: Proceedings of ISMA2018, pp. 79–92 (2018)
9. Pepe, G., Antonelli, D., Nesi, L., Carcaterra, A.: Flop: feedback local optimality control of the inverse pendulum oscillations. In: Proceedings of ISMA2016, pp. 93–106 (2018)
10. Pepe, G., Roveri, N., Carcaterra, A.: Prototyping a new car semi-active suspension by variational feedback controller. In: Proceedings of ISMA2018, pp. 231–245 (2016)
11. Paifelman, E., Pepe, G., Carcaterra, A.: An optimal indirect control of underwater vehicle. Int. J. Control. (2019), DOI: 10.1080/00207179.2019.1590737

Feedback Local Optimality Principle Applied to Rocket Vertical Landing (VTVL)

Dario Antonelli, Gianluca Pepe, Leandro Nesi, and Antonio Carcaterra

Abstract Vertical landing is becoming popular in the last 15 years, a technology known under the acronym VTVL, Vertical Takeoff and Vertical Landing. The interest in such landing technology is dictated by possible cost reductions, which impose spaceship's recycling. The rockets are not generally designed to perform landing operations, rather their design is aimed at takeoff operations, guaranteeing a very high forward acceleration to gain the velocity needed to escape the gravitational force. In this chapter, a new control method based on Feedback Local Optimality Principle, named FLOP, is applied to the rocket landing problem. The FLOP belongs to a special class of optimal controllers, developed by the mechatronic and vehicle dynamics lab of Sapienza, named Variational Feedback Controllers (VFC), that are part of an ongoing research and are recently applied in different field: nonlinear system and marine and terrestrial autonomous vehicles, multi-agent interactions, and vibration control. This chapter is devoted to show the robustness of the nonlinear controlled system, comparing the performances with the LQR, one of the most acknowledged methods in optimal control.

Keywords Vertical landing · Optimal control · Nonlinear dynamics

1 Introduction

Landing, as for the Apollo 11 mission to the Moon, is an operation deputed to a lander module of the rocket body, the Lunar Excursion Module (LEM). As a new frontier of space discovery, space vehicles are today required to be able to land with reliability on different surfaces. Among the multiple complexities implied by the vertical landing, the control strategy plays a critical role to obtain reliability and

D. Antonelli · G. Pepe · L. Nesi · A. Carcaterra (✉)

Department of Mechanical and Aerospace Engineering, Sapienza University of Rome, Rome, Italy

e-mail: dario.antonelli@uniroma1.it; gianluca.pepe@uniroma1.it; leandro.nesi@uniroma1.it; antonio.carcaterra@uniroma1.it

robustness. While takeoff operations are better predictable and can be specifically designed by using suitable launch infrastructures, the landing phase is affected by higher uncertainties due to weather disturbances and ground surface imperfections. The launch umbilical tower, evacuation vanes, shockwaves dissipation, vibrations insulation, and accurately designed attitude during the first phases of the launch help much in facilitating the takeoff operations. The return trajectory is instead weakly stable due to the presence of random disturbances. Hence, to improve the landing success probability, a feedback optimal trajectory is to be identified. The "Moon landing problem" is one of the prototype problems included in many control books, and it is an excellent example of a two-boundary optimization problems, that is difficult to approach by a feedback control strategy. Moreover, the vertical landing is a nonlinear problem with instabilities, analogous to the challenging control of the inverse pendulum. The Feedback Local Optimality Principle (FLOP) approach [1, 2] represents an interesting alternative to more classical solutions, as the LQR. The aim of this chapter is to define a robust and reliable control to land the vehicle safely. The quality of the control law is investigated considering the landing approach maneuver, starting from an assigned altitude, and varying the initial conditions, namely attitude and speed. The control actions involve the magnitude and the direction of the thrust, and orientable grid fins mounted on the top of the vehicle controlling the aerodynamic forces. The model of the system also includes actuators saturation effects.

2 FLOP: A New Local Optimality Principle

A new control strategy based on classical variational approach has been recently developed by the authors and named Feedback Local Optimality Principle or FLOP [1–5, 8, 9]. The method relies on a local optimality criterion, replacing the global one used in the optimal control theory based on the Pontryagin approach. By using this idea, the chance to obtain a feedback control law for nonlinear dynamic system is supported. In classical variational problem the performance index $\overline{J}$, represented by the integral of the cost function $E(x, u)$ subjected to the dynamic differential constraint, $\dot{x} = f(x, u)$ (representing the system dynamics) has to be minimized (or maximized) along the entire time interval $[0, T]$:

$$\min \overline{J} = \int_0^T E(x, u) + \lambda^T (\dot{x} - f(x(t), u(t))) \, dt \tag{1}$$

In Eq. (1), x is the system state, u the control vector, and $x(0) = x_0$ the initial condition. The differential constraint is introduced through Hamilton's formulation

using the Lagrange multiplier $\lambda(t)$. The solution of Eq. (1) provides both the optimal control $\boldsymbol{u}^*(t)$ and the corresponding optimal trajectory $\boldsymbol{x}^*(t)$. The Feedback Local Optimality Principle, or FLOP approach, starts splitting the original integral (Eq. 1) into $N = T/\Delta\tau$ integrals, where $\Delta\tau$ represents the time horizon of each of them (Eq. 2). The FLOP method requires a weaker minimization concept, based on the extremal value for each individual integral within the related time horizon $\Delta\tau$:

$$J = \sum_{i=1}^{N} J_i = \sum_{i=1}^{N} \int_{\mathrm{LB}_i}^{\mathrm{UB}_i} \mathcal{L}\left(\dot{\boldsymbol{x}}, \boldsymbol{x}, \boldsymbol{u}, \boldsymbol{\lambda}\right) dt \tag{2}$$

where $\mathcal{L}\left(\dot{\boldsymbol{x}}, \boldsymbol{x}, \boldsymbol{u}, \boldsymbol{\lambda}\right) = E\left(\boldsymbol{x}, \boldsymbol{u}\right) + \boldsymbol{\lambda}^T\left(\dot{\boldsymbol{x}} - \boldsymbol{f}\left(\boldsymbol{x}(t), \boldsymbol{u}(t)\right)\right)$. J is minimized following the optimality criterion:

$$\min\left(J_i\right) \quad \forall i$$

where UB_i and LB_i limits indicate the *upper bound* and *lower bound*, respectively. Each integral solution satisfies the boundary conditions:

$$\begin{aligned} \boldsymbol{x}_{\mathrm{LB}_i} &= \boldsymbol{x}_{\mathrm{UB}_{i-1}} \\ \boldsymbol{\lambda}_{\mathrm{UB}_i} &= 0 \end{aligned} \tag{3}$$

This approach provides three main advantages, with respect to the classical variational approach:

- The considered dynamic system can be described by a nonlinear model, namely belonging to the class of the affine systems $\dot{\boldsymbol{x}} = \boldsymbol{\phi}\left(\boldsymbol{x}\right) + \boldsymbol{B}\boldsymbol{u}$.
- A more general class of nonlinear penalty functions, with respect to the classical quadratic forms of the state $\boldsymbol{x}$, can be included into the cost function and represented by $g(\boldsymbol{x})$
- The FLOP approach provides a feedback solution for the control vector $\boldsymbol{u}$. This allows to overcome the main engineering drawback of the Pontryagin or the Bellman approaches. In fact, they both provide feed-forward control law, taking into account only one single information related to the initial state of the system, not using the information coming out, as the time marches, from the sensor measurements of the system state evolution.

The FLOP approach, in general, provides a solution, with a performance that depends on the choice of the variable $\Delta\tau$ that acts as a tuning parameter.

2.1 Resume of FLOP Technicality

The continuous counterpart of Eqs. (2) and (3) as shown in Refs. [5–9], leads to an augmented form of the variational set of equations. In fact, solving each integral of Eq. (2) with its boundary conditions (3), is equivalent to solve the integral Eq. (1) for the entire time interval [0–T], where the final constraint for $\lambda(T) = \mathbf{0}$ is replaced with a first-order differential equation $\dot{\lambda} = G\lambda$ as in the following:

$$
\begin{aligned}
\nabla_x E - \nabla_x f^T \lambda - \dot{\lambda} &= 0, \\
\nabla_u E - \nabla_u f^T \lambda &= 0, \\
\dot{x} &= f(x, u, t), \qquad \forall t \in [0, T] \\
\dot{\lambda} &= G\lambda
\end{aligned}
\tag{4}
$$

where $G = -\left(\frac{N}{T}\right) I$, i.e., the chosen horizon time interval $\Delta\tau$. The set of Eq. (4) can be, in general, explicitly solved for a penalty function $E(x, u)$ that is required to be quadratic in the control u and with any degree of nonlinearities in x, with $g(x)$ being differentiable. For affine systems, Eq. (4) leads to:

$$
\begin{aligned}
J &= \int_0^T \tfrac{1}{2} u^T R u + g(x) + \lambda^T (\dot{x} - (\phi(x) + Bu))\ dt \\
u_{FLOP} &= R^{-T} B^T \left[\nabla_x \phi(x)^T - G \right]^{-1} \nabla_x g(x)^T
\end{aligned}
\tag{5}
$$

The cost function $\frac{1}{2} u^T R u + g(x)$ exhibits a more general form than quadratic cost function in terms of the control variable, where additionally very weak hypotheses are required on $g(x)$, since it is sufficient if its differential at the first order exists.

3 Dynamic Model

In this section, the rocket dynamic model depicted in Fig. 1 is presented. The dynamic of the system is described by a six DOF rigid body motion with an additional equation describing the fuel mass consumption. The origin of the mobile frame is placed in the geometric center of the vehicle body, since the CoG longitudinal position changes during the flight, due to the mass variation of the system. As usual for aerial vehicles, the x axis is aligned along the longitudinal axis, the y axis is set on the wing's plane, and the z axis is orthogonal to the previous two (see Fig. 1).

The equations of motion are written within this frame in terms of the vehicle longitudinal, transverse, and vertical speed components $v = [u, v, w]$, along x, y and z, respectively, and in terms of the angular speed components $\omega = [p, q, r]$, along the axes, associated to the roll, pitch, and yaw motions, respectively. The absolute position $\eta = [X, Y, Z]$ of the rocket is described within an earth fixed, NED (North-
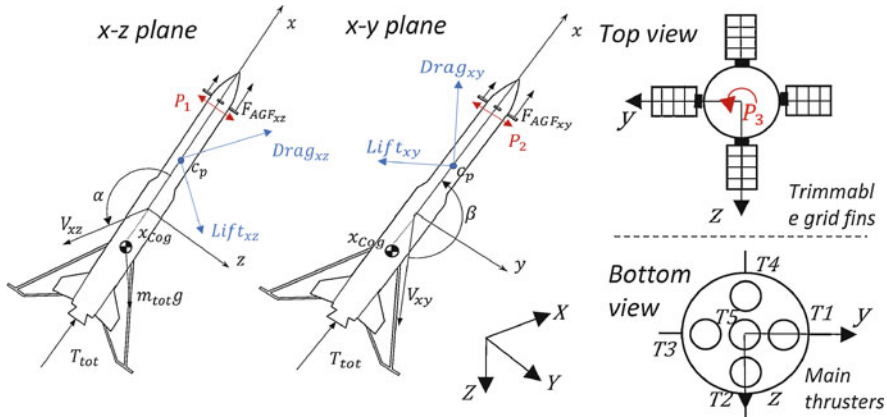
Fig. 1 Rocket main systems, body reference, and NED reference

East-Down) reference frame. To avoid gimbal lock when the rocket approaches the vertical attitude, the quaternion $q = [q_0, q_1, q_2, q_3]$ description is used. The state vector is arranged as $x = [\eta, q, v, \omega, m_{fuel}(t)]$ and the vehicle dynamic equation can be shortly written as:

$$M(t)\dot{x} + C(x)x = \tau \qquad (6)$$

where $M(t)$, $C(x)$ are the time variable, inertia, and the generalized Coriolis matrices, respectively. The mass variation due to fuel consumption is described by adding the equation:

$$\dot{m}_{fuel}(t) = -\gamma T_{tot} \qquad (7)$$

where the total thrust is $T_{tot} = T_1 + T_2 + T_3 + T_4 + T_5$, sum of the individual forces provided by the main engines and γ is a suitable engine constant.

The external forces τ collect the gravity action τ_g, the aerodynamic forces τ_{Aero} acting on the vehicle body, the ith main thrusters forces τ_{T_i}, the jth cold gas thrusters actions τ_{P_j}, and the kth forces generated by the trimmable grid fins τ_{AGF_k}:

$$\tau = \tau_g + \tau_{Aero} + \sum_{i=1}^{5} \tau_{T_i} + \sum_{j=1}^{3} \tau_{P_j} + \sum_{k=1}^{4} \tau_{AGF_k} \qquad (8)$$

where the generic $\tau_{\boxtimes} = [0_{7,1}; F_{\boxtimes}; M_{\boxtimes}; 0]$. The gravity action is $F_g = J^T(q_0, q_1, q_2, q_3)[0, 0, m_{fuel}g]^T$, where J is the transformation matrix from the vehicle to the NED Earth reference. Since the dynamic equations are written in the body frame, the CoG position varies during the flight, and the gravity action generates torque $M_g = [x_{CoG}, 0, 0] \times F_g$. Analogously, for aerodynamic action F_{Aero}, M_{Aero}. These last depend on the angle of attack $\alpha = atan(w/u)$, and

$\beta = \mathrm{atan}(v/u)$, the sideslip angle. Drag and Lift coefficients C_D, C_L for the forces acting in the two planes xy and xz are introduced, together with the effective cross section areas A, the position of the center of pressure c_p, and are expressed through nonlinear function of the attack and sideslip angles as $\quad C_{D_{xz}}(\alpha), C_{L_{xz}}(\alpha), C_{D_{xy}}(\beta), C_{L_{xy}}(\beta), A_{xz}(\alpha), A_{xy}(\beta), c_{p_{xz}}(\alpha), c_{p_{xy}}(\beta)$, while dependences from $\dot{\alpha}$ and $\dot{\beta}$ are neglected. These permit to evaluate the aerodynamic forces due to the airflow around the rocket body, with $i = y, z$ and $V_{xy}^2 = u^2 + v^2$, $V_{xz}^2 = u^2 + w^2$ the quadratic speed modulus in the x–y and x–z plane, respectively.

$$D_{xi} = -1/2\rho_{\mathrm{air}}(Z)A_{xi}C_{D_{xi}}V_{xi}^2, \quad L_{xi} = 1/2\rho_{\mathrm{air}}(Z)A_{xi}C_{L_{xi}}V_{xi}^2 \qquad (9)$$

The air density $\rho_{\mathrm{air}}(Z)$ is a nonlinear function of the height Z. Torque associated to the set of forces (10) is:

$$\boldsymbol{M}_{\mathrm{Aero}} = \left[c_{p_{xy}}, 0, 0\right] \times \left(\boldsymbol{R}(\beta)\,\boldsymbol{F}_{\mathrm{Aero}_{xy}}\right) + \left[c_{p_{xz}}, 0, 0\right] \times \left(\boldsymbol{R}(\alpha)\,\boldsymbol{F}_{\mathrm{Aero}_{xz}}\right) \qquad (10)$$

where $\boldsymbol{R}(\alpha)$ and $\boldsymbol{R}(\beta)$ are the rotation matrices around y and z, respectively, and $\boldsymbol{F}_{\mathrm{Aero}_{xi}} = [D_{xi}; 0; L_{xi}]$. Analogous expressions follow for $\boldsymbol{\tau}_{T_i}$ and $\boldsymbol{\tau}_{P_j}$, and these last due to cold gas thrusters P_1, P_2, P_3 are designated to control the vehicle attitude in the LEO (Low-Earth-Orbit).

When the vehicle approaches the atmosphere during the descent phase, the cold gas thrusters have not enough power to control the vehicle attitude. Hence, the action $\boldsymbol{\tau}_{\mathrm{AGF}_k}$ becomes predominant by suitable variations of their angles of attack δ_k stabilizing the vehicle's flight.

The forces and torques $(\boldsymbol{F}_{\mathrm{AGF}}, \boldsymbol{M}_{\mathrm{AGF}})$ are born because of the trimmable fins, and they are:

$$\boldsymbol{F}_{\mathrm{AGF}} = \sum_{k=1}^{4} \boldsymbol{F}_{\mathrm{AGF}_k}\left(D_{\mathrm{fin}_k}\right), \quad \boldsymbol{M}_{\mathrm{AGF}} = \sum_{k=1}^{4} \boldsymbol{b}_k \times \boldsymbol{F}_{\mathrm{AGF}_k}\left(D_{\mathrm{fin}_k}\right)$$
$$D_{\mathrm{fin}_k} = -1/2\rho_{\mathrm{air}}(Z)A_{\mathrm{fin}_k}C_{D_k}(\delta_k + \phi)V_k^2 q(\phi) \qquad (11)$$

where for the kth fin, A_{fin_k} is the wing section area, $C_{D_k}(\delta_k + \phi)$ is its drag coefficient, depending on δ_k and on the angle ϕ equal to α or β depending on the considered fin. V_k represents the component of the CoG velocity along the x axis, the parameter $q(\phi)$ is the shadowing coefficient that varies between 0 and 1 depending on its configuration, and finally $\boldsymbol{b}_k$ is the position vector of the kth fin.

4   Control

The simulations were carried out considering a control frequency loop of 100 Hz. The control action is performed introducing specific penalty functions, for each phase of the flight, this is represented by a quadratic penalty function of the state $\boldsymbol{x}$ and target $\boldsymbol{x}_T$:

$$g\left(\boldsymbol{x}\right) = \frac{1}{2}(\boldsymbol{x} - \boldsymbol{x}_{\mathrm{T}})^{T} \boldsymbol{Q}\left(\boldsymbol{x}\right)\left(\boldsymbol{x} - \boldsymbol{x}_{\mathrm{T}}\right) \tag{12}$$

The matrix $\boldsymbol{Q}$ is suitably varied during the flight. The vehicle flight is composed of three main phases as shown in Fig. 2: the first is the attitude correction in LEO. The vehicle actuates the FLIP maneuver to reach the desired pitch. The state target is referred to a specific attitude and null angle rates $\boldsymbol{x}_{T_{\mathrm{FLIP}}} = \left[0_{3\times1}, \boldsymbol{q}_{T}, 0_{3\times1}, 0_{3\times1}, 0\right]$, with suitable *k-gains* for $\boldsymbol{Q}_{\mathrm{FLIP}} = \mathrm{diag}\left([0_{3\times1}, K_{\boldsymbol{q}}1_{4\times1}, 0_{3\times1}, K_{\boldsymbol{\omega}}1_{3\times1}, 0]\right)$.

In the second phase, the vehicle reaches the reentry speed and pitch angle. The target is $\boldsymbol{x}_{T_{\mathrm{reentry}}} = \left[0_{3\times1}, \boldsymbol{q}_{T}, \boldsymbol{v}_{T}, 0_{3\times1}, 0\right]$, and $\boldsymbol{Q}_{\mathrm{reentry}} = \mathrm{diag}\left([0_{3\times1}, K_{\boldsymbol{q}}1_{4\times1}, K_{\boldsymbol{v}}1_{3\times1}, K_{\boldsymbol{\omega}}1_{3\times1}, 0]\right)$.

The third phase is the atmospheric flight terminating with the vertical landing operation. The target is $\boldsymbol{x}_{T_{\mathrm{landing}}} = \left[0_{3\times1}, \boldsymbol{q}_{T}, \boldsymbol{v}_{T}, 0_{3\times1}, 0\right]$, and $\boldsymbol{Q}_{\mathrm{landing}} = \mathrm{diag}\left([K_{\boldsymbol{\eta}}1_{3\times1}, K_{\boldsymbol{q}}1_{4\times1}, K_{\boldsymbol{v}}1_{3\times1}, K_{\boldsymbol{\omega}}1_{3\times1}, 0]\right)$.

The variation of the set $g(\boldsymbol{x})$ in dependence of the actual state of the vehicle is widely used in control application, such as the gained scheduled technique used for MPC.

5 Results

The simulations consider a rocket with the following characteristics (Table 1):
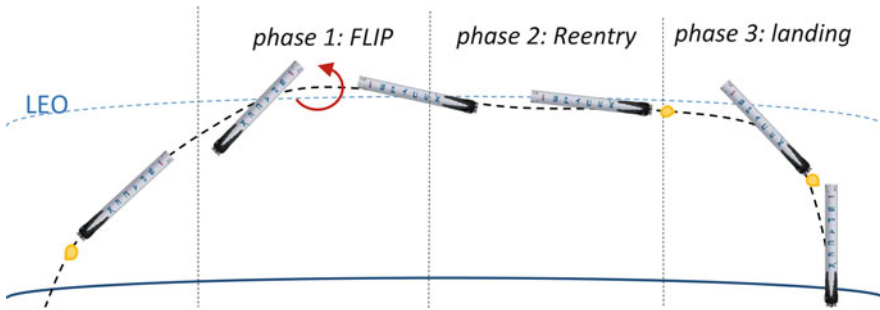
Fig. 2 Rocket flight phases

Table 1 Rocket's parameters

Characteristics	Value	Characteristics	Value
Rocket mass	20,000 kg	Number of lateral thrusters	8
Fuel mass	150,000 kg	Max lateral thrust	400 [N]
Number of main thrusters	5	Number of grid fins	4
Max thrust T	1521.4 kN	Max grid trim angle	±60 [°]

In the FLIP maneuver, the vehicle flies at 100 km above the earth surface at a speed of 10,000 km/h, with initial pitch 45°. The lateral thrusters provide the required force for the rotation that sets the vehicle at the desired pitch. Figure 3 shows the pitch evolution in time, its rate, and the thrust provided by the lateral thruster responsible of the pitch control.

In the second phase, the rocket is still in LEO, flying 100 km above earth surface, traveling at 10,000 km/h, with initial pitch 180°. The value required for the pitch to safely approach the atmosphere is 80°. Moreover, the vehicle approaches the atmosphere reducing the effect of gravity using the main engines (Fig. 4).

Eventually, the landing phase is shown in Fig. 5. Here the vehicle is traveling through the atmosphere starting from a height of 30 km at 4320 km/h, thanks to the grid fins and the main thrusters, and it safely performs the vertical landing.
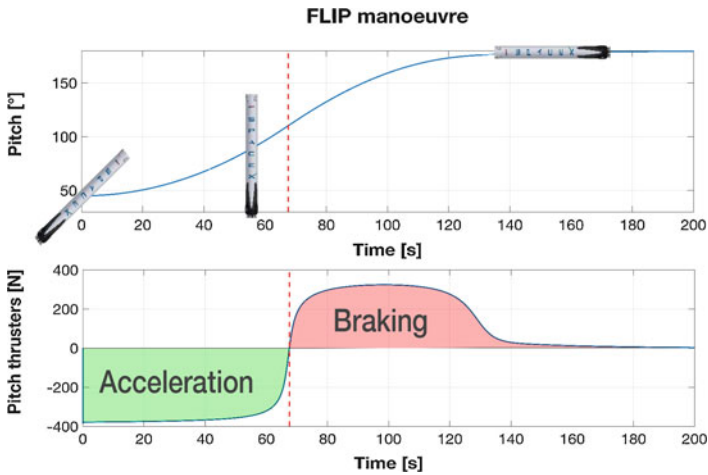
Fig. 3 FLIP maneuver
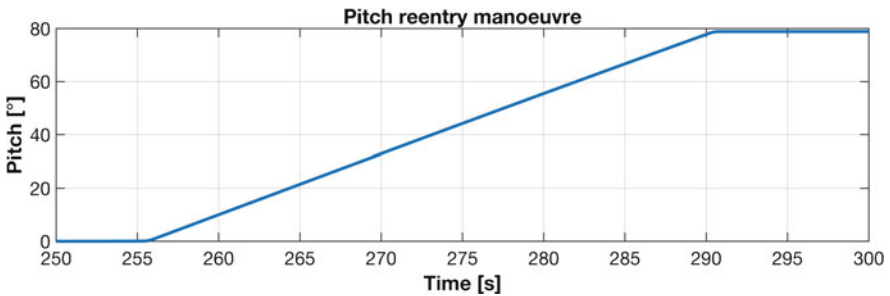
Fig. 4 Reentry maneuver
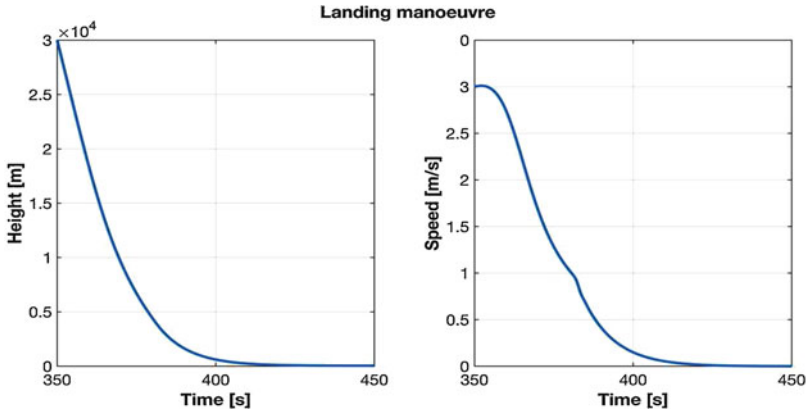
Fig. 5 Vertical landing maneuver

6   Conclusions

The FLOP control shows good performances in all phases that characterize the vehicle flight and landing, in a compound complex control operation. These results are possible thanks to the FLOP formulation, which allows to take into account the nonlinearities, typical of the rocket model. Further tests will be performed, introducing random disturbances, with state estimation algorithm in order to validate the performance shown in the present chapter.

References

1. Zhang, L., Wei, C., Wu, R., Cui, N.: Fixed-time extended state observer based non-singular fast terminal sliding mode control for a VTVL reusable launch vehicle. Aerosp. Sci. Technol. **82–83**, 70–79 (2018)
2. Tian, B., Fan, W., Su, R., Zong, Q.: Real-time trajectory and attitude coordination control for reusable launch vehicle in reentry phase. IEEE Trans. Ind. Electron. **62**(3), 1639–1650 (2015)
3. Min, C., Lee, D., Cho, K., Jo, S., Yang, J., Lee, W.: Control of approach and landing phase for reentry vehicle using fuzzy logic. Aerosp. Sci. Technol. **15**(4), 269–282 (2011)
4. Chu, H., Ma, L., Wang, K., Shao, Z., Song, Z.: Trajectory optimization for lunar soft landing with complex constraints. Adv. Space Res. **60**(9), 2060–2076 (2017)
5. Antonelli, D., Nesi, L., Pepe, G., Carcaterra, A.: A novel approach in optimal trajectory identification for autonomous driving in racetrack. In: European Control Conference (2019)
6. Pepe, G., Carcaterra, A.: VFC—variational feedback controller and its application to semi-active suspensions. Mech. Syst. Signal Proc. **76–77**, 72–92 (2016)
7. Paifelman, E., Pepe, G., La Gala, F., Carcaterra, A.: Control of fluctuations of a tethered unmanned-underwater-vehicle. In: ISMA2018, (2018)
8. Pepe, G., Antonelli, D., Nesi, L., Carcaterra, A.: Flop: feedback local optimality control of the inverse pendulum oscillations. In: ISMA2018, (2018)
9. Antonelli, D., Nesi, L., Pepe, G., Carcaterra, A.: Mechatronic control of the car response based on VFC. In: ISMA2018, (2018)

Time-Delayed Feedback Control Applied in a Nonideal System with Chaotic Behavior

Angelo M. Tusset (ID)**, Jose M. Balthazar** (ID)**, Rodrigo T. Rocha** (ID)**,
Mauricio A. Ribeiro** (ID)**, Wagner B. Lenz** (ID)**, and Frederic C. Janzen** (ID)

Abstract This chapter considers the application of time-delayed feedback control in a nonideal system. The system has as main characteristic the additional cubic nonlinearity. An electric DC motor with limited power supply that is driven by an unbalanced rotating mass provides a nonideal excitation to the system. To suppress the chaotic behavior presented by the nonideal system, the time-delayed feedback control is proposed, by considering the velocity of the rotating angle as a parameter to determine the time delay. In addition, it is considered a control for suppressing the chaotic behavior. Therefore, two control signals are considered in which one is the nonlinear feedforward controller to maintain the system in periodic orbit and the other one is the feedback controller obtained by the SDRE, which takes the system trajectory to the desired periodic orbit. Numerical simulations demonstrated the effectiveness of the control strategy in conducting the system from any initial condition to the desired orbit and the control of chaos by time-delayed feedback control.

Keywords Time-delayed feedback control · SDRE control · Nonideal system

1 Introduction

The study of problems that involve multiphysics couplings or coupling of several systems has attracted many researchers. Changes in structural characteristics of machines and dynamical systems were explored in [1]. Consequently, some phenomena were observed in dynamical systems due to supporting structures and rotating machines, where additional degrees of freedom and unbalancing of the rotating parts are the main causes of mechanical vibrations. In such systems, there is a need to consider a more realistic formulation including the action of an energy source with limited power supply (nonideal motor). In particular, the influence of

A. M. Tusset (✉) · J. M. Balthazar · R. T. Rocha · M. A. Ribeiro · W. B. Lenz · F. C. Janzen
Federal University of Technology—Paraná, Ponta Grossa, PR, Brazil
e-mail: a.m.tusset@gmail.com

the oscillatory system on the driving force and vice-versa should be considered. The time-delayed feedback controller was originally suggested by Pyragas [2] for ideal systems and considering a continuous control input U which stabilized a chaotic oscillation given by the difference between the current output and the previous one. Therefore, this work presents the application of the time-delayed feedback controller applied to a nonideal system case. Additionally, we considered a controller in order to inhibit the chaotic behavior and to control the system, i.e., a control signal is introduced in the system dynamics. The controller strategy involves the application of two signals, a nonlinear feedforward to maintain the controlled system in a periodic orbit, and other state feedback controller, obtained by the state-dependent Riccati equation (SDRE), to bring the system trajectory into the desired periodic orbit.

2 Mathematical Model

Figure 1 illustrates a nonideal oscillator that consists of a structure of mass m_1 connected to a damper and to a nonlinear spring with a nonlinear cubic stiffness. The proposed system is excited by a nonideal DC motor characterized by the moment of inertia J_M and the unbalanced mass m_0 with eccentricity r. The physical schematics of the DC motor is shown in Fig. 1a.

The equations of motion of the nonideal system are given in Ref. [3]:

$$
\begin{aligned}
m_1\ddot{x} + \mu\dot{x} - k_1 x + k_2 x^3 &= m_0 r \left(\dot{\varphi}^2 \sin\varphi - \ddot{\varphi}\cos\varphi \right), \\
\left(J + m_o r^2 \right) \ddot{\varphi} &= C_M \phi I - m_0 r \ddot{x} \cos\varphi, \\
\dot{I}_m &= -\frac{R_t}{L_t} I_m - \frac{C_E \phi}{L_t}\dot{\varphi} + \frac{U_m}{L_t}
\end{aligned}
\tag{1}
$$

where C_M and C_E are mechanical and electrical constants, respectively. The magnetic flux is represented by ϕ. And in Fig. 1b $\omega(t)$ is the angular velocity of the rotor. It is assumed that the external exciting current I_m and voltage U_m are constants, and then the magnetic flux ϕ is also constant. It is convenient to work
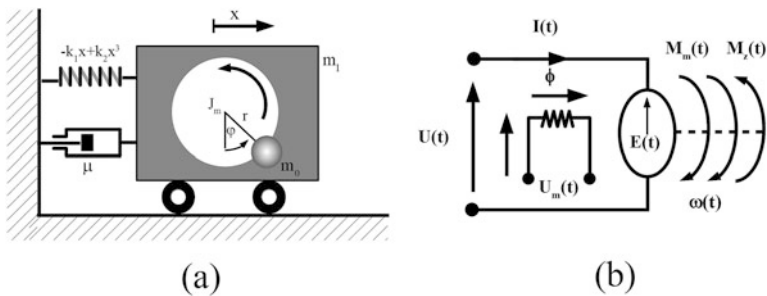
Fig. 1 (**a**) Nonideal oscillator and (**b**) the DC motor in the electrical schematics

with dimensionless position and time, namely $x_1 = \frac{x}{x_0}$ and $\tau = \omega_0 t$, respectively, where x_0 is the static displacement, and introducing the following variable $\tilde{I} = \frac{I}{I_0}$, where I_0 is a rated current in the armature, and $x_2 = \dot{x}_1$, $x_3 = \varphi$, $x_4 = \dot{\varphi}$, and $x_5 = \tilde{I}$. Then, the state-space formulation of the equations of motion becomes

$$
\begin{aligned}
\dot{x}_1 &= x_2, \\
\dot{x}_2 &= A \left(w_1 \left(x_4^2 \sin x_3 - p_3 x_5 \cos x_3 \right) - \beta x_2 + x_1 - \delta x_1^3 \right) + U \\
\dot{x}_3 &= x_4, \\
\dot{x}_4 &= A \left(p_3 x_5 - w_2 w_1 x_4^2 \sin x_3 \cos x_3 + w_2 \beta w \cos x_3 - w_2 \cos x_3 \left(x_1 - \delta x_1^3 \right) \right), \\
\dot{x}_5 &= -p_1 x_5 - p_2 x_4 + U_1
\end{aligned}
\tag{2}
$$

where U is the control signal, and the dimensionless parameters are denoted by: $\omega_0^2 = \frac{k_1}{m_1 + m_0}$, $\beta = \frac{\mu}{m_1 \omega_0}$, $\delta = \frac{k_2}{k_1} x_0^2$, $w_1 = \frac{m_0 r}{m_1 x_0}$, $w_2 = \frac{m_0 r x_0}{(J + m_0 r^2)}$, $p_1 = \frac{R_t}{L_t I_0 \omega_0}$, $U_1 = \frac{U}{L_t I_0 \omega_0}$, $p_2 = \frac{C_E \phi}{L_t I_0}$, $p_3 = \frac{C_M \phi I_0}{(J + m_0 r^2) \omega_0^2}$ and $A = \frac{1}{1 - w_1 w_2 (\cos x_3)^2}$.

3 Numerical Results

The numerical simulations of the nonideal system were carried out by considering the parameters of the DC motor and mechanical parameters. The dimensionless parameters are defined as $\delta = 0.1$, $w_1 = 0.2$, $w_2 = 0.3$, $p_1 = 0.3$, $p_2 = 3$, $p_3 = 0.15$, $\beta = 0.0337$, $\omega_0 = 46.3934$, $U_1 = 4$, $x_1(0) = 0$, $x_2(0) = 0$, $x_3(0) = 0$, $x_4(0) = 0$, and $x_5(0) = 0$, where the integration step is considered by $h = 0.001$ [3]. In Fig. 2, the chaotic behavior of the system (2) is observed.

Analyzing the numerical results, it was observed that for the parameters used the system has a chaotic behavior, being used in the positive δ simulations that represent a harder beam. For the cases in which a more flexible beam is desired, one can use a negative δ. These δ signal variations significantly alter the dynamical behavior of the system.

4 Time-Delayed Feedback Control

The time-delayed feedback control (TDF control) is proposed by Ref. [2]. The objective of the control is to stabilize a chaotic oscillation by the difference between the current output and the previous one [2, 4, 5]:

$$
U = \kappa \left\{ g \left[x_1 \left(\tau - T \right), x_2 \left(\tau - T \right) \right] - g \left[x_1 \left(\tau \right), x_2 \left(\tau \right) \right] \right\}
\tag{3}
$$
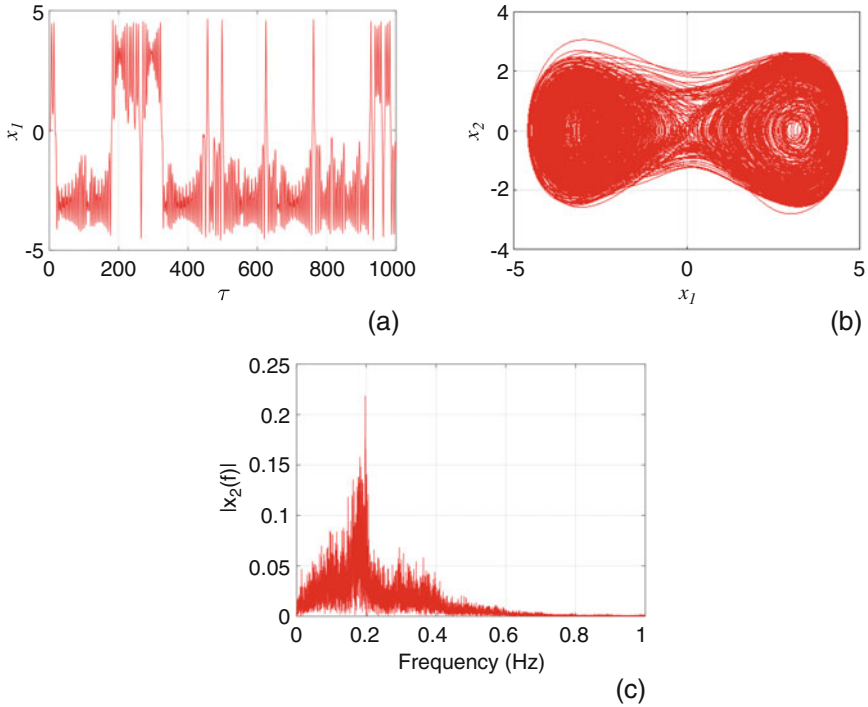
Fig. 2 (a) Displacement of the structure without control. (b) Phase portraits of the structure without control. (c) Power spectral density (FFT) to x_2

where $T = \frac{2\pi}{\Omega}$ is the time delay, κ the feedback gain, and Ω is the excitation frequency in rad/s, and signal U is given by

$$U = \kappa \left[x_2 \left(\tau - T \right) - x_2 \left(\tau \right) \right] \tag{4}$$

In Fig. 3, system (2) with time-delayed feedback control (4), and parameters $\kappa = 5$ and $\Omega = 4.364$, is observed.

5 Suppression of Chaotic Behavior

Considering a nonlinear system represented in the following way [6]:

$$\dot{\mathbf{x}} = \mathbf{A}\left(\mathbf{x}\right)\mathbf{x} + \boldsymbol{\Gamma} + \mathbf{U} \tag{5}$$

where $\mathbf{U}_{\text{SDRE}} = \mathbf{u}_{\text{ff}} + \mathbf{u}_{\text{fd}}$. The feedforward control $\mathbf{u}_{\text{ff}}$ and the feedback control $\mathbf{u}_{\text{fd}}$ are obtained from $\mathbf{u}_{\text{ff}} = -\boldsymbol{\Gamma}$ and $\mathbf{u}_{\text{fd}} = -\mathbf{R}^{-1}\mathbf{B}^{\text{T}}\mathbf{P}(\mathbf{x})\mathbf{x}$, respectively. The control $\mathbf{u}_{\text{fd}}$ is determined by using $\mathbf{K} = lqr(\mathbf{A}(\mathbf{x}), \mathbf{B}, \mathbf{Q}, \mathbf{R})$ which is a command of
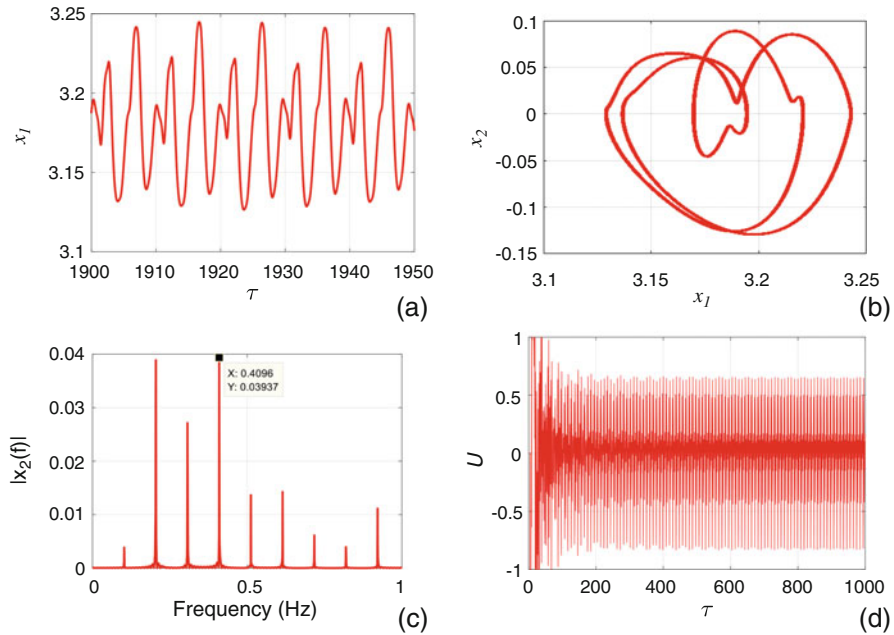
Fig. 3 (**a**) Displacement of the structure with control. (**b**) Phase plane of the structure with control. (**c**) Power spectral density (FFT) to x_2. (**d**) Signal control (U)

MATLAB$^{\circledR}$. Since $\mathbf{x}(0) = \mathbf{x}_0$, substituting $\mathbf{u}_{\mathrm{ff}} = -\boldsymbol{\Gamma}$ in Eq. (5), system (5) can be represented in the following way:

$$\dot{\mathbf{x}} = \mathbf{A}(\mathbf{x})\mathbf{x} + \mathbf{B}\mathbf{u}_{\mathrm{fd}} \tag{6}$$

The quadratic cost function for the regulator problem is given by:

$$J = \frac{1}{2}\int_{\tau_0}^{\infty}\left[\mathbf{x}^{\mathrm{T}}\mathbf{Q}\mathbf{x} + \mathbf{u}_{\mathrm{fd}}^{\mathrm{T}}\mathbf{R}\mathbf{u}_{\mathrm{fd}}\right]d\tau \tag{7}$$

where $\mathbf{Q}$ is a semi-positive-definite matrix and $\mathbf{R}$ is positive-definite. Assuming full state feedback, the control law is given by

$$\mathbf{u}_{\mathrm{fd}} = -\mathbf{R}^{-1}\mathbf{B}^{\mathrm{T}}\mathbf{P}(\mathbf{x})\mathbf{e} \tag{8}$$

where $\mathbf{e} = \begin{bmatrix} x_1 - x_1^* \\ x_2 - x_2^* \end{bmatrix}$, and x_j^* is a desired trajectory.

The state-dependent Riccati equation is solved to obtain $\mathbf{P}(\mathbf{x})$, which is given by:

$$\mathbf{A}^{\mathrm{T}}(\mathbf{x})\mathbf{P}(\mathbf{x}) + \mathbf{P}(\mathbf{x})\mathbf{A}(\mathbf{x}) - \mathbf{P}(\mathbf{x})\mathbf{B}\mathbf{R}^{-1}\mathbf{B}^{\mathrm{T}}\mathbf{P}(\mathbf{x}) + \mathbf{Q} = \mathbf{0} \tag{9}$$

For controllability, the matrix $[\mathbf{B} \vdots \mathbf{A}^n \mathbf{B}]$ has to be determined and different from zero.

For the SDRE method, we consider the algorithm proposed in [1].

5.1 Application of SDRE Control

The objective is to find the control such that x_1 stays in asymptotically stable periodic orbit $(x_1^* = 3.127 + 0.0585 \cos(2.5736\tau)$, with frequency and amplitude similar to that obtained with TDF control). Introducing the control $U_{\text{SDRE}} = U$ in system (2):

$$
\begin{aligned}
\dot{x}_1 &= x_2, \\
\dot{x}_2 &= A \left(w_1 \left(x_4^2 \sin x_3 - p_3 x_5 \cos x_3 \right) - \beta x_2 + x_1 - \delta x_1^3 \right) + U_{\text{SDRE}}, \\
\dot{x}_3 &= x_4, \\
\dot{x}_4 &= A \left(p_3 x_5 - w_2 w_1 x_4^2 \sin x_3 \cos x_3 + w_2 \beta w \cos x_3 - w_2 \cos x_3 \left(x_1 - \delta x_1^3 \right) \right), \\
\dot{x}_5 &= -p_1 x_5 - p_2 x_4 + U_1
\end{aligned}
\tag{10}
$$

Considering system (10), we see that the feedforward control is given by

$$
\mathbf{u}_{\text{ff}} = -A \left(w_1 \left(x_4^2 \sin x_3 - p_3 x_5 \cos x_3 \right) \right)
\tag{11}
$$

As the objective is to control the displacement of x_1, only the first two equations of system (9) will be considered, a control strategy similar to that used in [7]. Then, substituting Eq. (10) into Eq. (9), system (9) can be described in the following way:

$$
\dot{\mathbf{x}} = \mathbf{A}(\mathbf{x}) \mathbf{x} + \boldsymbol{\Gamma} + \mathbf{B} \mathbf{u}_{\text{fd}}
\tag{12}
$$

where

$$
\mathbf{A}(\mathbf{x}) = \begin{bmatrix} 0 & 1 \\ A \left(1 - 2\delta x_1^2 \right) & -A\beta \end{bmatrix}, \boldsymbol{\Gamma} = \begin{bmatrix} 0 \\ A \left(w_1 \left(x_4^2 \sin x_3 - p_3 x_5 \cos x_3 \right) \right) \end{bmatrix} \text{ and}
$$

$$
\mathbf{B} = \begin{bmatrix} 0 \\ 1 \end{bmatrix}.
$$

Defining $\mathbf{Q} = 10^3 \begin{bmatrix} 1 & 0 \\ 0 & 1 \end{bmatrix}$ and $\mathbf{R} = 10^{-3}$, in Fig. 4, we can observe system (2) with the application of SDRE control.
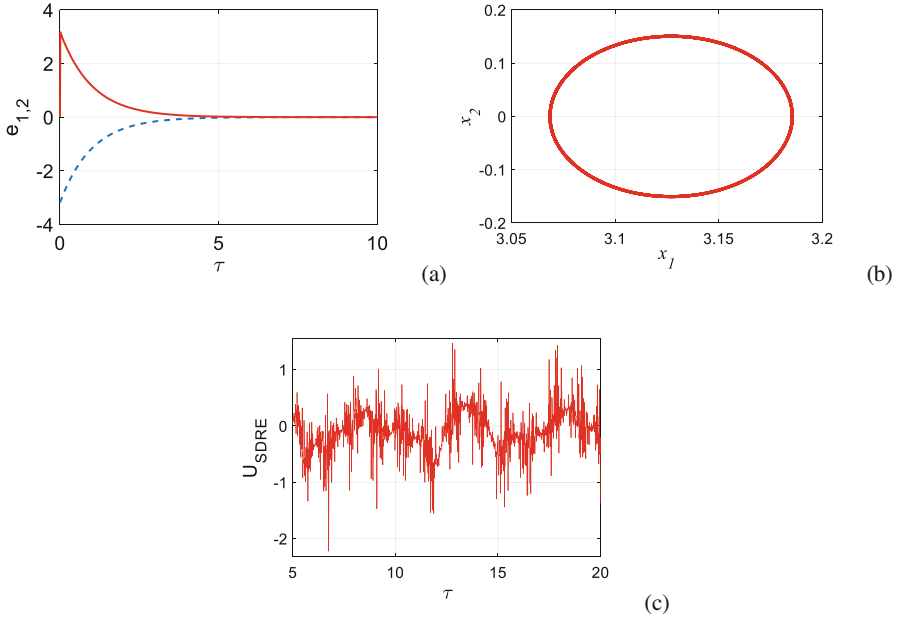
Fig. 4 (**a**) Desired trajectory error. (**b**) Phase portraits of the structure with control. (**c**) Signal control (U).

6 Conclusions

For control of chaos induced by a nonideal system, the delayed feedback control was designed and applied. Results were obtained by means of numerical analysis to inhibit the chaotic behavior of the system and maintain the amplitude of the nonideal system in a periodic orbit. With the proposal of feedforward and feedback controls, it is possible to control the oscillations in periodic orbits with the control signal close to that obtained with the TDF controller. The time-delayed control is not designed to take the system to any previously defined orbit, it is interesting to apply the SDRE control. As shown in Fig. 4, the SDRE control was efficient in taking the system to the next periodic orbit obtained by the time-delayed control. However, when the control signals of Figs. 3d and 4c are compared, it is observed that the SDRE control must maintain a signal to keep the system in the periodic orbit, generating high values of the cost for the time-delayed control. Thus, we conclude that the TDF is a great option, with the objective of leading the system to a periodic orbit with the lowest control effort. In addition, the SDRE control is also an option to be considered to enforce the desired orbit.

References

1. Litak, G., Manoach, E., Halvorsen, E.: Nonlinear and multiscale dynamics of smart materials in energy harvesting. Eur. Phys. J. Spec. Top. **224**, 2671–2673 (2015)
2. Pyragas, K.: Continuous control of chaos by self-controlling feedback. Phys. Lett. A. **170**, 421–428 (1992)
3. Piccirillo, V., Tusset, A.M., Balthazar, J.M.: Dynamical jump attenuation in a non-ideal system through a magnetorheological damper. J. Theor. Appl. Mech. **52**(3), 595–604 (2014)
4. Yu, H., Guo, S., Wang, F., Yang, Y.: Dynamic time-delayed feedback control of Westwood+ TCP flow control model with communication delay. IMA J. Math. Control Inf. **35**, 1005–1025 (2018)
5. Grawitter, J., Van Buel, R., Christian, S., Stark, H.: Dissipative systems with nonlocal delayed feedback control. New J. Phys. **20**, 113010-1–113010-18 (2018)
6. Tusset, A.M., Piccirillo, V., Bueno, A.M., Balthazar, J.M., Sado, D., Felix, J.L.P., Brasil, R.M.L.R.F.: Chaos control and sensitivity analysis of a double pendulum arm excited by an RLC circuit based nonlinear shaker. J. Vib. Control. **22**, 3621–3637 (2016)
7. Tusset, A.M., Piccirillo, V., Balthazar, J.M., Brasil, M.R.L.F.: On suppression of chaotic motions of a portal frame structure under non-ideal loading using a magneto-rheological damper. J. Theor. Appl. Mech. **53**, 653–664 (2015)

Distributed Event-Triggered Output Feedback Control for Semilinear Time Fractional Diffusion Systems

Fudong Ge and YangQuan Chen

Abstract This paper describes how to design distributed event-triggered output feedback controllers for the Mittag-Leffler stability of semilinear time fractional diffusion systems (TFDSs) under the Robin boundary conditions (BCs). To this end, an extended Luenberger-type observer is presented to solve the limitations caused by the impossible availability of full-state information. With this, we propose the distributed output feedback event-triggered controllers via backstepping technique under which the considered systems admit Mittag-Leffler stability. It is shown that the given event-triggered control strategy could significantly reduce the amount of transmitted control inputs while guaranteeing the desired system performance with the Zeno phenomenon being excluded. A numerical illustration is finally included.

Keywords Event-triggered control · Semilinear time fractional diffusion systems · Mittag-Leffler stabilization · Robin boundary conditions · Backstepping

1 Introduction

Over the past two decades, considerable attention has been attracted towards event-triggered control so as to deal with control issues such as state feedback control [1], output feedback control [2], and robust adaptive control [3] for lumped parameter systems governed by ordinary differential equations. This is due to the fact that event-triggered control could reduce workload of the network, slow down the actuators wear, save both computation and energy resources, and increase robustness to

F. Ge
School of Computer Science, China University of Geosciences, Wuhan, China
e-mail: gefd@cug.edu.cn

Y. Chen (✉)
Department of Mechanical Engineering (MESA-Lab), University of California, Merced, CA, USA
e-mail: ychen53@ucmerced.edu; yqchen@ieee.org

unexpected disturbances [4]. In recent years, the studies on event-triggered control have been extended to infinite-dimensional systems, e.g., reaction-diffusion systems [5], semilinear diffusion partial differential equations [6], and 1-dimensional linear hyperbolic systems [7]. For more knowledge in this direction, we refer the reader to [8, 9].

Nowadays, we recall that significant contributions to the study of anomalous subdiffusion phenomena observed in many spatially inhomogeneous environments have been made (see, e.g., [10, 11]). Due to the fact that fractional derivative is defined by using a kind of convolution and good at modeling the inverse power-law decay processes, TFDSs have been widely applied to describe these subdiffusion phenomena [11–13]. Therefore, it should be both interesting and challenging to discuss the distributed event-triggered control problems for semilinear TFDSs.

Motivated by these above considerations, the purpose of this paper is to study the event-triggered control problems of semilinear TFDSs. Notice that the full-state information, which is required to evaluate the triggering event and to conduct the control action, is not available in many practical applications due to the difficulties of measuring. To this end, we here design an extended Luenberger-type observer. A dynamic distributed event-triggered output feedback controller is then proposed to achieve the desired performance of the closed-loop system at hand. In addition, it is important to guarantee the existence of a positive lower bounded minimum inter-event time so as to avoid the occurrence of Zeno phenomenon [4].

As one of the most important notions in system analysis, stabilization is to determine a control law that forces the closed-loop system at hand to be stable. Since the solution of TFDS is usually expressed with respect to Mittag-Leffler functions, the Mittag-Leffler stabilization problem should be correspondingly discussed. As shown in [14], the backstepping technique was extended to efficiently stabilize the linear unstable TFDS with Dirichlet and Neumann BCs under time-triggered control strategy. In [15], both the event-triggered boundary state and output feedback control problems were investigated for linear TFDSs with unknown time-varying input uncertainties. Based on these, we continue to use the backstepping approach to obtain our main results. To the best of our knowledge, no related result is available on this topic.

The rest of this paper is organized as follows. In Sect. 2, we formulate our problems. The detailed observer-based event-triggered controller design and implementation for the considered system are given in Sect. 3. At last, we work out a numerical example to illustrate our results.

2 Problem Formulation

Let $L^2(0, l)$, $l > 0$ be the usual square integrable function space endowed with the inner product $(\cdot, \cdot)$ and the norm $\| \cdot \|$. In this paper, we deal with semilinear TFDSs under Robin BCs of the form:

$$\begin{aligned}
&{}_0^C D_t^\alpha y(x,t) = \triangle y(x,t) + f(y(x,t),x,t) + Bu(t) \text{ in } (0,l) \times (0,\infty), \\
&p_1 y_x(0,t) - p_2 y(0,t) = 0, \ q_1 y_x(l,t) + q_2 y(l,t) = 0 \text{ in } (0,\infty), \\
&y(x,0) = y_0(x) \text{ in } (0,l),
\end{aligned} \tag{1}$$

where $\triangle = \frac{\partial^2}{\partial x^2}$ is the Laplace operator, $p_1 > 0$, $p_2 \geqslant 0$ and $q_1, q_2 \geqslant 0$ with $q_1 + q_2 > 0$ are four constants, ${}_0^C D_t^\alpha$, $\alpha \in (0,1]$ and ${}_0 I_t^\alpha$ denote, respectively, the Caputo fractional derivative and the Riemann–Liouville fractional integral with respect to t given by

$$ {}_0^C D_t^\alpha y(\cdot,t) = {}_0 I_t^{1-\alpha} \frac{\partial y}{\partial t}(\cdot,t), \ \alpha \in (0,1] \text{ and } {}_0 I_t^\alpha y(\cdot,t) = \int_0^t \frac{(t-s)^{\alpha-1}}{\Gamma(\alpha)} y(\cdot,s) ds. $$

Let $(\lambda_n, \xi_n(x))_{n \geqslant 1}$ be the eigenvalue-eigenfunction paring of operator $\triangle$ under the domain $\mathcal{D}(A) = \{\phi \in L^2(0,l) : \text{satisfies the Robin BC in (1)}\}$. By Lemma 2 of [16], if $\lambda_n \neq 0$, there exists a constant $c_0 > 0$ such that $\lambda_n \leqslant -c_0 < 0$ for all $n = 1, 2, \cdots$ and besides, the set $\{\xi_n(x)\}_{n \geqslant 1}$ forms a Riesz basis of space $L^2(0,l)$. Then, any $\phi \in L^2(0,l)$ can be expressed as $\phi(x) = \sum_{n=1}^{\infty} (\phi, \xi_n) \xi_n(x)$. With these, we obtain that system (1) (with $u \equiv 0$) possesses arbitrarily many unstable eigenvalues if the semilinear function f is large enough.

Besides, let $E \triangleq L^2(0,\infty; L^2(0,l))$ be endowed with the norm $\|y\|_E = \sqrt{\int_0^\infty \|y(\cdot,t)\|^2 dt}$. The function $f : E \times (0,l) \times (0,\infty) \to E$ is assumed to satisfy

Assumption 1 Given a constant $R > 0$, y, $y^* \in E$ with $\|y\|_E$, $\|y^*\|_E \leqslant R$, there exists a constant $c = c(R) > 0$ such that

$$ (f(y(\cdot,t),\cdot,t) - f(y^*(\cdot,\tau),\cdot,\tau), \xi_n) \leqslant c (y(\cdot,t) - y^*(\cdot,\tau), \xi_n) \tag{2} $$

holds true for all $\xi_n \in L^2(0,l)$ and $t, \tau \geqslant 0$.

In addition, $u \in L^2(0,\infty; U)$ denotes the control input, U is Hilbert space, and $B : U \to L^2(0,l)$ represents the control operator. The measurement is given by

$$ z(t) = y(0,t) \text{ with } y(0,t) \not\equiv 0. \tag{3} $$

3 Event-Triggered Output Feedback Control

3.1 Observer Design

Herein, we propose the following semilinear extended Luenberger observer

$$\begin{aligned}
{}^{C}_{0}D^{\alpha}_{t}\hat{y}(x,t) &= \hat{y}_{xx}(x,t) + f(\hat{y}(x,t),x,t) + Bu(t) \\
&\quad + k_1(x)[z(t) - \hat{z}(t)] \text{ in } (0,l) \times (0,\infty), \\
p_1\hat{y}_x(0,t) &- p_2\hat{y}(0,t) = k_2[z(t) - \hat{z}(t)] \text{ in } (0,\infty), \\
q_1\hat{y}_x(l,t) &+ q_2\hat{y}(l,t) = 0 \text{ in } (0,\infty), \\
\hat{y}(x,0) &= \hat{y}_0(x) \text{ in } (0,l),
\end{aligned} \tag{4}$$

where $\hat{z}(t) = \hat{y}(0,t)$, $\hat{y}_0 \in L^2(0,l)$, $k_1(x)$ and k_2 are two observer gains to be determined to ensure the stability of observer error $e(x,t) \triangleq y(x,t) - \hat{y}(x,t)$. Besides, we get that $e(x,t)$ with $e_0(x) = y_0(x) - \hat{y}_0(x)$ is governed by

$$\begin{aligned}
{}^{C}_{0}D^{\alpha}_{t}e(x,t) &= e_{xx}(x,t) + f(e(x,t) + \hat{y}(x,t),x,t) \\
&\quad - f(\hat{y}(x,t),x,t) - k_1(x)e(0,t) \text{ in } (0,l) \times (0,\infty), \\
p_1e_x(0,t) &- (p_2 - k_2)e(0,t) = 0 \text{ in } (0,\infty), \\
q_1e_x(l,t) &+ q_2e(l,t) = 0 \text{ in } (0,\infty), \\
e(x,0) &= e_0(x) \text{ in } (0,l).
\end{aligned} \tag{5}$$

Taking into account the integral transformation

$$\omega(x,t) = e(x,t) - \int_0^x g(x,\varsigma)e(\varsigma,t)d\varsigma \tag{6}$$

with $\omega_0(x) = e_0(x) - \int_0^x g(x,\varsigma)e_0(\varsigma)d\varsigma$, we obtain the following equivalent transform, whose proof can be found in [17].

Proposition 1 *Let $k_1(x)$ and k_2 be chosen as*

$$k_1(x) = \int_0^x g(x,\varsigma)k_1(\varsigma)d\varsigma - g_\varsigma(x,0) + g(x,0)(g(0,0) + r_2/r_1) \tag{7}$$

and

$$k_2 = p_2 - p_1g(0,0) - p_1r_2/r_1. \tag{8}$$

Then if g is governed by
$$\begin{cases}
g_{xx}(x,\varsigma) - g_{\varsigma\varsigma}(x,\varsigma) = \mu g(x,\varsigma), & 0 < \varsigma < x < l, \\
2\frac{d}{dx}g(x,x) = -\mu, & 0 < x < l, \\
\begin{cases}
G(L,\varsigma) = 0, & \text{if } q_1, s_1 = 0; \\
\begin{cases}
s_1g_x(l,\varsigma) + s_2g(l,\varsigma) = 0, \\
g(l,l) = \frac{q_2}{q_1} - \frac{s_2}{s_1},
\end{cases} & \text{if } q_1, s_1 \neq 0,
\end{cases}
\end{cases}$$
the transformation (6) can equivalently convert the error dynamic (5) into

$$\begin{cases}
{}^{C}_{0}D^{\alpha}_{t}\omega(x,t) = \omega_{xx}(x,t) - \mu\omega(x,t) + \varphi \text{ in } (0,l) \times (0,\infty), \\
r_1\omega_x(0,t) - r_2\omega(0,t) = 0 \text{ in } (0,\infty), \\
s_1\omega_x(l,t) + s_2\omega(l,t) = 0 \text{ in } (0,\infty), \\
\omega(x,0) = \omega_0(x) \text{ in } (0,l),
\end{cases} \tag{9}$$

where $r_1 > 0$, $r_2, s_1, s_2 \geqslant 0$ are four constants, $\mu > 0$ is a constant and

$$
\begin{aligned}
\varphi &\triangleq \varphi(e(x,t), \hat{y}(x,t), x, t) \\
&= f(e(x,t) + \hat{y}(x,t), x, t) - f(\hat{y}(x,t), x, t) \\
&\quad - \int_0^x g(x, \varsigma)\big(f(e(\varsigma,t) + \hat{y}(\varsigma,t), \varsigma, t) - f(\hat{y}(\varsigma,t), \varsigma, t)\big)d\varsigma.
\end{aligned}
\tag{10}
$$

For the observer-based event-triggered control, observer (4) is rewritten as

$$
\begin{aligned}
{}_0^C D_t^\alpha \hat{y}(x,t) &= \hat{y}_{xx}(x,t) + f(\hat{y}(x,t), x, t) + Bu(t) \\
&\quad + k_1(x)e(0,t) \text{ in } (0,l) \times [t_k, t_{k+1}), \\
p_1\hat{y}_x(0,t) - p_2\hat{y}(0,t) &= k_2 e(0,t) \text{ in } [t_k, t_{k+1}), \\
q_1\hat{y}_x(l,t) + q_2\hat{y}(l,t) &= 0 \text{ in } [t_k, t_{k+1}), \\
\hat{y}(x,0) &= \hat{y}_0(x) \text{ in } (0,l),
\end{aligned}
\tag{11}
$$

where $\{t_k\}_{k\in\mathbb{N}}$ denotes the certain instants when the actuator signal is updated.

Let the observer-based event-triggered controller be defined as follows:

$$
Bu(t) = -f(\hat{y}(x, t_k), x, t_k), \ \forall t \in [t_k, t_{k+1}), \ k \in \mathbb{N}.
\tag{12}
$$

Similarly, by the integral transformation $\rho(x,t) = \hat{y}(x,t) - \int_0^x h(x, \varsigma)\hat{y}(\varsigma,t)d\varsigma$, the following proposition holds, whose proof is given in [17] too.

Proposition 2 Suppose that $k_1(x)$ and k_2 satisfy (7) and (8), respectively. Let $H(x) = k_1(x) - \int_0^x h(x, \varsigma)k_1(\varsigma)d\varsigma + \frac{k_2}{p_1}$ and

$$
\begin{aligned}
\psi &\triangleq \psi(\hat{y}(x,t), \hat{y}(x, t_k), x, t, t_k) \\
&= f(\hat{y}(x,t), x, t) - \int_0^x h(x, \varsigma)f(\hat{y}(\varsigma,t), \varsigma, t)d\varsigma \\
&\quad - f(\hat{y}(x, t_k), x, t_k) + \int_0^x h(x, \varsigma)f(\hat{y}(\varsigma, t_k), \varsigma, t_k)d\varsigma.
\end{aligned}
\tag{13}
$$

Then if h solves the equation
$$
\begin{cases}
h_{xx}(x, \varsigma) - h_{\varsigma\varsigma}(x, \varsigma) = \sigma h(x, \varsigma), 0 < \varsigma < x < l, \\
h(x,x) = \frac{-\sigma}{2}x, \ 0 < x < l, \\
h_\varsigma(x,0) = h(x,0)\frac{p_2}{p_1}, \ 0 < x < l
\end{cases}
$$
with $h(0,0) = 0$, the observer (11) is equivalent to

$$
\begin{aligned}
{}_0^C D_t^\alpha \rho(x,t) &= \rho_{xx}(x,t) - \sigma\rho(x,t) + H(x)e(0,t) + \psi \text{ in } (0,l) \times [t_k, t_{k+1}), \\
r_1\rho_x(0,t) - r_2\rho(0,t) &= k_2 e(0,t) \text{ in } [t_k, t_{k+1}), \\
s_1\rho_x(l,t) + s_2\rho(l,t) &= 0 \text{ in } [t_k, t_{k+1}), \\
\rho(x,0) &= \rho_0(x) \text{ in } (0,l)
\end{aligned}
\tag{14}
$$

for some constant $\sigma \in (0, \mu)$.

Remark 1 Here $\sigma \in (0, \mu)$ is used to shown that the convergence speed of the observer is higher than that of the controller so as to Mittag-Leffler stabilize the considered closed-loop system.

Definition 1 The solution of system (1) is said to be Mittag-Leffler stable if there exist constants $c > 0$, $\varepsilon > 0$, $s > 0$ such that

$$\|y(\cdot, t)\| \leqslant c\left\{E_\alpha(-\varepsilon t^\alpha)\right\}^s \|y_0\|, \ t \geqslant 0, \tag{15}$$

where $E_\alpha(t) = \sum\limits_{k=0}^{\infty} \frac{t^k}{\Gamma(\alpha k+1)}, \alpha > 0, t \geqslant 0$ denotes the Mittag-Leffler function in one parameters.

3.2 Stability of the Closed-Loop Control System

Based on (a) of Fig. 1, assume that $t_0 = 0$ and $\|\hat{y}(\cdot, t)\| \not\equiv 0$, the event-triggered condition which depends explicitly on the observer state is designed as

$$t_{k+1} = \min\left\{t > t_k : \left\|\hat{y}(\cdot, t) - \hat{y}(\cdot, t_k)\right\| \geqslant \check{e}\|\hat{y}(\cdot, t)\|\right\}, \ k \in \mathbb{N}, \tag{16}$$

where $\check{e} > 0$ is the event threshold.

Remark 2 As cited in [4, 18], the zero-order-hold (ZOH), which is very common in computer-controlled systems, is to convert the discrete-time control signal into the continuous-time signal simply by holding it constant over the sampling intervals. In this paper, ZOH unit in (a) of Fig. 1 aims to convert discrete event-triggered control signal governed by Eq. (12) to be continuous. More precisely, when the inequality (16) is breached, it will invoke a transmission. If there are no control signal received, then the last received sensor value will be used since the sensor data just fluctuate within a small range from the previous data. With this, ZOH has the advantages that it can be used for non-periodic sampling and besides, to significantly reduce the burden of the network communication.

From Proposition 1 and 2, we have $\max\limits_{0\leqslant\varsigma\leqslant x\leqslant l}|g(x,\varsigma)| \leqslant C_g$, $\max\limits_{0\leqslant\varsigma\leqslant x\leqslant l}|h(x,\varsigma)| \leqslant C_h$ and there exists a constant $\nu > 0$ satisfying

$$\|e(\cdot, t)\| \leqslant \nu\|\omega(\cdot, t)\|, \|\omega_0\| \leqslant \nu\|e_0\|, \|\hat{y}(\cdot, t)\| \leqslant \nu\|\rho(\cdot, t)\|, \|\rho_0\| \leqslant \nu\|\hat{y}_0\|. \tag{17}$$

The following is our main result and we present the detailed proof in [17].

Theorem 1 *Suppose that Assumption 1, all conditions of Proposition 1 and 2 hold. Let $\|e_0\| + \|\hat{y}_0\| \leqslant R_0$ for some constant $R_0 > 0$. If $r_1^{-1}r_2 \geqslant \frac{1}{4}$, $r_1 r_2 \geqslant 2$ and there exist two constants σ, $\varepsilon > 0$ satisfying*

$$2\sigma \geqslant c^* + \varepsilon \tag{18}$$
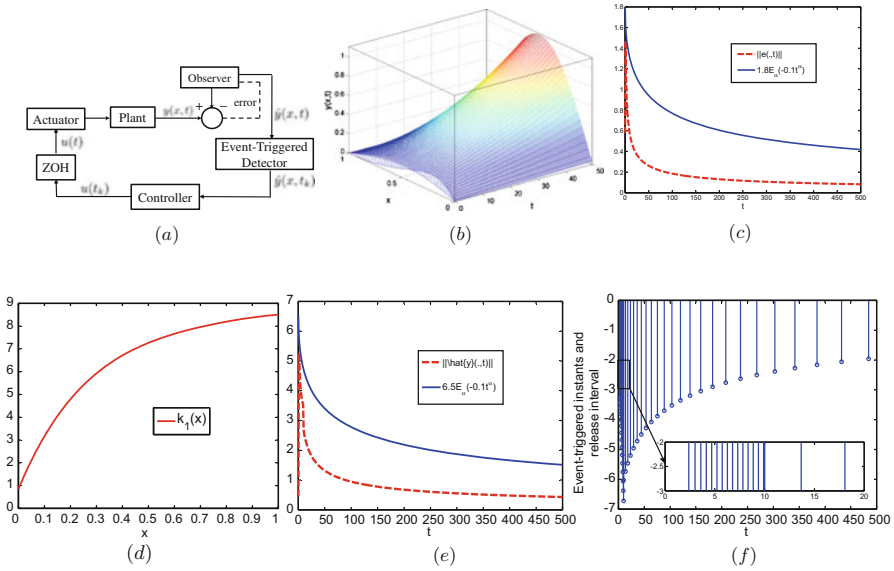
Fig. 1 Evolution of the closed-loop event-triggered control system. (**a**) The structure of event-triggered control. (**b**) Plots of considered system with $u \equiv 0$. (**c**) L^2-norm of the error. (**d**) The observer gain $k_1(x)$. (**e**) L^2-norm of the observer. (**f**) Event-triggered instants

with $c^* \triangleq \max \left\{ v + \frac{C_g l^{3/2}}{\sqrt{3}} v, \ 2\|H\|^2 + \check{e}v + \frac{C_h l^{3/2}}{\sqrt{3}} \check{e}v \right\}$, *then the system consisting of the plant* (1), *observer* (11), *and controller* (12) *under the event-triggered rule* (16) *is closed-loop Mittag-Leffler stable in* $L^2(0, l)$ *and* $\|y\|_E \leqslant R$ *with* $R = \sqrt{2}v^2 R_0$.

3.3   Minimum Inter-Event Time

To avoid the Zeno phenomenon, a positive lower bounded minimum inter-event time should be guaranteed. For this purpose, we give the following results, whose detailed proof can be found in [17].

Theorem 2 *Assume that all conditions of Theorem 1 are satisfied. Then the minimum inter-event time* $T_{\min}$ *given by*

$$T_{\min} = \min_{k=0,1,2,\cdots} \{t_{k+1} - t_k\} \tag{19}$$

is lower bounded provided that t_k *is defined as* (16).

4 Numerical Simulation

Consider the TFDSs with $\alpha = 0.5$, $l = 1$ and $f(y, x, t) = 5y + 5e^{-t}\left[\sqrt{y^2 + 1} - 1\right]$. Given R such that $\|y\|_E \leqslant R$, clearly, *Assumption* 1 holds true for $c = 10R$. The initial condition is assigned as $y_0(x) = 2x(1 - x)^2 e^{-2x}$ and the coefficients of the BCs are $p_1 = 3$, $p_2 = q_1 = 1$ and $q_2 = 2$. According to (b) of Fig. 1, the solution of the considered TFDS with $u \equiv 0$ is unstable.

From Sect. 3, an extended Luenberger observer should be designed to estimate the system. Let $\hat{y}_0(x) = x(1 - x)^2 e^{-2x}$ and the target system is parameterized as $r_1 = 3$, $r_2 = s_1 = 1$ and $s_2 = 2$. Then $e_0(x) = x(1 - x)^2 e^{-2x}$. Let $\mu = 10$. (c) of Fig. 1 implies that error system (5) with observer gain k_1 shown in (d) of Fig. 1 and $k_2 = 3$ is Mittag-Leffler stable.

To test our event-triggered control approach, we take $\check{e} = 0.05$ in (16) and set $\sigma = 5$. Then $\max\{|g(x, \varsigma)|, \ |h(x, \varsigma)|\} \leqslant Ne^{2Nx}$, where $N = \sigma(1 + e^{-2})$ [19]. Then (18) holds true for $\varepsilon = 0.1$. As a result, we compare the spatial L^2-norm of $\hat{y}(x, t)$ with event-trigged controller in (e) of Fig. 1. Moreover, (f) of Fig. 1 shows the event-triggered instants when the control input is updated.

5 Conclusions

In this paper, the idea of using observer-based event-triggered control to Mittag-Leffler stabilizef TFDS is presented via backstepping. To address the problems caused by the lack of full-state measurement, the observer-based distributed output feedback event-triggered controllers under which the considered closed-loop systems admit Mittag-Leffler stability are proposed with the Zeno phenomenon being excluded. Moreover, since the use of event-triggered control strategy could degrade the performance of controllers and then enlarge the value of control inputs, if we, however, want to figure out how many values of the improvement of control inputs caused by event-triggered control strategy for semilinear TFDSs, more constraints on systems are required. This is beyond the scope of this paper. We conclude that event-triggered control for more complex nonlinear TFDSs as well as further investigations on the effect of event-triggered strategy to control inputs are of great interest.

References

1. Lunze, J., Lehmann, D.: A state-feedback approach to event-based control. Automatica **46**(1), 211–215 (2010)
2. Yan, S., Shen, M., Zhang, G.: Extended event-driven observer-based output control of networked control systems. Nonlinear Dyn. **86**(3), 1639–1648 (2016)

3. Mu, C., Wang, D., Sun, C., Zong, Q.: Robust adaptive critic control design with network-based event-triggered formulation. Nonlinear Dyn. **90**(3), 2023–2035 (2017)
4. Zhang, X., Han, Q., Zhang, B.: An overview and deep investigation on sampled-data-based event-triggered control and filtering for networked systems. IEEE Trans. Ind. Inf. **13**(1), 4–16 (2017)
5. Dong, T., Wang, A., Zhu, H., Liao, X.: Event-triggered synchronization for reaction–diffusion complex networks via random sampling. Physica A **495**, 454–462 (2018)
6. Selivanov, A., Fridman, E.: Distributed event-triggered control of diffusion semilinear PDEs. Automatica **68**, 344–351 (2016)
7. Espitia, N., Girard, A., Marchand, N., Prieur, C.: Event-based control of linear hyperbolic systems of conservation laws. Automatica **70**, 275–287 (2016)
8. Jiang, Z., Cui, B., Wu, W., Zhuang, B.: Event-driven observer-based control for distributed parameter systems using mobile sensor and actuator. Comput. Math. Appl. **72**(12), 2854–2864 (2016)
9. Wang, J., Chen, M., Shen, H.: Event-triggered dissipative filtering for networked semi-Markov jump systems and its applications in a mass-spring system model. Nonlinear Dyn. **87**(4), 2741–2753 (2017)
10. Metzler, R., Klafter, J.: The random walk's guide to anomalous diffusion: a fractional dynamics approach. Phys. Rep. **339**(1), 1–77 (2000)
11. Ge, F., Chen, Y., Kou, C.: Regional Analysis of Time-Fractional Diffusion Processes. Springer, Berlin (2018)
12. Gorenflo, R., Mainardi, F., Moretti, D., Paradisi, P.: Time fractional diffusion: a discrete random walk approach. Nonlinear Dyn. **29**(1–4), 129–143 (2002)
13. Liang, J., Chen, Y., Fullmer, R.: Boundary stabilization and disturbance rejection for time fractional order diffusion–wave equations. Nonlinear Dyn. **38**(1–4), 339–354 (2004)
14. Ge, F., Chen, Y., Kou, C.: Boundary feedback stabilisation for the time fractional-order anomalous diffusion system. IET Control Theory Appl. **10**(11), 1250–1257 (2016)
15. Ge, F., Chen, Y.: Event-triggered boundary feedback control for networked reaction-subdiffusion processes with input uncertainties. Inf. Sci. **476**, 239–255 (2019)
16. Meurer, T.: Flatness-based trajectory planning for diffusion–reaction systems in a parallelepipedon—a spectral approach. Automatica **47**(5), 935–949 (2011)
17. Ge, F., Chen, Y.: Observer-based event-triggered control for semilinear time fractional diffusion systems with distributed feedback. Nonlinear Dyn. (2018), Submitted (No. NODY-D-18-02960). https://doi.org/10.1007/s11071-019-05338-2
18. Guo, G., Lu, Z., Shi, P.: Event-driven actuators: to zero or to hold? Int. J. Robust Nonlinear Control **24**(17), 2761–2773 (2014)
19. Smyshlyaev, A., Krstić, M.: Closed-form boundary state feedbacks for a class of 1-D partial integro-differential equations. IEEE Trans. Autom. Control **49**(12), 2185–2202 (2004)

Control Performance Assessment of the Disturbance with Fractional Order Dynamics

Kai Liu, YangQuan Chen, and Paweł D. Domański

Abstract The fractional order system is the generalization of the conventional integer order control system. In this paper, we have shown that there is an effect of the controller tuning on the Hurst exponents as well as crossover points in different time scales. Error signals from the control system subject to the disturbance with fractional order dynamics are analyzed by multiple Hurst fitting lines with crossovers. Simulation results and real industry data are given to assess the performance of the control system with proposed detrended fluctuation analysis (DFA) method with crossover points.

Keywords Control performance assessment · Fractional order dynamics · Hurst exponent · Crossover point

1 Introduction

The statistical control quality measures are widely used in the current industry to assess control loops, which are based on the classical Gaussian approach. However, non-Gaussian signals and noises tend to produce large-amplitude fluctuations from the average value more frequently than Gaussian ones do, such as long range dependency (LRD), self-similarity, power-law of autocorrelation, infinite variance, spiky signals. In reality, most industrial data are not compliant with the prevailing

K. Liu
School of Engineering, University of California, Merced, CA, USA
e-mail: ychen53@ucmerced.edu

Y. Chen (✉)
Department of Mechanical Engineering (MESA-Lab), University of California, Merced, CA, USA

P. D. Domański
Institute of Control and Computation Engineering, Warsaw University of Technology, Warszawa, Poland

assumption about the Gaussian properties of the variables. These complicated phenomena originated from the fractional calculus.

Due to the complexity, correlation, time varying delays, and human interventions, the majority of the real life industrial process data has the fat-tailed property after reviewing of data from industrial process [1]. Liu et al. proposed a novel control performance assessment (CPA) method with the fractional order signal processing (FOSP) techniques in [2]. Strong correlations between process variables at different time instants characterize scenarios of long range dependence, non-stationary and spiky signals. Such time non-Gaussian series may be precisely described with auto-regressive fractionally integrated moving average (ARFIMA) models, rather than arbitrarily ignored as outliers.

In this paper, we will discuss and assess the control system under the disturbance with fractional order dynamics. A novel FOSP technique is proposed to better understand and assess the system with fractional Gaussian behaviors. The detrended fluctuation analysis (DFA) is modified with multiple crossover points, where the crossover points in the scaling-law curve are located and made use of dividing the whole scaling-law curve into several different scaling regions, in each of which a single Hurst exponent can be estimated. Finally, the estimated double Hurst exponents in different scaling ranges as well as the crossover points are used as feature parameters for assessing the control performance of the fractional order system.

The remainder of this paper is structured as follows: Sect. 2 introduces the DFA methods and the relation with the Hurst exponent. Section 3 gives some simulation examples to illustrate the method. Section 4 presents a real chemical industry case study with the proposed algorithm. Section 5 concludes the whole article.

2 DFA Method with Crossover Points

2.1 Hurst Exponent

In general, the Hurst exponent H is the indication of the smoothness of the time series: the smaller the H, the rougher the time series [3]. LRD, which is characterized by the Hurst exponent, means that there is a strong coupling effect between values at different time separations. For practical purposes, process engineers are usually interested in the possibility of using substantially shorter time series. Although this asymptotic scaling exponent may serve as a useful index for selected diagnostic purposes, a drawback is that very long data sets are required for statistically robust results. It is probably due to the fact that on very short time scales the transient control signals are dominated by the relatively smooth fluctuation, thus leading to a large local value H. For longer scales, the repeatable signals reflect the intrinsic dynamics of a complex system. Therefore, the Hurst exponent H is a good indicator to characterize the dynamics of a system in different time scales.

2.2 Algorithm of the DFA with Crossover Points

The DFA algorithm is a robust and powerful tool for detecting long range correlations buried in non-stationary data [3]. For a series x_i with the length N, the DFA process is as follows.

1. Construct a cumulative series $X(i)$

$$X(i) = \sum_{j=1}^{i}(x_j - \bar{x}),$$

$$\bar{x} = \frac{1}{N}\sum_{i=1}^{N}x_i.$$

(1)

2. Divide the whole series into non-overlapping segments with equal length s. Since the total length N may not be divisible by s, some portion of $X(i)$ will be left unused. In order to take the advantage of the whole range series, the same operation will be carried out from the end side of the series $X(i)$. Thus, $2K$ segments are obtained accordingly.
3. Use the least squares regression algorithm to fit the local polynomial trend for each of the $2K$ segments and calculate the variance:

$$F^2(v, s) = \frac{1}{s}\sum_{i=1}^{s}(X[(v-1)s+i] - x_v(i))^2.$$

(2)

Thus, for the vth segment, $v = 1, 2, 3 \ldots K$

$$F^2(v, s) = \frac{1}{s}\sum_{i=1}^{s}(X[N - (v-K)s+i] - x_v(i))^2.$$

(3)

4. Compute the root-mean-square deviation (RMSD) fluctuation function $F(s)$

$$F(s) = \sqrt{\frac{1}{2K}\sum_{v=1}^{2K}F^2(v, s)}.$$

(4)

5. Modify the scale s and repeat the above 4 steps. If x_i is long range dependence (correlated), the Hurst exponent can be illustrated by the following power law:

$$F(s) \sim s^H.$$

(5)

6. Use the polynomial curves to fit the two parts of $F(s)$ separated by the moving crossover point c in a log–log plot, respectively. Then select the crossover point c^* with the minimum summed fit error squares E of two polyfitted parts:

$$E_{c^*} = \min \left(\sum_{k=1}^{c} e_k^2 + \sum_{k=c}^{s} e_k^2 \right). \tag{6}$$

2.3 The Fractional Gaussian Noise

In time series analysis, the auto-regressive (AR) model is to build the short memory of the previous data and moving average (MA) is to model the random noise. The fractional integrated (FI) is to characterize the long memory properties. The ARFIMA (p, d, q) model of a time series X_t is defined as follows [4]:

$$\left(1 - \sum_{i=1}^{p} \phi_i B^i \right) (1 - B)^d (X_t - \mu) = \left(1 + \sum_{i=1}^{q} \theta_i B^i \right) \varepsilon_t, \tag{7}$$

where $\phi_1, \cdots, \phi_p$ are AR parameters, $\theta_1, \cdots, \theta_q$ are MA parameters, μ is the expectation of X_t, ε_t is the white noise, and B denotes the unit delay. In contrast to the ordinary auto-regressive integrated moving average (ARIMA) process, the difference operator d in ARFIMA (p, d, q) is allowed to take non-integer (fractional) values. Hosking defined the fractional difference operator by a binomial series ∇^d [5]:

$$\nabla^d = (1 - B)^d = \sum_{k=0}^{\infty} \binom{d}{k} (-B)^k = \sum_{k=0}^{\infty} \frac{\Gamma(d+1)}{\Gamma(k+1)\Gamma(d+1-k)} (-B)^k. \tag{8}$$

To the best of our knowledge, the control system under the LRD noise has not yet been studied in the CPA. In this paper, we will build the control system simulation with the fractional order Gaussian noise by changing the value of d in the fractional order difference filter $(1 - B)^d$ in Eq. (7). In the following sections, we are targeting these two major questions: How does the LRD noise affect the control system? How to assess the control performances based on different tunings of the PID controller?

3 Simulation Analysis

In the simulation, the first order plus time delay (FOPTD) system $\frac{1}{2s+1} e^{-0.5s}$ is used to simulate the process model in Fig. 1. Discrete PID controller parameters: $P = 1.5$, $I = 1.0$, $D = 0.1$; Sampling rate: 50 Hz. Control errors $e_t = y^* - y_t$ are
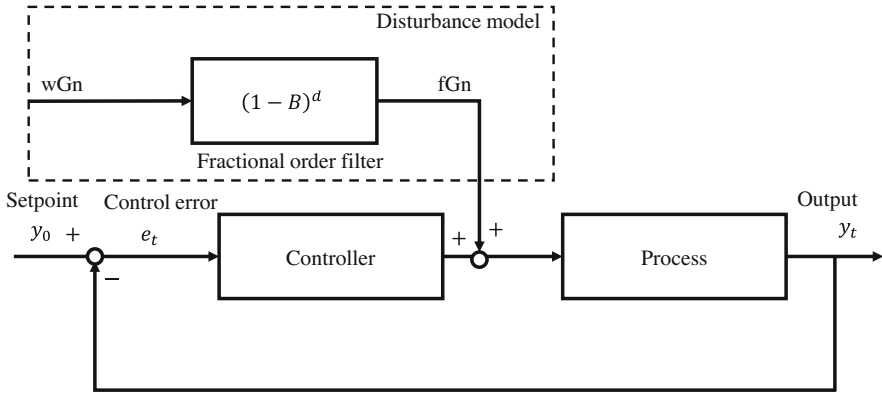
Fig. 1 The control system under the fractional order disturbances. The disturbance is modeled by the fractional Gaussian noise (fGn), which is driven by the white Gaussian noise (wGn)

used to assess the control performance, where y^* is the setpoint (target) and y_t is the feedback signal. The fractional Gaussian noise is modeled and simulated by the ARFIMA(0,d,0) with LRD disturbances $d \in [-0.5, 0.5]$. $d = 0$ corresponds to the white noise and fractional order integral (derivative) coefficient d changes the slope H in the DFA plot.

Since the original DFA Hurst fitting method does not consider the LRD (coupling) property of the time series, it should be modified to the multiple Hurst fitting algorithm with multiple polynomial lines. The fractional order difference parameter d affects the Hurst exponent H shown in the DFA plot. A larger fractional order d results in a higher H, meaning a more sluggish control. For LRD disturbance with larger d values, CPA should choose the multiple Hurst fitting results in different ranges. The crossover points move to the smaller range with increasing PID gains in Fig. 2. The DFA results with multiple Hurst exponents under different PID tunings are summarized in Table 1. This explains the response of the systems becoming faster with high PID tunings. From Table 2, it shows exactly the fact that the crossover points are moving towards shorter memories with aggressive tunings. In addition, the crossover points are moving upwards with the increasing fractional integrated order filter d, since the Hurst exponents (i.e., the slope of DFA plot) are increased accordingly in the small range. The sluggish control relates to the larger crossover, which indicates longer control and longer transient periods.
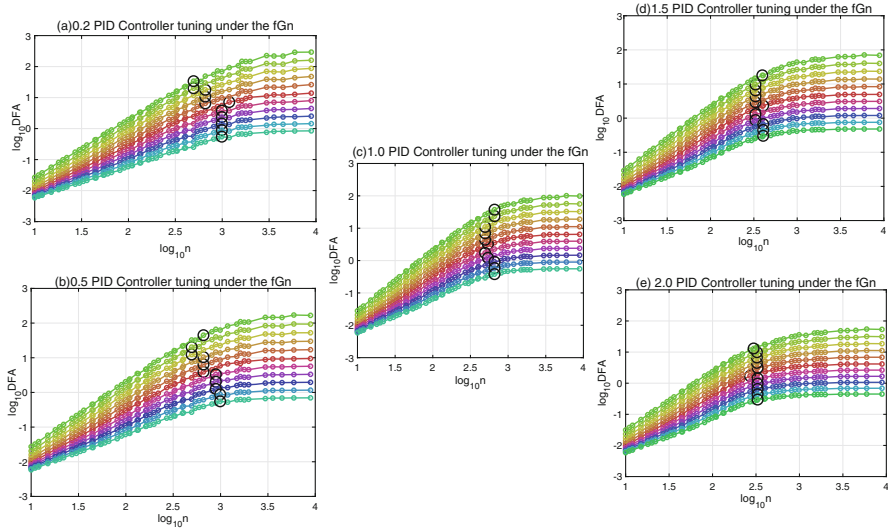
Fig. 2 DFA plots with crossover points in different PID tunings: From (**a**) to (**e**), with the increasing PID gains, the crossover points move to the small range. In each plot $d \in [-0.5, 0.5]$, the upper fitting line represents the DFA plot with $d = -0.5$, while the lower fitting line is the DFA plot with $d = 0.5$. (**a**) 0.2 PID Controller tuning under the fGn. (**b**) 0.5 PID Controller tuning under the fGn. (**c**) 1.0 PID Controller tuning under the fGn. (**d**) 1.5 PID Controller tuning under the fGn. (**e**) 2.0 PID Controller tuning under the fGn

Table 1 PID tunings results with multiple Hurst exponents

d	0.2 PID		0.5 PID		1.0 PID		1.5 PID		2.0 PID	
	H_1	H_2	H_1	H_2	H_1	H_2	H_1	H_2	H_1	H_2
-0.5	1.829	0.836	1.791	0.513	1.749	0.360	1.787	0.448	1.817	0.436
-0.4	1.777	0.787	1.777	0.588	1.709	0.326	1.767	0.436	1.775	0.371
-0.3	1.694	0.641	1.721	0.550	1.701	0.398	1.726	0.396	1.738	0.329
-0.2	1.624	0.594	1.627	0.411	1.642	0.368	1.674	0.361	1.693	0.292
-0.1	1.545	0.546	1.553	0.379	1.574	0.340	1.613	0.328	1.631	0.246
0.0	1.421	0.323	1.472	0.332	1.496	0.264	1.525	0.231	1.597	0.257
0.1	1.354	0.346	1.370	0.245	1.417	0.288	1.467	0.271	1.498	0.194
0.2	1.266	0.305	1.283	0.215	1.322	0.237	1.383	0.245	1.420	0.173
0.3	1.177	0.270	1.194	0.188	1.217	0.164	1.280	0.185	1.336	0.154
0.4	1.085	0.241	1.099	0.143	1.129	0.144	1.190	0.165	1.247	0.138
0.5	0.992	0.220	1.008	0.122	1.038	0.125	1.098	0.145	1.154	0.123

Table 2 Crossover positions at different PID tunings

d	0.2 PID	0.5 PID	1.0 PID	1.5 PID	2.0 PID
0.5	(2.695, 1.529)	(2.820, 1.651)	(2.820, 1.573)	(2.598, 1.254)	(2.473, 1.116)
0.4	(2.695, 1.302)	(2.695, 1.306)	(2.820, 1.372)	(2.519, 0.986)	(2.519, 0.986)
0.3	(2.820, 1.252)	(2.695, 1.094)	(2.695, 1.040)	(2.519, 0.812)	(2.519, 0.812)
0.2	(2.820, 1.032)	(2.820, 1.018)	(2.695, 0.844)	(2.519, 0.640)	(2.519, 0.640)
0.1	(2.820, 0.814)	(2.820, 0.807)	(2.695, 0.643)	(2.519, 0.466)	(2.519, 0.466)
0.0	(3.075, 0.856)	(2.820, 0.593)	(2.732, 0.506)	(2.607, 0.365)	(2.607, 0.365)
−0.1	(2.996, 0.580)	(2.950, 0.520)	(2.695, 0.237)	(2.519, 0.117)	(2.519, 0.117)
−0.2	(2.996, 0.372)	(2.950, 0.310)	(2.732, 0.085)	(2.519, −0.058)	(2.519, −0.058)
−0.3	(2.996, 0.163)	(2.950, 0.102)	(2.820, −0.039)	(2.607, −0.175)	(2.607, −0.175)
−0.4	(2.996, −0.048)	(2.996, −0.058)	(2.820, −0.231)	(2.607, −0.347)	(2.607, −0.347)
−0.5	(2.996, −0.260)	(2.996, −0.257)	(2.820, −0.419)	(2.607, −0.517)	(2.519, −0.525)

4   Case Study: Real Industry Data

4.1   Non stationarity Tests

Process industry data show that the majority of the available measurements and process disturbances time series exhibits non-linear, non-Gaussian, non-stationary, self-similar properties. The authors have reviewed a lot of industrial data for the validation of the above hypothesis. Some exemplary time series for real process data are presented in Fig. 3.

Visual inspection of the sketched time series shows rapid changes, unexpected significant spikes (outlier values), oscillations, and noises. As the visual impressions may be misleading further statistical analysis is performed. The prepared diagrams present histograms together with fitted probabilistic density functions (PDF) for three distributions, i.e., classical bell-shaped Gaussian, fat-tailed α-stable, and the robust (Huber) one.

The fractional dynamics hypothesis may be validated using stationarity tests for one or many samples, estimation of the memory parameter based on sample using wavelets and resampling, estimation of the self-similarity index based on sample p-variation, or by ARFIMA parameter estimation.

The stationarity tests have been run to verify the non-stationarity hypothesis for the considered exemplary time series. Running the augmented Dickey–Fuller test (DF-GLS) and Kwiatkowski–Phillips–Schmidt–Shin test (KPSS) tests over the considered data confirms in all the cases the non-stationarity hypothesis. As these tests are important tools useful in the context of the ARFIMA model, the hypothesis that industrial variables perform similarly to the fractional processes is true. This observation forms a strong rationale for the presented work.
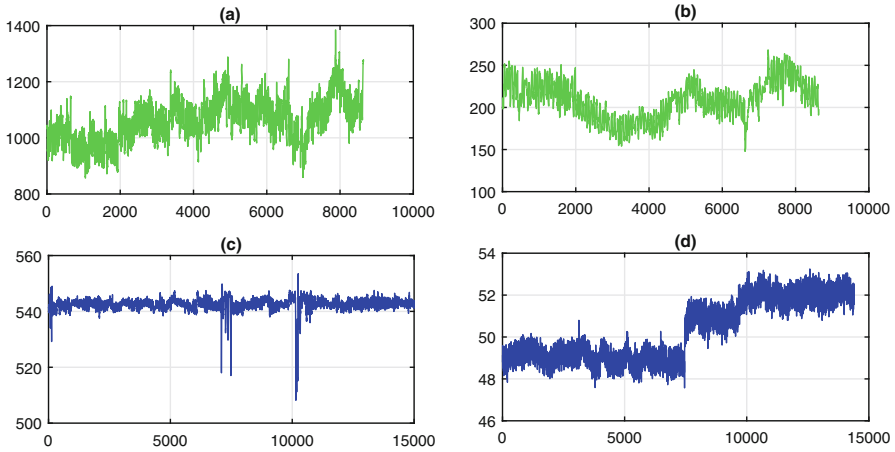
Fig. 3 Examples of the real industrial process variables time series. (**a**) Time trend of process gas flow. (**b**) Time trend of inlet gas flow. (**c**) Time trend of column inlet. (**d**) Time trend of separator level

4.2 DFA Method with Multiple Hurst Exponents Applied to the Real Data

Following the algorithm introduced in Sect. 2, the DFA method with multiple Hurst exponents has been applied to the real data in Fig. 4. In this regard, it should be noted that apparent crossovers are exhibited for the scaling behavior indicated with black circles.

Figure 4a, the DFA fitting line is straight with no significant crossover point, indicating the consistency of the control performances. From the perspective of control engineers, this control behavior is acceptable. The most interesting result is Fig. 4b. It seems that DFA fitting plot should be separated into 3 segments, since periodicities or repeated signals may be contained in the original series. It can be observed from the original series plot Fig. 3b.

In Fig. 4c, the overall DFA results are in the convex form, i.e., $H_1 > H_2$ meaning the system controller performance is going to be stabilized in the long run. In contrast, the badly controlled data set shows a very different crossover pattern. In Fig. 4d, the overall DFA results are in the concave form, i.e., $H_1 < H_2$, meaning the control performance is degrading (worse). For very short time scales, the fluctuation is quite random since $H \approx 0.5$, while for the larger time scale, the fluctuation becomes smoother and asymptotically approaching Brownian noise, $H \approx 1.5$. These findings are consistent with the previous report in [6]. Thus, the proposed method in this paper is a good quantitative description and can monitor the short term and long term of the control system.
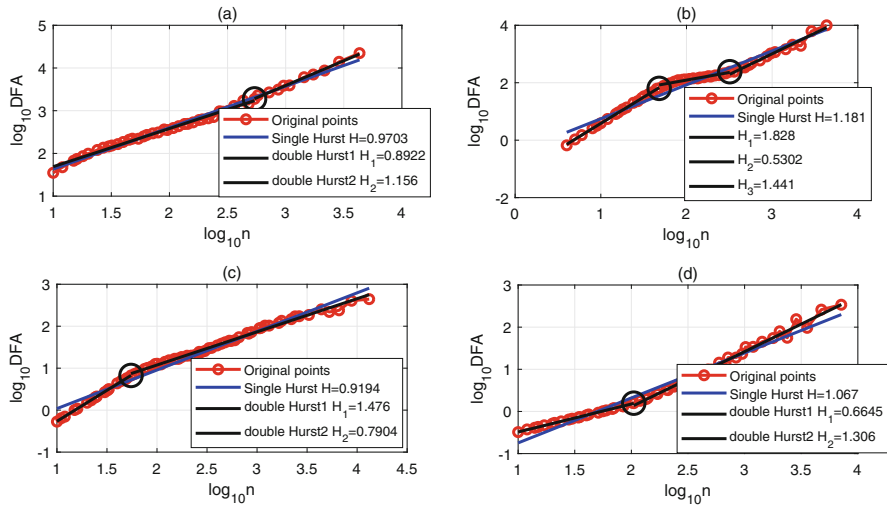
Fig. 4 DFA method with multiple Hurst exponents applied to the real data. (**a**) Time trend of process gas flow. (**b**) Time trend of inlet gas flow. (**c**) Time trend of column inlet. (**d**) Time trend of separator level

5   Conclusions

The paper analyzes the control system subject to the disturbance with fractional dynamics by using the FOSP techniques. The original DFA method is modified with multiple Hurst fittings with crossover points. In the simulation results, we have shown that there is an effect of the controller tuning on the crossover points and Hurst exponents. The industrial data validate the fact that the proposed CPA method for the system with the fractional order dynamics is helpful and may be applied in various situations.

References

1. Domański, P.D.: Non-Gaussian properties of the real industrial control error in SISO loops. In: 19th International Conference on System Theory, Control and Computing (ICSTCC), pp. 877–882. IEEE, Piscataway (2015)
2. Liu, K., Chen, Y.Q., Domanski, P. D., Zhang, X.: A novel method for control performance assessment with fractional order signal processing and its application to semiconductor manufacturing. Algorithms **11**(7), 90 (2018). https://doi.org/10.3390/a11070090
3. Peng, C.K., Havlin, S., Stanley, H.E., Goldberger, A.L.: Quantification of scaling exponents and crossover phenomena in nonstationary heartbeat time series. Chaos Interdisciplinary J. Nonlinear Sci. **5**(1), 82–87 (1995)

4. Granger, C.W., Joyeux, R.: An introduction to long memory time series models and fractional differencing. J. Time Ser. Anal. **1**(1), 15–29 (1980)
5. Hosking, J.R.: Fractional differencing. Biometrika **68**(1), 165–176 (1981)
6. Domański, P.D., Golonka, S., Marusak, P.M., Moszkowski, B.: Robust and asymmetric assessment of the benefits from improved control Industrial validation. IFAC-PapersOnLine **51**(18), 815–820 (2018)

Model Correction-Based Multivariable Predictive Functional Control for Uncertain Nonlinear Systems

Weiqiang Tang, Yongda Qi, Mengke Guo, and Haiyan Gao

Abstract An improved multivariable predictive functional control algorithm is proposed for a class of uncertain nonlinear systems. The system nonlinear dynamics are firstly transformed into a linear-like structure via the extended linearization method. And then the uncertainty acting on the system is identified using a disturbance observer. The identified value is used to improve the accuracy of the prediction model. Finally, the control input is obtained through receding horizon optimization. The proposed scheme is applied to the tracking control of a hypersonic vehicle, the results show that the scheme is effective, and the robustness of the closed-loop system is enhanced.

Keywords Uncertain nonlinear systems · Predictive functional control · Extended linearization · Disturbance observer · Robustness

1 Introduction

Model predictive control (MPC) or receding horizon control (RHC) is a class of advanced computer algorithms that utilize an explicit model to predict the future response to a plant. At each sampling instant, an optimal control sequence is yielded by optimizing a quadratic performance index subjected to constraints over a future horizon, and its first component is applied to the plant. This characteristic of receding optimization in MPC is the main difference from other control algorithms which adopt pre-computed control laws [1]. However, receding optimization of MPC requires a lot of computing resources, which could be an obstacle to its

W. Tang · (✉) Y. Qi · M. Guo
College of Electrical and Information Engineering, Lanzhou University of Technology, Lanzhou, China
e-mail: twqzjh@163.com

H. Gao
High-Voltage Key Laboratory of Fujian Province, Xiamen University of Technology, Xiamen, China

applications. A simplified MPC method, named predictive functional control (PFC), is an effective alternative for the conventional MPC [2]. While retaining the merits of MPC, PFC can greatly reduce online computational burden.

In practice, the robustness of the closed-loop system is very important to ensure the normal operation of the system due to the uncertainties. However, some approaches, for example, robust control [3], remove the effects caused by the uncertainties on the systems in a negative way, i.e., the controller design based on boundaries of the uncertainties. As a result, the performances of the closed-loop systems may greatly fluctuate facing heavy uncertainties due to the limited regulatory capacity of these controllers.

In order to enhance the robustness of the closed-loop systems, the uncertainties should be considered in the controller design, i.e., an active way. It is well known that the disturbance observer-based control strategy provides a feasible way to treat the heavy uncertainties. In Ref. [4], the unmeasured disturbances were identified by disturbance observers (DOs), and then they were incorporated into the prediction model in the control of a missile. The same idea is applied to dry clutch control [5] and permanent magnet synchronous motor system control [6]. In essence, this scheme aims to improve the accuracy of the prediction model accommodating the effects of uncertainty on the system. Although the above-mentioned PFC schemes achieve satisfactory uncertainty rejection for single-input single-output (SISO) systems, multi-input multi-output (MIMO) systems have been not involved yet. As we know that most industrial plants exhibit multivariable characteristics. Therefore, it is very necessary to investigate multivariable predictive function control based on the idea of model correction.

In fact, most plants are not only multivariable but nonlinear. In order to facilitate the application of linear system theory for the controller design, the nonlinear dynamics generally are linearized in advance. In the state-dependent Riccati control theory, a nonlinear system should be expressed as a linear-like structure through state-dependent coefficient technique, i.e., extended linearization [7]. The extended linearization parameterizes nonlinear dynamics into the state vector and the product of a matrix-valued function, which can fully capture the nonlinearity of a system in a more intuitive way.

Motivated by the merits of the DO and the extended linearization, an improved multivariable predictive functional control (IMPFC) algorithm is proposed for a class of uncertain nonlinear MIMO systems.

2 Improved Multivariable Predictive Functional Control

Consider the following uncertain nonlinear affine system:

$$\dot{x} = f_1(x) + g_1(x)u + g_2(x)d \tag{1}$$

where x in R^n is the state, u in R^m is the input, y in R^q is the output, and d in R^n is the uncertainty.

A nonlinear DO for identifying d is given for the system (1) [8], as

$$
\hat{d} = z + p(x)
$$
$$
\dot{z} = -l(x)g_2(x)z - l(x)[g_2(x)p(x) + f_1(x) + g_1(x)u]
$$

(2)

where $\hat{d}$, z, $p(x)$, and $l(x)$ are the estimate of the uncertainty, the internal state of the nonlinear observer, the nonlinear function, and the nonlinear observer gain, respectively. As stated in Ref. [8], $\hat{d}$ can approach d exponentially as long as $p(x)$ is chosen appropriately.

According to the principle of extended linearization, the system (1) can be linearized as

$$
\dot{x} = f(x)x + g_1(x)u + g_2(x)d
$$

(3)

with $f(x)x = f_1(x)$. This is a linear-like structure widely used in the state-dependent Riccati equation control approach. The design of predictive controller usually involves output prediction, reference trajectory, optimization, and so on.

By discretizing the system (3) at each sampling instant, the prediction model can be acquired as

$$
x(k+1) = Ax(k) + Bu(k) + Nd(k),
$$
$$
y(k) = Cx(k)
$$

(4)

where $A = e^{f(x)T_s}$, $B = \int_0^{T_s} e^{f(x)T_s} g_1(x)dt$, and $N = \int_0^{T_s} e^{f(x)T_s} g_2(x)dt$. C and T_s are the output matrix and discrete sample period, respectively. It is assumed that $f(x)$, $g_1(x)$, and $g_2(x)$ keep unchanged in the prediction horizon. This assumption is reasonable because model (4) is only used to find the control input at time k. In PFC, the control input is supposed to be a linear combination of several simple base functions. Therefore, in case of multi-input situation, a component of the control input at time $k + i$ can be described as

$$
u_j(k+i) = \begin{bmatrix} b_{j1}(i) & \cdots & b_{jn_b}(i) \end{bmatrix} \begin{bmatrix} \mu_{j1} \\ \vdots \\ \mu_{jn_b} \end{bmatrix} = b_j(i)\mu_j
$$

(5)

where n_b is the number of base functions, μ_{jl} is the weighting coefficient corresponding to the base function $b_{jl}(\cdot)(j = 1, \ldots, m, l = 1, \ldots, n_b)$. Based on this description, the control input can be expressed as

$$u(k+i) = \begin{bmatrix} u_1(k+i|k) \\ \vdots \\ u_m(k+i|k) \end{bmatrix} = \begin{bmatrix} b_1(i)\mu_1 \\ \vdots \\ b_m(i)\mu_m \end{bmatrix} = b(i)\mu \qquad (6)$$

with $b(i) = \begin{bmatrix} b_1(i) & \cdots & o \\ \vdots & \cdots & \vdots \\ o & \cdots & b_m(i) \end{bmatrix}, \mu = \begin{bmatrix} \mu_1 \\ \vdots \\ \mu_m \end{bmatrix}$.

By iterating system (4), the state at time $k+i$ can be written as

$$x(k+i) = A^i x(k) + \sum_{l=0}^{i-1} A^l Bu(k+i-1-l) + \sum_{l=0}^{i-1} A^l Nd(k+i-1-l) \quad (7)$$

Usually, the future $d(k+i-1-l)(k+i-1-l>1)$ cannot be available. For ease of calculation, it is assumed that the future $d(k+i-1-l)$ equals the present $d(k)$, i.e., $d(k+i-1-l) = d(k)(k+i-1-l>1)$. As a result, the state prediction (7) can be given by

$$x(k+i) = A^i x(k) + \sum_{l=0}^{i-1} A^l Bu(k+i-1-l) + \sum_{l=0}^{i-1} A^l Nd(k) \qquad (8)$$

Thus, the output prediction at time $k+i$ can be expressed as

$$y(k+i) = CA^i x(k) + \sum_{l=0}^{i-1} CA^l Bu(k+i-1-l) + \sum_{l=0}^{i-1} CA^l Nd(k) \qquad (9)$$

As shown in Eq. (9), the future output $y(k+i)$ consists of three parts, namely the free output $CA^i x(k)$ caused by the present state, the forced output $\sum_{l=0}^{i-1} CA^l Bu(k+i-1-l)$ caused by the control input, and the additional output $\sum_{l=0}^{i-1} CA^l Nd(k)$ caused by the uncertainty. Obviously, the additional output term will have a noticeable effect on the output prediction under the serious uncertainty.

Substituting Eq. (6) into Eq. (9) gives

$$y(k+i) = v(i)x(k) + w(i)\mu + s(i) \qquad (10)$$

where $v(i) = CA^i$, $w(i) = \sum_{l=0}^{i-1} CA^l Bb(k+i-1-l)$, and $s(i) = \sum_{l=0}^{i-1} CA^l Nd(k)$.

Besides, a first-order exponential reference trajectory model is used, i.e.,

$$y_r\,(k+i) = y_c\,(k+i) - \begin{bmatrix} \beta_1^i & \cdots & 0 \\ \vdots & \ddots & \vdots \\ 0 & \cdots & \beta_q^i \end{bmatrix} \left[y_c(k) - y_p(k) \right] \qquad (11)$$

where β_l^i, $y_c(\cdot)$, and $y_p(\cdot)$ denote the softness factor, the set point, and the process output, respectively.

Minimizing the following performance index finds the coefficient vector μ.

$$J = \sum_{a_i \in A_c} q\,(a_i)\,[y\,(k+a_i) - y_r\,(k+a_i)]^2 \qquad (12)$$

where $A_c = \{a_1, a_2, \ldots, a_c\}$ is a coincidence set, and its elements selected from the prediction horizon $q(\cdot)$ is the weighting coefficient. By introducing several symbolic variables, the performance index can be written in vector-matrix form:

$$J = \|Vx(k) + W\mu + S - Y_r\|_Q^2 \qquad (13)$$

where $V = \begin{bmatrix} v\,(a_1) \\ \vdots \\ v\,(a_c) \end{bmatrix}$, $W = \begin{bmatrix} w\,(a_1) \\ \vdots \\ w\,(a_c) \end{bmatrix}$, $S = \begin{bmatrix} s\,(a_1) \\ \vdots \\ s\,(a_c) \end{bmatrix}$, $Q = \begin{bmatrix} q\,(a_1) & & \\ & \ddots & \\ & & q\,(a_c) \end{bmatrix}$,

$Y_r = \begin{bmatrix} y_r\,(k+a_1) \\ \vdots \\ y_r\,(k+a_c) \end{bmatrix}$. Furthermore, define $\xi = Y_r - Vx(k) - S$, then Eq. (13) can be

rewritten as

$$J = \|W\mu - \xi\|_Q^2 = \mu^\mathrm{T} L \mu - 2\mu^\mathrm{T} M + \xi^\mathrm{T} Q \xi \qquad (14)$$

with $L = W^\mathrm{T} Q W$, $M = W^\mathrm{T} Q \xi$. By finding the gradient of J with respect to μ and setting it to zero, one can obtain the weighting vector $\mu = (L)^{-1} M$. Finally, the control input can be represented as

$$u(k) = f(0)\mu = f(0)(L)^{-1} M \qquad (15)$$

In implementation, $d(k)$ should be replaced by $\hat{d}(k)$ shown in Eq. (2).

3   Mathematical Model of a Hypersonic Vehicle

Consider the longitudinal dynamics of a typical hypersonic vehicle developed by the NASA Langley Research Center [9]. The mathematical model of the vehicle can be described by a set of five first-order differential equations as follows:

$$\dot{V} = \frac{T \cos \alpha - D}{m} - \frac{\mu \sin \gamma}{r^2} \tag{16}$$

$$\dot{\gamma} = \frac{L + T \sin \alpha}{mV} - \frac{(\mu - V^2 r) \cos \gamma}{V r^2} \tag{17}$$

$$\dot{h} = V \sin \gamma \tag{18}$$

$$\dot{\alpha} = q - \dot{\gamma} \tag{19}$$

$$\dot{q} = \frac{M_{yy}}{I_{yy}} \tag{20}$$

where V, γ, h, α, and q are the velocity, the flight-path angle, the altitude, the angle of attack, and the pitch rate, respectively. More information about this model can be found in [9].

Consider the parameter variations, the dynamics of the hypersonic vehicle Eqs. (16)–(20) can be rewritten as

$$\dot{x} = [f_1(x) + \Delta f] + [g_1(x) + \Delta g] u \tag{21}$$

where $u = [\beta, \delta_e]^{\mathrm{T}}$ and Δf and Δg are the parameter variations. Further operation on Eq. (21), it can be expressed as

$$\dot{x} = f_1(x) + g_1(x)u + d \tag{22}$$

where $d = \Delta f + \Delta g \cdot u$ is the lumped uncertainty.

The control objective for the vehicle is that the velocity and altitude can quickly track the desired commands around the trimmed cruise flight.

4 Simulation Results

The control parameters were chosen as $A_c = \begin{bmatrix} 50 & 100 & 150 & 200 \end{bmatrix}$, $T_s = 0.01\,\mathrm{s}$, and $f_{11}(\cdot) = 1$, $f_{21}(\cdot) = 1$. In order to highlight the advantage of the proposed IMPFC, a comparative study was carried out against the conventional multivariable PFC (CMPFC) in the presence of parameter variations. The additive variations were set to be -10% for parameters of $(m, \bar{c}, I_{yy}, S, \rho, c_e, C_{M\alpha})$, i.e. $\Delta = -10\%$. The simulation results were described in Fig. 1, where the velocity stepped from 15,060

Fig. 1 Response curves of system outputs and inputs in the presence of parameter variations under IMPFC and CMPFC, $\Delta = -10\%$
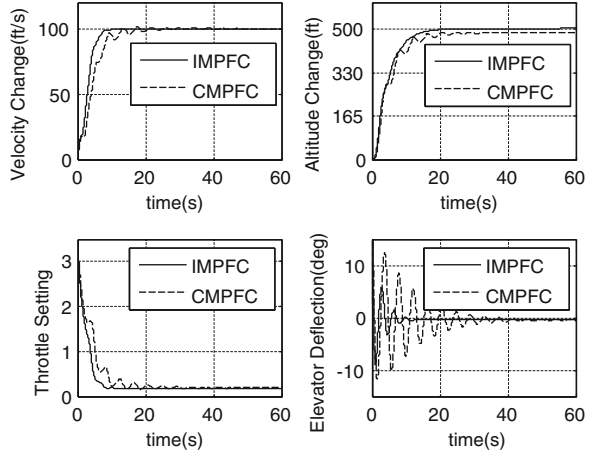
Fig. 2 Response curves of system outputs and inputs in the presence of output uniform noises under IMPFC
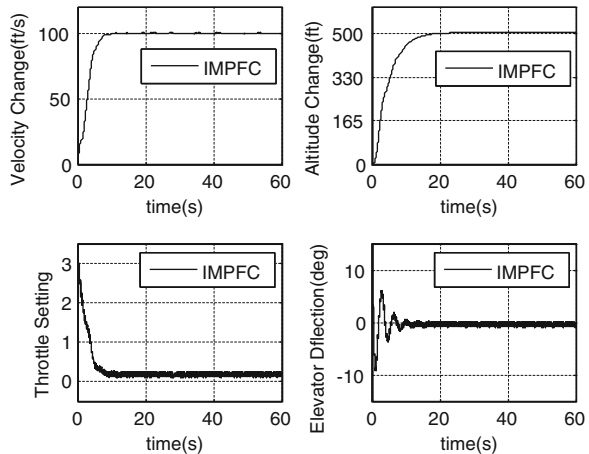
to 15,160 ft/s and the altitude tracked the step change with magnitude 500 ft. It can be seen that IMPFC achieves better tracking performance in settling time and steady-state error. To be specific, the altitude tracking has a steady error under the CMPFC. In addition, there need less efforts for the elevator deflection under the IMPFC.

Furthermore, in order to test the robustness of the system to parameter variations more comprehensively, assume that the output is subjected to uniform noise, specifically the interval $\begin{bmatrix} -2.5 & 2.5 \end{bmatrix}$ ft/s for the velocity and the interval $\begin{bmatrix} -4 & 4 \end{bmatrix}$ ft for the altitude. The simulation results were described in Fig. 2 where it can be observed that the system outputs can well track the reference commands. However, there are slight high-frequency oscillations in the throttle setting and elevation deflection. It is because the control inputs have to adapt to changes in noises.

According to the simulation results, it can be inferred that the closed-loop system under the IMPFC has strong robustness to parameter variations and measurement

noises. It is due to the fact that the improved prediction model takes account of the uncertainty, which can greatly reduce the effects of the uncertainty on the system.

5 Conclusions

In combination with the disturbance observer and extended linearization approach, an improved multivariable predictive functional control algorithm is presented for uncertain nonlinear systems. The accuracy of the prediction model is effectively improved by taking the estimated uncertainty into account, which can greatly enhance the disturbance rejection ability of the closed-loop system. Additionally, the design process can be shortened by using the extended linearization method. Therefore, the proposed predictive functional control scheme is promising for nonlinear uncertain systems. The simulation results of a hypersonic vehicle show that the closed-loop system under the presented controller has some robustness at the presence of parameter variations.

References

1. Mayne, D.Q., Rawlings, J.B., Rao, C.V., et al.: Constrained model predictive control: stability and optimality. Automatica. **36**(6), 789–814 (2000)
2. Tang, W., Long, W., Gao, H.: Model predictive control of hypersonic vehicles accommodating constraints. IET Control Theory Appl. **11**(15), 2599–2606 (2017)
3. Sun, H., Yang, Z., Zeng, J.: New tracking-control strategy for airbreathing hypersonic vehicles. J. Guidance Control Dyn. **36**(3), 846–859 (2013)
4. Zhang, Y., Yang, H., Jiang, Z., et al.: Robust predictive functional control for flight vehicles based on nonlinear disturbance observer. Int. J. Aerosp. Eng. **2015**, 1–16 (2015)
5. Li, L., Wang, X., Hu, X., et al.: A modified predictive functional control with sliding mode observer for automated dry clutch control of vehicle. J. Dyn. Syst. Meas. Control. **138**(6), 16–25 (2016)
6. Wang, S., Fu, J., Yang, Y., et al.: An improved predictive functional control with minimum-order observer for speed control of permanent magnet synchronous motor. J. Electr. Eng. Technol. **12**(1), 272–283 (2017)
7. Cimen, T.: Systematic and effective design of nonlinear feedback controllers via the state-dependent Riccati equation (SDRE) method. Annu. Rev. Control. **34**(1), 32–51 (2010)
8. Chen, W.H.: Nonlinear disturbance observer-enhanced dynamic inversion control of missiles. J. Guidance Control Dyn. **26**(1), 161–166 (2003)
9. Yang, J., Zhao, Z., Li, S., et al.: Composite predictive flight control for airbreathing hypersonic vehicles. Int. J. Control. **87**(9), 1970–1984 (2014)

Part III
Sensors and Actuators

Compensation Strategies for Actuator Rate Limit Effect on First-Order Plus Time-Delay Systems

Jie Yuan, Shumin Fei, and YangQuan Chen

Abstract Rate limit of system actuators is one of the major restrictions in the physical world. However, the actuator rate limit has always been neglected in classical and modern control design. The rate limiter generates amplitude attenuation and phase delay, which will deteriorate control performance and may even lead to system instability. In this study, the Bode step control method was applied to first-order plus time-delay (FOPTD) systems to mitigate the magnitude reduction and phase caused by the rate limiter. An illustrative example was given to show the effectiveness of the Bode step compensation method.

J. Yuan
School of Automation, Southeast University, Nanjing, China

Key Laboratory of Measurement and Control of CSE, Ministry of Education, School of Automation, Southeast University, Nanjing, China

Mechatronics, Embedded Systems and Automation Lab, University of California, Merced, CA, USA
e-mail: jieyuan@seu.edu.cn

S. Fei
Key Laboratory of Measurement and Control of CSE, Ministry of Education, School of Automation, Southeast University, Nanjing, China
e-mail: smfei@seu.edu.cn

Y. Chen (✉)
Department of Mechanical Engineering (MESA-Lab), University of California, Merced, CA, USA
e-mail: ychen53@ucmerced.edu; yqchen@ieee.org

1 Introduction

Restrictions are ubiquitous in most of the control systems; for instance, the plant has no capacity to act aggressively due to mechanical limitations, and the control signal cannot exceed to a specific value to guarantee system safety. Actuator saturation is one of the most concerned issues by engineers and it includes amplitude saturation and rate limit. Amplitude saturation has drawn various researchers' attention, and many control strategies have been developed to compensate the amplitude saturation [1]. However, the controller design methods which consider the actuator rate limit effect have not been extensively developed. Li et al. reshaped the control signal according to rate saturation in time domain [2]. Hanke developed the describing function of the rate limiter as a theoretical basis to analyze the handling qualities of the open-loop and closed-loop systems in frequency domain [3]. It has been found that the fully saturated rate limiter may lead to system instability, and one of the evidence is the Pilot-in-the-Loop Oscillation (PIO) in aircrafts and unmanned vehicle systems. Thus, it is essential to compensate the rate limit effect in aggressive systems or precision control systems. In [4], a nonlinear filter was proposed to compensate the phase delay of the control signal after a rate limiter to prevent the PIO. In [5], the fractional-order proportional–integral (PI) controller was applied to FOPTD process and was found to have benefit to the rate limit effect compared with traditional proportional–integral–derivative (PID) controller.

The Bode step method is a robust feedback controller design approach which was first produced by Bode in [6]. It is developed to maximize the feedback area with the highest possible gain in low frequency. The gain curve of the ideal loop transfer function has a constant magnitude at a certain frequency range which provides a better system robustness. The steep roll-off in high frequency improves the noise rejection capacity.

Motivated by the benefits of the aforementioned Bode step feedback controller design method, this strategy will be applied to FOPTD systems to mitigate the actuator rate limit effect. The flat gain curve in the middle frequency range is able to mitigate the magnitude reduction and phase delay resulting from actuator rate limit.

The main contributions of the paper are to (1) introduce the concept of the Bode step method, which is one of the effective loop shaping methods; (2) utilize the advantages of the Bode step to mitigate the rate limit effect. The remainder of the paper is organized as follows: The nature of the rate limiter and the concept of Bode step method are given in Sects. 2 and 3, respectively. An illustrative example is given in Sect. 4, where the Bode step controller is first designed based on the specifications of gain margin, phase margin, and gain crossover frequency. A classical PI controller is also designed for a fair comparison. The results have shown that Bode step controller generates more robust performance under different actuator rate limit values and is able to mitigate the rate limit effects. Conclusions are drawn in the last section.

2 The Nature of the Rate Limiter

The rate limiter saturates the rate of the output signal within a specific value. For the sinusoidal input

$$x(t) = A \sin(\omega t),$$

the rate of the input is

$$\dot{x}(t) = \omega A \cos(\omega t).$$

The rate of output signal $f(t)$ cannot exceed a specific value R, which satisfies

$$\left| \dot{f}(t) \right| \leq R,$$

where R is called the rate limit value. When the actuator is fully saturated, the output signal becomes a pure triangular wave and contains magnitude reduction and phase delay compared with the input signal.

3 Asymptotic Bode Step Method

Bode proposed a desired asymptotic gain plot of the open-loop system which is shown in Fig. 1. The Bode step response achieves the highest possible gain in the low frequency range over a given bandwidth ω_b. The high gain in low frequency is beneficial for disturbance rejection. The constant gain at a certain frequency range from ω_d to ω_c contributes to the strong robustness to the parameter perturbation and noise interference, and this flat gain curve is called "Bode step." The Bode gain plot also has a steep roll-off with $-20n$ dB/dec in high frequency range which improves the system noise rejection capacity. n is the relative order of the ideal loop transfer function.

Fig. 1 The Bode gain plot of the ideal Bode step open-loop system
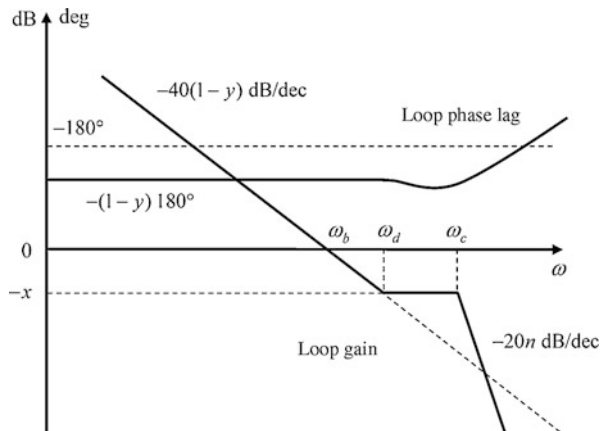
In order to make the system robust to the plant parameter perturbation and disturbance effect, two frequency performance indices are specified in the Bode step method, which are gain margin x dB and relative phase margin y ($y = \varphi_m/180°$, φ_m isthephasemargindegree). To guarantee the system response speed, the gain crossover frequency ω_b rad/sec is set to be the third design specification in this method. Based on these design specifications, the corner frequencies of the Bode step open-loop gain curve can be calculated by the following equations:

$$\frac{\omega_c}{\omega_d} = \frac{n + \frac{\pi}{2}|B_n(\omega_c)|}{2(1-y)}, \tag{1}$$

$$\omega_d = 10^{\frac{x}{40(1-y)}}\omega_b, \tag{2}$$

where $B_n(\omega_c)$ is the nonminimum phase lag at ω_c.

In the frequency range below ω_d, the slope of the gain curve is $-40(1-y)$ dB/dec, which means the order of the operator s is a fraction rather than an integer. The desired constant slope can be decomposed into a rational part and an irrational part: $s^{-2(1-y)} = s^{-1}s^{-1+2y}$. This irrational slope can be implemented by a rational function which contains several pairs of real poles and zeros. The average slope of the approximated rational function should equal $20(-1+2y)$ dB/dec.

The rational approximation of the Bode step and steep roll-off in high frequency can be implemented by cascading a second order function

$$G_b(s) = \frac{s^2 + 2\xi_1\omega_d s + \omega_d^2}{s^2 + 2\xi_2\omega_c s + \omega_c^2},$$

where, ξ_1 ad ξ_2 are damping coefficients.

For an FOPTD process in the form of

$$G(s) = G_0(s)e^{-Ls} = \frac{K}{Ts+1}e^{-Ls},$$

where K, T, L are the steady-state gain, time constant, and delay, respectively. Once the ideal loop transfer function $H(s)$ is obtained, the compensator can be easily calculated as

$$C(s) = \frac{H(s)}{G_0(s)} = \frac{H(s)(Ts+1)}{K},$$

where the delay part cannot be reversed due to physical feasibility. The closed-loop system response based on the Bode step method is expected to have a large overshoot. An additional notch prefilter is cascaded to the closed-loop system to reduce the response overshoot:

$$Q(s) = \frac{s^2 + \omega_b s + \xi_3^2\omega_b^2}{s^2 + a\omega_b s + \xi_3^2\omega_b^2},$$

where a and ξ_3 are tuning parameters to determine the notch position and notch depth.

In this study, the objective is to design a controller to mitigate the actuator rate limit effect. Motivated by the benefits of the Bode step concept, the Bode step controller is applied to the FOPTD process. Four specifications are required: gain margin x^* dB, relative phase margin y^*, gain crossover frequency ω_b^* rad/sec, and relative order of the ideal loop transfer function n. An asymptotic Bode magnitude plot of the ideal loop transfer function is firstly obtained and implemented by using the above method, as shown in Fig. 1.

The detailed design procedures of the Bode step controller are:

1. Specify the design performance: gain margin x^* dB, relative phase margin y^*, gain crossover frequency ω_b^* rad/sec, and the relative order of the ideal loop transfer function n.
2. Calculate corner frequencies based on Eqs. (1)–(2) and draw asymptotic Bode magnitude plot of the ideal loop transfer function.
3. Implement the asymptotic Bode plot with $H(s)$, which is composed of several cascaded rational loop transfer functions.
4. Cascade the $H(s)$ with the inverse of minimum part of the plant $G_0(s)$, then the controller is obtained as $\frac{H(s)}{G_0(s)}$.
5. Choose parameters of the prefilter $Q(s)$ by trial and error to reduce the overshoot of the closed-loop response.

4 An Illustrative Example

In this section, an illustrative example will be given to show the effectiveness of Bode step method in control systems which is affected by the rate limit. The FOPTD system is considered as

$$G(s) = \frac{1}{2s+1} e^{-0.1s}.$$

The controller design specifications are chosen as: gain margin $x^* = 10$ dB, phase margin $\varphi^* = 30°$ ($y^* = \frac{1}{6}$), and the crossover frequency $\omega_b^* = 1$ rad/sec. The relative order of the desired open-loop system is chosen as $n = 3$. According to Eqs. (1) and (2), the corner frequencies are obtained: $\omega_d = 2$ rad/sec and $\omega_c = 4.28$ rad/sec. Approximated with several rational links, the ideal open-loop transfer function based on the Bode step method is obtained as

$$H(s) = \frac{6.47}{s+0.058} \frac{s+0.042}{s+1.4} \frac{2.33}{s+2.33} \frac{s^2+2.4s+4}{s^2+3.42s+14.83} \frac{1}{s}. \tag{3}$$

The controller is

$$C(s) = \frac{6.47}{s + 0.058} \frac{s + 0.042}{s + 1.4} \frac{2.33}{s + 2.33} \frac{s^2 + 2.4s + 4}{s^2 + 3.42s + 14.83} \frac{2s + 1}{s}.$$

The achieved frequency characteristics of the open-loop system (3) are: gain crossover frequency $\omega_b = 1.00$ rad/sec, gain margin $x = 11.33$ dB, phase margin $\varphi_m = 30.91°$, which satisfied the design requirements. An additional prefilter is cascaded to the closed-loop system to reduce the response overshoot:

$$Q(s) = \frac{s^2 + s + 0.81}{s^2 + 2s + 0.81}.$$

In order to fairly illustrate the effectiveness of the Bode step method, a PI controller is designed based on two specifications: $\omega_b^* = 1$ rad/sec and $\varphi_m^* = 30°$. The corresponding PI controller is

$$C_{PI}(s) = 0.356 + \frac{2.21}{s}.$$

The Bode plots of the open-loop system containing the Bode step controller or the PI controller are shown in Fig. 2. The closed-loop step response without the rate limit of these two systems is shown in Fig. 3. From Fig. 2, the gain curve of the Bode step controlled system in low frequency is much higher than the one employs PI controller, which means the Bode step controller has better disturbance rejection ability. The lower gain plot for the Bode step method in high frequency increases the capacity of noise reduction. In the middle frequency range, the Bode step method generates a flat gain curve, thus the system has better performance robustness to the parameter perturbations and noise contamination. As shown in Fig. 3, the Bode step

Fig. 2 The Bode plot of the open-loop system
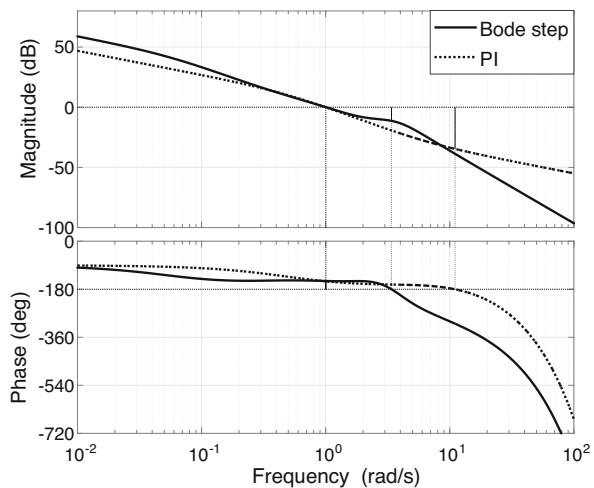
Fig. 3 The closed-loop step
response without considering
the rate limit
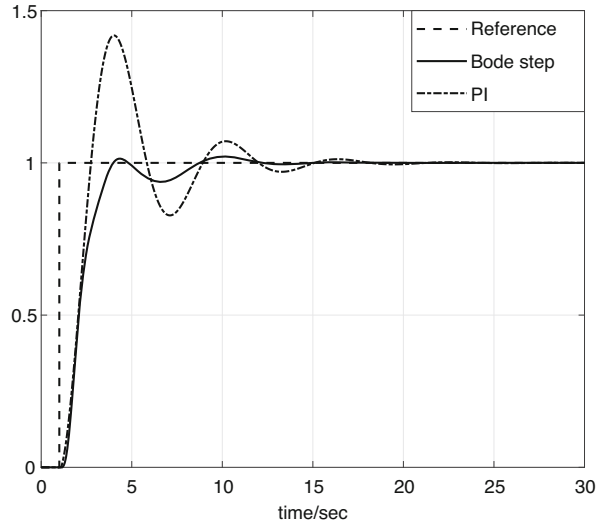
method generates stable output with slight oscillations while PI controller results in a more aggressive response.

When taking actuator rate limit into consideration, the step responses based on the Bode step method and the corresponding control signals with respect to different rate limit values are shown in Fig. 4a, b. The step responses with the PI controller and corresponding control signals under different rate limit values are given in Fig. 4c, d. It can be observed that the Bode step controller generates more robust system performance than the PI controller under different rate limit values. For $R \geq 1$, the system response based on PI controller is unstable, and the control signal is fully saturated. While based on the Bode step method, the system is still stable when $R = 0.8$. As an observation, the Bode step controller can stand lower rate limit value which results from the better performance robustness.

5   Conclusions

This paper employs the Bode step controller design method to the FOPTD process containing the rate limit and has found that the Bode step controller enables to mitigate the rate limit effect. The flat Bode step gain curve of ideal open-loop transfer function contributes to the performance robustness. The illustrative example has demonstrated that the Bode step controller allows for lower rate limit value and improves performance robustness compared with traditional PI controller. In our future research, we will focus on compensating magnitude reduction and phase delay of the rate limiter directly in ideal Bode step gain plot. More flat gain curves can be alternatively added to achieve for different robustness requirements.
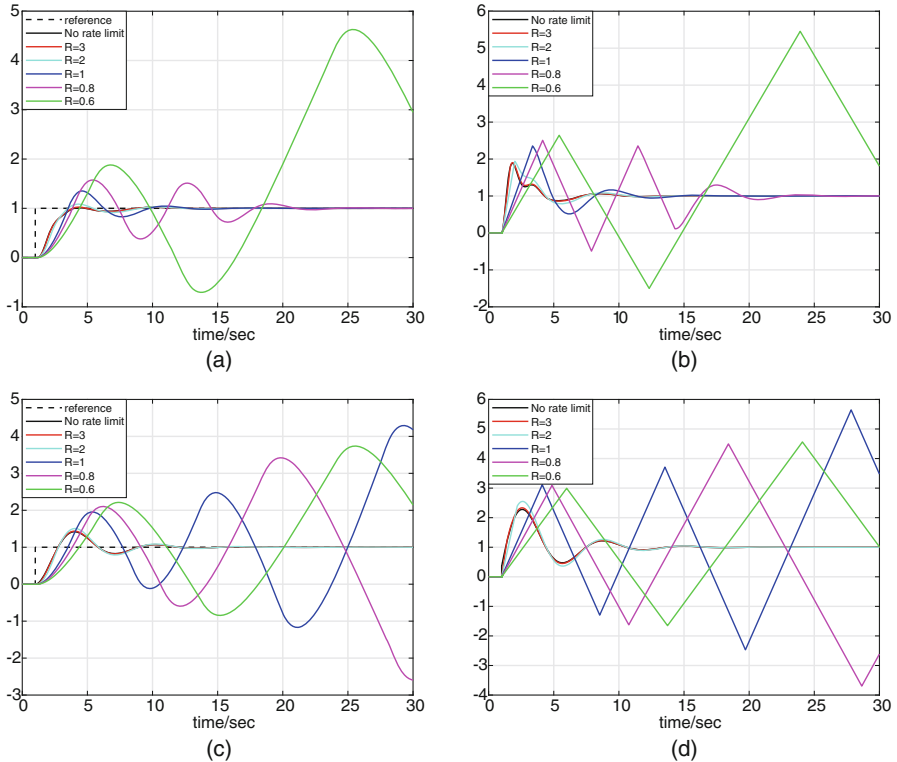
Fig. 4 Simulation results under different rate limit values with the Bode step controller: step responses (**a**), control signals (**b**); with the PI controller: step responses (**c**), control signals (**d**)

References

1. Sun, W., Gao, H., Kaynak, O.: Vibration isolation for active suspensions with performance constraints and actuator saturation. IEEE/ASME Trans. Mechatron. **20**(2), 675–683 (2015)
2. Li, Y., Sun, M., Wang, Z., Chen, Z.: Proportional–integral–derivative attitude control subject to dynamic rate saturation of elevator through explicit command reshaping: an engineering approach. Proc. Inst. Mech. Eng. I J. Syst. Control Eng. **230**(6), 562–577 (2016)
3. Hanke, D.: Handling qualities analysis on rate limiting elements in flight control systems. In: Flight Vehicle Integration Panel Workshop on Pilot Induced Oscillations, AGARD-AR-335 (1994)
4. Alcala, I., Gordillo, F., Aracil, J.: Phase compensation design for prevention of PIO due to actuator rate saturation. In: Proceedings of American Control Conference, pp. 4686–4691 (2004)
5. Yuan, J., Chen, Y.Q., Fei, S.: Analysis of actuator rate limit effects on first-order plus time-delay systems under fractional order proportional integral control. In: Proceedings of the 3rd IFAC Conference on Advances in Proportional-Integral-Derivative Control, pp. 9–11 (2018)
6. Bode, W.H.: Network analysis and feedback amplifier design, vol. 52. D. vanNostrand, New York (1945)

Reliable Output-Feedback Control for Markovian Jump Descriptor Systems with Sensor Failure and Actuator Saturation

Check for updates

Chan-eun Park, Nam Kyu Kwon, and PooGyeon Park

Abstract This paper proposes dynamic output-feedback networked control with actuator saturation and sensor failure for Markovian jump descriptor systems (MJDS). First, the mode-dependent dynamic output-feedback controller is described as a quasi-linear parameter varying system. Then, the stochastic admissibility criterion for the closed-loop system with sensor failure and actuator saturation is obtained as matrix inequalities. To obtain the feasible solution of the non-convex condition, this paper successfully obtains the equivalent condition in terms of strict linear matrix inequalities (LMIs) and the controller gains. A numerical example shows the validity of the proposed result.

Keywords Singular system · Markovian jump system · Input saturation · Sensor failure

1 Introduction

Descriptor systems, which are also called singular systems or generalized state-space systems, are models that express both dynamic behavior and non-dynamic properties of the system state. Therefore, descriptor system has received considerable attention because it can be a useful tool to express many real plants. Otherwise, Markovian jump systems (MJSs), which are a type of stochastic jump system, have been studied extensively for over few decades and widely used in practical applications due to its ability to represent the unexpected changes or sudden changes in the plant. Therefore, there has been an increasing interest in the issue of both

C.-e. Park · P. Park (✉)
Division of Electrical Engineering, Pohang University of Science and Technology, Pohang, Korea
e-mail: chane2727@postech.ac.kr; ppg@postech.ac.kr

N. K. Kwon
Division of Electrical Engineering, Yeungnam Unicersity, Gyeongsan, Korea
e-mail: namkyu@yu.ac.kr

descriptor system and MJS, which are known as Markov jump descriptor systems (MJDSs).

On the other hand, networked control systems (NCSs), which is a control scheme that sensor-controller and controller-actuator share a common communication signal, has been one of the hot topic in not only academia but also industry for many decades [1]. This is evidenced by *Google Scholar* searches of the term "Networked control systems," which returns over 45,000 items until May 2019. However, there are some critical issues in NCS such as sensor failure and actuator saturation. These factors generate the system non-linearity which degrades the performance of system or even causes the instability of system. To consider this phenomena, [2] dealt with dissipative control for MJDS with sensor failure, and [3] solved filtering problem for MJSs with sensor failure. The research on control problem with time-varying delay and actuator saturation was also published [4]. Recently, the authors of [5] considered $\mathcal{H}_\infty$ filtering for MJDS with time-varying delays and sensor failures. However, to the best of the authors' knowledge, there is no study that considers reliable control problem for MJDS with sensor failure and actuator saturation. This is the motivation behind this paper. Further, since output-feedback control can handle the system with immeasurable states, this paper designs a dynamic output-feedback control for MJDS.

This paper suggests the dynamic output-feedback control for continuous-time MJDS. To consider the actuator saturation, the proposed control is designed in the form of quasi-linear parameter varying (QLPV) system. First, the stochastic admissibility criterion for the closed-loop system is obtained as matrix inequalities with time-varying components which come from sensor failure. Next, with the help of sensor failure model, the upper bound of the matrix inequalities are taken. Then, by applying congruence transformation to the matrix inequalities, the equivalent condition is derived in terms of strict linear matrix inequalities (LMIs). A numerical example verifies the validity of the result. The notation in this paper is fairly standard. For a matrix X, X^T means the transpose matrix of X. If X is square, the notation $sym(X) = X + X^T$ is defined. For a vector x, $[x]_k$ denotes $k-$th element of x. The set $\mathbb{N}_k^+ = \{1, 2, \cdots, k\}$. In symmetric matrix, $(*)$ is used as an ellipsis for terms that are induced by symmetry.

2 Problem Statement

Consider the following continuous-time singular Markovian jump systems with input saturation:

$$
\begin{aligned}
E\dot{x}(t) &= A(q_t)x(t) + B(q_t)\sigma(u(t)), \\
y(t) &= C(q_t)x(t),
\end{aligned}
\tag{1}
$$

where the notations $x(t) \in \mathbb{R}^n$, $u(t) \in \mathbb{R}^m$, $y(t) \in \mathbb{R}^p$ denotes the state, control input, and the measurement output, respectively. The saturation operator $\sigma(\cdot)$ is defined as follows:

$$[\sigma(u)]_k \triangleq \begin{cases} sgn([u]_k)\mu & |[u]_k| \geq \mu, \\ [u]_k & |[u]_k| < \mu, \end{cases} \qquad (2)$$

where $sgn(\cdot)$ is signum function and $\mu > 0$ is a saturation level. The operation mode $\{q_t\}$ is a continuous-time Markov process which takes values in a finite set $\mathbb{N}_N^+$ with transition rates π_{ij} given by

$$\Pr(\eta_{t+\delta t} = j | \eta_t = i) = \begin{cases} \pi_{ij}\delta t + o(\delta t), & \text{if } j \neq i, \\ 1 + \pi_{ii}\delta t + o(\delta t), & \text{otherwise,} \end{cases}$$

where $\delta t > 0$, $\lim_{\delta t \to 0} (o(\delta t)/\delta t) = 0$, π_{ij} is the transition rate from mode i at time t to mode j at time $t + \delta t$, and $\pi_{ij} \geq 0$ if $i \neq j$, $\sum_{j \in \mathcal{N}} \pi_{ij} = 0$. To simplify the notation, the mode-dependent matrix can be rewritten with the subscription i when the Markov process q_t stays at mode i, i.e., $A(q_t = i) \triangleq A_i$. Also, to describe the singular system, the matrix $E \in \mathcal{R}^{n \times n}$ is supposed to have rank $r < n$. Without loss of generality, the matrix $E = diag\{I_r, 0\} \in \mathcal{R}^{n \times n}$ will be used. To treat the singular matrix E, we define the matrices: the full-rank matrices R, S and matrices E_L, E_R such that $RE = 0$, $ES = 0$, and $E_L^T E_R = E$. The goal of this note is to design a dynamic output-feedback control which works normally under the sensor failure and input saturation (see Fig. 1). To deal with this problem, we assume the following conditions:

Assumption 1 *The pairs (A_i, B_i, C_i) are minimal for all $i \in \mathbb{N}_N^+$.*

Assumption 2 *When there exist failures in the sensor which receive the system output $y(t)$, it can be modeled as $y_F(t) = \mathcal{F}y(t)$, where $y_F(t)$ means the adopting signal in control system sent from sensors and $\mathcal{F} = diag(f_1, f_2, \cdots, f_p)$ with $0 \leq f_k \leq 1$ for all $k \in \mathbb{N}_p^+$. Also, the lower and upper bound of f_k is known [6].*

The following lemmas will be used in the next section.

Lemma 1 ([7]) *The input saturation $\sigma(u(t))$ can be expressed as a convex combination of control input $u(t)$ and a virtual input $v(t)$, where all components of the virtual input should be bounded by saturation level, i.e., $|[v(t)]_k| \leq \mu$,*

Fig. 1 System description with sensor failure and input saturation problem
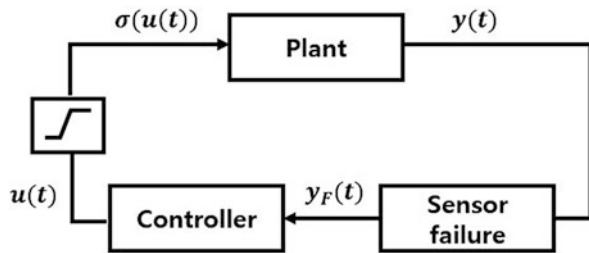
$$\sigma(u(t)) = \sum_{l \in \mathbb{N}_{2m}^+} \zeta_l \{ H_l u(t) + H_l^- v(t) \}, \tag{3}$$

where H_l denotes a diagonal matrix whose diagonal elements are either 0 or 1, $H_l^- = I - H_l$, $\sum_{l \in \mathbb{N}_{2m}^+} \zeta_l = 1$, and $\zeta_l \geq 0$.

Next, due to the Assumption 2, the sensor failure model can be rewritten such that $y_F(t) = (\hat{\mathcal{F}} + \Delta_t \check{\mathcal{F}}) y(t)$, where

$$\hat{\mathcal{F}} = \text{diag}\left(\frac{\bar{f}_1 + \underline{f}_1}{2}, \cdots, \frac{\bar{f}_p + \underline{f}_p}{2} \right), \ \check{\mathcal{F}} = \text{diag}\left(\frac{\bar{f}_1 - \underline{f}_1}{2}, \cdots, \frac{\bar{f}_p - \underline{f}_p}{2} \right), \tag{4}$$

and Δ_t is a diagonal matrix whose all elements are varying in the range between -1 and 1.

Remark 1 As shown in Fig. 1, both the actuator saturation and sensor failure generate the system non-linearity. In the case of actuator saturation problem, Lemma 1 introduces a virtual input to represent the nonlinear input signal to be linear combination of input signals. Otherwise, the time-varying sensor failure model in Assumption 2 can be remodeled as the convex combination of the bounds of sensor failure components.

3 Main Result

We suggest the dynamic output-feedback controller such that

$$E\dot{x}_c(t) = \sum_{l \in \mathbb{N}_{2m}^+} \zeta_l(x_c(t)) A_{ci,l} x_c(t) + B_{ci} y_F(t), \\ u(t) = C_{ci} x_c(t), \tag{5}$$

where $x_c(t)$ is the control state, $A_{ci,k}$, B_{ci} and C_{ci} are mode-dependent controller gain at mode i. When the control input $u(t)$ in (5) is saturated, with the help of Lemma 1,

$$\sigma(C_{ci} x_c(t)) = \sum_{l \in \mathbb{N}_{2m}^+} \zeta_l \{ H_l C_{ci} + H_l^- K_{ci} \} x_c(t), \tag{6}$$

where K_{ci} is the virtual input gain. This expression is valid under the region such that $\mathcal{L}(K x_c(t)) = \{ x_c(t) \mid |[K x_c(t)]_k| \leq \mu, \ \forall k \in \mathbb{N}_m^+ \}$. Here, the convex parameter ζ_l in (5), (6) depends on $x_c(t)$. The way how to determine ζ_l is stipulated in Lemma 2 of [8]. Then the closed-loop system is obtained as follows:

$$\bar{E}\dot{\bar{x}}(t) = \sum_{l \in \mathbb{N}_{2m}^+} \zeta_l \bar{A}_i \bar{x}(t), \tag{7}$$

where $\bar{A}_i = \begin{bmatrix} A_i & B_i(H_l C_{ci} + H_l^- K_{ci}) \\ \mathcal{B}_{ci}\mathcal{F}C_i & A_{ci} \end{bmatrix}$, $\bar{x}(t) = [x^T(t) \ x_c^T(t)]^T$, and $\bar{E} =$ diag(E, E). From [9], the stochastic admissibility of (7) is guaranteed if there exist symmetric matrix P_i, and non-singular matrix Q_i for all $i \in \mathbb{N}_N^+, l \in \mathbb{N}_{2m}^+$ such that

$$0 < \bar{E}_L^T P_i \bar{E}_L, \tag{8}$$

$$0 > \text{sym}(\bar{A}_i^T (P_i E + R^T Q_i S^T)) + \sum_{j \in \mathbb{N}_N^+} \pi_{ij} \bar{E}^T P_j \bar{E}, \tag{9}$$

where $\bar{E}_L = \text{diag}(E_L, E_L)$. Next, we formulate the set invariant condition. Let us define an ellipsoid such as $\mathcal{E}(\bar{E}^T P_i \bar{E}) \triangleq \{\bar{x}(t) \mid \bar{x}^T(t)\bar{E}^T P \bar{E}\bar{x} \leq 1\}$. To hold the region $\mathcal{L}(Kx_c(t))$, the ellipsoid should be in the region of $\mathcal{L}(Kx_c(t))$ which means

$$\bar{x}^T(t)\bar{K}_i^T e_k e_k^T \bar{K}_i \bar{x}(t) \leq \mu^2 \bar{x}^T(t)\bar{E}^T P_i \bar{E}\bar{x}(t), \ \forall i \in \mathbb{N}_N^+, \ k \in \mathbb{N}_m^+, \tag{10}$$

where $e_k \in \mathcal{R}^n$ is column vector whose $k-$th element is 1 and others are 0, and $\bar{K}_i = [0 \ K_i]$. Also, we can use the upper bound of (8).

$$0 > \text{sym}(\bar{A}_{ci}^T \Sigma_i) + \sum_{j \in \mathbb{N}_N^+} \pi_{ij} \bar{E}^T P_j \bar{E} + \Sigma_i^T \bar{B}_{ci} \bar{B}_{ci}^T \Sigma_i + \bar{C}_i^T \bar{C}_i, \tag{11}$$

where $\Sigma_i = P_i \bar{E} + \bar{R}^T Q_i \bar{S}^T$, $\bar{A}_{ci} = \begin{bmatrix} A_i & B_i(H_l C_{ci} + H_l^- K_{ci}) \\ \mathcal{B}_{ci}\hat{\mathcal{F}}C_i & A_{ci} \end{bmatrix}$, $\bar{B}_{ci} = \begin{bmatrix} 0 \\ \mathcal{B}_{ci} \end{bmatrix}$, $\bar{C}_i = \begin{bmatrix} C_i^T \check{\mathcal{F}}^T \\ 0 \end{bmatrix}^T$, $\bar{S}(\bar{R}) = \text{diag}(S(R), S(R))$. However, since (11) is expressed in terms of non-convex condition, we have to convert it into convex conditions to find the controller gains.

Theorem 1 *For the states in invariant set $\mathcal{E}(\bar{E}^T P_i \bar{E})$, the following statements are equivalent.*

(A) *There exist symmetric matrix P_i, non-singular matrix Q_i, and matrix K_i such that for all $i \in \mathbb{N}_N^+, \ l \in \mathbb{N}_{2m}^+$*

$$0 < \begin{bmatrix} \bar{E}_L^T P_i \bar{E}_L & \bar{E}_L^T \bar{K}_i^T e_l \\ e_l^T \bar{K}_i \bar{E}_L & \mu^2 I \end{bmatrix}, \tag{12}$$

$$0 > sym(\bar{A}_{ci}^T \Sigma_i) + \sum_{j \in \mathbb{N}_N^+} \pi_{ij} \bar{E}^T P_j \bar{E} + \Sigma_i^T \bar{B}_{ci} \bar{B}_{ci}^T \Sigma_i + \bar{C}_i^T \bar{C}_i. \tag{13}$$

(B) *There exist $P_{1i}, \bar{P}_{1i}, Q_{1i}, \bar{Q}_{1i}, B_{1i}, B_{2i}, C_{1i}, C_{2i}$ and K_{1i} such that for all $i \in \mathbb{N}_N^+$, $l \in \mathbb{N}_{2m}^+$*

$$0 < \begin{bmatrix} E_R^T \bar{P}_{1i} E_R & (*) & (*) \\ I & E_L^T P_{1i} E_L & (*) \\ e_l^T K_{1i} E_R & 0 & \mu^2 I \end{bmatrix}, \tag{14}$$

$$0 > \begin{bmatrix} (1,1)_a & E^T B_{1i} + S B_{2i} \\ (*) & -I \end{bmatrix}, \tag{15}$$

$$0 > \begin{bmatrix} (1,1)_b & (\bar{P}_{1i} E + S Q_{1i} R)^T C_i^T \check{\mathcal{F}}^T & \left[\sqrt{\pi_{ij}} E \bar{P}_{1i} E_R \right]_{j \in \mathbb{N}_N^+ / \{i\}} \\ (*) & -I & 0 \\ (*) & (*) & -diag \left[E_R^T \bar{P}_{1j} E_R \right]_{j \in \mathbb{N}_N^+ / \{i\}} \end{bmatrix}, \tag{16}$$

where

$$(1,1)_a = sym((P_{1i} E + R^T Q_{1i} S^T)^T A_i + (E^T B_{1i} + S B_{2i}) \hat{\mathcal{F}} C_i)$$
$$+ \sum_{j \in \mathbb{N}_N^+} \pi_{ij} E^T P_{1j} E + C_i^T \check{\mathcal{F}}^T \check{\mathcal{F}} C_i,$$

$$(1,1)_b = sym((A_i + B_i(H_l C_{ci} + H_l^- K_i))(\bar{P}_{1i} E^T + S \bar{Q}_{1i} R)) + \pi_{ii} E X_i E.$$

Proof The equivalent of (12) and (14) is already shown in [10]. Therefore, we only proof the others.

(A)→(B) Let us divide P_i, Q_i, Σ_i in (12),(13) into the following block matrices:

$$P_i = \begin{bmatrix} P_{1i} & P_{2i} \\ P_{2i}^T & P_{3i} \end{bmatrix}, \ Q_i = \begin{bmatrix} Q_{1i} & Q_{2i} \\ Q_{3i} & Q_{4i} \end{bmatrix}, \ \Sigma_i = \begin{bmatrix} \Sigma_{1i} & \Sigma_{2i} \\ \Sigma_{3i} & \Sigma_{4i} \end{bmatrix}. \tag{17}$$

By [11], Σ_i is non-singular and its inverse is defined as $\Sigma_i^{-1} = \bar{P}_i \bar{E}^T + \bar{S} \bar{Q} \bar{R}$, where $\bar{P}_i$ and $\bar{Q}_i$ are the block matrices such that $\bar{E}_R^T \bar{P}_i \bar{E}_R = (\bar{E}_L^T P_i \bar{E}_L)^{-1}$, $\bar{Q}_i = (\bar{S}^T \bar{S})^{-1} Q_{1i}^{-1} (\bar{R} \bar{R}^T)^{-1}$. Let us set the block matrix $\bar{P}_i$ as follows:

$$\bar{P} = \begin{bmatrix} \bar{P}_{1i} & \bar{P}_{2i} \\ \bar{P}_{2i}^T & \bar{P}_{3i} \end{bmatrix}. \tag{18}$$

Note that $\bar{E}_R^T \bar{P}_i \bar{E}_R = (\bar{E}_L^T P_i \bar{E}_L)^{-1}$ holds that

$$E_R^T \bar{P}_{1i} E_R = \left\{ E_L^T P_{1i} E_L - \left(E_L^T P_{2i} E_L \right) \left(E_L^T P_{3i} E_L \right)^{-1} \left(E_L^T P_{2i}^T E_L \right) \right\}^{-1}. \tag{19}$$

By considering the above condition, set the following invertible matrices:

$$T_{1i} = \begin{bmatrix} E_R^T \bar{P}_{1i} E_R & I\ 0 \\ -\left(E_L^T P_{3i} E_L\right)^{-1} E_L^T P_{2i}^T E \bar{P}_{1i} E_R\ 0\ 0 \\ 0 & 0\ I \end{bmatrix}, T_{2i} = \begin{bmatrix} \Sigma_{1i}^{-1} & I \\ \Sigma_{1i}^{-1} - \Sigma_{1i}\ 0 \end{bmatrix}. \quad (20)$$

Then applying congruence transformation to (12) and (13) by T_{1i} and T_{2i}. Then it is easily shown that (12) and (13) guarantee (14), (15), and (16), respectively.

(B)→(A) Let us construct the following matrices:

$$P_i = \begin{bmatrix} P_{1i} & P_{2i} - P_{1i} \\ \mathcal{P}_{2i}^T - P_{1i}^T\ P_{1i} - P_{2i} \end{bmatrix}, Q_i = \begin{bmatrix} & Q_{1i}\ Q_{2i} - Q_{1i} \\ \mathcal{Q}_{2i}^T - Q_{1i}^T & Q_{1i} - Q_{2i} \end{bmatrix}, \quad (21)$$

$$E_R^T P_{2i} E_R = \left(E_L^T \bar{P}_{1i} E_L\right)^{-1}, \quad Q_{2i} = \left(S^T S\right)^{-1} \bar{Q}_{1i}^{-1} \left(R R^T\right)^{-1}. \quad (22)$$

Then we can define the following non-singular matrices:

$$\bar{T}_{1i} = \begin{bmatrix} E_R^T \bar{P}_{1i} E_R\ I\ 0 \\ E_R^T \bar{P}_{1i} E_R\ 0\ 0 \\ 0 & 0\ I \end{bmatrix}, \bar{T}_{2i} = \begin{bmatrix} \bar{\Sigma}_{1i}\ I \\ \bar{\Sigma}_{1i}\ 0 \end{bmatrix}, \quad (23)$$

where $\bar{\Sigma}_i = \bar{P}_{1i} E^T + S \bar{Q}_{1i} R$. Note that since we set the condition (22), $\bar{\Sigma}_i$ is guaranteed by in [11]. Next applying congruence transformation to (12) by $\bar{T}_{1i}$. Then, the condition (12) can be rewritten as (14) by Schur complement. In the condition (13), the result of congruence transformation by $\bar{T}_{2i}$ is

$$0 > \begin{bmatrix} \mathcal{L}_{1i}(\bar{P}_{1i}, \bar{Q}_{1i}, C_{1i}, C_{2i}) & (*) \\ \mathcal{L}_{2i}^T(P_{1i}, \bar{P}_{1i}, Q_{1i}, \bar{Q}_{1i}, A_{ci}, B_{ci}, C_{ci})\ \mathcal{L}_{3i}(P_{1i}, Q_{1i}, B_{1i}, B_{2i}) \end{bmatrix}. \quad (24)$$

Here, we can set A_{ci}, B_{ci}, C_{ci} to hold $\mathcal{L}_{2i}(\cdot) = 0$. Then the above condition is equivalent to (15), (16) by Schur complement.

4 Numerical Example

Consider the following system matrices:

$$A_1 = \begin{bmatrix} -2\ 3 \\ 1\ 1 \end{bmatrix}, A_2 = \begin{bmatrix} -1.7\ 1.5 \\ 1\ 1 \end{bmatrix}, B_1 = \begin{bmatrix} 0 \\ -1 \end{bmatrix}, B_2 = \begin{bmatrix} 0 \\ -1 \end{bmatrix}, \quad (25)$$

$$C_1 = \begin{bmatrix} -1.5 \\ 1 \end{bmatrix}^T, C_2 = \begin{bmatrix} 2 \\ -2 \end{bmatrix}^T, \Pi = \begin{bmatrix} -3\ 3 \\ 5\ -5 \end{bmatrix}. \quad (26)$$

Fig. 2 State trajectories with the proposed dynamic output-feedback control
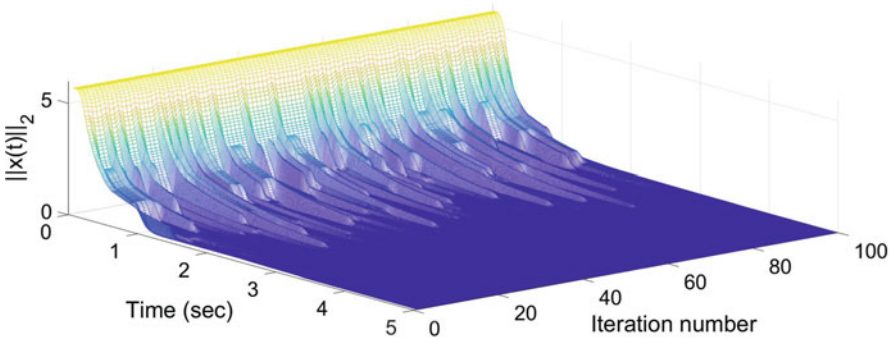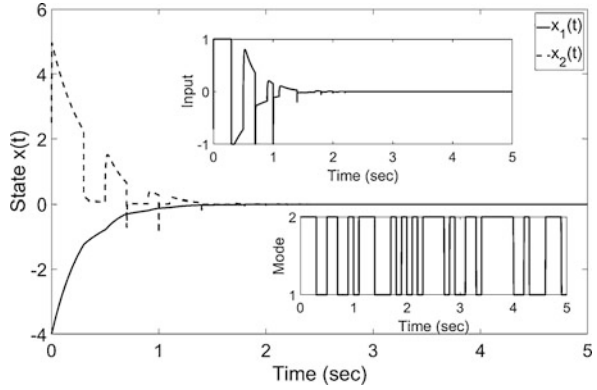
Fig. 3 Euclidean norm of state from Monte Carlo simulation result

The lower and upper bound of sensor failure model are given as $\underline{f}_1 = 0.05$, $\underline{f}_2 = 0.1$, $\bar{f}_1 = 0.8$, $\bar{f}_2 = 1$. The saturation level $\mu = 1$ is considered. The state trajectories with the proposed controller, mode transition, and saturated input signals are shown in Fig. 2. Also, in order to generalize the result, the Euclidean norm of state trajectories for Monte Carlo simulation with 100 rounds is also provided (see Fig. 3). It can be seen that the closed-loop system with the proposed controller is stable for 100 rounds simulations.

5 Conclusions

This paper designed a dynamic output-feedback control for Markovian jump descriptor systems under input saturation and sensor failure. By introducing virtual control input which is in the range of saturation level and sensor failure model, the closed-loop system is expressed in the form of quasi-linear parameter varying systems. Since the stochastic admissibility criterion for the closed-loop system is obtained in terms of matrix inequality, the equivalent condition of non-convex

condition is derived in terms of strict linear matrix inequalities. The dynamic output-feedback controller is constructed from the solution of proposed LMIs. A numerical example is provided to show the effectiveness of the result.

References

1. Gupta, R.A., Chow, M.Y.: Networked control system: overview and research trends. IEEE Trans. Ind. Electron. **57**(7), 2527–2535 (2010)
2. Feng, Z., Lam, J.: Reliable dissipative control for singular Markovian systems. Asian J. Control **15**(3), 901–910 (2013)
3. Wu, Z.G., Dong, S., Shi, P., Su, H., Huang, T.: Reliable filtering of nonlinear Markovian jump systems: the continuous-time case. IEEE Trans. Syst. Man Cybern. Syst. **49**(2), 386–394 (2017)
4. Ma, Y., Jia, X., Liu, D.: Robust finite-time $\mathcal{H}_\infty$ control for discrete-time singular Markovian jump systems with time-varying delay and actuator saturation. Appl. Math. Comput. **286**, 213–227 (2016)
5. Liu, G., Xu, S., Park, J.H., Zhuang, G.: Reliable exponential filtering for singular Markovian jump systems with time-varying delays and sensor failures. Int. J. Robust Nonlinear Control **28**(14), 4230–4245 (2018)
6. Shen, H., Wu, Z.G., Park, J.H.: Reliable mixed passive and filtering for semi-Markov jump systems with randomly occurring uncertainties and sensor failures. Int. J. Robust Nonlinear Control **25**(17), 3231–3251 (2015)
7. Cao, Y.Y., Lin, Z., Shamash, Y.: Set invariance analysis and gain-scheduling control for LPV systems subject to actuator saturation. Syst. Control Lett. **46**(2), 137–151 (2002)
8. Wu, F., Lin, Z., Zheng, Q.: Output feedback stabilization of linear systems with actuator saturation. IEEE Trans. Autom. Control **52**(1), 122–128 (2007)
9. Park, C.e., Kwon, N.K., Park, P.: Optimal $\mathcal{H}_\infty$ filtering for singular Markovian jump systems. Syst. Control Lett. **118**, 22–28 (2018)
10. Park, C.e., Kwon, N.K., Park, P.: Output-feedback control for singular Markovian jump systems with input saturation. Nonlinear Dyn., 1–10 (2018)
11. Uezato, E., Ikeda, M.: Strict LMI conditions for stability, robust stabilization, and $\mathcal{H}_\infty$ control of descriptor systems. In: Proceedings of the 38th IEEE Conference on Decision and Control, vol. 4, pp. 4092–4097. IEEE, Piscataway (1999)

Part IV
Network Synchronization

Synchronization Analysis of Coupled Oscillatory Network with Different Node Arrangement

Li-xin Yang and Xiao-jun Liu

Abstract This chapter studies the impacts of node arrangement on the frequency synchronization of coupled oscillatory network. We mainly focus on the oscillatory model with chain-like and tree-like topologies. Moreover, we address the numerical simulations on the role of node arrangement in the phenomenon of onset of frequency synchronization in power network modeled by second-order Kuramoto oscillators. It is revealed that coupling strategies play an important role in collective behavior of coupled oscillatory network. It is also discovered that the threshold of coupling strength for frequency synchronization may be different for different arrangements of the consumer and generator nodes. More specifically, the closer to each other the nodes which are more heterogeneous, the stronger the synchronizability of oscillatory network is. In particular, the closer to each other the nodes which are less heterogeneous, the weaker the synchrony ability of the coupled oscillatory network is.

Keywords Oscillatory network · Critical coupling strength · Synchronization

1 Introduction

It is well known that the frequency synchronization in coupled oscillatory network is one important issue in the nonlinear dynamics and complex networks [1–3]. Generally, the successful model for studying the synchronization problem was introduced by Kuramoto oscillators. During the last decades, the oscillator model has simulated various studies from many fields [4–7]. The Kuramoto model shows the evolution of coupled oscillators via a set of time differential equations,

L.-x. Yang (✉)
School of Arts and Sciences, Shaanxi University of Science and Technology, Xi'an, China
e-mail: jiaodayanglixin@163.com

X.-j. Liu
Tianshui Normal University, Tianshui, China

$$\dot{\theta}_i = \omega_i + K \sum_{j=1}^{N} \beta_{ij} \sin\left(\theta_j - \theta_i\right), \quad i = 1, 2, \ldots, N, \tag{1}$$

where θ_i denotes instantaneous phase of the ith oscillator, ω_i is its natural frequency, K is the global coupling strength and matrix $B = (\beta_{ij})_{N \times N}$ is the adjacency matrix of network. If oscillators i and j are connected, then $\beta_{ij} = 1$, otherwise $\beta_{ij} = 0$.

On the other hand, in order to characterize the degree of synchrony of oscillatory network, the order parameter is defined within the formula

$$z(t) = r(t)e^{i\Psi(t)} = \frac{1}{N} \sum_{j=1}^{N} e^{i\theta_j(t)}, \tag{2}$$

where $z(t)$ denotes a complex valued vector on the complex plane, $r(t)$ is the collective amplitude. When $r \approx 1$ indicates that all the oscillators come to a single tight clump, and when $r \approx 0$ denotes that the system exhibits low synchrony. As the coupling strength K increases, then a cluster of phase-locked oscillators appear, characterized by an order parameter $0 < r(t) < 1$.

More importantly, second-order Kuramoto oscillatory network can be interpreted as a realistic physical model of consumers and generators working in a power network [8–11]. Researchers provided the physical motivation via the Kruamoto oscillator to model power grids [12]. They distinguish between two kinds of oscillators: The generator nodes that deliver electrical power and the consumer node that consume the power. Thus, it is important that all the nodes in the power network operate at the same frequency to guarantee a steady power flow, otherwise severe problems like large blackouts are bound to occur. To keep energy balance, synchronization between distributed nodes of a power grid is an essential aspect for its proper operation. As known, collective behavior of oscillatory network is mainly determined by the topology structure and the coupling strength. In fact, node arrangements play crucial roles on the topology structure of oscillatory network [13–15]. However, existing results have discussed the dynamics of power networks composed of equal coupled oscillators. But power network is composed of nodes with different physical and dynamical properties. Hence, for coupled oscillatory power network, if node arrangements are different, then the critical coupling strength may be different. For this reason, we pay our particular attention to understand what features of a network inhibit or enhance the ability to support collective dynamics. The objective of this chapter is to study the influence of node arrangements in the coupled network with chain topology and tree topology structures.

This chapter is organized as follows. A coupled oscillatory power network model and synchronous conditions are presented in Sect. 2. Then, in Sect. 3, firstly, synchronous state of a simple power network model is studied. This allows us to investigate the synchronization ability of coupled power network with complex coupling strategies in the following subsection, exploring the relationship between

synchronizability and the node arrangement schemes. The conclusions of this work are drawn in Sect. 4.

2   Model for Synchronous Oscillatory Power Network

Following Ref. [11], a coupled oscillatory power network with the dynamics described by the second-order Kuramoto model, the system equations can be written as:

$$\begin{cases} \dot{\phi}_i = \omega_i, \\ \dot{\omega}_i = -\alpha\omega_i + P_i + K \sum_{j=1}^{N} a_{ij} \sin\left(\phi_j - \phi_i\right), \quad i = 1, 2, \ldots, N. \end{cases} \tag{3}$$

This equation can be derived from a power-conservation law in the generator. The parameter α is the damping parameter and K is the coupling strength. Two kinds of oscillators are considered.

Each element of the power network either generates ($P_i > 0$) or consumes ($P_i < 0$). This means that the electrical power distribution of the oscillatory power network should be bimodal. The phase of each element is then written as $\theta_j(t) = \Omega t + \omega_i$. Notably, the total consumption equals the total amount of generation, i.e., $\sum_{i=1}^{N} P_i = 0$.

In this chapter, we assume the power distribution with the binary form

$$P_i = (-1)^{i+1} P, \quad i = 1, 2, \ldots, N - 1. \tag{4}$$

That is, the power is generated at the odd modes and the power is consumed at the even nodes.

2.1   The Stability Condition of Coupled Oscillatory Power Network

As known, the power network keeps synchronous state of generators is essential. To get the stability conditions of the synchronous state, we linearize Eq. (3) around a steady state $\left(\theta_i^*, \omega_i^*\right)$. Perturbations around the equilibrium are expressed as $\theta_i = \theta_i^* + \delta\theta_i$, $\omega_i = \omega_i^* + \delta\omega_i$. Vectors $\mathbf{X}_1$ and $\mathbf{X}_2$ are introduced, which are defined as

$$\begin{aligned} \dot{\mathbf{X}}_1 &= \mathbf{X}_2, \\ \dot{\mathbf{X}}_2 &= -\mathbf{L}\mathbf{X}_1 - \mathbf{A}\mathbf{X}_2, \end{aligned} \tag{5}$$

where **L** denotes a Laplacian matrix of representing the topology of power network, defined as

$$
L_{ij} = \begin{cases} -K_{ij}\cos\left(\theta_i^* - \theta_j^*\right), & i \neq j, \\ -\sum\limits_{l \neq i}^{n} L_{il}, & i \neq j. \end{cases} \tag{6}
$$

and A denotes the damping matrix.

Because **L** is the Laplacian matrix, one can diagonalize by substituting $\mathbf{J} = \mathbf{Q}\mathbf{L}\mathbf{Q}^{-1}$, where **Q** is composed of the eigenvectors of **L** and **J** is the diagonalized matrix composed of u_j. Then Eq. (5) can be rewritten in the following form via the transformation $\mathbf{Y}_1 = \mathbf{Q}^{-1}\mathbf{X}_1$, $\mathbf{Y}_2 = \mathbf{Q}^{-1}\mathbf{X}_2$.

$$
\begin{bmatrix} \dot{\mathbf{Y}}_{1j} \\ \dot{\mathbf{Y}}_{2j} \end{bmatrix} = \begin{bmatrix} 0 & 1 \\ -\mathbf{J} & -\mathbf{A} \end{bmatrix} \begin{bmatrix} \mathbf{Y}_{1j} \\ \mathbf{Y}_{2j} \end{bmatrix}. \tag{7}
$$

It is well known that the synchronous state stability is determined by the following eigenvalues:

$$
\lambda_{\pm,j} = \frac{-\lambda_A \pm \sqrt{\lambda_A^2 - 4u_j}}{2}, \quad \text{for } j = 1, 2, \ldots, n. \tag{8}
$$

So the synchronous state of the system is stable if and only if the real parts of the eigenvalues are negative, that is,

$$
\max \Re\left(\lambda_{\pm,j}\right) < 0. \tag{9}
$$

3   Synchronization Analysis of Coupled Oscillatory Network

In this section, we focus our attention on the analysis of the synchronization state in coupled oscillatory power network with different node arrangement schemes. For simplicity, we refer the node with different frequency as the heterogeneous node and the node with identical frequency as the homogeneous node. In this chapter, the results are derived in the following sections via numerical simulations. Also, we will mainly perform simulations by sweeping up and down the coupling strength, following two different node arrangements.

3.1   Coupled Oscillatory Power Network with Chain-Like Topology

Firstly, a simple model composed of four oscillators is considered. Two generators and two consumers are placed on a ring. Different node arrangements are described as shown in Fig. 1a, b. Moreover, in Fig. 1a, generator nodes and consumer nodes are cross distributed, but in Fig. 1b, two generator and two consumer nodes are adjacent, respectively. In what follows, the critical coupling strengths of two networks with different structural correlations are presented. The initial phases of the oscillators are selected as $\theta_i(0) = 0$, $i = 1, 2$ and the natural frequencies having values as either -1 or $+1$.

First of all, the process of evolution of order parameter r is depicted, as shown in Fig. 4. The coupling strength is increased in steps of $\Delta K = 0.5$. In Fig. 2, we see that there exists a critical value of the coupling strength K_C, above which the network can achieve synchronization. As the coupling strength K continues to increase, the order parameter is growing. Furthermore, it can be observed that the critical values of the coupling strength are different for adjusting node arrangement schemes. The blue line denotes the order parameter of the network with generator nodes and consumer nodes severally distributed. Meanwhile, the red line shows the order parameter of the network with generator nodes and consumer nodes that are
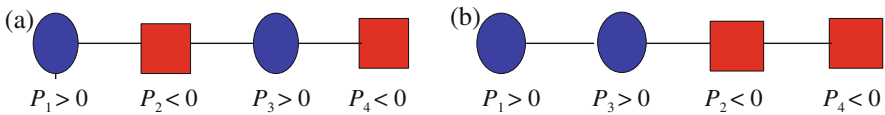
Fig. 1 The chain oscillatory networks with different node arrangements. Circle nodes denote generators and square nodes are consumers

Fig. 2 Order parameter r versus the coupling strength K. For cross arrangement scheme, the critical strength $K_C = 0.8$. For adjacent arrangement, the critical strength $K_C = 1$, order parameter cannot reach 1
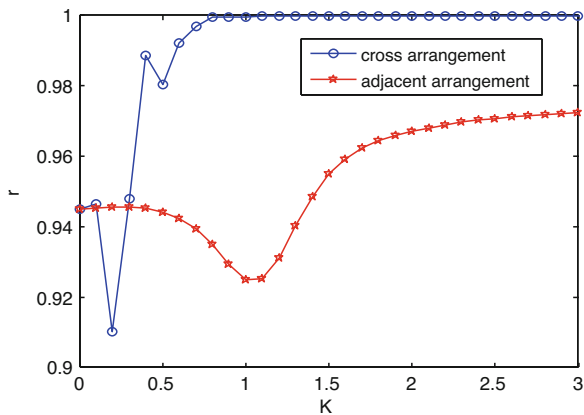
adjacently distributed. It is remarkable that the critical coupling strength K_C of the adjacently arranged strategy is larger than the scheme that is in cross arrangement. Certainly, the larger the critical strength is, the weaker the synchronous ability is. In fact, the shorter the distance between homogeneous nodes is, the weaker the synchronizability of the chain power network is. On the contrary, the closer to each other the nodes that are more heterogeneous, the stronger the synchronizability of the chain power network is.

In order to further investigate the impacts of node arrangement on synchronous ability of the oscillatory power network with the chain topology, we expand the network scale $N = 10$, then we select typically arranged strategies selected for simulation. The first scheme is the generator nodes and consumer nodes arranged in a staggered formation with heterogeneous and homogeneous nodes adjacently arranged on the chain. The second strategy is all the nodes are classified into two different groups, where the homogeneous nodes and the heterogeneous nodes are separated from each other. Analogously, we investigate the changes in the evolution of order parameter caused by topological adjust within the network. In Fig. 3, it is found that the longer the distance between the heterogeneous nodes on the chain, the worse the synchronizability the power network will have. Also, the longer the distance between the homogeneous nodes, the better the synchronizability the power network will have.

As found from Figs. 2 and 3, the larger scales of $N = 10$ come to the same observations. On average, the closer to heterogeneous nodes, the smaller the critical coupling strength needed for oscillatory power network to realize synchronization is; the closer to homogeneous nodes, the larger the critical coupling strength needed for oscillatory network to achieve frequency synchronization is.

Fig. 3 When the network scale $N = 10$, for cross arrangement scheme, the critical coupling strength $K_C = 1.3$. For adjacent arrangement, the critical coupling strength $K_C = 1.8$
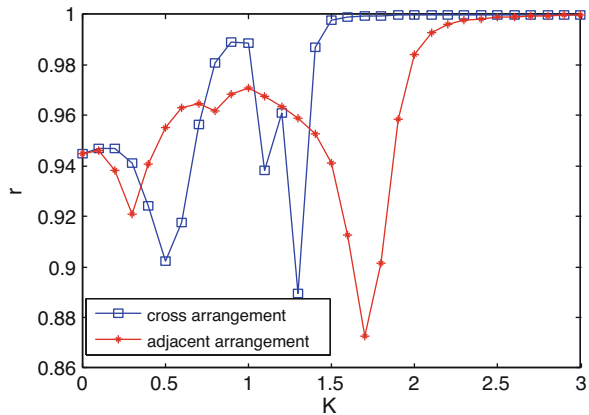
3.2 *Coupled Oscillatory Power Network with Tree-Like Topology*

In this subsection, we consider the network with tree structure and investigate the influence of node arrangement on synchronizability. Hence Fig. 4a, b can be served as the scheme of generator and consumer connected with different schemes. It is clearly found that the heterogeneous node is connected in Fig. 4a,

In what follows, to further reveal the underlying mechanism of dynamics in power network with different arrangement strategies, collective dynamics of oscillatory tree networks with different scales and different arrangement are investigated.

From Figs. 5 and 6, it can be observed that the synchronizability for cross arrangement is indicated to be stronger than the case of adjacent arrangement schemes. It is noteworthy that the process of evolution of order parameter r with coupling strength K varies with arrangement strategy.

According to the above results, node arrangement plays important role on the synchronous dynamics of oscillatory network with chain and tree structures.
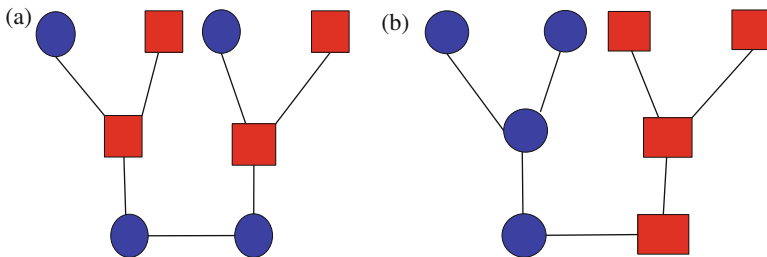
Fig. 4 The tree oscillatory networks with different nodes arrangements. Circle nodes denote generators and square nodes are consumers

Fig. 5 The evolution of order parameter r, and each of the arrangement schemes
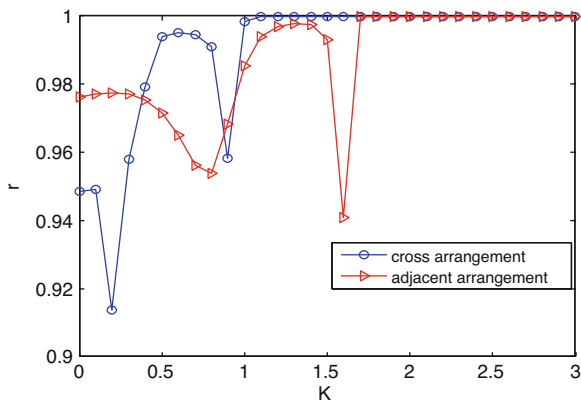
Fig. 6 The evolution of order parameter of system, *r,* and each of the arrangement schemes
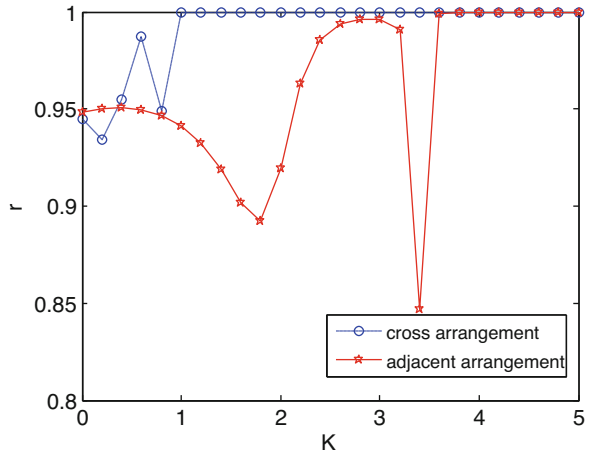
4   Conclusions

We have studied the influence of different node arrangement categories in synchronizability of oscillatory power network with chain and tree structures. Our study presented the following results obtained via numerical simulations. First, we established that the closer to the heterogeneous nodes, the better the synchronous ability of oscillatory network is. Nevertheless, the closer to homogeneous node, the weaker the synchronizability of network is. Furthermore, the critical coupling strength of achieving synchronous state is nonidentical for different node arrangement schemes. The work may provide a framework to design the topology of future power networks and will enhance our understandings of the collective behavior in oscillatory network with heterogeneous coupling strategies.

References

1. Rodrigues, F.A., Peron Thomas, K.D.M., Ji, D.: The Kuramoto model in complex networks. Phys. Rep. **610**, 91–98 (2016)
2. Wang, C.W., Grebogi, C., Baptista, M.S.: Control and prediction for blackouts caused by frequency collapse in smart grids. Chaos **26**, 093119 (2016)
3. Carareto, B., Aptista, M.S., Grebogi, C.: Natural synchronization in power-grids with anti-correlated unit. Commun. Nonlinear Sci. Numer. Simulat. **3**, 4–15 (2013)
4. Schafer, B., Witthaut, D., Timme, M.: Dynamically induced cascading failures in power grids. Nat. Commun. **9**, 1975 (2018)

5. Hancock, E.J., Gottwald, G.A.: Model reduction for Kuramoto models with complex topologies. Phys. Rev. E. **98**, 012307 (2018)
6. Florian, D., Michael, C., Francesco, B.: Synchronization in complex oscillator networks and smart grids. Proc. Natl. Acad. Sci. **110**, 2005–2010 (2013)
7. Auer, S., Hellmann, F., Krause, M.: Stability of synchrony against local intermittent fluctuations in tree-like power grids. Chaos **27**, 127003 (2017)
8. Kim, H., Lee, S.H., Holme, P.: Community consistency determines the stability transition window of power grid. New J. Phys. **17**, 113005 (2015)
9. Pourbeik, P., Kundur, P.S., Taylor, C.W.: The anatomy of a power grid blackout-root causes and dynamics of recent major blackouts. Power Energy Mag. IEEE. **4**, 22–29 (2006)
10. Rohden, M., Timme, M., Sorge, A.: Self-organized synchronization in decentralized power grids. Phys. Rev. Lett. **109**, 064101 (2012)
11. Witthaut, D., Timme, M.: Braess's paradox in oscillator networks, desynchronization and power outage. New J. Phys. **14**, 083036 (2012)
12. Filatrella, G., Nielsen, A.H., Pedersen, N.F.: Analysis of a power grid using a Kuramoto-like model. Eur. Phys. J. B Condens. Matter Complex Syst. **61**, 485–491 (2008)
13. Yang, L.X., Jiang, J.: Impacts of link addition and removal on synchronization of an elementary power network. Physica A **479**, 99–107 (2017)
14. Manik, D., Timme, M., Witthaut, D.: Cycle flows and multistability in oscillatory networks. Chaos **083123**, 27 (2017)
15. Lozano, S., Buzna, L., Diaz-Guilera, A.: Role of network topology in the synchronization of power systems. Eur. Phys. J. B. **85**, 231–239 (2012)

On the Synchronization of Unbalance Vibration Exciters, Mounted on a Resiliently Supported Rigid Body, Near Resonance

Grigory Panovko and Alexander Shokhin

Abstract This chapter presents the results of an experimental analysis of the self-synchronization effect of two asynchronous-type unbalance exciters installed on an oscillating system in the resonance frequency range. The amplitude-frequency responses of the system, as well as the speed and phase of the debalance rotation depending on the frequency of the voltage supplying the electric motors are analyzed. It is shown that in the close vicinity of the resonance frequencies of the linearized system, instability in average angular velocity of the debalance rotation arises and an increase in their mutual phase shift is observed, up to an abrupt change in both the type of synchronization and the system oscillation mode during passage through resonance.

Keywords Oscillating system · Vibration exciter · Self-synchronization · Resonance · Experiment

1 Introduction

The tasks of several unbalance exciters self-synchronization are of great practical importance in modern vibration engineering [1–4]. Under the self-synchronization of two or more unbalance exciters, their rotation with the same or multiple angular velocities of the debalances and a strictly defined ratio between their angles of rotation are implied. This effect appears in case of the presence of the so-called weak coupling between vibration exciters mounted on an oscillatory system [5–8]. It is known that the type of synchronization of debalance rotation and the form of system oscillations have a mutual influence on each other [5, 9, 10]. Ensuring the synchronous rotation of debalances with the given phase relations is one of the principal tasks in vibration machine development [1, 3, 11–13]. In most cases, the

G. Panovko · A. Shokhin (✉)
Mechanical Engineering Research Institute of the Russian Academy of Sciences, Moscow, Russia
e-mail: gpanovko@yandex.ru; shohinsn@mail.ru

analysis is focused on the self-synchronization beyond the resonance oscillation modes as the least sensitive to possible fluctuations of the system parameters and process loads [2, 4, 14].

Currently, much attention is paid to the use of resonant vibration modes [4, 8, 9, 15]. The main problem is to ensure the stability of these modes. Under the conditions of varying parameters of the system and technological load, the control systems are used [9, 15, 16]. At the same time, the issues of synchronization of debalances driven by asynchronous electric motors near the resonances have not been studied in sufficient detail, which makes it difficult to estimate the frequency of oscillation jump into beyond-resonant region and reduces efficiency of the control system.

This chapter describes the results of an experimental study of the self-synchronization effect of two unbalance asynchronous-type vibration exciters installed on a planar single-mass oscillatory system, near resonances. Special attention is paid to the analysis of the rotational speeds and phase angles of the debalances near the resonant frequencies.

2 Experimental Model

The experimental model consists of a rigid metal plate attached to a fixed base by springs, and two motor vibrators mounted symmetrically on the plate (see Fig. 1). Corresponding design scheme is shown in Fig. 2. Debalances with equal imbalance values and the same initial arrangement are installed at both the ends of shaft of each asynchronous-type motors. The model has the following main parameters: the mass and moment of inertia of the plate with the motor vibrators are $m = 12$ kg and $J = 0.106$ kg•m^2, reduced stiffness of the springs in horizontal direction $c_x = 480$ kN/m, in vertical direction $c_y = 600$ kN/m, and in angular direction $c_\varphi = 1750$ N· m, imbalanced mass of each vibration exciter $m_{e1} = m_{e2} = 0.067$ kg, eccentricity $r_1 = r_2 = 0.005$ m, the rated power of each motor 0.18 kW, and the nominal speed of rotation 1500 rpm at power supply frequency of 50 Hz.

The motors are powered from a single inverter, and their shafts rotate in opposite directions. The vectors of inertia forces arising from rotation of each of the vibrators are located in a vertical plane perpendicular to the axes of rotation. Thus, the system's oscillations are only excited in a vertical plane. Depending on the frequency of excitation, three main resonances and different types of debalance self-synchronization with a phase shift of 0° or 180° appear in the system.

To measure the angular position and the rotational speed of the debalances, there are encoders installed at one of the shaft ends of each of the motor vibrators. Three accelerometers are used to measure plate oscillations: two for measuring vertical oscillations installed in the center and at the edge of the plate, and one for measuring horizontal vibrations of the plate's center. For test control and data processing, a software and hardware complex based on the NI-cRIO real-time controller and LabVIEW software was used.

Fig. 1 Experimental model
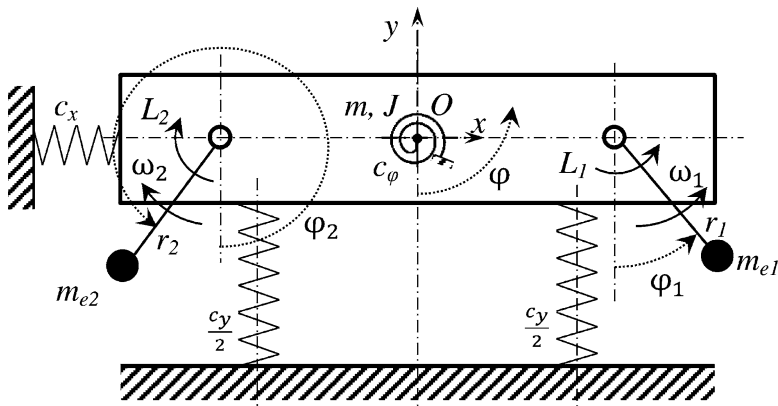
Fig. 2 Design scheme

3 Experimental Methods

The experimental methods include determining the amplitude–frequency responses of the system by vibration signals measured by accelerometers, establishing relationships between the frequency f_e of the supply voltage and the rotational speed f of the debalances, and determining mutual angular position $\Delta\varphi$ of the debalances. The tests were carried out with a discrete change in power supply frequency in the range from 20 to 86 Hz, and, accordingly, the rotational speeds of the debalances in the range from 10 to 43 rev/s. In order to identify possible nonlinearities of the system, the studied characteristics were obtained with both increasing and decreasing rotational speed of the debalances. The frequency step was 0.5 Hz with an exposure time of 5 s, which is necessary for establishing steady oscillations. Near the first resonant frequency, it decreased to 0.1 Hz. Thus, the necessary accuracy

of building the studied characteristics was achieved. The oscillation forms were determined from the comparison of the accelerometers' oscillation phases. The measurement of the mutual phase shift of the debalance rotation was carried out by the time interval between the leading edges of the pulses from optical encoders of each motor vibrators

4 Main Results

Figures 3 and 4 show amplitude–frequency responses of the system, obtained respectively at increasing and decreasing the power supply frequency f_e. Three resonance frequencies at 20.5, 32, and 35 Hz are found in the investigated frequency range. With increasing frequency, there are jumps in the amplitudes and oscillation frequencies from 20.5 to 21.2 Hz when passing through the first resonance, from 32 to 34.5 Hz when passing through the second resonance, and from 35 to 36 Hz when passing through the third resonance. In case of test at decreasing frequency, there is a sharp increase in the oscillations amplitudes and a decrease in their frequency from 36.2 to 35.4 Hz when passing through the third resonance, from 32.6 to 31.7 Hz when passing through the second resonance, and from 20.7 to 20.4 Hz when passing through the first resonance. The amplitudes of vertical oscillations near the second resonance frequency, measured at the center and at the edge of the plate, are almost identical, which indicates the excitation of only unidirectional oscillations and complete self-synchronization of the debalances with zero mutual phase angle. Characteristic jumps in amplitude and frequency when passing through resonances
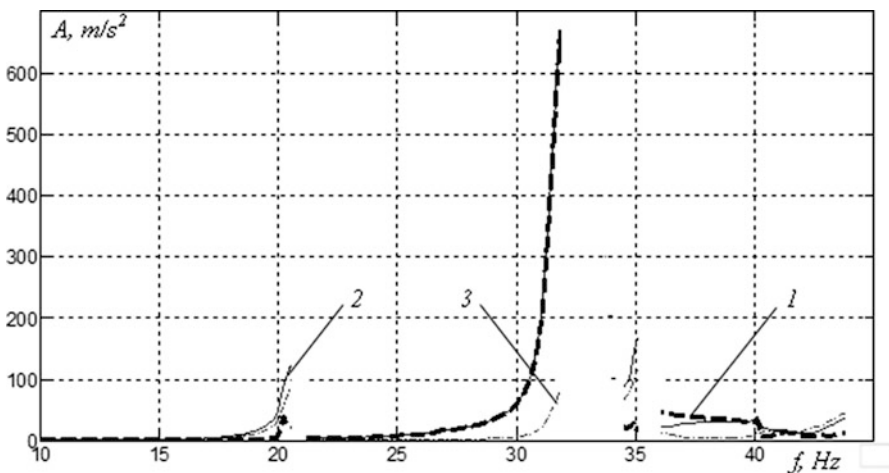
Fig. 3 Amplitude frequency responses at increasing power supply frequency: 1—vertical oscillations of the plate's center, 2—vertical oscillations of the plate's edge, 3—horizontal oscillations of the plate's center
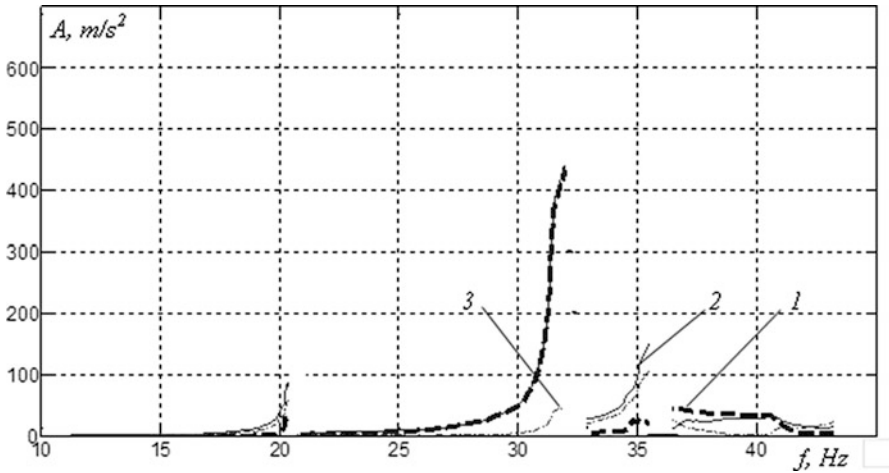
Fig. 4 Amplitude frequency responses at decreasing power supply frequency: 1—vertical oscillations of the plate's center, 2—vertical oscillations of the plate's edge, 3—horizontal oscillations of the plate's center
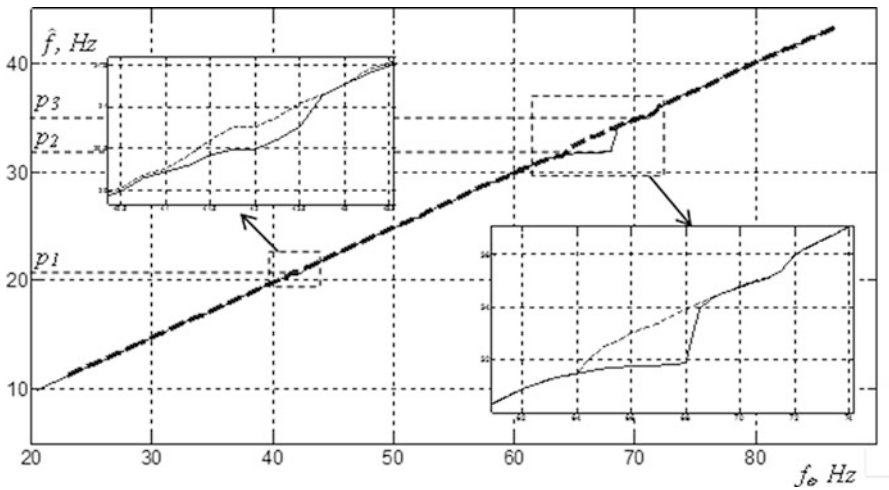
Fig. 5 Rotor's averaged speed depending on the power supply frequency

indicate the nonlinear behavior of the system in these frequency ranges due to the interaction of the system with the asynchronous electric drive of unbalance vibration exciters

Figure 5 shows the graphs of the debalance averaged rotational speed $\hat{f}$ depending on the frequency of the power supply at its increasing (solid line) and decreasing (dashed line). The rectangular areas highlight the resonant regions shown on an enlarged scale. One can see that with an increase in power supply frequency

near the resonant frequencies, a slowdown in the rate of rotational speed change is observed. Moreover, this deceleration is more noticeable near the second resonance frequency. This is due to the slip in asynchronous motors, when their rotational speed practically does not change with increase in power supply frequency. When decreasing power supply frequency, the slip phenomenon is less noticeable.

The results of measuring the debalance rotational speeds during the passage of the second resonance as a function of time t, with increasing and decreasing supply frequency are shown in Figs. 6 and 7, respectively. Each step change in the average speed corresponds to a change in the frequency of the supply voltage. One can see that at each step in power supply frequency after attenuation of transients, the debalances rotate on average with the same frequency. As approaching to the frequency of jump to beyond-resonance region (point A in Fig. 6), the unevenness in rotational speeds of the debalances increases. Jumps in the speed of left-hand-side
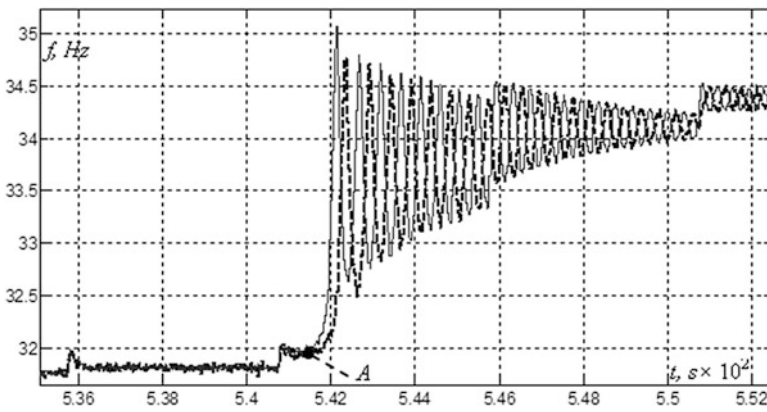
Fig. 6 Rotor's speed jump when passing through second resonance at increasing frequency
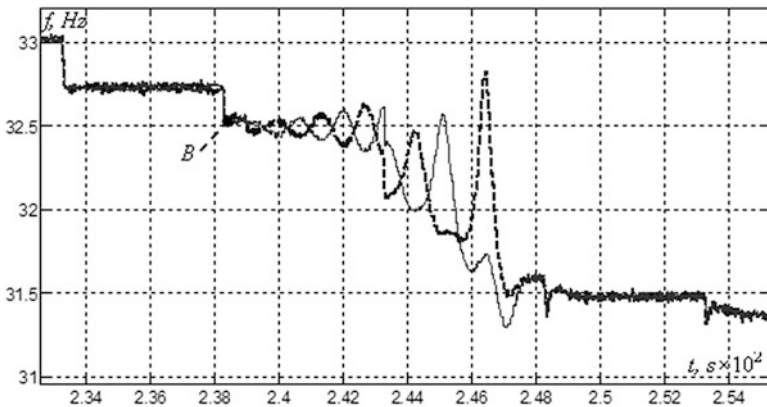
Fig. 7 Rotor's speed jump when passing through second resonance at decreasing frequency

and right-hand-side motors do not occur simultaneously, causing a sharp change in the type of the debalance synchronization, and lead to the appearance of speed oscillations relative to the new average value. These speed oscillations occur in antiphase and fade out in time. In case of decreasing frequency, as approaching to the frequency of jump to pre-resonant area (point B in Fig. 7), an increase in unevenness of the debalance rotation frequency is also observed. As in the previous case, the speed jumps occur non-simultaneously, leading to their oscillations with the subsequent stabilization near the new average value. In this case, the antiphase mode of the speeds oscillations is replaced by the in-phase mode, which can be explained by a change in the oscillation mode of the system.

Figures 8 and 9 show the results of measuring the mutual phase shift of the left-hand-side and right-hand-side debalance rotation as a function of the power
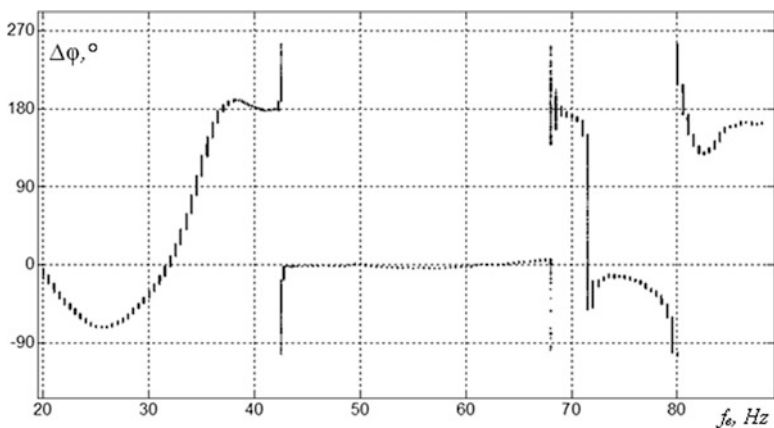
Fig. 8 Phase shift at increasing frequency
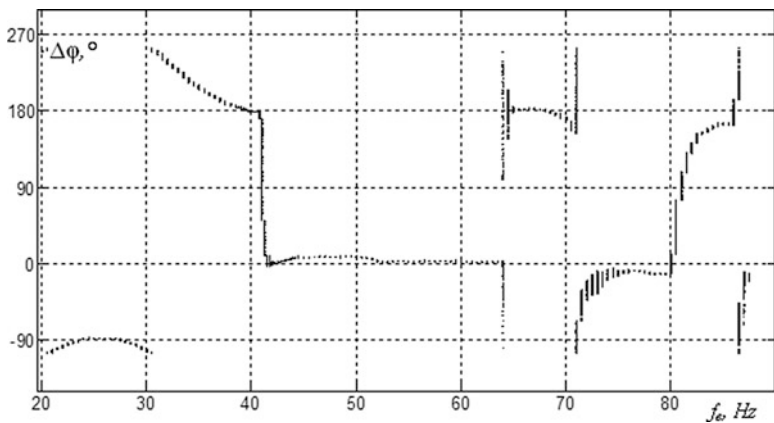
Fig. 9 Phase shift at decreasing frequency

supply frequency, respectively, as it increases and decreases. Each point on the graph corresponds to magnitude of the debalance mutual phase shift $\Delta\varphi$ measured successively through one complete turn of the left-hand-side debalance. Thus, the height of "column" of these points characterizes the change in the debalance mutual phase at a given power supply frequency, and accordingly the degree of synchronism of their rotational speeds—the smaller the height of the column, the closer the debalance rotational speeds to each other. When $\Delta\varphi = 0°$ the debalances rotate in opposite directions in-phase synchronously, and when $\Delta\varphi = 180°$ the debalances rotate synchronously in anti-phase.

One can see in Fig. 8 that in the frequency range almost up to the first resonance, there is no stable synchronization of the debalances, which is explained by the small amplitudes of the excited oscillations. Starting from the power supply frequency of 38 Hz, the phase shift stabilizes near 180°. At the same time, intensive angular oscillations of the plate, accompanied by relatively small horizontal oscillations, are excited. As the power frequency increases, the height of the "columns" increases immediately before the jump, indicating a degradation of synchronization. A sudden change in the type of the debalances self-synchronization ($\Delta\varphi \approx 180°$) is observed immediately after the oscillations jump during the passage of the first resonance. With a further increase in power supply frequency, the phase difference stabilizes near 0°, which indicates the presence of synchronous in-phase rotation of the debalances. When approaching the second resonant frequency, immediately before the jump, an increase in the height of the "columns" is observed, indicating violation of the debalance synchronization. A further increase in power supply frequency leads to a jump and a sharp change in the type of the debalance synchronization ($\Delta\varphi \approx 180°$). When approaching the third resonant frequency, the phase difference is set near 180°, but there is no high phasing stability, which is apparently due to the narrow frequency range between the second and third resonances.

With a decreasing power supply frequency (Fig. 9), when approaching the second resonance frequency, the phase shift stabilizes near 180°. With a further decrease in power supply frequency, an increase in phasing instability is observed, followed by an abrupt change in the type of synchronization by $\Delta\varphi \approx 180°$. The passage through the first resonance is also preceded by an increase in instability of the debalance mutual phasing and is accompanied by a sharp change in its magnitude by $\Delta\varphi \approx 180°$. In the frequency range below the first resonance, stable phasing is not observed.

Note that in the presented graphs, there is one more resonance region near 83 Hz in terms of power supply frequency, which appears due to inaccuracies made in the manufacturing of the model. However, these inaccuracies do not significantly affect the results in the frequency ranges including the first three resonance frequencies.

5   Conclusions

As a result of the experiments performed, the character of changes in the debalance mutual phase shift and its velocities in the close vicinity of resonance frequencies was revealed. It was found that when approaching the resonance frequency near the frequency of the oscillation jump, a violation of the debalances rotational speeds synchronization is observed, leading to the instability of their mutual phase shift. It was found that with a jump in oscillations, the change in the debalance rotational speeds does not occur simultaneously. The features of self-synchronization of unbalance vibration exciters in the resonance frequency ranges require additional consideration when developing resonance vibrating machines

References

1. Blekhman, I.: Vibrational Mechanics: Nonlinear Dynamic Effects, General Approach, Applications. World Scientific, Singapore (2000)
2. Lavendelis E.: Vibration in the Technics. Handbook, vol. 4. Vibration Processes and Machines. Mechanical Engineering, Moscow (1981)
3. Vaisberg, L., Zarogatsky, L., Turkin, V.: Vibrating Crushers. Basics of Calculation, Design and Technological Application. Izdatelstvo VSEGEI, St. Peterburg (2004)
4. Vaisberg, L.: Design and Calculation of Vibrating Screens. Nedra, Moscow (1986)
5. Blekhman, I.: Synchronization of Dynamical Systems. Nauka, Moscow (1971)
6. Nijmeijer, H., Rodriguez-Angeles, A.: Synchronization of Mechanical Systems. World Scientific Publishing, Singapore (2003)
7. Astashev, V., Kolovsky, M., Babitsky, V.: Dynamics and Control of Machines. Springer, Berlin (2000)
8. Nagaev, R.: Dynamics of Synchronizing Systems. Springer, Berlin (2003)
9. Bleckman, I., Fradkov, A., Tomchina, O., Bogdanov, D.: Self-synchronization and controlled synchronization: general definition and example design. Math. Comput. Simul. **58**(4–6), 367–384 (2002)
10. Nagaev, R., Shishkin, E.: Self-synchronization of inertial vibration exciters of vibratory cone crusher. Obogashchenie Rud. **1**, 33–36 (2003)
11. Shishkin, E., Kazakov, S.: Self-synchronization of vibration exciters of cone crusher with three-mass system. Obogashchenie Rud. **5**, 32–37 (2016)
12. Balthazar, J., Felix, J., Brasil, R.: Short comments on self-synchronization of two non-ideal sources supported by a flexible portal frame structure. J. Vib. Control. **10**(12), 1739–1748 (2004)
13. Paz, M., Cole, D.: Self-synchronization of two unbalanced rotors. J. Vib. Acoust. **114**(1), 37–41 (1992)
14. Dimentberg, M., Gobb, E., Mensehing, J.: Self-synchronization of transient rotations in multiple shaft systems. J. Vib. Control. **7**(2), 221–232 (2001)

15. Panovko, G., Shokhin, A., Eremeykin, S., Gorbunov, A.: Comparative analysis of two control algorithms of resonant oscillations of the vibration machine driven by an asynchronous AC motor. J. Vibroeng. **17**(4), 1903–1911 (2015)
16. Eremeikin, S., Krestnikovskii, K., Panovko, G., Shokhin, A.: Experimental analysis of the operability of a system to control the oscillations of a mechanical system with self-synchronizing vibration exciters. J. Mach. Manuf. Reliab. **45**(6), 553–558 (2016)

Mixed Synchronization in Unidirectionally Coupled Chaotic Oscillators

Jonatan Pena Ramirez and Joaquin Alvarez

Abstract This work is focused on a particular type of synchronization observed in coupled systems interacting via unidirectional coupling, namely mixed synchronization: part of the state variables of the coupled systems achieve complete synchronization, whereas the remaining state variables exhibit anti-phase synchronization. This chapter paper presents a modified master–slave scheme, in which the master system interacts with the slave system via a second order dynamic coupling. In the analysis, the stability of the mixed synchronous solution is investigated by using the well-known master stability function approach. A classical chaotic system, namely the Lorenz system, is considered as a particular example.

Keywords Mixed synchronization · Dynamic coupling · Lorenz system

1 Introduction

An interesting phenomenon occurring in coupled systems is synchronization—the behavior of the systems eventually coincides in time [1]. There exists, however, a particular type of systems—namely chaotic systems—for which the onset of synchronization is not evident at first sight. This is in part due to the fact that chaotic systems are very sensitive to small variations in their initial conditions and therefore, two uncoupled chaotic systems starting arbitrarily close to each other will quickly diverge. However, as originally demonstrated by Fujisaka and Yamada [2], chaotic systems can be enforced to synchronize by using diffusive-like couplings.

J. P. Ramirez (✉)
CONACYT-CICESE, Applied Physics Division, Electronics and Telecommunications Department, Ensenada, BC, Mexico
e-mail: jpena@cicese.mx

J. Alvarez
CICESE, Applied Physics Division, Electronics and Telecommunications Department, Ensenada, BC, Mexico
e-mail: jqalvar@cicese.mx

315

A particular type of synchronization occurring in certain chaotic systems with axial symmetry is *mixed synchronization*: part of the state variables of the coupled systems converge to complete synchronization while the remaining variables synchronize in anti-phase [3]. At this point it is worth mentioning that mixed synchronization may find interesting applications in, for example, the study of the creation and interaction of counter-rotating vortices in the atmosphere or in the ocean [4], in secure wireless communications [5], and in the design of controllers for humanoid robots, where some of the components of the robot should move in complete synchrony, whereas other components should move in anti-phase [6].

There exist several works addressing the occurrence of mixed synchronization, see e.g. [7] and the references therein. A common feature in these works is that the coupling between the systems is *static*, i.e., (part of) the state variables are used to construct a coupling signal for interconnecting the systems. In contrast, this work proposes the use of a second order *dynamic* coupling for inducing mixed synchronization in chaotic systems. The obtained results suggest that the use of dynamic coupling enhances the onset of mixed synchronization, and it has the advantage that a faster convergence to the mixed synchronous solution is achieved, compared to the static case.

The stability of the mixed synchronous state is investigated by using the master stability function formalism. Specifically, a variational equation is derived and the corresponding largest transverse Lyapunov exponent is computed in order to determine the local stability of the synchronous solution. A traditional chaotic system, namely the Lorenz system, is considered as a particular example. Furthermore, a comparison between the classical static coupling reported in the literature and the dynamic coupling considered in this work is provided.

This manuscript is organized as follows. First, the unidirectional coupling scheme via dynamic coupling is introduced in Sect. 2. Then, Sect. 3 presents the tools for investigating the local stability properties of the mixed synchronous solution. Next, in Sect. 4, the proposed coupling scheme is applied to the Lorenz system. Finally, some conclusions are provided in Sect. 5.

2 Proposed Coupling Scheme

Recently, a modified master–slave synchronization scheme has been presented in [8]. The novelty in this scheme is that the master and the slave oscillators are not connected through common signals. Instead, the slave system interacts with the master system through a dynamical system. Consequently, the interaction between the systems is indirect.

The coupling scheme is described by

$$\dot{x}_m = F(x_m), \tag{1}$$

$$\dot{x}_s = F(x_s) - B_1 h, \tag{2}$$

$$\dot{h} = Ah - kB_2(x_m - x_s), \tag{3}$$

where x_m, $x_s \in \mathbb{R}^n$ denote the state vectors of the master and slave oscillators, respectively, $h \in \mathbb{R}^2$, is the state vector of the dynamic coupling, k is the coupling strength, and $B_1 \in \mathbb{R}^{n \times 2}$ and $B_2 \in \mathbb{R}^{2 \times n}$ are suitably chosen coupling matrices. The vector field F is assumed to be sufficiently smooth and nonlinear and matrix $A \in \mathbb{R}^{2 \times 2}$ is given by

$$A = \begin{bmatrix} -\alpha & 1 \\ -\gamma_1 & -\gamma_2 \end{bmatrix}, \tag{4}$$

where γ_1, γ_2, and α are positive constants, to be chosen.

In order to investigate the onset of mixed synchronization in the coupled systems (1)–(3), it is convenient to perform the following partition of the state vectors corresponding to the master and slave systems

$$x_m = \begin{bmatrix} x_{m_a} \\ x_{m_c} \end{bmatrix}, \quad x_s = \begin{bmatrix} x_{s_a} \\ x_{s_c} \end{bmatrix}, \tag{5}$$

where $x_{m_a} \in \mathbb{R}^m$ and $x_{s_a} \in \mathbb{R}^m$ denote the part of the state vector of the master and slave, respectively, that converge to anti-phase synchronization, whereas the vectors $x_{m_c} \in \mathbb{R}^{(n-m)}$ and $x_{s_c} \in \mathbb{R}^{(n-m)}$ contain the variables that reach complete synchronization. Furthermore, to be consistent with the partition of the state, see Eq. (5), the function F and the coupling matrices B_1 and B_2 in Eqs. (1)–(2) are also partitioned as follows:

$$F(x_j) = \begin{bmatrix} F_a(x_{j_a}, x_{j_c}) \\ F_c(x_{j_a}, x_{j_c}) \end{bmatrix}, \quad j = m, s, \quad B_1 = \begin{bmatrix} B_{1_a} \\ B_{1_c} \end{bmatrix} \quad B_2 = \begin{bmatrix} B_{2_a} & B_{2_c} \end{bmatrix}, \tag{6}$$

where $F_a : \mathbb{R}^m \times \mathbb{R}^{(n-m)} \to \mathbb{R}^m$, $F_c : \mathbb{R}^m \times \mathbb{R}^{(n-m)} \to \mathbb{R}^{(n-m)}$, $B_{1_a} \in \mathbb{R}^{m \times 2}$, $B_{1_c} \in \mathbb{R}^{(n-m) \times 2}$, $B_{2_a} \in \mathbb{R}^{2 \times m}$, and $B_{2_c} \in \mathbb{R}^{2 \times (n-m)}$. Furthermore, it is assumed that functions $F_a(\cdot)$ and $F_c(\cdot)$ satisfy

$$F_a(x_{j_a}, x_{j_c}) = -F_a(-x_{j_a}, x_{j_c}) \text{ and } F_c(x_{j_a}, x_{j_c}) = F_c(-x_{j_a}, x_{j_c}), \text{ for } j = m, s. \tag{7}$$

As discussed in [3], Eq. (7) guarantees the existence of the mixed synchronization manifold.

Next, it will be assumed that the coupling term h can only be applied to the equations describing the dynamics of the x_{s_c} part and likewise, it is assumed that only the x_{m_c} and x_{s_c} variables are available for measurement. In other words, it will be assumed that the matrices B_{1_a} and B_{2_a} are zero matrices.

Under these assumptions and using (5)–(6), system (1)–(3) takes the form

$$\textbf{Master} : \begin{cases} \dot{x}_{m_a} = F_a(x_{m_a}, x_{m_c}), \\ \dot{x}_{m_c} = F_c(x_{m_a}, x_{m_c}), \end{cases} \tag{8}$$

$$\textbf{Slave} : \begin{cases} \dot{x}_{s_a} = F_a(x_{s_a}, x_{s_c}), \\ \dot{x}_{s_c} = F_c(x_{s_a}, x_{s_c}) - \boldsymbol{B}_{1_c}\boldsymbol{h}, \end{cases} \tag{9}$$

$$\textbf{Dynamic coupling} : \left\{ \dot{\boldsymbol{h}} = \boldsymbol{A}\boldsymbol{h} - k\boldsymbol{B}_{2_c}(x_{m_c} - x_{s_c}). \right. \tag{10}$$

This coupling scheme is considered through this work. Specifically, the occurrence of mixed synchronization in the dynamically coupled systems (8)–(10) is investigated as a function of the coupling strength k.

Finally, a formal definition of mixed synchronization is provided.

Definition 1 The unidirectionally coupled systems (8)–(9) with dynamic coupling (10) is said to achieve asymptotic mixed synchronization if

$$\lim_{t\to\infty} \boldsymbol{x}_{s_a} = -\boldsymbol{x}_{m_a}, \quad \lim_{t\to\infty} \boldsymbol{x}_{s_c} = \boldsymbol{x}_{m_c}, \quad \lim_{t\to\infty} \boldsymbol{h} \equiv 0. \tag{11}$$

3   Local Stability Analysis

The local stability of the mixed synchronous solution (11) is investigated by using the master stability function (MSF) approach presented in [9].

As a first step, the following synchronization errors are defined:

$$\boldsymbol{e}_a = \boldsymbol{x}_{m_a} + \boldsymbol{x}_{s_a}, \quad \boldsymbol{e}_c = \boldsymbol{x}_{m_c} - \boldsymbol{x}_{s_c}, \quad \text{and } \boldsymbol{h}, \tag{12}$$

where $\boldsymbol{e}_a$ and $\boldsymbol{e}_c$ denote the anti-phase and complete synchronization errors, respectively, and $\boldsymbol{h}$ is considered as an "error" because it should vanish when the master and slave systems achieve mixed synchronization, see Eq. (11).

Then, by using the MSF formalism [9], the following *variational equation* is obtained:

$$\dot{\boldsymbol{e}} = \boldsymbol{D}\boldsymbol{e}, \quad \boldsymbol{D} = \begin{bmatrix} \boldsymbol{D}_{x_{sa}}\boldsymbol{F}_a & -\boldsymbol{D}_{x_{sc}}\boldsymbol{F}_a & \boldsymbol{O} \\ -\boldsymbol{D}_{x_{sa}}\boldsymbol{F}_c & \boldsymbol{D}_{x_{sc}}\boldsymbol{F}_c & \boldsymbol{B}_{1_c} \\ \boldsymbol{O}^T & -k\boldsymbol{B}_{2_c} & \boldsymbol{A} \end{bmatrix}, \quad \boldsymbol{e} = \begin{bmatrix} \boldsymbol{e}_a \\ \boldsymbol{e}_c \\ \boldsymbol{h} \end{bmatrix}, \tag{13}$$

where $\boldsymbol{O} \in \mathbb{R}^{m\times 2}$ is a zero matrix and

$$\boldsymbol{D}_{x_{sv}}\boldsymbol{F}_u = \left. \frac{\partial \boldsymbol{F}_u}{\partial \boldsymbol{x}_{s_v}} \right|_{x_{sa}=-x_{m_a}, x_{sc}=x_{m_c}}, \quad u, v = a, c. \tag{14}$$

Finally, the local stability of the mixed synchronous solution (11) is determined by the largest transverse Lyapunov exponent $\lambda_{\max}^{\perp}$,

$$\lambda_{\max}^{\perp} = \lim_{t \to \infty} \frac{\ln |e(t)| - \ln |e(0)|}{t}, \tag{15}$$

which is determined from Eq. (13). If $\lambda_{\max}^{\perp} < 0$, then the mixed synchronous solution (11) is (locally) stable, i.e., small disturbances will vanish. On the other hand, if $\lambda_{\max}^{\perp} > 0$, the synchronous solution is unstable [9].

Remark 1 Note that the parameter values of the dynamic coupling (10), including the coupling strength k, should be chosen such that the largest transverse Lyapunov exponent (15), computed from the variational equation (13), is negative. However, it is still necessary to derive a formal procedure for tuning the parameters in the dynamic coupling. This, however, is the topic of our ongoing research.

4 Application to the Lorenz System

A classical chaotic system is the Lorenz system, which is described by [10]

$$\dot{x} = \sigma(y - x), \quad \dot{y} = \rho x - xz - y, \quad \dot{z} = xy - \beta z, \tag{16}$$

where σ, ρ, and β are positive parameters. This system is invariant under the transformation

$$(x_j, y_j, z_j) \to (-x_j, -y_j, z_j), \tag{17}$$

and consequently, the Lorenz system has the symmetry properties necessary for the onset of mixed synchronization, see Eq. (7).

In this part, the occurrence of mixed synchronization in a pair of Lorenz system interacting through the proposed scheme (8)–(10) is investigated. As a first step, the state vectors and the nonlinear functions corresponding to the master and slave, respectively, are defined as follows:

$$\boldsymbol{x}_{j_a} = \begin{bmatrix} x_j \\ y_j \end{bmatrix}, \quad \boldsymbol{x}_{j_c} = z_j, \quad \boldsymbol{F}_a = \begin{bmatrix} \sigma(y_j - x_j) \\ \rho x_j - x_j z_j - y_j \end{bmatrix}, \quad \boldsymbol{F}_c = x_j y_j - \beta z_j, \tag{18}$$

for $j = m, s$. Furthermore, the coupling terms $\boldsymbol{B}_{1_c}$ and $\boldsymbol{B}_{2_c}$ in (9)–(10) are chosen as follows:

$$\boldsymbol{B}_{1_c} = \begin{bmatrix} 0 & 1 \end{bmatrix}, \quad \text{and} \quad \boldsymbol{B}_{2_c} = \begin{bmatrix} 0 & 1 \end{bmatrix}^T. \tag{19}$$

The choice of $\boldsymbol{B}_{1c}$ indicates that only the second variable of the dynamic coupling (10) will be applied to the slave, and likewise, $\boldsymbol{B}_{2_c}$ is chosen such that only the second equation of the dynamic coupling is affected.

Then, by replacing (4), and (18)–(19) into (8)–(10) yields

$$\text{Master:} \quad \begin{cases} \dot{x}_m = \sigma(y_m - x_m), \\ \dot{y}_m = \rho x_m - x_m z_m - y_m, \\ \dot{z}_m = x_m y_m - \beta z_m, \end{cases} \tag{20}$$

$$\text{Slave:} \quad \begin{cases} \dot{x}_s = \sigma(y_s - x_s), \\ \dot{y}_s = \rho x_s - x_s z_s - y_s, \\ \dot{z}_s = x_s y_s - \beta z_s - h_2, \end{cases} \tag{21}$$

$$\text{Dynamic coupling:} \quad \begin{cases} \dot{h}_1 = -\alpha h_1 + h_2, \\ \dot{h}_2 = -\gamma_1 h_1 - \gamma_2 h_2 - k(z_m - z_s). \end{cases} \tag{22}$$

The local stability of the mixed synchronous solution $x_s = -x_m$, $y_s = -y_m$, $z_s = z_m$, and $h_1 = h_2 = 0$ in system (20)–(22) is investigated by using the results presented in Sect. 3. First, note that the corresponding variational equation is as given in (13), with

$$\boldsymbol{e}_a = \begin{bmatrix} x_m + x_s \\ y_m + y_s \end{bmatrix}, \quad \boldsymbol{e}_c = z_m - z_s, \quad \tilde{\boldsymbol{D}} = \begin{bmatrix} -\sigma & \sigma & 0 & 0 & 0 \\ \rho - z_m & -1 & -x_m & 0 & 0 \\ y_m & x_m & -\beta & 0 & 1 \\ 0 & 0 & 0 & -\alpha & 1 \\ 0 & 0 & -k & -\gamma_1 & -\gamma_2 \end{bmatrix}. \tag{23}$$

Next, the largest transverse Lyapunov exponent $\lambda_{\max}^{\perp}$ is computed, as a function of k and γ_2, from the variational equation (13) with $\tilde{D}$ as given in (23). For the computation, the following parameter values are used: $\sigma = 10$, $\rho = 28$, $\beta = 8/3$. For these parameter values, the uncoupled Lorenz systems exhibit chaotic behavior [10]. On the other hand, the parameters of the dynamic coupling, see Eq. (4), are chosen as follows: $\alpha = \gamma_1 = 1$. The coupling strength k is varied in the interval $k \in [0, 200]$ in steps of 1 and the parameter γ_2 of the dynamic coupling is also varied in the interval $\gamma_2 \in [0, 200]$ in steps of 1.

Figure 1 shows the obtained results. Clearly, there exists a large region (dark gray area) on the $(k, \gamma_2)-$plane for which the mixed synchronous solution is locally stable.

Fig. 1 $\lambda^{\perp}_{\max}$ as a function of
the coupling strength k and
parameter γ_2. In the dark gray
region, the mixed
synchronous solution is
locally stable
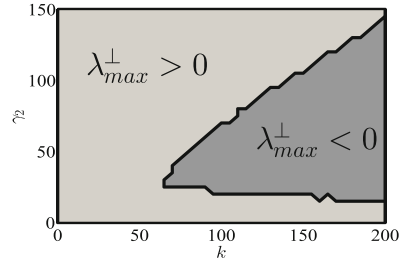
4.1 Comparison to the Classical Scheme

Finally, a comparison between the dynamic coupling scheme (8)–(10) is introduced
here, and the results obtained when using the classical master–slave scheme with
static coupling are presented for the case of Lorenz system. First, note that the static
version of the dynamically coupled Lorenz systems (20)–(22) is simply described by

$$
\text{M:} \begin{cases} \dot{x}_m = \sigma(y_m - x_m), \\ \dot{y}_m = \rho x_m - x_m z_m - y_m, \\ \dot{z}_m = x_m y_m - \beta z_m, \end{cases} \quad \text{S:} \begin{cases} \dot{x}_s = \sigma(y_s - x_s), \\ \dot{y}_s = \rho x_s - x_s z_s - y_s, \\ \dot{z}_s = x_s y_s - \beta z_s + k(z_m - z_s), \end{cases} \tag{24}
$$

and the corresponding variational equation is

$$
\begin{bmatrix} \dot{e}_x \\ \dot{e}_y \\ \dot{e}_z \end{bmatrix} = \begin{bmatrix} -\sigma & \sigma & 0 \\ (\rho - z_m) & -1 & -x_m \\ y_m & x_m & -\beta - k \end{bmatrix} \begin{bmatrix} e_x \\ e_y \\ e_z \end{bmatrix}. \tag{25}
$$

As a next step, the largest transverse Lyapunov exponent $\lambda^{\perp}_{\max}$ is computed for the
dynamic and static case. For the former, the variational equation (13)–(23) is used,
whereas for the latter the variational equation (25) is considered. For both cases,
the following parameter values are used: $\sigma = 10$, $\rho = 28$, $\beta = 8/3$, $\gamma_1 = 1$, and
$k = 200$. Additionally for the dynamic coupling we take: $\alpha = \gamma_1 = 1$, and $\gamma_2 = 30$.
The obtained results are shown in Fig. 2, from which it is clear that the dynamic
coupling has a better performance: $\lambda^{\perp}_{\max}$ is more negative and consequently, the
synchronous state is achieved faster. Additionally, system (20)–(22) and system (24)
have been numerically integrated by using the same parameter values mentioned
above. The initial conditions $x_m(0)$ and $x_s(0)$ are varied in the interval $[-10, 10]$
in steps of 0.02, and the remaining initial conditions are set to zero. The simulation
time is 300 [s] and, in the computations, the Runge–Kutta method with a time step
of 0.001 has been considered. The obtained results are shown in Fig. 3, where panel
(a) corresponds to the dynamic coupling and panel (b) to the static coupling. Clearly,
the regions of in-phase and mixed synchronization have a well-defined pattern for
the proposed scheme, whereas for the static configuration the obtained pattern is
rather scattered.

Fig. 2 $\lambda_{\max}^{\perp}$. Green: dynamic coupling. Red: static coupling
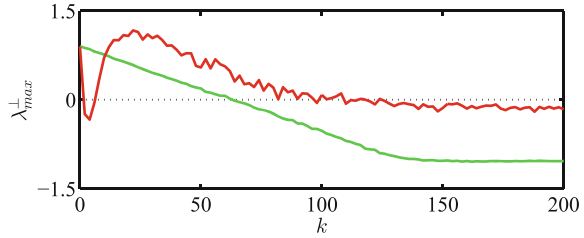
Fig. 3 Onset of mixed synchronization in a pair of coupled Lorenz systems. (**a**) Proposed coupling scheme (20)–(22). (**b**) Standard master–slave configuration (24). Yellow areas: mixed synchronization. Blue areas: complete synchronization
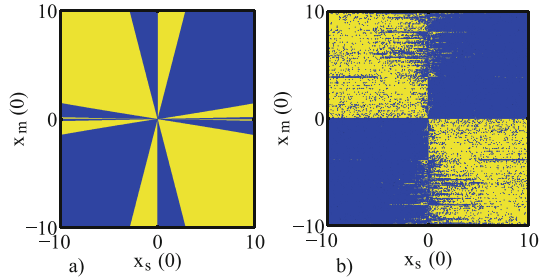
5   Discussion and Conclusions

We have presented a synchronization scheme for inducing mixed synchronization in unidirectionally coupled chaotic oscillators. The novelty in the proposed scheme is that the interaction between the systems is indirect via a dynamic coupling. One of the advantages of the proposed scheme is that the convergence to the mixed synchronous state is achieved faster than in the traditional scheme with static coupling.

Although here we have discussed the particular case of Lorenz system, the proposed synchronization scheme is applicable to other systems having the symmetry properties given in Eq. (7), as is the case with the Chen system [11] and the Sprott system [12]. For these systems, we have verified that the synchronization scheme presented here successfully induces mixed synchronization (although the results have not been included in this manuscript).

Also, it should be emphasized that further studies are required. For example, it is still necessary to conduct a formal analysis in order to determine the "optimal" parameters in the proposed dynamic coupling (10) and also, stronger stability conditions should be derived.

Finally, it is worth mentioning that the mixed synchronization phenomenon does not restrict to chaotic systems but it can be observed in several systems. For example, in the human body one can distinguish both in-phase and anti-phase correlations—i.e., mixed synchronization—in the motions of its components namely, arms, legs, knees, hips, anti-phase rotation of upper and lower body, among others. Furthermore, the phenomenon also finds interesting engineering applications, like for example, in synchronizing a network of heterogeneous mechanical systems [13].

References

1. Strogatz, S.: Sync. The Emerging Science of Spontaneous Order. Hyperon, New York (2003)
2. Fujisaka, H., Yamada, T.: Stability theory of synchronized motion in coupled-oscillator systems. Prog. Theor. Phys. **69**(1), 32–37 (1983)
3. Belykh, V.N., Belykh, I.V., Hasler, M.: Hierarchy and stability of partially synchronous oscillations of diffusively coupled dynamical systems. Phys. Rev. E **62**, 6332–6345 (2000)
4. Murakami, Y., Fukuta, H.: Stability of a pair of planar counter-rotating vortices in a rectangular box. Fluid Dyn. Res. **31**, 1–12 (2002)
5. Vigneshwaran, M., Dana, S.K., Padmanaban, E.: Mixed coherent states in coupled chaotic systems: design of secure wireless communication. EPL IOP Sci. **116**, 50010 (2016)
6. Bakker, R.S., Selen, L.P., Medendorp, W.P.: Stability of phase relationships while coordinating arm reaches with whole body motion. PLoS One **10**, 0146231 (2015)
7. Prasad, A.: Universal occurrence of mixed-synchronization in counter-rotating nonlinear coupled oscillators. Chaos, Solitons Fractals **43**, 42–46 (2010)
8. Pena Ramirez, J., Arellano-Delgado, A., Nijmeijer, H.: Enhancing master-slave synchronization: the effect of using a dynamic coupling. Phys. Rev. E **98**, 012208 (2018)
9. Pecora, L.M., Carroll, T.L.: Master stability functions for synchronized coupled systems. Phys. Rev. Lett. **80**, 2109–2112 (1998)
10. Lorenz, E.N.: Deterministic nonperiodic flow. J. Atmos. Sci. **20**, 130–141 (1963)
11. Chen, G., Ueta, T.: Yet another chaotic attractor. Int. J. Bifurcation Chaos **9**, 1465–1466 (1999)
12. Sprott, J.C.: Some simple chaotic flows. Phys. Rev. E **50**, R647–R650 (1994)
13. Alvarez, J., Cuesta, R., Rosas, D: Robust output synchronization of second-order systems. Eur. Phys. J. Spec. Top. **223**, 757–772 (2014)

Synchronized Hopping Induced by Interplay of Coupling and Noise

V. Manaoj Aravind, K. Murali, and Sudeshna Sinha

Abstract We explore the behaviour of coupled bistable systems subject to noise from two independent uncorrelated noise sources, over a range of coupling and noise strengths. We find that the interplay of coupling and noise leads to the emergence of four behavioural regimes: no synchrony and no hopping; unsynchronized hopping; synchronized hopping; synchrony without hopping. We show the occurrence of this phenomenon in a variety of bistable systems including the synthetic genetic network model, in the presence of both uniform and Gaussian noise, indicating the generality of this phenomenon. Further, we experimentally verify the different regimes of behaviour in coupled bistable electronic circuits, thus establishing its robustness.

1 Introduction

Synchronization has emerged as a very significant phenomenon in fields as diverse as electronic circuits and biological systems. The key element in synchronization is the coupling. It has been observed in a large class of systems that, increasing the coupling strength induces the onset of synchronization [1].

In another direction, the phenomena of escape from locally stable states induced by noise have seen long-standing attention. It has crucial bearing on fields ranging from chemical kinetics to diffusion in solids.

The central focus of this work is to combine these two important threads: first, noise induces hopping in bistable systems and the second is the onset of synchronization in the presence of sufficient coupling. The question we investigate is the following: when does the random hopping events induced by noise become synchronous in coupled bistable systems? Importantly, the systems here are subject

V. M. Aravind (✉) · S. Sinha
Indian Institute of Science Education and Research Mohali, Punjab, India
e-mail: manaojaravind@iisermohali.ac.in; sudeshna@iisermohali.ac.in

K. Murali
Department of Physics, Anna University, Chennai, India
e-mail: kmurali@annauniv.edu

to *independent random influences*. This uncorrelated noise *is expected to hinder synchronization*, as it is does not provide a common drive to the sub-systems. On the other hand, noise will *aid frequent switches* between the locally stable wells. A balance of these two opposing trends may yield synchronized switching of states. The aim of this work is to explore this possibility in a range of bistable systems, under different kinds of noise.

Note that the phenomenon we are exploring is distinct from the phenomenon of stochastic resonance, and also distinct from the phenomenon of synchronization aided by common noise. In stochastic resonance, the effect of increasing noise on a bistable system has revealed counterintuitive phenomena: it has been found that noise can enhance the response of the bistable system to weak sub-threshold signals, periodic driving or wide-band input signals. This phenomenon, known as stochastic resonance [2], has been demonstrated in many natural and engineered systems, and has also been utilized to increase reliability of computations [3, 4]. However, here we have *no external signal* driving the coupled bistable systems, and so if synchronized hopping emerges in our system, its origin cannot be understood in terms of an external drive.

The phenomena here is also distinct from noise-aided synchronization, which arises in systems experiencing *common noise* or the parameters of the system experience common random fluctuations [5]. Here on the other hand the noise on the two sub-systems is *uncorrelated*, and is therefore expected to *inhibit* synchronization.

2 Model

Consider a system of coupled bistable systems whose dynamical equations have the general form:

$$\dot{x_1} = F(x_1) + c(x_2 - x_1) + D\,\eta_1(t), \tag{1}$$
$$\dot{x_2} = F(x_2) + c(x_1 - x_2) + D\,\eta_2(t)$$

where F is a nonlinear function that gives rise to a bistable potential, and the coupling is linear and bidirectional.

We consider the additive noise $\eta_1(t)$ and $\eta_2(t)$ in the two sub-systems to be independent and uncorrelated, and we have considered both (a) uniform noise drawn from a uniform distribution in the range $[-1 : 1]$, and (b) zero mean Gaussian noise with variance 1, with the parameter D indicating the noise strength, with $D \in [0 : 1]$.

We start with the illustrative example where F in Eq. 2 is a simple nonlinear function of the form

$$F(x_i) = a_1(x_i - a_2 x_i^3) \tag{2}$$

Specifically, with no loss of generality, we choose the values $a_1 = 4$ and $a_2 = 5$. This system gives rise to two stable fixed points $x_+ > 0$ and $x_- < 0$, separated by an unstable fixed point (the "barrier") at zero. We denote the state characterized by positive-valued state variables as the "positive well", and the state characterized by negative-valued state variables as the "negative well".

We focus on two features of the dynamical patterns of the state variables x and y of the two sub-systems. First is the propensity of the sub-systems to jump between the two wells, i.e. the probability of *hopping*. The second feature of significance is *synchrony*. Note that synchrony here *does not imply complete synchronization*, where $x_1(t) = x_2(t)$ for all t after transient time. Rather it implies that the two sub-systems are confined to the same well, with both x_1 and x_2 being in the neighbourhood of the same fixed point, i.e both sub-systems are in the basin of attraction of x_+, or both are in the basin of x_-. The combination of these two features dictates the different classes of dynamical patterns.

Our central observation in this system is the following:

Depending on the noise strength and coupling strength four behavioural regimes emerge:

1. The first regime occurs when both coupling and noise are low, and is characterized by no hops at all during the time of observation (which was very long) and additionally there was no synchrony either.
2. The second type of behaviour arises for low coupling strengths and high noise strengths, and is characterized by the sub-systems switching between the wells. However, this hopping is not synchronized. So when one sub-system is in the positive well, the other sub-system may be in the negative well.
3. Thirdly, for strong coupling and weak noise one finds that the two sub-systems are synchronized and remain confined to the same well during the entirety of the long run-time, i.e. there is synchrony without hopping.
4. Lastly, for a specific range of noise strength D and coupling constant c, the system exhibits random hopping between the two wells in a synchronous manner. That is, the two sub-systems jump together from one well to another. We label this special dynamical pattern as *synchronized hopping*.

Figure 1 displays these different behaviours, observed in different ranges of coupling c and noise strength D. In this work we explore the range $c \in [0, 6]$ and $D \in [0, 1]$.

Note that an early result on coupled bistable systems driven by independent noise sources [6] had indicated that the stochastic processes in the sub-systems become coherent when the strength of coupling achieves a critical value (namely, the dynamical pattern 4. However, the full implications of the *interplay* of coupling strength and noise strength on the emergence of synchronized hopping were not explored. Also, the dynamical patterns in the regions outside synchronized hopping, in the extended parameter space of coupling strength and noise strength, were not obtained. In this work we will address these open questions. We will also obtain an understanding of the range of coupling, as well the range of noise, that yields synchronized hopping, and the relationship between them. This will allow
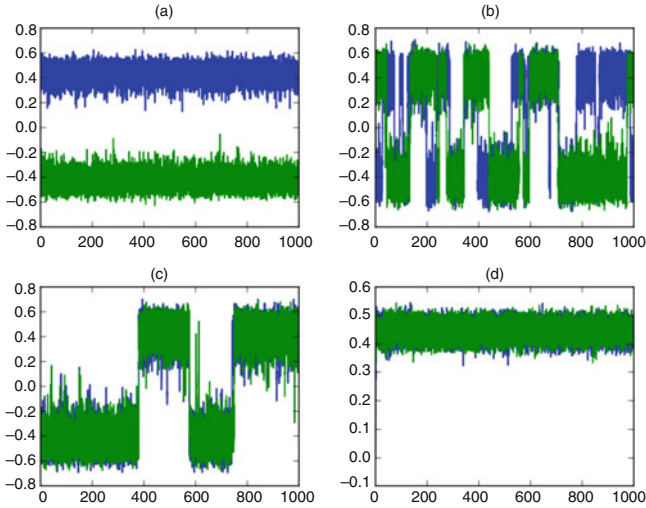
Fig. 1 Timeseries of the two state variables x_1 (blue) and x_2 (green) of the two sub-systems, for four illustrative values of noise strength D and coupling strength c, displaying different dynamical patterns: (**a**) no synchronization and no hopping, when $D = 0.2$, $c = 0.1$; (**b**) unsynchronized hopping, when $D = 0.3$, $c = 0.2$; (**c**) synchronized hopping, when $D = 0.32$, $c = 1$; (**d**) synchrony without hopping, when $D = 0.1$, $c = 1$

us to judge the prevalence of the phenomena. Lastly, we will verify our results in electronic circuit experiments.

3 Characterization

Now we will attempt to quantify the qualitative behaviour observed above, using a measure analogous to synchronization error, along with an estimate of the probability of hopping. The aim here was to precisely characterize the observed synchronized hopping in the system by finding the window of coupling strengths and noise strengths where there is a concurrence of *reasonable synchrony* and *sufficiently frequent switching*.

First we introduce a variant of synchronization error Z, defined as the probability of the states of the two systems to be in different wells. This is estimated by following the states of the two systems over long times, and finding the fraction of time the two systems reside in different wells.

When $Z = 0$, the states of the two systems are always in the basin of attraction of the same fixed point, namely the states of the systems are on the same side of the barrier, i.e., both states are in the "positive well" or both in the "negative well". Note that our measure of synchronization error is not the usual measure reflecting deviation from complete synchronization. Rather it reflects the degree to which the

two multi-stable systems reside in the same well. Note that when the systems are in the same well (i.e. either both are positive, or both negative) the sign of the product of the state variables of the two sub-systems x_1 and x_2 at a given instant of time is positive. On the other hand, if the systems are in different wells, the sign of the product of the state variables of the two sub-systems at a given instant of time is negative. So our synchronization error Z is easily defined mathematically as,

$$Z = \frac{1}{N} \sum_{i=1}^{N} H(x_1[i] \times x_2[i]) \tag{3}$$

This quantity then serves as an order parameter that can reflect the transition from the case where both systems are in the same well at all times, to the case where they inhabit different wells for significant amounts of time.

The second important quantity is the probability of hopping h, which is estimated through the number of jumps between the two wells, in either system, over a prescribed very long (though necessarily finite) period of time. The key feature to note when the systems switch between positive and negative wells is that the sign of the product of the state variables just before the hop and just after the hop is negative. So the hopping probability can be estimated readily by

$$h = \frac{1}{N-1} \sum_{i=1}^{N} H(x_1[i] \times x_1[i-1]) \tag{4}$$

where N is the total number of timesteps in the observed timeseries, with N being very large, and H given as

$$H(x_i) = \begin{cases} 1 & x_i < 0 \\ 0 & x_i \geq 0 \end{cases}$$

Both Z and h are averaged over a large sample of initial conditions, chosen randomly from the interval $[-1, 1]$.

Figure 2a, b shows the dependence of the synchronization error on coupling and noise strengths. It is clear that for low coupling and low noise, the states of the sub-systems are almost uncorrelated. Since the synchronization order parameter is averaged over a sample of initial conditions uniformly distributed across the two wells, the two sub-systems maybe in the same well, or in different wells, with equal probability. So Z is close to 0.5 when c and D are very small. As coupling strength increases (cf. Fig. 2a), synchronization between the sub-systems is induced. It is also evident from Fig. 2b that for high coupling strengths the synchronization error increases monotonically after a minimum noise threshold. However, interestingly, *for low coupling strengths the degree of synchronization varies non-monotonically with noise strength*. For low noise strengths the system is largely unsynchronized, after which there is a *window of moderate noise where the synchronization error is*
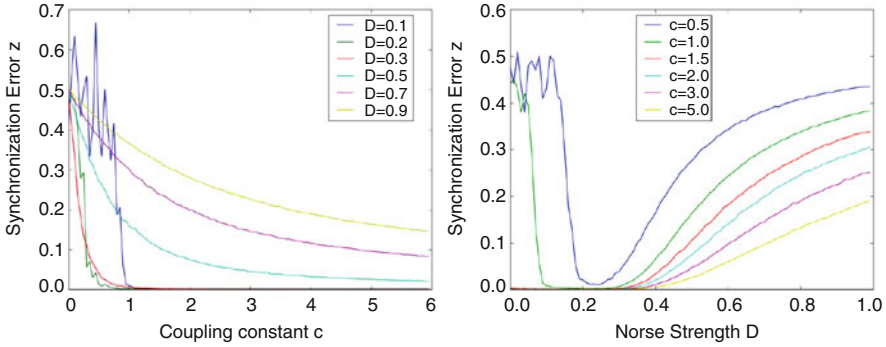
Fig. 2 Dependence of the synchronization error Z on (left) coupling strength c, and (right) noise strength D
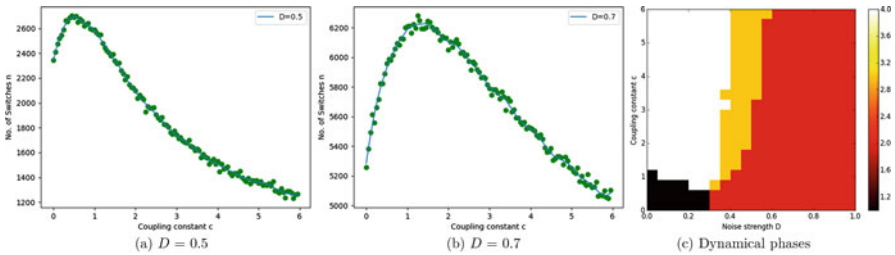
Fig. 3 (**a**) and (**b**) Dependence of the probability of hopping on coupling constant c, for various noise strengths D. (**c**) Different dynamical behaviors in the parameter space of coupling strength and noise strength. The colours indicate the following: BLACK—No synchrony, and extremely low probability of hopping; RED—No synchrony, with reasonable probability of hopping; ORANGE—Synchronized hopping, namely where there is reasonable synchronization as well as reasonable probability of hopping; WHITE—Synchronized sub-systems with extremely low probability of hopping

very low. For noise strengths beyond this window the synchronization error again rises, as is intuitively expected.

The second measure, the probability of switches, simply reflects how often the sub-systems switch between the two wells. This gives a measure of the average amount of time spent in a particular well, under varying D and c. As clearly evident from Fig. 3, the *hopping probability varies non-monotonically with increasing coupling strengths*. That is, there exists an optimal value of coupling strength c for which the probability of switches in maximized. The value of the optimal coupling strength is dependent on noise strength D. The switching is significant only after a minimum noise threshold. This is expected, since a minimum strength of noise is needed in order to drive a system to cross the barrier to the other well. So there is a monotonous increase in the probability of hopping with increasing noise strength D. The threshold of noise strength D after which synchronization error Z and

probability of hopping assume significant finite values is the same (within statistical error).

So, for sufficiently large noise strengths, the noise can push the sub-systems to hop between the two wells. At these high noise strengths, if the coupling is also sufficiently high, the sub-systems switch between wells in synchrony: namely, we observe synchronized random hops. Such a phenomena will be seen only if the system lies in the window of noise where synchronization error is small and the probability of hopping is sufficiently large, provided these two windows have a reasonable overlap. Further the system has to simultaneously lie in the window of coupling strengths that is sufficiently high to induce approximate synchronization between the sub-systems, and the window of coupling where the probability of hopping is sufficiently large. Again if this intersection of parameter regions is a null set, we will not obtain the synchronized hopping phenomena. Note that the synchronized hopping phenomena is also non-trivial as the dependence of both synchronization and the hopping probability is non-monotonic with respect to coupling and noise strength. In general, the synchronized hopping phase lies on the boundary of the dynamical phase of unsynchronized hopping and synchrony with (almost) no hopping.

To quantitatively demarcate the different behaviours in parameter space, we first introduce a threshold for both synchrony and hopping probability. We consider the following: if synchronization error $Z < 0.01$ then the two systems are considered synchronized, and if the probability of switching $h > 5 \times 10^{-5}$ then we consider the system to be "hopping". Using these conditions the various behaviours in parameter space are shown in Fig. 3c. We see synchronized hopping occurs in a somewhat narrow region of parameter space (marked by orange). The exact boundaries of the region are dependent of the synchronization and hopping probability threshold chosen to describe the phase. However, qualitatively the phenomena emerge independent of the exact thresholds employed in the definition of the dynamical phase.

We have checked the generality of the observations above for the case of uniformly distributed noise. The synchronized hopping again occurs in a region of moderate noise and sufficiently high coupling, as evident from the results displayed in Fig. 4.

Lastly, we study the dynamics of two other bistable systems, in order to check the robustness and generality of our observations above. First we consider a single gene synthetic genetic network model developed in [7]. It describes the regulation of the operator region of a λ phage, whose promoter region consists of three operator sites. With suitable rescaling and considering the total concentration of DNA promoter sites to be constant, the reactions describing this network attain the form,

$$\dot{x} = \frac{m(1 + x^2 + \alpha \sigma_1 x^4)}{1 + x^2 + \sigma_1 x^4 + \sigma_1 \sigma_2 x^6} = F(x) \tag{5}$$

where, x is the concentration of the repressor. $\sigma_1 = 2$, $\sigma_2 = 0.08$ and $\alpha = 11$ for the operator region of the λ phage and number of plasmids $m = 1$.
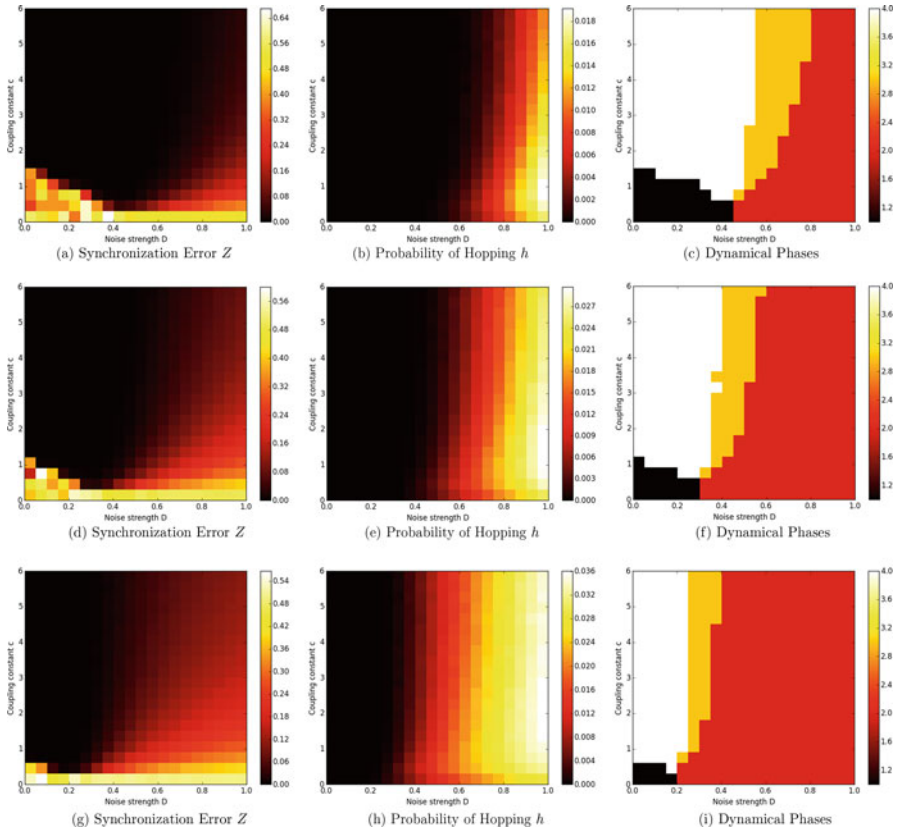
Fig. 4 (**a**) Dependence of the synchronization error Z in the coupled bistable system under uniform noise, on coupling strength c and noise strength D. (**b**) Dependence of the probability of hopping h on the coupling strength c and noise strength D. (**c**) Different dynamical behaviors in the parameter space of coupling strength and noise strength. The colours scheme is the same as indicated in Fig. 3c. (**d**), (**e**) and (**f**) present the corresponding plots for the synthetic gene network model in Eq. 5. (**g**), (**i**) and (**h**) present the same for the piecewise linear model in Eq. 7

This biological model exhibits bi-stability and given that biological systems are intrinsically noisy, it is of considerable interest to see if synchronized hopping emerges here as well.

We further investigate another coupled system, relevant for electronic circuits (Eq. 7). It is clearly evident from Fig. 4a–i that our results hold for these bistable systems as well. This suggests that the phenomenon of synchronized hopping is quite general and occurs whenever coupling is sufficiently high and noise is in a moderate window.

4 Experimental Implementation

In order to establish the robustness of the observed phenomena we constructed two simple bistable piecewise linear circuits and coupled them via a resistor. Figure 5 shows the schematic representation of the constructed circuit. The non dimensional equation governing the circuit reads:

$$\dot{x}_1 = F(x_1) + c(x_2 - x_1) + D\, \eta_1(t), \qquad (6)$$
$$\dot{x}_2 = F(x_2) + c(x_1 - x_2) + D\, \eta_2(t)$$

where F is a piecewise linear function given by

$$F(x_i) = \begin{cases} -(x_i + 1) & x_i < -0.5 \\ x_i & -0.5 \le x_i \le 0.5 \\ -(x_i - 1) & x_i > 0.5 \end{cases}$$

The time trails of the two capacitor voltages for various values coupling and noise strength are also shown in Fig. 5. The four dynamical regimes of behaviour are clearly evident, thus establishing the wide real world prevalence of the phenomenon.

(a) No synchrony and no hopping   (b)   Unsynchronized hopping

(c) Syncronized hopping   (d) Synchrony without hopping
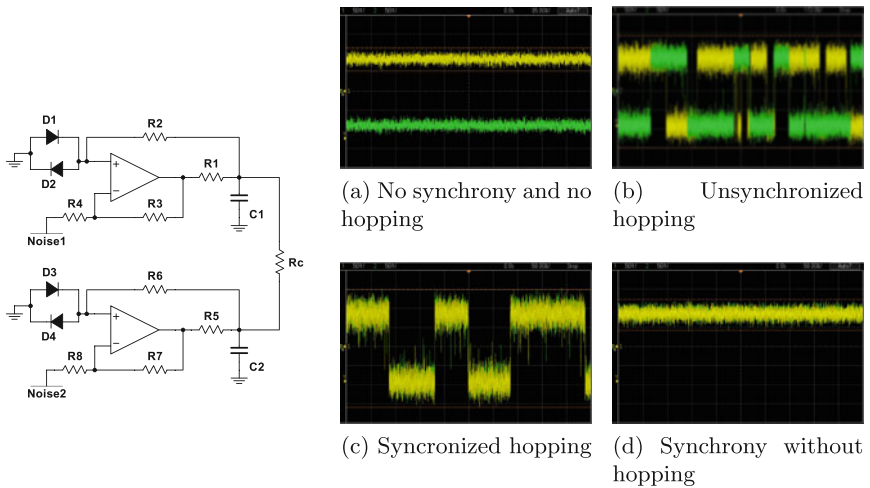
Fig. 5 Left: Schematic representation of the circuit. Here, resistances R_1, $R_5 = 70\Omega$, R_2, R_3, R_4, R_6, R_7, $R_8 = 10k\Omega$ and capacitances $C_1, C_2 = 470\mu F$. **Right:** Experimental observation of the four different behavioral patterns, including synchronized hopping, for different values of coupling resistance R_c and noise amplitude D. **(a)** $R_c = 1k\Omega$, $D = 450mV$ **(b)** $R_c = 9.15k\Omega$, $D = 950mV$ **(c)** $R_c = 180\Omega$, $D = 1.30V$ **(d)** $R_c = 180\Omega$, $D = 700mV$

5 Conclusions

We explored the behavior of coupled bistable systems subject to noise from two independent noise sources, over a range of coupling and noise strengths. We found that the interplay of coupling and noise leads to the emergence of four behavioral regimes: no synchrony and no hopping; unsynchronized hopping; synchronized hopping; synchrony without hopping. We demonstrated the occurrence of this phenomenon in a variety of bistable systems, in the presence of both uniform and Gaussian noise. Further, we experimentally verified the different regimes of behavior in coupled bistable electronic circuits, thus establishing its robustness. Different theoretical approaches to analyze the phenomena is an open problem. Information theoretic measures to characterize the observed phenomena and solving the relevant Fokker–Planck equations [8] would be useful directions for future work.

References

1. Pikovsky, A., Rosenblum, M., Kurths, J.: Synchronization: A Universal Concept in Nonlinear Sciences, vol. 12. Cambridge University Press, Cambridge (2003)
2. Gammaitoni, L., Hänggi, P., Jung, P., Marchesoni, F.: Stochastic resonance. Rev. Mod. Phys. **70**, 223 (1998)
3. Murali, K., Sinha, S., Ditto, W.L., Bulsara, A.R.: Reliable logic circuit elements that exploit nonlinearity in the presence of a noise floor. Phys. Rev. Lett. **102**, 104101 (2009)
4. Aravind, M., Murali, K., Sinha, S.: Coupling induced logical stochastic resonance. Phys. Letts. A **382**, 1581–1585 (2018)
5. Kiss, I.Z., Hudson, J.L., Escalona, J., Parmananda, P.: Noise-aided synchronization of coupled chaotic electrochemical oscillators. Phys. Rev. E **70**, 026210 (2004)
6. Neiman, A.: Synchronizationlike phenomena in coupled stochastic bistable systems. Phys. Rev. E **49**, 3484 (1994)
7. Hasty, J., Isaacs, F., Dolnik, M., McMillen, D., Collins, J.J.: Designer gene networks: towards fundamental cellular control. Chaos **11**, 207–220 (2001)
8. Perkins, E., Balachandran, B.: Effects of phase lag on the information rate of a bistable Duffing oscillator. Phys. Letts. A **379**, 308–313 (2015)

Author Index

A

Abdou, L., 178, 180, 187, 191, 193
Ahmadi, G., 111, 114
Alakshendra, V., 208, 213, 215
Alarcon, F., 218
Alcala, I., 276
Alexander, N.A., 64
Alvarez, J., 315–322
Anderson J., 130, 131
Anderson, S.J., 158
d'Andréa-Novel, B., 23–31
Andreaus, U., 119–120, 125, 127
De Angelis, M., 119, 120, 125–127
Antonelli, D., 217–219, 227–235
Aptista, M.S., 295
Aracil, J., 276
Aragones, J.L., 218
Aravind, V.M., 325–334
Arellano-Delgado, A., 316
Arena, A., 129–135
Arnold, F.R., 100
Astashev, V., 305
Åström, K.J., 147
Atalik, T.S., 111
Auer, S., 295
Avramov, K.V., 80
Awrejcewicz, J., 180

B

Babitsky, V., 305
Badwe, A.S., 148
Bakker, R.S., 316
Balachandran, B., 334
Balendra, T., 44

Balthazar, J., 305
Balthazar, J.M., 79, 80, 237–238, 240, 242, 243
Baptista, M.S., 295
Baragatti, P., 120
Basu, B., 44
Bellen, A., 140
Belykh, I.V., 316
Belykh, V.N., 316
Ben-Jacob, E., 218
Bergman, L., 13
Bergman, L.A., 119
Bernard, M.C., 115
Bernstein, D.S., 26
Bernuau, E., 24, 26
Bezanson, J., 84
Bhat, S.P., 26
Bhushan, B., 60
Bielak, J., 198
Billings, S., 14
Bleckman, I., 305, 306
Blekhman, I., 305
Bobber, R.J., 24
Boccamazzo, A., 99–101, 104, 106
Bode, W.H., 276
Bogdanoff, J., 115
Bogdanov, D., 305
Boral, C., 60
Borrelli, F., 158
Botto, D., 197–205
Bouabdallah, S., 178, 187, 189
Bouc, R., 101
Brasil, R., 305
Brasil, R.M.L.R.F., 240
Brasil, M.R.L.F., 242

Subject Index